

UNCLASSIFIED

AD NUMBER
AD819915
NEW LIMITATION CHANGE
TO Approved for public release, distribution unlimited
FROM Distribution authorized to U.S. Gov't. agencies and their contractors; Administrative/Operational Use; JUN 1967. Other requests shall be referred to Air Force Flight Dynamics Lab., Wright-Patterson AFB, OH 45433.
AUTHORITY
AFFDL ltr, 1 Feb 1973

THIS PAGE IS UNCLASSIFIED

AD819915

**AERODYNAMIC DEPLOYABLE DECELERATOR
PERFORMANCE-EVALUATION PROGRAM**

PHASE II

E. BLOETSCHER

GOODYEAR AEROSPACE CORPORATION

TECHNICAL REPORT AFFDL-TR-67-25

JUNE 1967

This document is subject to special export controls and each transmittal to foreign governments or foreign nationals may be made only with prior approval of the Air Force Flight Dynamics Laboratory.

**AIR FORCE FLIGHT DYNAMICS LABORATORY
RESEARCH AND TECHNOLOGY DIVISION
AIR FORCE SYSTEMS COMMAND
WRIGHT-PATTERSON AIR FORCE BASE, OHIO**

**Best
Available
Copy**

NOTICE

When Government drawings, specifications, or other data are used for any purpose other than in connection with a definitely related Government procurement operation, the United States Government thereby incurs no responsibility nor any obligation whatsoever; and the fact that the Government may have formulated, furnished, or in any way supplied the said drawings, specifications, or other data, is not to be regarded by implication or otherwise as in any manner licensing the holder or any other person or corporation, or conveying any rights or permission to manufacture, use, or sell any patented invention that may in any way be related thereto.

Copies of this report should not be returned unless return is required by security considerations, contractual obligations, or notice on a specific document.

AFFDL-TR-67-25

**AERODYNAMIC DEPLOYABLE DECELERATOR
PERFORMANCE-EVALUATION PROGRAM**

PHASE II

F. BLOETSCHER

This document is subject to special export controls and each transmittal to foreign governments or foreign nationals may be made only with prior approval of the Air Force Flight Dynamics Laboratory.

FOREWORD

The work described in this report was performed by Goodyear Aerospace Corporation, Akron, Ohio, under the authority of Project 6065, Task 606505, entitled "Aerodynamic Deployable Decelerator Performance-Evaluation Program, Phase II"; and Air Force Contract No. AF33(615)-1513.

Mr. S. McFarland and Mr. W. R. Pinnell of the Flight Dynamics Laboratory, Research and Technology Division, served as contract monitors.

The authors and contributing personnel of Goodyear Aerospace were W. V. Arnold, project engineer; F. Bloetscher, decelerator evaluation; W. W. Sowa, thermal analysis; I. M. Jaremenko, aerodynamic analysis; R. E. Altgelt, design and analysis; J. Schlemmer, trajectory analysis; W. A. Barr, decelerator design; D. Topping, decelerator structural analysis; J. J. Dean, missile development; R. G. Slayman, materials; and A. C. Aebischer, field testing.

Goodyear Aerospace acknowledges the support and technical information supplied by the following Recovery and Crew Station personnel for programs supporting decelerator research:


Mr. S. R. Metres

Mr. W. R. Pinnell

The contractor's number for this report is GER-12907.

This manuscript was released by the authors April 1967 for publication as an RTD technical report.

This technical report has been reviewed and approved.



GEORGE A. SOLT, JR.

Chief, Recovery & Crew Station Branch
Vehicle Equipment Division
AF Flight Dynamics Laboratory

ABSTRACT

The Aerodynamic Deployable Decelerator Performance-Evaluation Program (ADDPEP) aims to advance the state of the art by developing the most effective analytical and empirical techniques for designing aerodynamic deployable decelerators and for evaluating these engineering techniques through wind-tunnel and free-flight tests. During ADDPEP Phase II, two types of decelerators were investigated: large reefed supersonic parachutes and ram-inflated balloon-type BALLUTES. The areas investigated included analytical and engineering design, material capabilities, fabrication techniques, and wind-tunnel and free-flight tests. In general, efforts were successful in developing engineering techniques for the design of decelerators capable of performing in severe environments. More specifically: (1) Free-flight tests were performed on a hemisflo parachute having a nominal 16-ft-diameter canopy, a 10-percent extended skirt, and a 14-percent porosity. This design was tested for 200,000-lb opening loads; deployment Mach numbers were 1.50, 1.63, and 1.84 at altitudes of 13,700, 15,500, and 10,500 ft, respectively. The results confirmed that this parachute has excellent aerodynamic characteristics and adequate strength. (2) Five-foot-diameter BALLUTES, both textile and metal, were fabricated. These were designed for a broad spectrum of deployment conditions ranging from Mach 2.7 at 73,000 ft to Mach 10 at 225,000 ft. The textile BALLUTES were wind-tunnel and free-flight tested; the metal BALLUTES were wind-tunnel tested only. Flight tests were limited to Mach 9.7, and wind-tunnel tests to Mach 3. The flight test data supported wind-tunnel data, which indicated that excellent stability and structurally adequate designs can be attained with five-foot-diameter BALLUTES.

TABLE OF CONTENTS

<u>Section</u>	<u>Title</u>	<u>Page</u>
I	INTRODUCTION AND SUMMARY.	1
	1. Background	1
	2. ADDPEP Phase I	1
	3. ADDPEP Phase II	2
II	FREE-FLIGHT TEST CAPABILITY.	5
	1. Test Vehicle A/Booster System	5
	2. Test Vehicle C/Booster System	9
	3. Ground Support.	9
	4. Summary and Conclusions	14
III	LARGE PARACHUTE DECELERATOR	15
	1. General	15
	2. Exploratory Free-Flight Tests.	18
	3. Aerodynamic Analysis.	25
	4. Large Parachute Geometry	51
	5. Structural Loads and Material Selections	57
	6. Thermodynamic Analysis	60
	7. Material, Seam, and Joint Testing	66
	8. Design and Fabrication	70
	9. Deployment System and Packing Procedure	73
	10. Summary and Conclusions	80
IV	TEXTILE BALLUTE DECELERATOR	85
	1. General	85
	2. Wind-Tunnel and Free-Flight Tests.	91
	3. Aerodynamic Analysis	101
	4. BALLUTE Geometry	108
	5. Structural Loads	110
	6. Thermodynamic Analysis	120
	7. Material, Seam, and Joint Testing	131
	8. Design and Fabrication	135
	9. Deployment Sequence and Packing Procedure	138
	10. Summary and Conclusions	141

TABLE OF CONTENTS

AFFDL-TR-67-25

<u>Section</u>	<u>Title</u>	<u>Page</u>
V	METAL BALLUTE DECELERATOR	147
	1. General	147
	2. Wind-Tunnel Tests	147
	3. Aerodynamic Analysis.	149
	4. BALLUTE Geometry	150
	5. Structural Analysis	152
	6. Thermodynamic Analysis	158
	7. Material Testing	160
	8. MB-1 Design and Fabrication	167
	9. Deployment Sequence and Packing Procedure	169
	10. Summary and Conclusions	169
VI	CONCLUSIONS	171
	1. General	171
	2. Free-Flight Test Capability	171
	3. Large Parachute Decelerator	171
	4. Textile and Metal BALLUTE Decelerators. .	172
<u>Appendix</u>		
I	AMBIENT CONDITIONS AT 12.622-SEC POINT OF LP-5 TRAJECTORY.	173
II	AMBIENT CONDITIONS AT 12.472-SEC POINT OF LP-5 TRAJECTORY.	175
III	SPECIFICATION FOR COATING ADDPEP BAL- LUTES WITH D-65	177
IV	AERODYNAMIC HEATING RATES AND TEM- PERATURE RESPONSE	179
	LIST OF REFERENCES	191

LIST OF ILLUSTRATIONS

<u>Figure</u>	<u>Title</u>	<u>Page</u>
1	Test Vehicle A	7
2	Test Vehicle C	11
3	Field Operations Flow	13
4	Drag Area versus Mach Number (Wind-Tunnel Testing)	17
5	Nominal Drag Coefficient versus Inlet Reefing Ratio (Wind-Tunnel Testing)	18
6	General Arrangement of 16-Ft D ₀ Hemisflo Parachute	19
7	LP-3: (A) Performance Curves; (B) Inlet Area Variation with Time	22
8	LP-4: (A) Performance Curves; (B) Inlet Area Variation with Time	24
9	LP-5: (A) Performance Curves; (B) Inlet Area Variation with Time	26
10	Comparison of Small-Scale and Free-Flight Data	27
11	LP-3, LP-4, LP-5: (A) Mach Number versus Time; (B) Dynamic Pressure versus Time	28
12	LP-3, LP-4, LP-5: Load or Deceleration versus Time	29
13	LP-3, LP-4, LP-5: Load/Dynamic Pressure and Nominal Surface Drag Coefficient versus Time	30
14	LP-3, LP-4, LP-5: Load/Dynamic Pressure and Nominal Surface Drag Coefficient versus Mach Number	30
15	Reefing Line Length (RLL) and Reefed Inlet Area (RIA) versus Coefficients (K).	32
16	Geometric Nomenclature	34
17	LP-3 Deployment: Calculated and Measured Force-Time Relationship	39

<u>Figure</u>	<u>Title</u>	<u>Page</u>
18	LP-4 Deployment: Calculated and Measured Force-Time Relationship	40
19	LP-5 Deployment: Calculated and Measured Force-Time Relationship	41
20	LP-5: Inlet Area, Acceleration, and Force versus Time	42
21	Stress-Strain Relationships of Suspension-Line Webbing	48
22	Sixteen-Foot D ₀ Hemisflo Profile Dimensions	54
23	Ribbon Arrangement for Typical Gore.	54
24	Reefing Line Layout and Construction for LP-4 and Subsequent LP-5	61
25	Calculated LP-9 Trajectory from Deployment	62
26	Reefed 16-Ft D ₀ Hemisflo Parachute	63
27	Thermal Models	64
28	Temperature versus Time from Deployment.	66
29	Suspension Line Loops Test Specimen.	69
30	Suspension Line Skirt Band Joint	71
31	Reefing Ring Attachment Test Configuration	71
32	Deployment Sequence of 16-Ft D ₀ Hemisflo Test Parachute	74
33	Folding Canopy.	75
34	Suspension Line: (A) Grouping at Attachment Loops; (B) Stacking for Tacking.	77
35	Parachute Packing Procedure	79
36	Packed Parachute.	81
37	Textile BALLUTES: Mach Number and Altitude versus Time (Predicted for Design).	87
38	Textile BALLUTES: Dynamic Pressure and Load Factor versus Time (Predicted for Design)	88

LIST OF ILLUSTRATIONS

AFFDL-TR-67-25

<u>Figure</u>	<u>Title</u>	<u>Page</u>
39	Textile BALLUTES: Reynolds Number versus Free-Flight Velocity (Predicted for Design).	89
40	Textile BALLUTE Decelerators	90
41	Wind Tunnel Deployment Characteristics: (A) TB-1BWT; (B) TB-4WT.	93
42	TB-1A Performance	95
43	TB-1B Performance	97
44	TB-2 Performance	98
45	TB-3 Performance	100
46	TB-4 Performance	102
47	BALLUTE Flight Tests: Drag and Projected Areas versus Mach Number	103
48	BALLUTE Surface Pressure Distribution: (A) Mach = 6, $x/D = 9$; (B) Mach = 10, $x/D = 10$. . .	105
49	Textile and Metal BALLUTES: Inlet and Internal Pressure Coefficient Data	107
50	Textile and Metal BALLUTES: Drag Coefficient versus Mach Number	109
51	Flight-Test and Wind-Tunnel Configurations.	111
52	Isotenoid BALLUTE Shapes for C_{p_i} and K Values	113
53	Nomex Strength (Percent of Room Temperature Strength) versus Temperature	118
54	Payload and BALLUTE Flow Field Schematic	124
55	Pressure Distribution Over BALLUTE	125
56	Cold Wall Heat Flux Rate: (A) Deployment; (B) Re-entry	127
57	Unified Wake Transition Criterion	128
58	Flight Test TB-4: Predicted and Measured Temperature.	129
59	Calculated BALLUTE Internal Pressures and Temperatures Based on TB-3 Flight Test Conditions . .	132

LIST OF ILLUSTRATIONS

AFITDL-TR-67-25

<u>Figure</u>	<u>Title</u>	<u>Page</u>
60	BALLUTE Deployment Sequence	139
61	TB-4 Longitudinal Pleating Arrangement	140
62	Deployment Bag Lacing Technique	142
63	Closing Cord and Cutter Arrangement	142
64	MB-1 Metal BALLUTE	148
65	MB-1 Wind-Tunnel Deployment: (A) Pressure and Temperature versus Time; (B) Drag Force versus Time	150
66	MB-1 Configuration	151
67	BALLUTE Wind-Tunnel and Free-Flight Test Data (C_D and C_{P_i} versus Time)	152
68	Cloth B Strength and Loading versus Time	155
69	Cloth B Strength versus Temperature	156
70	Flight Test MB-1: Predicted Surface Temperature Data.	160
71	Leak Rates for CS-105 Coating	163
72	Material Testing: Seams and Splices	165
73	Trajectory Parameters: Mach 5.7 at Deployment	180
74	Trajectory Parameters: Mach 6.7 at Deployment	181
75	Trajectory Parameters: Mach 9.95 at Deployment	181
76	Test Configuration	182
77	Unified Wake Transition Criteria	185
78	Flow Field Model	186
79	Cold Wall Heat Flux Rates	187
80	Temperature Response: Y/R = 0.5, Mach 5.7 Deployment.	189

LIST OF TABLES

<u>Table</u>	<u>Title</u>	<u>Page</u>
I	Summary of Decelerator Designs and Tests . . .	3
II	Performance-Deployment Conditions for Test Vehicle A	6
III	Instrumentation Performance for Test Vehicle A.	6
IV	Performance-Deployment Conditions for Test Vehicle C	10
V	Instrumentation Performance for Test Vehicle C.	10
VI	Desired Test Points of High-Q Parachute	16
VII	Summary of Large Parachute Test Conditions . .	21
VIII	Inflation Time of Large Parachute Canopies . . .	21
IX	Large Parachute Dimensional and Loading Parameters	31
X	Large Parachute Maximum-Loading Coefficients .	32
XI	Opening Load Calculations for LP-3, LP-4, LP-5 (Geometric).	36
XII	Opening Load Calculations for LP-3, LP-4, LP-5 (Environmental).	37
XIII	Ribbon and Web Dimensions for Typical Gore . .	55
XIV	Material Tests	67
XV	Ribbon Splice Test Results.	68
XVI	Suspension Line Loop Test Results	69
XVII	Textile BALLUTE: Design Test Points Based on Predicted Trajectories	86
XVIII	Textile BALLUTES: Summary of Test Conditions	94
XIX	Textile BALLUTE Loads, Design Factors, and Material Requirements Predicted.	119
XX	Textile BALLUTE: Thermal Properties of Materials in Flight Test.	130

LIST OF TABLES

AFFDL-TR-67-25

<u>Table</u>	<u>Title</u>	<u>Page</u>
XXI	Nomex Test Results and Characteristics	134
XXII	Test Results of Materials Using Heat Tunnel. . .	135
XXIII	Metal BALLUTE Initial Flight Parameters at De- ployment.	148
XXIV	MB-1 Loads, Design Factors, and Material Re- quirements.	159
XXV	Thermal Properties of Materials for Flight-Test Metal BALLUTE	160
XXVI	CS-105 Hot Roc Tests	162
XXVII	CS-105 Permeability Tests	162
XXVIII	Interpolation of Flight Conditions (12.622 Sec) . .	173
XXIX	Interpolation of Flight Conditions (12.472 Sec) . .	175
XXX	BALLUTE Deployment Points for Hypersonic Flight Testing	179
XXXI	Thermal Properties of Nomex and D-65.	188

LIST OF SYMBOLS

1. GENERAL

- A = area (sq ft) or reefing line length divided by n (in.)
 a = velocity of sound (fps)
 B, C = BALLUTE gore shaping factors
 C = suspension line confluence factor
 C_D = drag coefficient
 $C_D A$ = drag area (sq ft)
 C_{D_o} = drag coefficient based on nominal surface
 C_{D_p} = drag coefficient based on projected surface
 C_p = external pressure coefficient
 C_{p_i} = internal or inlet pressure coefficient
 D = base diameter of payload (ft) or drag force (lb)
 D_c = construction diameter (in.)
 D_i = inlet diameter (in.)
 D_o = nominal diameter of canopy (ft or in.)
 D_p = projected diameter of canopy (ft)
 E_L = modulus of riser line (lb)
 F' = fabric pressure coefficient
 F_o = peak load (lb)
 F_{RL} = reefing line force (lb)
 F_{sl} = suspension line strength (lb)
 f = fabric stress (lb/in.)
 g = gravitational constant

LIST OF SYMBOLS

AFFDL-TR-67-25

- j = safety factor
- K = ratio meridian pressure load-to-total pressure load or parachute opening shock factor
- K_{RIA} = reefed inlet area coefficient
- K_{RLL} = reefing line length coefficient (ft)
- L = airload (lb)
- L_S = suspension line length (ft)
- M = Mach number (V/a)
- n = number of gores or suspension lines
- P or P' = pressure across fabric (psf)
- P_c = critical pressure (psf)
- P_s = stagnation pressure (psf)
- p = static pressure (psf)
- pps = pulses per second
- QE = quadrant elevation angle (deg)
- q = dynamic pressure (psf)
- R = geometrical radius (in. or ft)
- R_c = construction radius (in.)
- S = drag area (sq ft)
- S_o = canopy surface area (sq ft)
- S_p = canopy projected surface area (sq ft)
- T = static tension in inlet hoop (lb)
- t = radial force per line (lb) or time (sec)
- U = seam efficiency factor
- V = air velocity (fps)
- v_c = critical specific volume (cu ft/lb)
- v_s = specific volume (cu ft/lb)

LIST OF SYMBOLS

AFFDL-TR-67-25

w_s = specific weight (pcf)

X = shock factor

X/R , Y/R = BALLUTE coordinate shaping factors

X , X = components of parachute radial member (ft)

X , Z = canopy gore shaping coordinates (in.)

x = distance between decelerator and payload (ft)

Y_s = confluence half angle (deg)

Z = number of canopy gores

λ = geometric porosity (percent)

ξ = inlet reefing ratio or reefed inlet area/constructed inlet area

ρ = density (as defined in text)

2. THERMODYNAMIC

A = geometrical area (sq ft)

A^* = throat area (sq ft)

C^* = characteristic velocity (fps)

C_{fo} = friction coefficient

c = specific heat of material (Btu/lb-F)

c_p = specific heat of gas (Btu/lb-F)

D_t = throat diameter (ft)

d' or D_o = maximum diameter of decelerator (ft)

$G(x)$ = form factor

H_1 = total enthalpy of stream (Btu/lb)

h = heat transfer coefficient (Btu/sq ft-hr-F)

h^* = reference enthalpy (Btu/lb)

h' = static enthalpy at edge of decelerator boundary layer (Btu/lb)

h_{aw} = adiabatic wall enthalpy at edge of decelerator boundary layer (Btu/lb)

LIST OF SYMBOLS

AFFDL-TR-67-25

- h_c = surface heat transfer coefficient (Btu/sq ft-hr-F)
- h_{cone} = heat transfer coefficient on equivalent cone
- h_{cw} = cold wall enthalpy (Btu/lb)
- h_w = static enthalpy at wall temperature (Btu/lb)
- k = thermal conductivity (Btu/ft-hr-F)
- M' = Mach number at edge of decelerator boundary layer
- M_e = Mach number at edge of viscous wake
- M_∞ = free stream Mach number
- Pr = Prandtl number
- P_t = total pressure (psf)
- p = static pressure (psf)
- p' = static pressure on decelerator (psf)
- p_{cone} = static pressure on cone (psf)
- p_∞ = ambient free-stream pressure (psf)
- \dot{q}_{cw} = cold wall heat flux rate (Btu/sq ft-sec)
- \dot{q}_w = wall heat flux rate (Btu/sq ft-sec)
- R = maximum radius of decelerator (ft)
- Re = Reynolds number
- Re_θ = momentum Reynolds number
- $Re_{x_{tr}}$ = Reynolds number for distance taken from base of leading body
- r = geometrical radius (ft)
- r' = radial coordinate of decelerator
- r_e = radius of curvature of ribbon edge (in.)
- s = distance along decelerator surface taken from apex (ft)
- T = temperature (F)

LIST OF SYMBOLS

AFFDL-TR-67-25

- T_{aw} = adiabatic wall temperature
- T_{cw} = cold wall surface temperature
- T_i = node temperature
- T_i' = previous node temperature
- T_l = surface temperature
- T_s = effective temperature of space
- T_w = surface temperature (F or R)
- u' = local velocity at edge of decelerator boundary layer
- V_{∞} = free-stream velocity (fps)
- x = distance along surface of leading body (ft)
- x' = distance taken from apex of decelerator
- x_{tr} = distance from base of leading body
- Y = axial distance of decelerator (ft)
- y = thickness (ft)
- Z = altitude (ft)
- α = thermal diffusivity (sq ft/hr)
- β = one-half cone angle (deg)
- γ = ratio of specific heats
- δ = total wall thickness (ft)
- ϵ = emissivity
- θ = momentum thickness
- μ = viscosity (lb-sec/sq ft)
- μ_{∞} = free-stream viscosity (lb-sec/sq ft)
- μ^* = reference viscosity (lb-sec/sq ft)
- μ_n = viscosity at edge of boundary layer (lb-sec/sq ft)
- μ_w = viscosity at wall temperature (lb-sec/sq ft)

LIST OF SYMBOLS

AFFDL-TR-67-25

μ_1 = viscosity at edge of boundary layer temperature (lb-sec/sq ft)

ρ = material density (pcf)

ρ_∞ = free-stream density (slugs/cu ft)

ρ^* = reference density (slugs/cu ft)

ρ' = density on decelerator at edge of boundary layer temperature (slugs/cu ft)

ρ_e = density at edge of boundary layer (slugs/cu ft)

ρ_w = density at wall temperature (slugs/cu ft)

ρ_1 = density at edge of boundary layer temperature (slugs/cu ft)

σ = viscosity-density factor or Stefan-Boltzmann constant

τ = time (sec)

SECTION I

INTRODUCTION AND SUMMARY

1. BACKGROUND

As part of the United States Air Force's investigation into the problems associated with the development of supersonic and hypersonic decelerators, the Air Force Flight Dynamics Laboratory (AFFDL) has authorized a three-phase applied research program known as ADDPEP (Aerodynamic Deployable Decelerator Performance-Evaluation Program). The overall objective of this program is to advance the state of the art by developing the most effective analytical and empirical techniques for (1) designing aerodynamic deployable decelerators and (2) evaluating these engineering techniques through wind-tunnel and free-flight tests. Three types of decelerators are assigned for investigation. These decelerators and their respective goals are:

1. Small supersonic parachute canopy - The goal is to establish the configuration, loadings, design, and structural materials for attaining a stable performance for flight speeds up to Mach 5 and for dynamic pressures to 500 psf.
2. Large reefed supersonic parachute canopy - The goal is to establish the configuration, loadings, design, and structural materials for attaining an initial load of 200,000 lb at supersonic speeds by appropriately reefing the canopy. The performance range of interest extends from transonic speeds to Mach 3, with a dynamic pressure of 10,000 psf.
3. Ram-inflated balloon-type decelerator known as a BALLUTE¹ - The goal is to establish the configuration, loadings, design, and structural materials for flight speeds to Mach 10 and for dynamic pressures to 500 psf.

The areas of investigation for these three decelerator types include analytical and engineering design, material capabilities, fabrication techniques, and wind-tunnel and free-flight tests.

2. ADDPEP PHASE I

Goodyear Aerospace conducted ADDPEP Phase I under Contract AF33(657)-10955. Analytical and empirical techniques were used to design and build the three types of decelerators and to evaluate them through wind-tunnel and free-flight tests on the basis of the aforementioned goals. Moreover, to provide a free-flight basis for evaluating the analytical and empirical techniques, it was necessary to design, develop, build, and evaluate two types of test vehicles that were adapted to be launched by combinations of

¹TM, Goodyear Aerospace Corporation, Akron, Ohio.

existing boosters. This work has been documented in Technical Report AFFDL TR-65-27 (Reference 1).

3. ADDPEP PHASE II

Goodyear Aerospace has conducted ADDPEP Phase II under Contract AF33(615)-1513. Essentially, Phase II has consisted of a continued evaluation of the design techniques for two decelerator types: (1) large reefed supersonic parachute and (2) BALLUTE. The areas investigated for these decelerator types have included analytical and engineering design, material capabilities, fabrication techniques, and wind-tunnel and free-flight tests. The laboratory tests were conducted at Goodyear Aerospace, Akron, Ohio; and the free-flight tests, at Eglin Air Force Base, Fla., Holloman Air Force Base, N.M., and White Sands Missile Range, N.M. In addition, Goodyear Aerospace provided a consultant for wind-tunnel tests conducted by AFFDL personnel at Arnold Engineering Development Center, Tenn.

This report details the work conducted during ADDPEP Phase II. Section II, dealing with the free-flight test capability for the decelerator types considered, describes work in modifying and evaluating the two types of test vehicle/booster systems that were developed previously as part of Phase I. Section III deals with the evaluation of the large parachute (LP) design techniques. Sections IV and V deal, respectively, with the evaluation of the textile-cloth and metal-cloth BALLUTE (TB and MB) design techniques that were considered during Phase II. Section VI presents overall Phase II conclusions.

Each section of this report concludes with a summary and a statement of conclusions. Table I summarizes the characteristics of the LP, TB, and MB decelerator designs, as well as the tests that were conducted.

For the large parachute decelerators, tests were performed on a hemispherical parachute design having a nominal 16-ft-diameter canopy, a 10-percent extended skirt, and a 14-percent porosity. This design was tested for 200,000-lb opening loads; deployment Mach numbers were 1.50, 1.63, and 1.84 at altitudes of 13,700, 15,500, and 10,500 ft, respectively. The behavior during the tests confirmed that this parachute has excellent aerodynamic characteristics and adequate strength. The same parachute will be deployed at increasing Mach numbers during ADDPEP Phase III.

For the textile and metal BALLUTE decelerators, the designs were made for a broad spectrum of deployment conditions ranging from Mach 2.7 at 73,000 ft to Mach 10 at 225,000 ft. Five-foot-diameter BALLUTES were fabricated from both coated textile and metal cloths. Fabrication techniques for the textile designs were evaluated by wind-tunnel and/or free-flight tests. The metal cloth designs were evaluated only by wind-tunnel tests. Flight tests were limited to Mach 9.7, and wind-tunnel tests to Mach 3. The wind tunnel tests indicated that excellent stability and structurally adequate designs can be attained with five-foot-diameter units within the limits of the testing capability. In general, the free-flight data supported these findings. However, the flight test data at the highest Mach number (9.7) were too limited for drag and stability comparisons.

SEC

TABLE I - SUMMARY OF DECELERATOR DESIGN

Decelerator type	Principal material	Coating	Design test point data				
			Test method *	Mach no.	Altitude (10 ³ ft)	Dynamic pressure (psf)	Total temperature of air (F)
Large parachute (LP)			Vehicle A				
LP-1	Nylon	None	Airdrop	1.20	14.4	1240	170
LP-2	Nylon	None	Airdrop	1.20	14.4	1240	170
LP-2	Nylon	None	N-N	1.60	17.0	2600	233
LP-3	Nomex	None	N-N	1.48	13.9	1900	214
LP-4	Nomex	None	N-N	1.64	12.4	2600	268
LP-5	Nomex	None	N-N	1.80	10.8	3300	331
Textile BALLUTE (TB)			Vehicle C				
TB-1	Nylon	Neoprene	HJ-N	2.47	85.0	195	400
TB-1A	Nylon	Neoprene	HJ-N	2.40	84.0	200	440
TB-1B	Nylon	Polyurethane CUR 71A	HJ-N	2.78	71.0	484	513
TB-2	Nomex	Silastic 131	HJ-N-N	3.80	104.0	197	1,134
TB-3	Nomex	Silastic 131	HJ-N-N	3.70	98.0	250	1,008
TB-4	Nomex	Dynatherm D-65	XM-33/2XM-19-L	9.95	200.0	20	8,627
TB-5	Nomex	Dynatherm D-65	HJ-L-L	6.70	131.0	200	4,030
TB-6	Nomex	Dynatherm D-65	HJ-N-L	5.66	122.0	198	2,784
Metal BALLUTE (MB)							
MB-1	304 stainless steel	CS-105	HJ-N-L	5.70	120.0	220	2,794
MB-2	René 41	CS-105	HJ-L-L	7.00	130.0	215	4,380
MB-3	René 41	CS-105	XM-33/2XM-19-L	11.00	220.0	15	10,040

* Booster definitions: N = Nike; HJ = Honest John; L = Lance.

SECTION I - INTRODUCTION AND SUMMARY

AFFDL-TR-67-25

OF DECELERATOR DESIGNS AND TESTS

Point data			Remarks	Canopy		Load factor (g)	Drag area (sq ft)
Altitude (ft)	Dynamic pressure (psf)	Total temperature of air (°F)		Surface area (sq ft)	Porosity (percent)		
4	1240	170	Not tested	201.1	29	62.40	100.0
4	1240	170	Premature release	201.1	15	62.40	100.0
0	2600	233	Vehicle checkout	201.1	15	62.40	100.0
9	1900	214	Good test, obtained required data	201.1	14	100.00	100.0
4	2600	263		201.1	14	100.00	100.0
6	3300	331		201.1	14	100.00	100.0
0	195	40	Not deployed, Phase I effort	86.5	Negligible	9.70	19.6
0	200	440	Good test, obtained required data	86.5	Negligible	9.90	19.6
0	484	513		86.5	Negligible	23.80	19.6
0	197	1,134		86.5	Negligible	6.80	13.7
0	250	1,008	Good test, obtained limited data	86.5	Negligible	8.50	13.5
0	20	8,627		86.5	Negligible	0.68	13.5
0	200	4,030		86.5	Negligible	6.80	13.5
0	198	2,784	Available for test	86.5	Negligible	6.75	13.5
	220	2,794	Successfully tested in PWT at AEDC, $q = 120$ at $M = 2.8$, using alcohol/water partial inflation technique	86.5	Negligible	2.40	13.5
	215	4,380	Substitution of Nomex units precluded fabrication and test of Rene units	86.5	Negligible	7.80	13.5
	15	10,040		86.5	Negligible	0.34	13.5

(Reverse is blank)

SECTION II

FREE-FLIGHT TEST CAPABILITY

1. TEST VEHICLE A/BOOSTER SYSTEM

a. General

A basic goal of ADDPEP Phase II (Aerodynamic Deployable Decelerator Performance-Evaluation Program) was to continue advancing the state of the art of large supersonic parachute design methods at high dynamic pressures. Parachutes with 16-ft diameters (D_0) were subjected to a Mach 1.8 regime; ultimate objectives approached Mach 3 at low altitudes. The requirements for subjecting the large parachutes to the Phase II test regime were adequately fulfilled by Test Vehicle A, launched by a Nike-Nike (N-N) booster combination to Mach 1.8.

b. Design and Configuration

For the ADDPEP Phase II requirements, the overall configuration and design of Test Vehicle A remained basically the same as the design established for Phase I (Reference 1). A photograph of Test Vehicle A and the general configuration are shown in Figure 1.

c. Vehicle Integrity Tests

Static tests were conducted on the first A vehicle (Reference 2). Except for an actual test decelerator, the vehicle was complete. The entire sequence of operations normally accomplished in flight was demonstrated successfully. Criteria for quality of the static test were based on vehicular instrumentation data, external shock data, and photographic results.

Vibration tests were conducted on another A vehicle to ascertain the reliability of the event programming system in a vibratory environment similar to that expected in free-flight. The vehicle was subjected to vibration; the forcing input was along its longitudinal axis. Simulated electroexplosive devices were wired to the event programming system. During vibration, the vehicle timers were cycled, resulting in the detonation, in sequence, of the simulated electroexplosive devices to evaluate the flight event signal generating system. Telemetry instrumentation was functional for the monitoring of test and recovery timing sequences.

The performance of Test Vehicle A and its structural integrity were acceptable.

d. Free-Flight Performance

Table II summarizes the Test Vehicle A performance as a test point deployment control for large parachutes (LP) tests with the boosters utilized. Table III summarizes the Test Vehicle A data acquisition (instrumentation) system performance.

TABLE II - PERFORMANCE-DEPLOYMENT CONDITIONS FOR
TEST VEHICLE A

Test	QE* (deg)	Boosters	Altitude (ft)		Mach no.		Dynamic pressure (psf)	
			Calculated	Actual	Calculated	Actual	Calculated	Actual
LP-1	+	B-52 airdrop	14,400	+	1.2	+	1240	+
LP-2	0	B-52 airdrop	14,400	+	1.2	+	1240	+
LP-3	40	N-N	13,900	13,660	1.48	1.50	1900	1988
LP-4	40	N-N	12,400	15,539	1.64	1.63	2600	2118
LP-5	40	N-N	10,800	10,538	1.80	1.84	3300	3383

* Quadrant elevation angle

† Not tested

‡ Premature release, data not useful

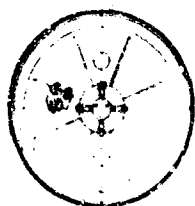
TABLE III - INSTRUMENTATION PERFORMANCE FOR
TEST VEHICLE A

Test	Telemetry instrumentation							Camera operation	
	100-pps monitor	Static press	Diff press	PAM*	Accel	Drag	Shock	(500 fps)	(100 fps)
LP-1	1 [†]	1	1	1	1	1	1	1	1
LP-2	2	2	2	2	2	2	2	2	2
LP-3	3	3	3	3	3	4	4	3	4
LP-4	3	3	3	3	3	3	3	3	3
LP-5	3	3	3	3	3	3	3	3	3

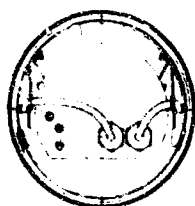
* Pulse-amplitude modulation

† Notes:

1. Not tested
2. Data not useful or not obtained during test period
3. Satisfactory data obtained for test period
4. Data obtained for only portion of test period



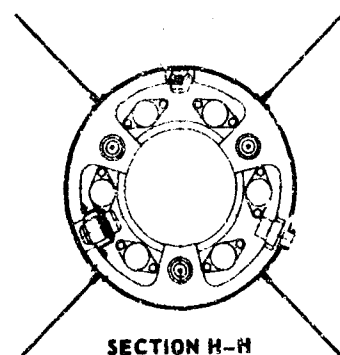
SECTION B-B



SECTION D-D



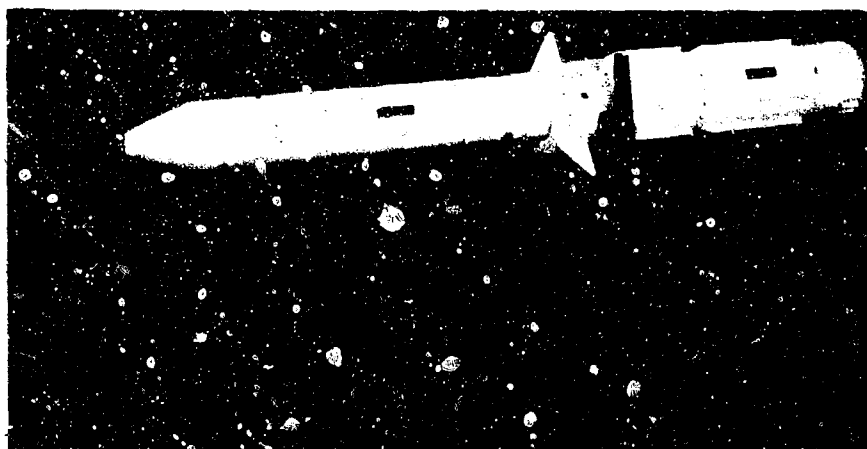
SECTION F-F



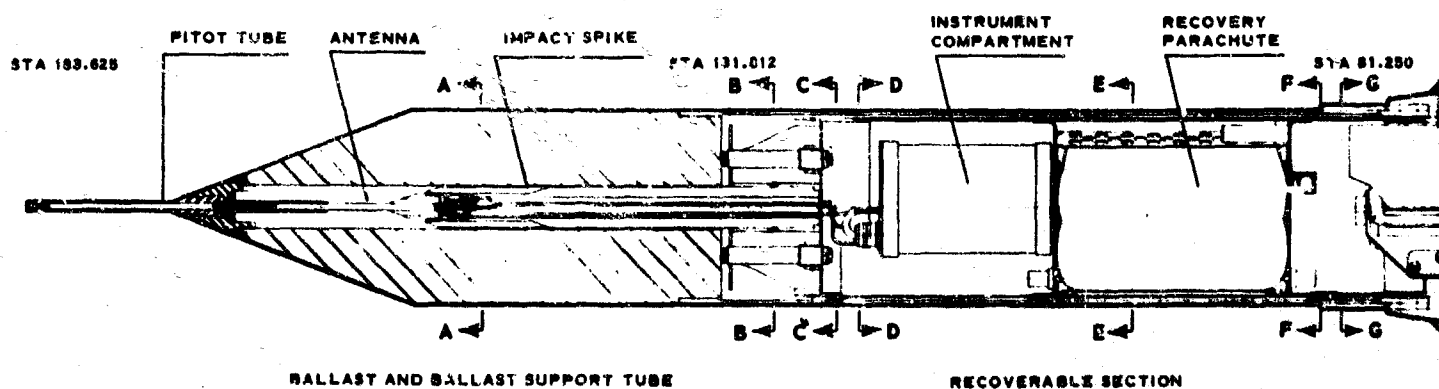
SECTION H-H



SECTION J-J



SECTION K-K



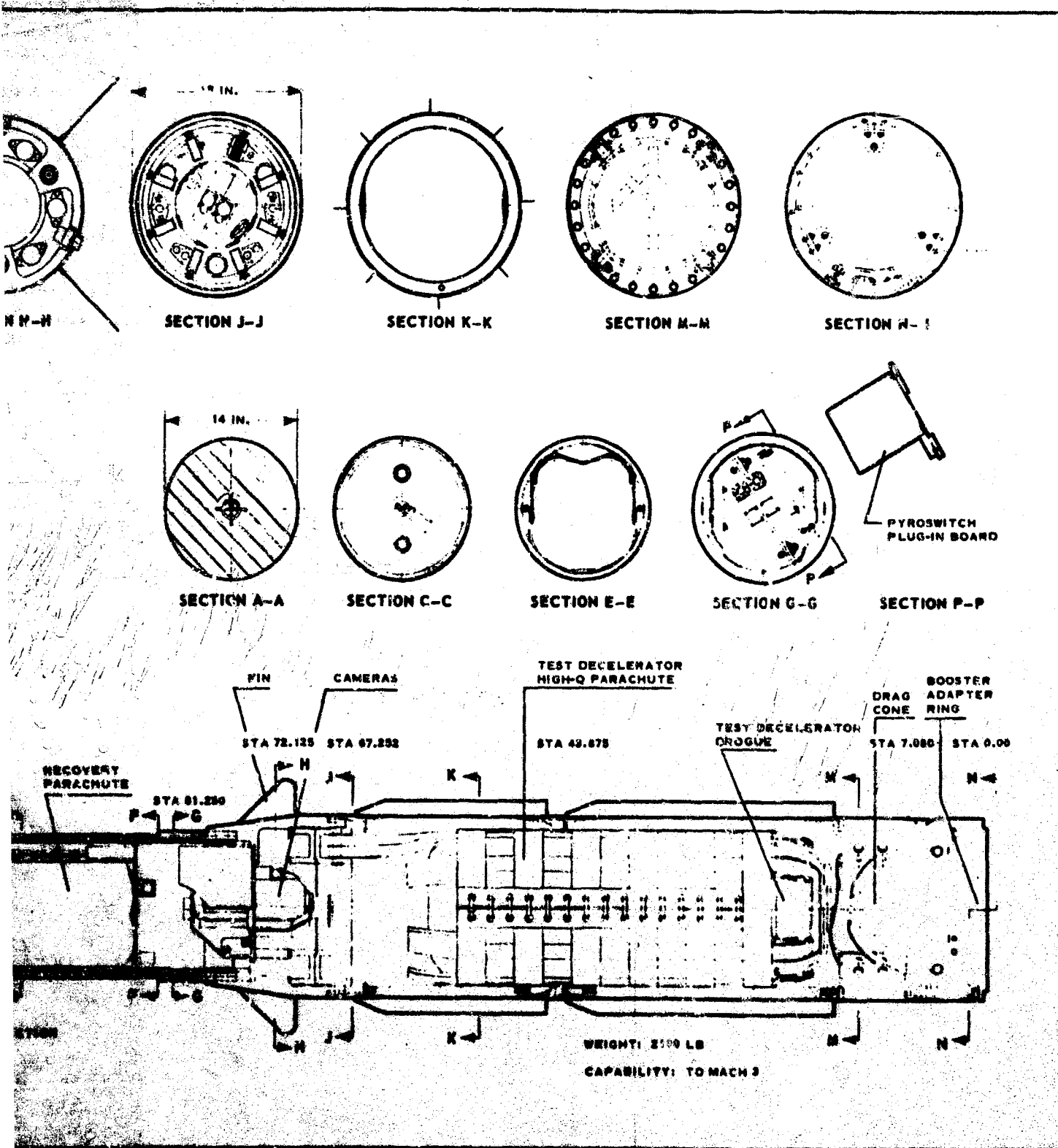


Figure 1 - Test Vehicle A

(Reverse is blank)

2. TEST VEHICLE C/BOOSTER SYSTEM

a. General

Required under ADDPEP Phase II was a series of BALLUTE deployments at speeds to Mach 10, altitudes to 225,000 ft, and dynamic pressures to 500 psf. The testing of BALLUTES was accomplished utilizing capability C test vehicles launched by Honest John-Nike (HJ-N), Honest John-Nike-Nike (HJ-N-N), Honest John-Nike-Lance (HJ-N-L), and XM-33/2XM-19-Lance booster combinations.

b. Design and Configuration

For ADDPEP Phase II requirements, the overall design and configuration of Test Vehicle C remained basically the same as Test Vehicle B/C established for Phase I (Reference 1). However, the Test Vehicle C design was modified, to enhance vehicle performance, decelerator data acquisition, and vehicle refurbishment. A photograph of Test Vehicle C and the general configuration are shown in Figure 2.

Vehicle performance design changes included addition of an auxiliary flotation BALLUTE, increase in pyrotechnic sequence voltage, addition of provisions for use of retrorockets when required for high altitude booster separation, incorporation of a larger container for testing of more bulky test items, and flotation system improvements (References 4 - 8).

From the standpoint of decelerator data acquisition, the Test Vehicle C telemetering system was modified to permit use of more BALLUTE temperature thermocouples, and provisions were incorporated to current limit the shock, drag, and BALLUTE pressure sensor electrical circuits (References 6, 9, 10).

To decrease the complexity of refurbishment and to decrease refurbishment time, pyrotechnic switches were installed on plug-in boards, and provisions were incorporated to permit external monitoring and charging of the flotation reservoir (References 5, 6).

c. Free-Flight Performance

Table IV summarizes the Test Vehicle C performance as a test point deployment control for BALLUTE testing with the boosters utilized. Both textile-coated and metal coated BALLUTES are considered (TB and MB). Table V summarizes the Test Vehicle C data acquisition (instrumentation) system performance. Predicted and demonstrated capabilities are presented.

3. GROUND SUPPORT

a. General

ADDPEP Phase II free-flight test support was required in two test areas (as listed on page 13):

TABLE IV - PERFORMANCE-DEPLOYMENT CONDITIONS FOR
TEST VEHICLE C

Test	QE ⁺ (deg)	Boosters	Altitude (ft)		Mach no.		Dynamic pressure (psf)	
			Calculated	Actual	Calculated	Actual	Calculated	Actual
TB-1 ⁺	83	HJ-N	85,000	86,950	2.47	2.42	195	172.0
TB-1A	83	HJ-N	80,000	85,000	2.5	2.40	255	242.0
TB-1B	83	HJ-N	73,000	74,700	2.71	2.17	415	360.0
TB-2	83	HJ-N-N	104,000	96,000	3.8	3.25	197	245.0
TB-3	84	HJ-N-N	94,200	98,500	3.62	4.00	250	279.0
TB-4	70	XM-33-L [‡]	210,000	226,700	9.95	9.70	20	9.4
TB-5 [‡]	65	HJ-L-L	131,000	...	6.7	...	200	...
TB-6 [‡]	85	HJ-N-L	122,000	...	5.66	...	198	...
MB-1 [‡]	85	HJ-N-L	120,000	...	5.7	...	220	...
MB-2 [‡]	85	HJ-L-L	130,000	...	7.0	...	215	...
MB-3 [‡]	70	XM-33-L	220,000	...	11.0	...	15	...

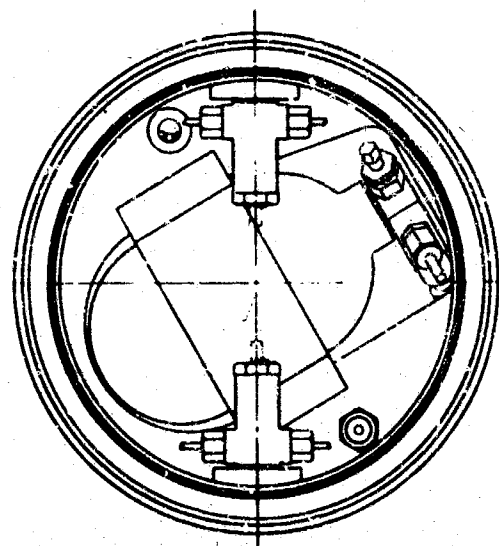
⁺ Quadrant elevation angle⁺ Condition at deployment signal[‡] Projected flights[‡] XM-33/ZXM-19-L

TABLE V - INSTRUMENTATION PERFORMANCE FOR TEST VEHICLE C

Test	Telemetry instrumentation							Camera operation (200 and 700 fps)
	BALLUTE press	Static press	Diff press	PAM [‡]	Accel	Drag	Shock	
TB-1A	1 ⁺	1	1	1	1	1	1	2
TB-1B	2	2	2	2	2	2	2	2
TB-2	3	2	2	2	2	2	2	2
TB-3	2	1	1	2	2	2	2	2
TB-4	2	2	1	2	2	1	1	4
TB-5	5
TB-6	5
MB-1	6
MB-2	5
MB-3	5

[‡] Pulse-amplitude modulation⁺ Notes:

1. Data not useful or not obtained during test period
2. Satisfactory data obtained for test period
3. Data obtained for only portion of test period
4. Unknown
5. Not tested
6. Wind-tunnel tested



SECTION D-D

RECOVERY PARA
GAS GENERATOR

STATION 100.0

STA 79.8

HUSK PRODU

FLOTATION SYSTEM

TELEMETRY ANTENNA

DESPIN RESERVOIR

INSTRUMENT COMPARTMENT

BATTERY PACK

WEIGHT: 800 LB

CAPACITY: 70 GAL

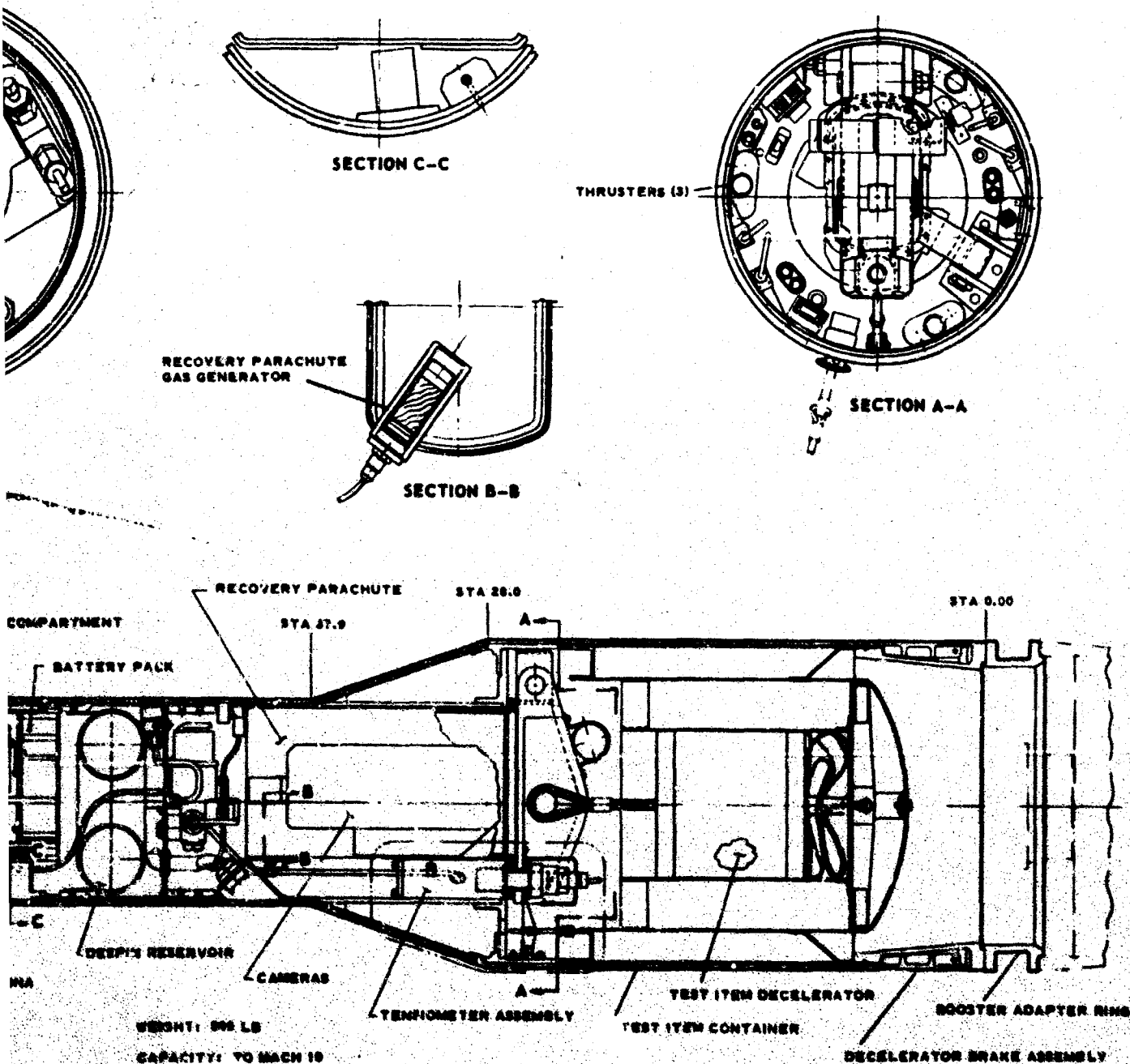


Figure 2 - Test Vehicle C

(Reverse is blank)

1. Large parachute (LP) free-flight tests and data reductions were accomplished at Holloman Air Force Base, N. M., and White Sands Missile Range, N. M. The first test was a missile qualification air drop conducted at White Sands. The B-52 aircraft for conducting the drop operated from Kirtland Air Force Base, N. M.
2. BALLUTE free-flight tests and data reductions were accomplished at Eglin Air Force Base, Fla.

b. Field Operations

Field test operations followed the pattern shown in Figure 3. During the free-flight tests, the Goodyear Aerospace field test crew assumed responsibility for the test and checkout of all vehicle systems, as well as for vehicle refurbishment. The range agency, Holloman or Eglin AFB, assumed responsibility for storage, use, and check out of the booster vehicle; range safety; radar tracking; ground acquisition of the telemetered and photometric test data; and data reduction of vehicle flight and test decelerator deployment data.

c. Field Personnel

The field-test crew consisted of three engineers and two technicians. In addition, a pyrotechnics engineer was assigned part time. Basically the responsibilities were as listed on page 14:

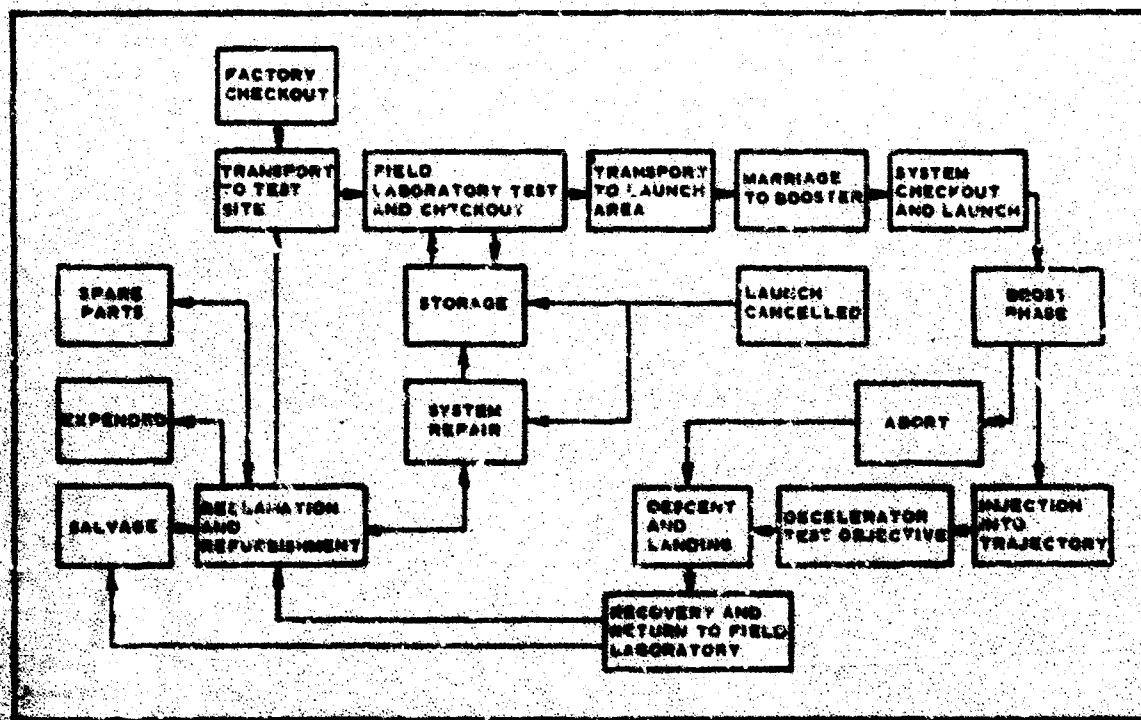


Figure 3 - Field Operations Flow

1. Project engineer - program management
2. Instrumentation engineer - onboard data acquisition
3. Development engineer - vehicle systems and assembly
4. Electronics technician - assistance for instrumentation
5. Electrical technician - assistance for vehicle assembly
6. Pyrotechnics engineer - loading and assembly for explosive devices (accomplished on a periodic visit basis)

4. SUMMARY AND CONCLUSIONS

The evaluation of the test vehicle systems is summarized as follows:

1. Test Vehicle A/Booster - The test results indicated that vehicle performance can be predicted with confidence and that the data system is adequate. Recovery and reusability met design goals.
2. Test Vehicle C/Booster - The test results indicated that vehicle performance can be predicted with confidence. The data transmittal range was excellent. Beacon dropout occurred on some occasions. When recovered, the vehicle met design goals for reusability.

SECTION III

LARGE PARACHUTE DECELERATOR

1. GENERAL

a. History

The goal of the large supersonic parachute effort under ADDPEP (Aero-dynamic Deployable Decelerator Performance-Evaluation Program) is to establish the parachute configuration, loadings, design, and structural materials for attaining an initial load of 200,000 lb at supersonic speeds and low altitudes. The performance range to be investigated extends from transonic speeds to Mach 3, with a dynamic pressure (q) of 10,000 psf.

The work on a large supersonic high- q parachute decelerator was initiated during ADDPEP Phase I and continued during Phase II. This large parachute (LP) effort has been concentrated on two basic design types:

1. Conical
2. Hemisflo

Two conical parachute test items, LP-1 and LP-2, were designed and fabricated during ADDPEP Phase I. Three hemisflo parachute test items, LP-3, LP-4, and LP-5, were designed and fabricated during ADDPEP Phase II. The final canopy size chosen was a 16-ft nominal diameter, D_0 .

The design and fabrication of LP-1 and LP-2 are detailed in Section V of the ADDPEP Phase I technical report (Reference 1, AFFDL-TR-65-27). The test results for LP-2 (20-deg conical ribbon) are included in this Phase II report. Since LP-1 was delivered to AFFDL-RTD for drop-testing to prove the parachute opening characteristics, no test data for LP-1 are in this report.

b. Test Point Conditions

The conditions for test points of LP-2 through LP-5 were established by trajectory analysis and concurrence by AFFDL-RTD. The desired deployment values to be achieved by Test Vehicle A and booster combinations are shown in Table VI.

c. Configuration Selection

As already indicated, the basis for design, the fabrication details, and a physical description of large parachute test item LP-2 are given in Reference 1. With respect to LP-3, LP-4, and LP-5, published data from wind tunnel tests (References 11, 12, 13), as well as the results of AFFDL-RTD programs, were reviewed, analyzed, and used as a basis for selecting the parachute type and porosity for a family of reefed diameters. Further analysis of small- and large-model tests indicated that the porosity must be reduced for reefed (hemisflo or conical)

TABLE VI - DESIRED TEST POINTS OF HIGH-Q PARACHUTE

Design configuration	Initial conditions					
	Mach no.	Altitude (ft)	Dynamic press (psf)	Flight path angle (deg from horiz)	Reynolds no.	Booster comb
LP-2, flt 1	1.20	14,400	1240	-70.0	5.70	*
LP-2, flt 2	1.60	17,000	2600	18.0	7.00	N-N ⁺
LP-3	1.48	13,900	1900	14.2	7.10	N-N ⁺
LP-4	1.64	12,400	2600	18.0	3.20	N-N ⁺
LP-5	1.80	10,800	3300	20.3	9.45	N-N ⁺

* B-52 airdrop

⁺ Nike-Nike booster combination

parachutes at supersonic Mach numbers. The wind-tunnel tests also indicated that an improvement in inflation stability was obtained by using midgore reefing that doubled the restraining points for the skirt band. The steady-state data from References 11 and 12 are shown in Figure 4. The C_{DA} (constant drag area) values for 200,000 lb at sea level are presented as a solid line for reference.

More recent wind-tunnel test results are presented in Reference 13. For these tests, the reefing ratio (ξ) was varied at four different Mach numbers (reefing ratio defined as ratio between reefed canopy inlet area and fully inflated inlet area). The parachute displaying the best performance was a 14.14-percent total porosity and 10-percent extended skirt hemisflo, with 2 D_0 lines. The wind-tunnel test results are shown in Figure 5.

Based on those data and test observations, a hemisflo type was chosen over the conical parachute design for continued decelerator investigation under ADDPEP Phase II. The 16-ft D_0 size was selected to investigate reefing necessary throughout the test spectrum, to achieve the desired peak opening load of 200,000 lb, and to permit storage of the parachute within the test vehicle.

The hemisflo general dimensions are shown in Figure 6, and the configuration details are summarized as follows (list continued on page 18):

1. Nominal diameter of canopy: $D_0 = 16$ ft
2. Shape: hemisflo ribbon with 10-percent extended skirt
3. Number of gores: 32
4. Porosity: 14-percent nominal evenly distributed

EQUIVALENT TO A 16-FT D_0 PARACHUTE BASED ON TESTS OF SMALL AND LARGE MODELS

TYPE	LINE LENGTH	D_0 (IN.)	REEFING (PERCENT)	POROSITY (PERCENT)	REFERENCE
○ HEMISFLO	2 D_0	19.3	20.7	14	11
□ CONICAL	2 D_0	19.3	20.7	14	11
◇ HEMISFLO	2 D_0	19.3	29.3	14	11
△ CONICAL	2 D_0	120.0	15.0	15	12
▽ CONICAL	2 D_0	120.0	15.0	15	12
◐ HEMISFLO	1 D_0	120.0	20.0	15	12

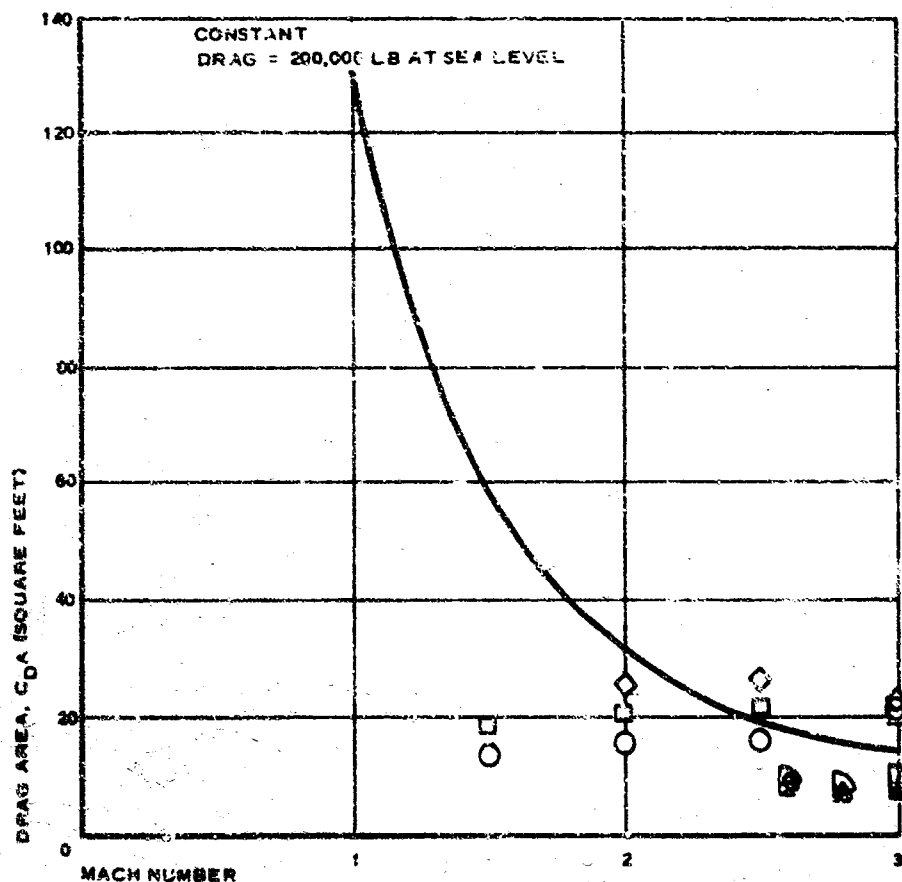


Figure 4 - Drag Area versus Mach Number (Wind-Tunnel Testing)

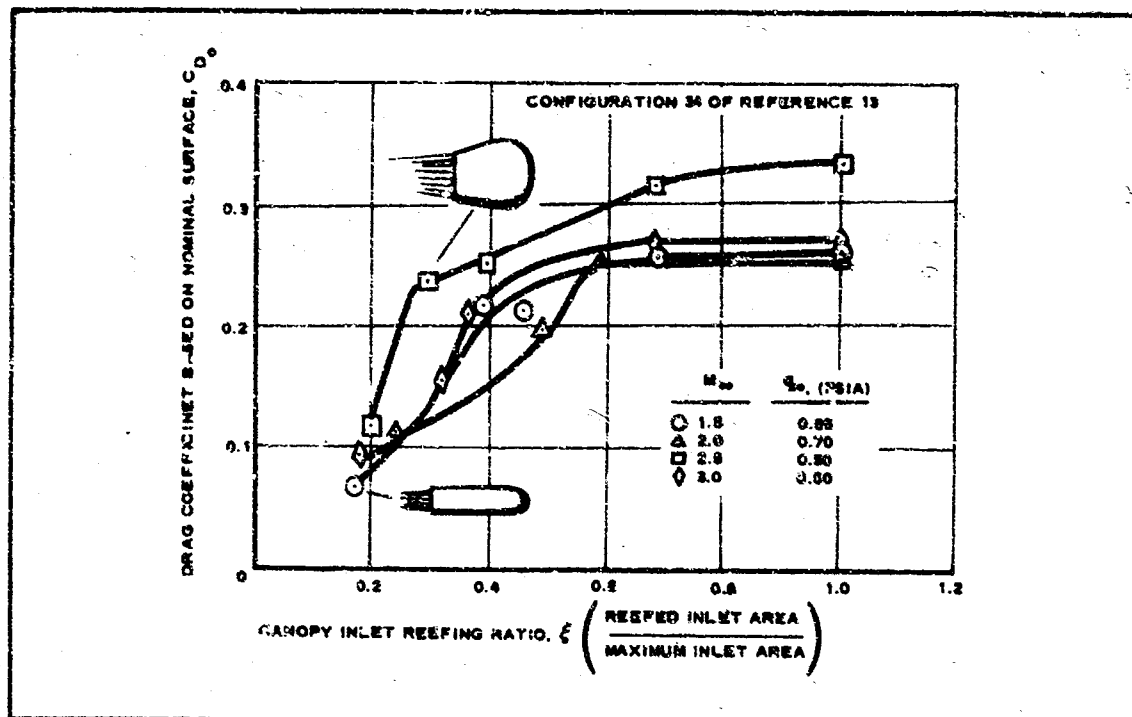


Figure 5 - Nominal Drag Coefficient versus Inlet Reefing Ratio (Wind-Tunnel Testing)

5. Suspension line length (effective) $L_S = 2 D_0$ ft
6. Attachment: 8 points, 1-in. diameter by 2-5/8 in. wide, pin clearance
7. Weight: 130 lb

2. EXPLORATORY FREE-FLIGHT TESTS

a. Conical Large Parachute LP-2

Conical parachute LP-2 was subjected to two free-flight tests. In the first test, the LP-1 unit was air-dropped onboard Test Vehicle A. The desired deployment test points are noted earlier in Table VI (page 16). Test Vehicle A was released from a B-52 aircraft at a 49,415-ft altitude and was very stable during free-fall to 17,200 ft (mean sea level). At 17,200 ft, premature baroswitch actuation caused separation of the forward test item container and prevented deployment of LP-2. A complete case history of the LP-2 drop test is given in Reference 14.

The purposes of the second LP-2 free-flight test was to test (1) the Vehicle A launcher capability for operational support of the vehicle with its boosters, and (2) the parachute deployment capability of Test Vehicle A (Reference 15). The desired deployment test points are noted in Table VI. Telemetry instrumentation was not used. The ground launch of Test

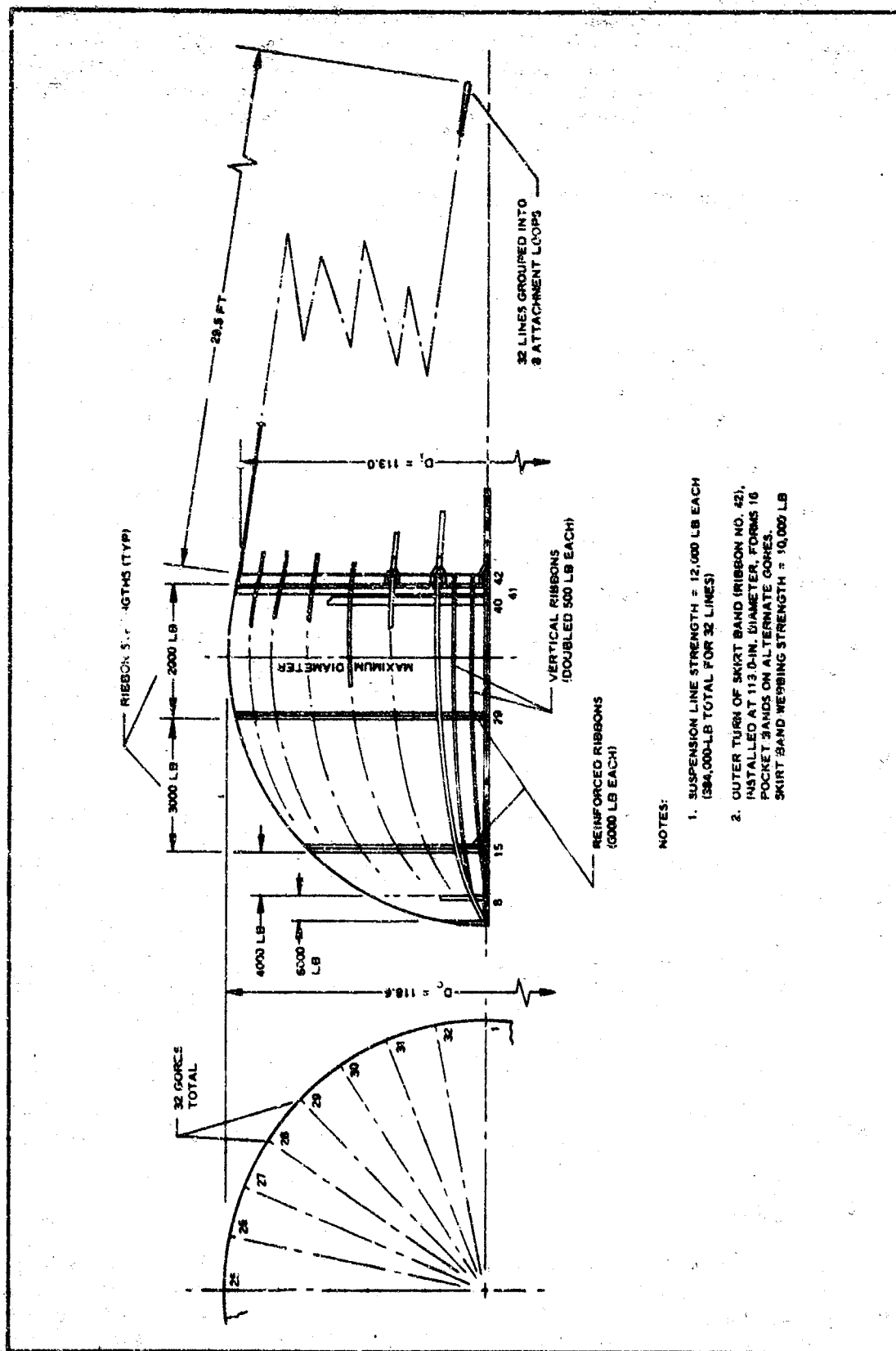


Figure 6 - General Arrangement of 16-Ft D Hemisflo Parachute

Vehicle A by a Nike-Nike (N-N) booster combination was satisfactory; based on data obtained from White Sands Missile Range (WSMR, Reference 16), the LP-2 deployment was close to the desired test points. As a result of this free-flight test, the Test Vehicle A and booster combination operation was considered satisfactory for fully configured boosted flight.

b. Hemisflo Large Parachutes LP-3, LP-4, LP-5

(1) General

Free-flight tests were conducted on hemisflo parachutes LP-3, LP-4, and LP-5. In each flight, the test item was deployed by Test Vehicle A, which was air-launched by a Nike-Nike (N-N) booster combination. Data obtained from the flights showed that the 16-ft D_0 hemisflo parachute performed well in the reefed conditions to Mach 1.8, the limit of testing. Parachute behavior in the tests confirmed wind-tunnel results.

Table VII summarizes the test point conditions achieved for the LP-3, LP-4, and LP-5 tests; the conditions at the time of test-item container separation, initial full-line stretch, and maximum load are presented. The inflation time for LP canopies is presented in Table VIII.

(2) LP-3 Free-Flight Summary

The LP-3 hemisflo test parachute was deployed near a calculated test loading dynamic pressure, q , of 1900 psf. The reefing line was 20 ft 6 in. long after sewing and consisted of two webs rated at 6000 lb tacked together. The test parachute was extracted and deployed by a 4-ft D_0 hemisflo pilot parachute positioned 69-in. aft of the test item deployment bag.

Premature disreefing occurred approximately one-tenth of a second after inflation to the reefed shape due to reefing line failure. Maximum inflation g 's were approximately 100 for the reefed shape and 80 for the disreefed shape. Supersonic and subsonic stability were excellent. The test item was recovered undamaged.

Figure 7A shows the performance curves of LP-3, beginning at test item container separation and continuing for three seconds, the period of most significant change. A performance summary is given in Table VII. Data for the performance curves were obtained from WSMR data reduction reports (References 17, 18) or the test vehicle telemetry signal plots.

Figure 7B shows the LP-3 inlet area variation with respect to time on a selective scale. Data for the inlet area plot were generated from the on-board motion picture coverage.

(3) LP-4 Free-Flight Summary

The LP-4 hemisflo parachute was tested near the calculated test loading q of 2600 psf. The reefing line was 14 ft 10 in. long after sewing and consisted of a 6000- and a 12,000-lb web sewn together. Extraction and deployment of LP-4 were accomplished by a 4-ft D_0 hemisflo pilot parachute

TABLE VII - SUMMARY OF LARGE PARACHUTE TEST CONDITIONS

Test item	Event	Range time (hr: min: sec)	Load (10 ³ lb)	Conditions		
				Mach no.	q* (psf)	Alt (ft)
LP-3	Test item container separation	16: 10: 28.64	. . .	1.502	1988	13,660
	Initial line stretch	16: 10: 28.97	50.0	1.341	1590	13,770
	Maximum load	16: 10: 29.10	154.5	1.24	1350	13,815
LP-4	Test item container separation	23: 15: 13.75	. . .	1.631	2118	15,539
	Initial line stretch	23: 15: 14.12	30.0	1.531	1920	15,842
	Maximum load	23: 15: 14.28	108.85	1.40	1642	15,934
LP-5	Test item container separation	17: 00: 10.30	. . .	1.837	3383	10,538
	Initial line stretch	17: 00: 10.61	40.0	1.725	2950	10,710
	Maximum load	17: 00: 10.81	152.6	1.560	2410	10,948

*Dynamic pressure

TABLE VIII - INFLATION TIME OF
LARGE PARACHUTE CANOPIES

Configuration	Mach no. *	q* (psf)	Inflation time [†] (sec)
LP-3	1.34	1590	0.13
LP-4	1.53	1920	0.16
LP-5	1.725	2950	0.20

*Dynamic pressure at line stretch

[†]Time from line stretch to maximum load

permanently reefed to an inlet diameter of 2 ft, positioned 120 in. aft of the test item deployment bag; at the end of a 2-sec programmed delay period, the reefing line was severed cleanly by the 2 cutters. Maximum inflation g's were approximately 61 for the reefed shape and 9 for the dis-reefed shape.

The parachute was recovered with the canopy in an undamaged condition; however, three suspension lines were broken one to four feet from the

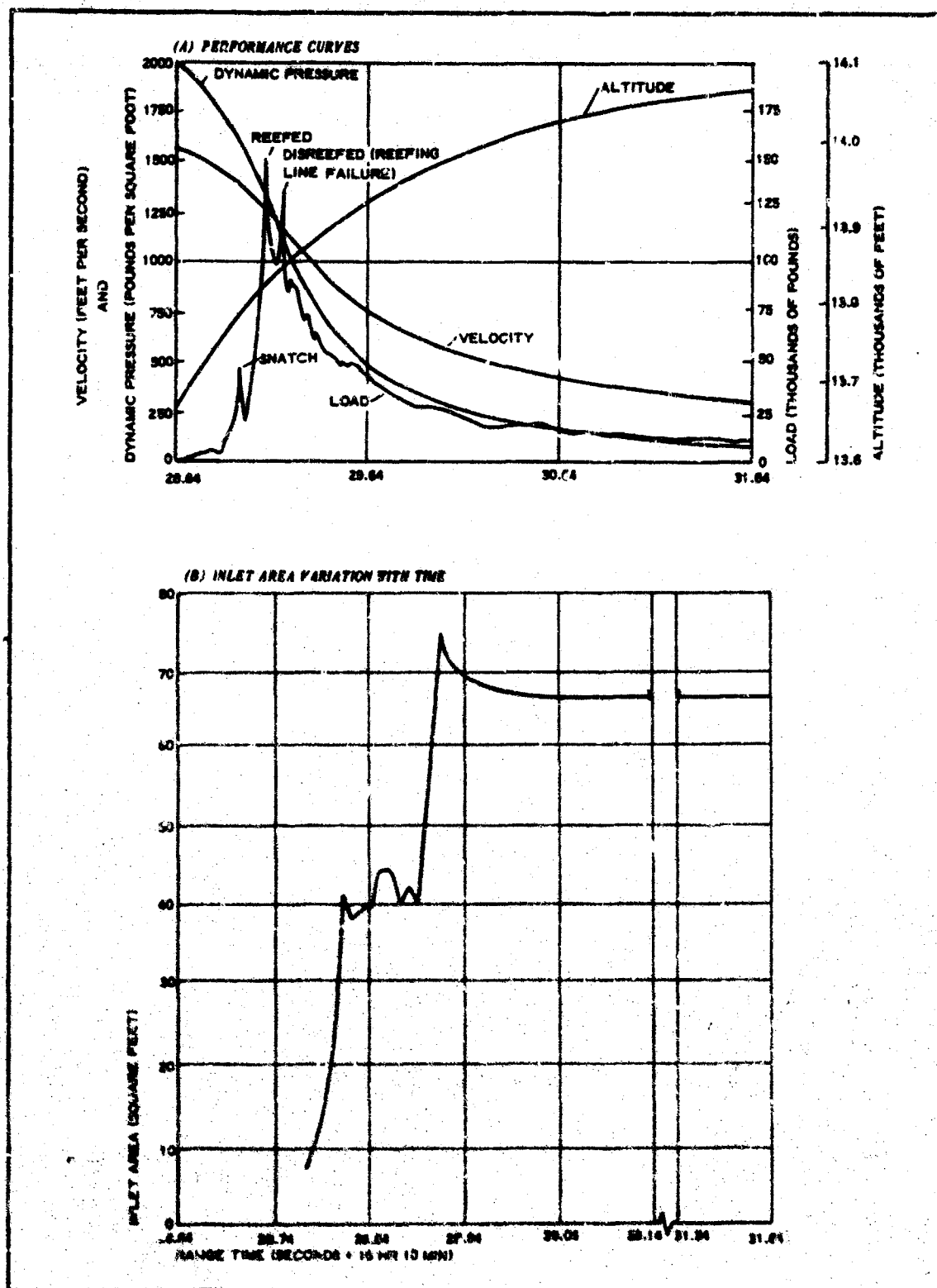


Figure 7 - LP-3: (A) Performance Curves; (B) Inlet Area Variation with Time

canopy, and one of the same broken lines was broken four feet from the test vehicle. Onboard motion picture films indicated that the deployment followed the planned sequence. Further examination of the film footage indicated a much higher than planned missile spin velocity at a deployment of approximately four to six revolutions per second. The spin velocity resulted in a 1.5-turn twist in the suspension lines 4 to 6 ft from the test vehicle. This same region of the lines had one of the broken suspension lines welded to another line. The parachute despun the missile in 1-1/2 revolutions and damped the spin oscillations to low values prior to disreef. The effect of the twist was determined to be limited, as the lines were approximately 30 ft long, and the twist was 24 to 26 ft from the skirt. The diameter of the twist was also limited by the diameter of the suspension line attachment ring. The approximate geometry is presented in the following sketch:

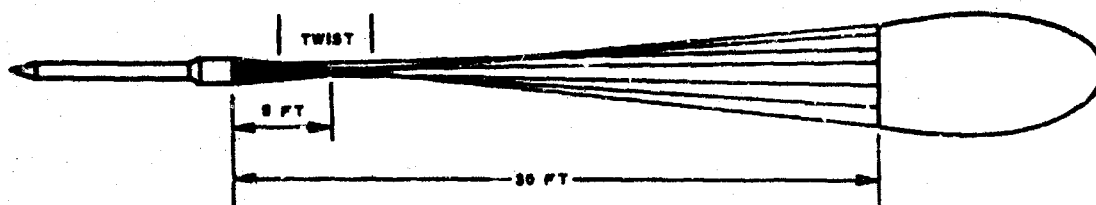


Figure 8A shows the performance curves of LP-4, beginning at test item container separation and continuing for three seconds. A performance summary is given in Table VII. Data for the performance curves were obtained from WSMR data reduction reports (References 19, 20) or the telemetry signal plot (Reference 9).

Figure 8B shows the LP-4 inlet area variation with respect to time on a selective time scale. Data from the onboard motion picture footage were used as a basis for the inlet area plot.

(4) LP-5 Free-Flight Summary

The LP-5 hemisflo test parachute was deployed very near the calculated test loading q of 3300 psf. The canopy exhibited good inflation and stability. The reefing line was 14 ft 10 in. long after sewing and consisted of a 6000- and 12,000-lb web sewn together. The test parachute was extracted and deployed by a 4-ft D_0 hemisflo pilot parachute permanently reefed to an inlet diameter of 15 in. This inlet diameter was five inches less than the pilot parachute inlet diameter used for deploying FP-4. The smaller diameter was chosen to reduce the deployment rate. The pilot chute inlet was located 120 in. aft of the test item deployment bag. The reefing line cutters were not initiated because the lanyards failed and did not pull out the firing pin mechanisms; as a result, disreefing did not take place. Maximum inflation g 's were approximately 85 for the reefed shape.

The parachute was recovered with the canopy in general undamaged either by loadings or heating. Detail examination revealed several verticals were damaged or broken at or near their attachment to the inlet webbing. Suspension line numbers 8, 29, and 32 were broken 5, 6, and 7 ft, respectively, from the skirt. Lines 8/9 and 28/32 were fused into pairs approximately 8 ft from the test vehicle. Examination of the onboard

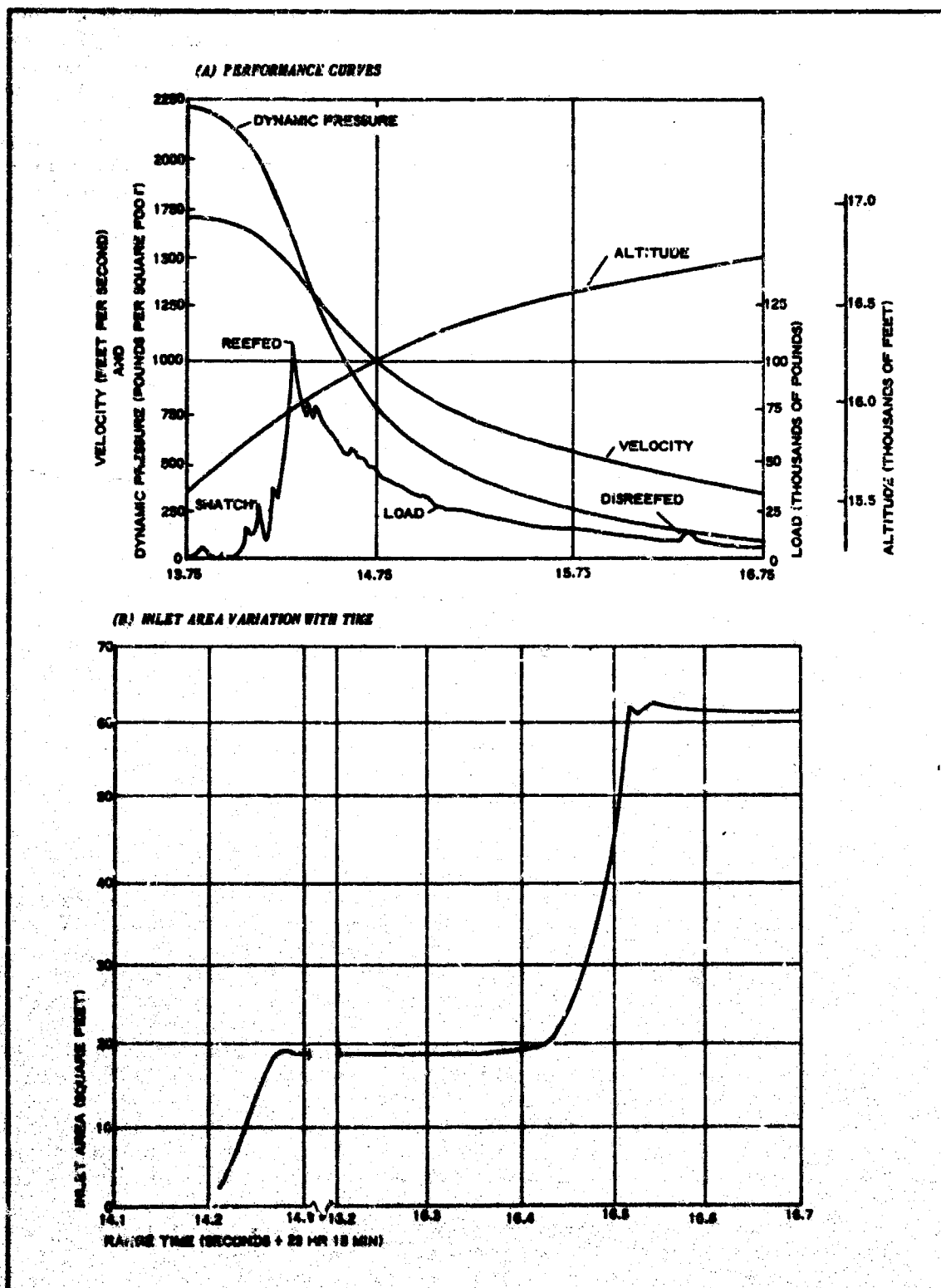


Figure 8 - LP-4: (A) Performance Curves; (B) Inlet Area Variation with Time

motion picture film footage indicated that test item LP-5 had spun in a manner similar to LP-4, with resultant twisting of the lines.

It was determined that the test vehicle introduced the spin torque to produce the line twist. The remedy was relocation of the outboard camera (described in Appendix C of Reference 9).

Figure 9A shows the performance curves of LP-5, beginning at test item container separation and continuing for three seconds. Data for the performance curves were obtained from WSMR reduction reports (References 21, 22) or the test vehicle telemetering signal plots (Reference 4).

Figure 9B shows the LP-5 inlet area variation with respect to time. Data from the onboard motion picture footage were used as a basis for the inlet area plot.

3. AERODYNAMIC ANALYSIS

a. General

Since the configuration and dimensions for the large high-q parachutes were established by previous AFFDL-RTD wind-tunnel tests (References 11, 12, 13), the principle aerodynamic task for ADDPEP Phase II was to determine the reefing line length necessary to keep the parachute peak opening load near 200,000 lb for each deployment. Three approaches to solving the reefing problem were investigated; these were based on wind-tunnel tests, free-flight tests, and analytical methods.

b. Reefing Based on Wind-Tunnel Tests

The AFFDL-RTD wind-tunnel results in References 11, 12, and 13 include deployment load values for the large-model parachutes (10-ft D_0) and steady-state values for both the large- and small-model parachutes (13- and 19.3-in. D_0). The opening shock values are higher in the wind tunnel than in free flight, as would be expected. The wind-tunnel steady-state drag coefficient values for the large and small parachute models vary more than would be anticipated, based on the design differences between the models (see Figure 4).

Figure 10 compares the wind-tunnel model data with the flight data excluding the opening shock period. This figure was made by adding flight values for nominal surface drag coefficient versus reefing ratio to the data given earlier in Figure 5. It is apparent that the drag coefficient values for flight test are above those for small-scale wind-tunnel models at the same reefing ratio (Reference 13). Based on the comparison of small-scale wind-tunnel data and the free-flight data, it appears that the correlation is not sufficiently accurate for direct use of small-scale data. Insufficient large-scale, directly applicable wind-tunnel data are available for establishing reefing-line lengths with confidence.

c. Reefing Based on Free-Flight Data

Free-flight data from one test can be used to calculate or predict reefing requirements for other test conditions. Hence, in Phase II, each test

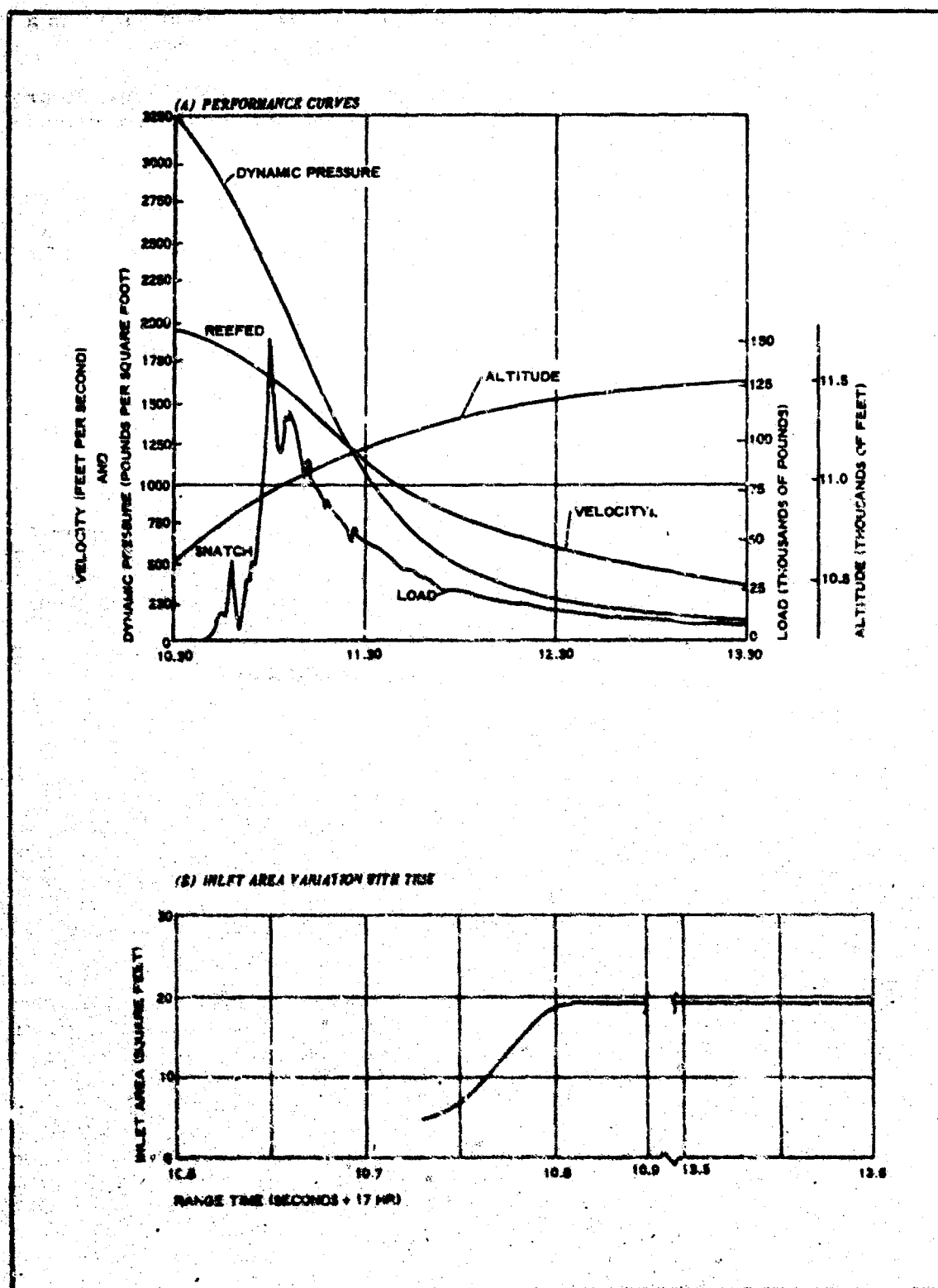


Figure 9 - LP-5: (A) Performance Curves; (B) Inlet Area Variation with Time

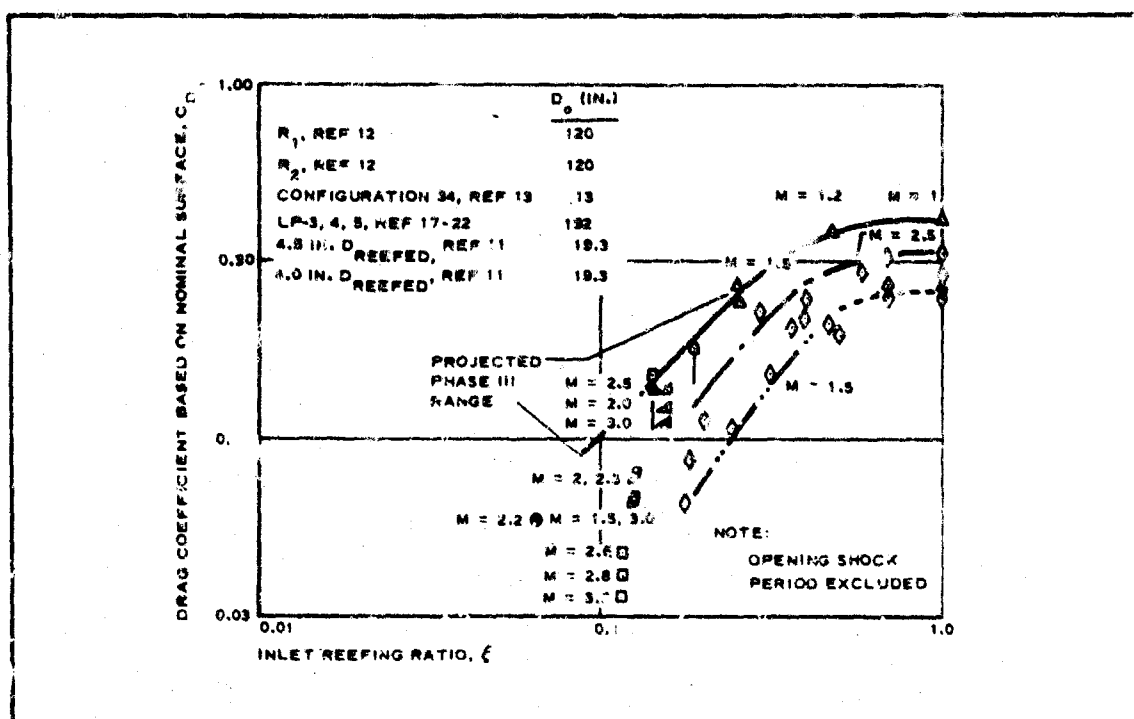


Figure 10 - Comparison of Small-Scale and Free-Flight Data

aided in predicting the reefing requirements for the next test. Three tests of the heavy-duty hemisflo parachutes were made from Mach 1.5 through 1.84, with accompanying deployment dynamic pressures from 1988 to 3383 psf. Table VII (shown earlier) summarizes the test conditions.

Figure 11A shows the Mach number values versus time covered by the LP-3, LP-4, and LP-5 large parachute tests for a selective time period (time starts at container separation and continues for three seconds); this figure illustrates the practice of extending the envelope of demonstrated parachute-operating capability in regular increments. Figure 11B presents the corresponding range of dynamic pressures versus time.

Figures 12 and 13 show the resulting load measured by the strain link and load/dynamic pressure versus time for parachutes LP-3, LP-4, and LP-5. In each instance, the first small peak after approximately 0.3 sec is produced by line stretch. The large twin peaks of the LP-3 correspond to the opening loads reefed and disreefed. The disreefed load of LP-4 occurs within three seconds. Comparison of these curves demonstrate that the reefing line is an effective means of controlling the peak loads. The reefing line circumferences, measured under 40-lb tension, are 20.5, 14.93, and 14.93 ft., respectively, for LP-3, LP-4, and LP-5. The measured load dynamic pressure divided by Mach number is shown in Figure 14. The initial small peaks are produced by line-stretch loads.

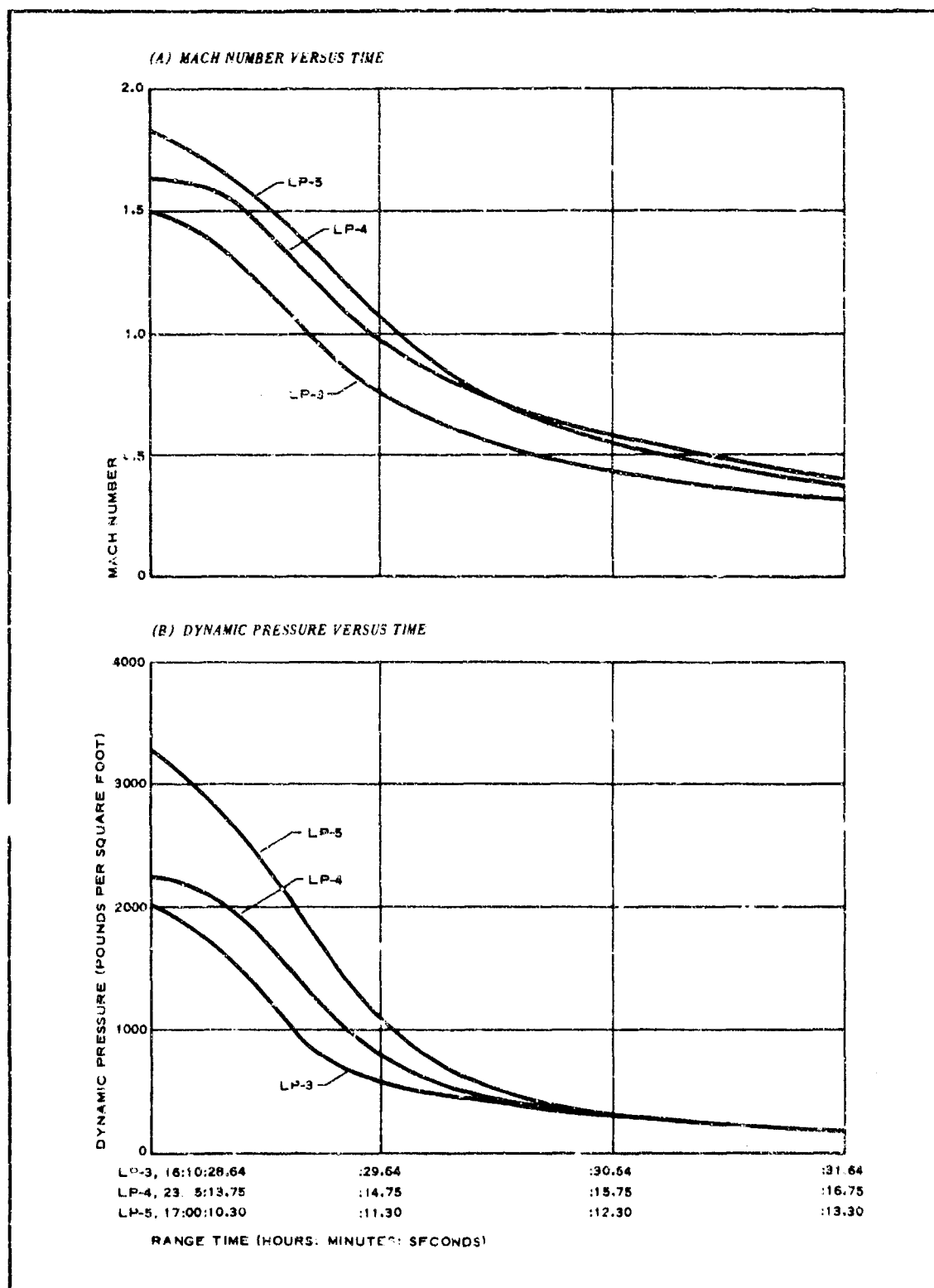


Figure 11 - LP-3, LP-4, LP-5: (A) Mach Number versus Time;
(B) Dynamic Pressure versus Time

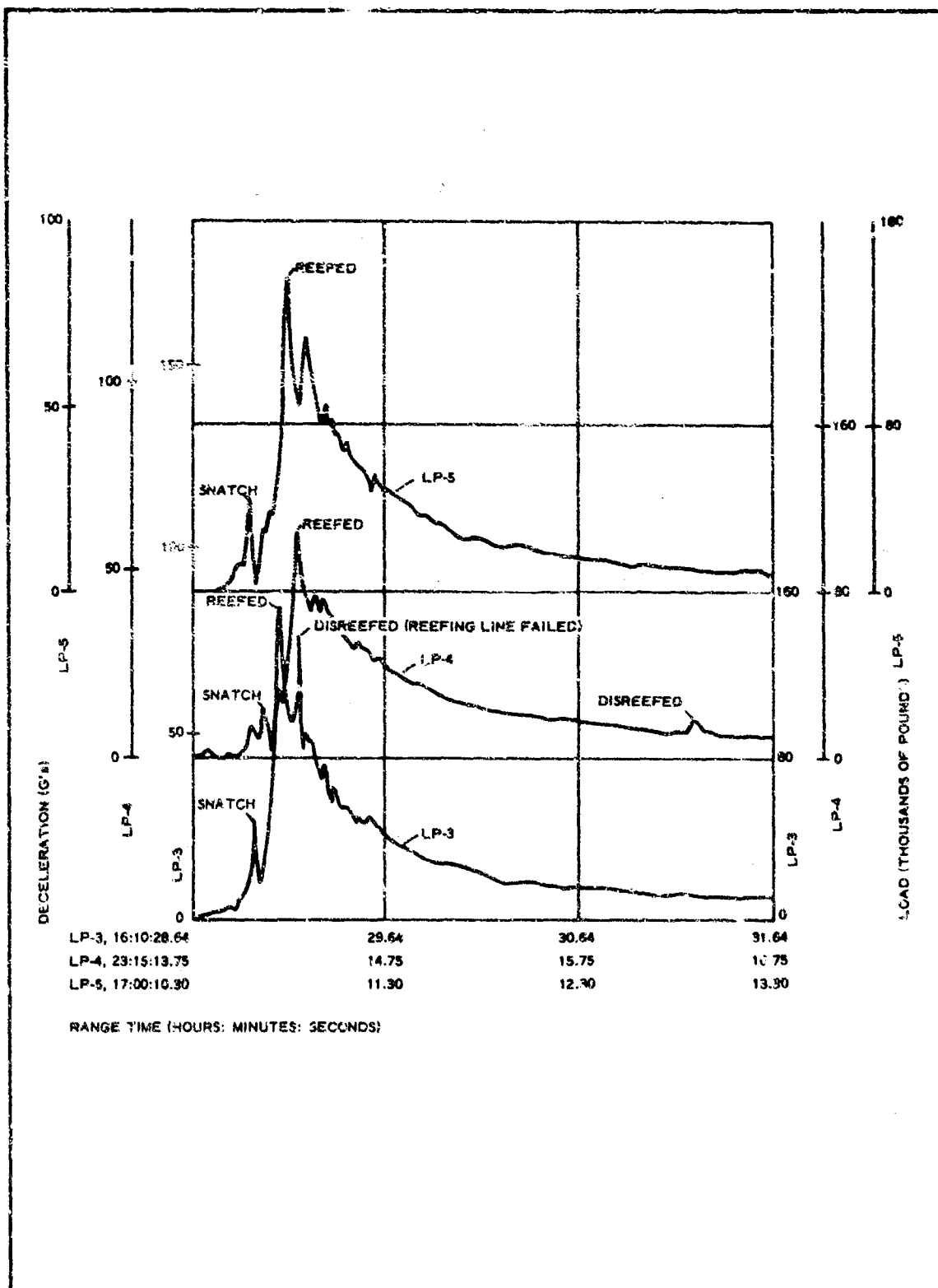


Figure 12 - LP-3, LP-4, LP-5: Load or Deceleration versus Time

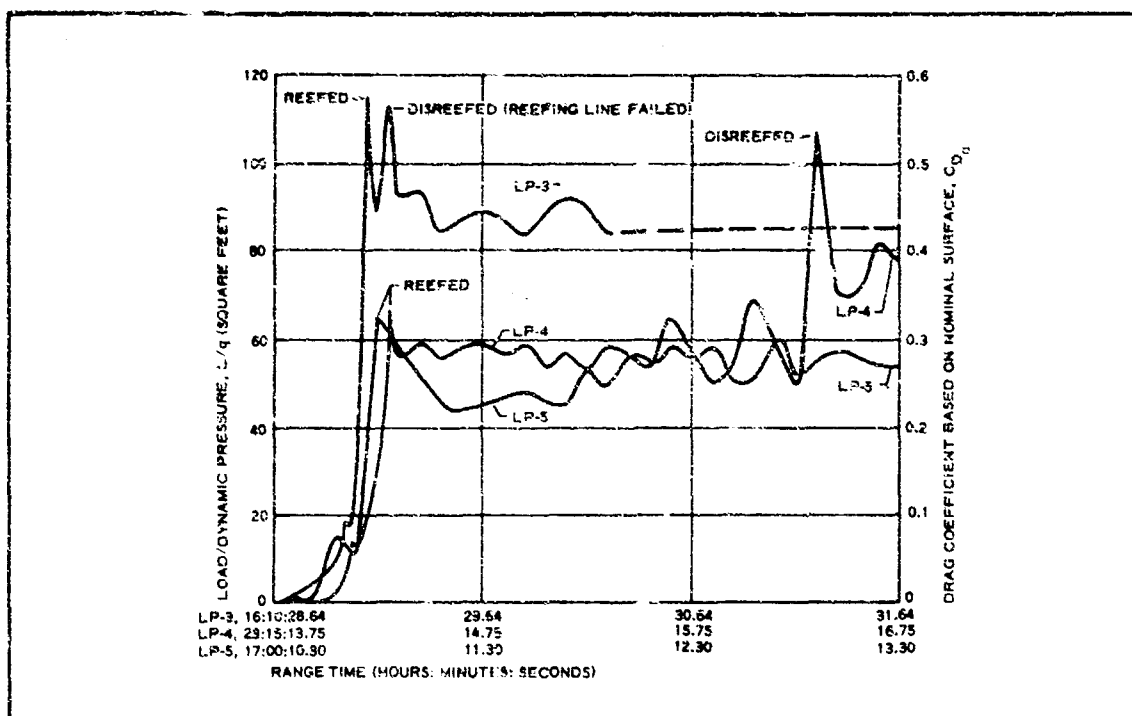


Figure 13 - LP-3, LP-4, LP-5: Load/Dynamic Pressure and Nominal Surface Drag Coefficient versus Time

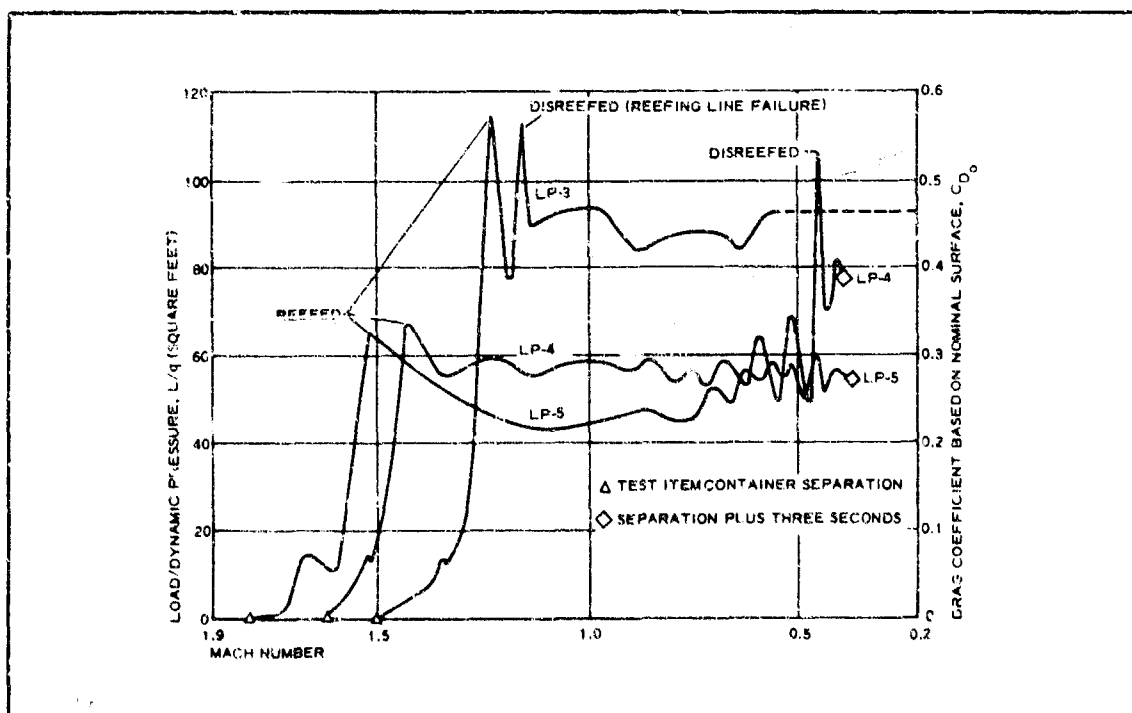


Figure 14 - LP-3, LP-4, LP-5: Load/Dynamic Pressure and Nominal Surface Drag Coefficient versus Mach Number

Table IX gives the dimensional and loading parameters; the loading parameters are based on conditions at maximum loading. The values presented in Columns 4 through 7 are reduced from the digitized range data. Column 8 values are based on the values plotted in Figure 14. Nearly constant load/dynamic pressure (L/q) values for LP-4 and LP-5 are evident after the parachutes have opened to the reefed shape. However, the value for LP-3 required extrapolation considering the values of LP-4 and LP-5. Column 9 is an opening shock factor, K , defined as Column 7 divided by Column 8. Because only two nearly constant L/q values for the reefed shape are directly evident compared to three L/q values at maximum load, the three values were selected for extrapolating to correspond with the shorter reefing line lengths required for higher Mach numbers and dynamic pressure tests.

TABLE IX - LARGE PARACHUTE DIMENSIONAL AND
LOADING PARAMETERS

1	2	3	4	5	6	7	8	9
Test item	Reefing line length, RLL (ft)	Reefed inlet area, RIA (sq ft)	Test altitude at L_{max} (ft)	Test Mach at L_{max}	Test q at L_{max} (psf)	Test L/q at L_{max} (sq ft)	Test L/q after opening (sq ft)	Test shock factor, K^*
LP-3	20.5	33.60	13,815	1.24	1350	114	77	1.480
LP-4	14.83	17.55	15,934	1.40	1642	67	57	1.175
LP-5	14.83	17.55	10,948	1.56	2410	63	50	1.260

* Column 7/Column 8

Past practices have presented the effect of reefing as drag coefficient (C_D) or drag area (C_DA) versus reefing line length (RLL). Another parameter to consider is the reefed inlet area (RIA). The two coefficients, K_{RLL} and K_{RIA} , are shown in Columns 4 and 6 of Table X. The value is equal to:

$$K_{RLL} (ft) = \frac{L/q \text{ at } L_{max} (ft^2)}{RLL (ft)} \quad (1)$$

The value of K_{RIA} is equal to:

$$K_{RIA} = \frac{L/q \text{ at } L_{max} (ft^2)}{RIA (ft^2)} \quad (2)$$

Both coefficient values are plotted in Figure 15 and extrapolated to other

reefing sizes. The constructing of the curves was aided by the fact that the values of both coefficients should be equal when the values of the other parameters are equal. This occurs at a reefing line length of 4π , where the value of the reefed inlet area is also 4π . These curves can be used to calculate values of L/q at maximum load for other reefing sizes.

TABLE X - LARGE PARACHUTE MAXIMUM-
LOADING COEFFICIENTS

1	2	3	4	5	6
Test item	Test L/q at L_{\max} (sq ft)	Reefing line length, RLL (ft)	Coefficient, K_{RLL}^* (ft)	Reefed inlet area, RIA (sq ft)	Coefficient, K_{RIA}^+
LP-3	114	20.5	5.56	33.60	3.4
LP-4	67	14.83	4.51	17.55	3.82
LP-5	63	14.83	4.25	17.55	3.59

* Column 2/Column 3

† Column 4/Column 5

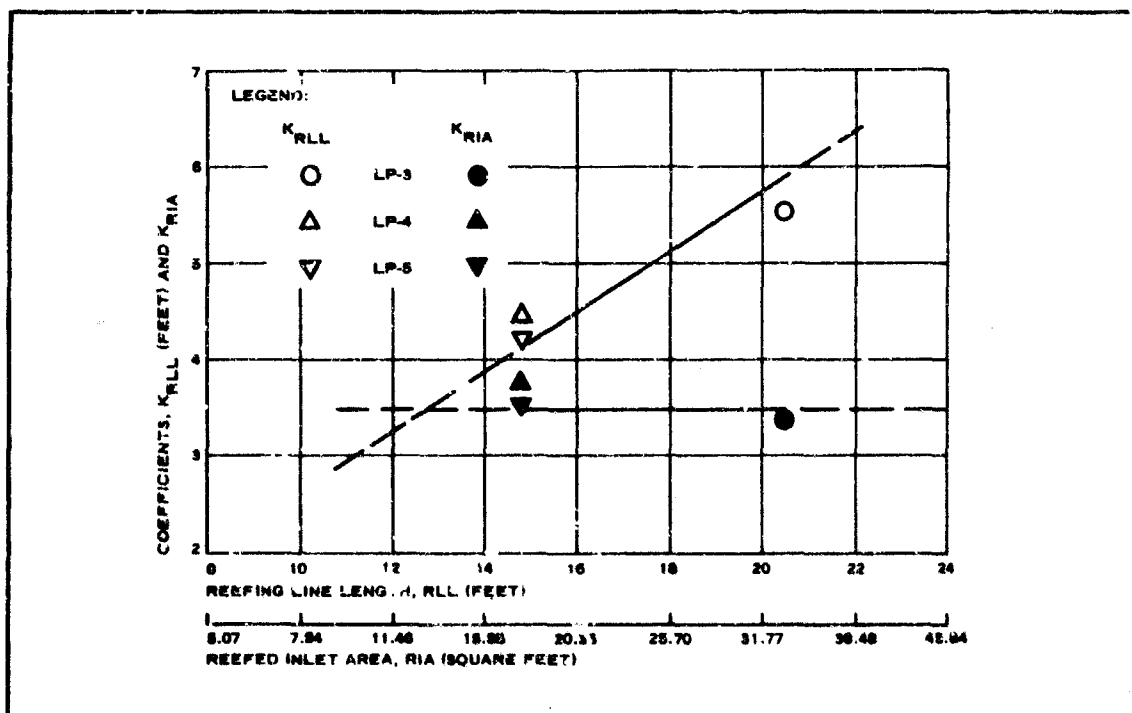


Figure 15 - Reefing Line Length (RLL) and Reefed Inlet Area (RIA) versus Coefficients (K)

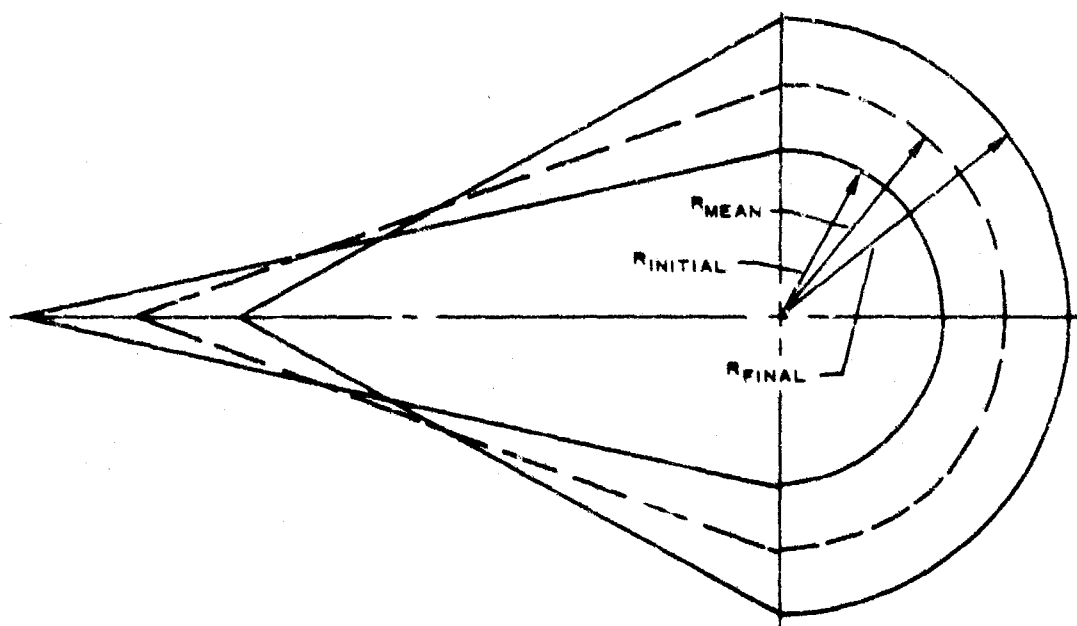
d. Reefing Based on Analytical Methods(1) Approach

In the analytical approach used to obtain an opening load near 200,000 lb for each deployment, the parachute-opening loads are considered as consisting of two principal parts. The first part is the aerodynamic drag of the shape itself, which is treated as being generated by a drag coefficient (C_D) times the area (A) and dynamic pressure (q). The area is based on the canopy-inlet area at the time considered. The other part of the opening load is caused by acceleration of the net air mass that is being acquired by the canopy during filling, as contrasted to a low or zero net gain of mass after opening. The force generated by the net-acquired mass is a function of the acquisition time or opening time.

To determine the acquisition time, a step calculation is used based on an assumed canopy-suspension-line geometry. It is assumed that the canopy is formed by the opening loads into a shape consisting of a cone coincident with a hemisphere (see Figure 16).

The degree of inflation establishes the size of the hemisphere. The radial member length is divided into X and Y components, and the inlet diameter is established. The leakage area is considered to be only in the hemispherical portion of the canopy and is based on the nominal geometric porosity (λ).

Because the canopy can be expected to open at different rates during its opening, the opening sequence is calculated in steps. To simplify the mathematics, the canopy geometry is made the basis of the steps; the hemispherical radius is increased by regular increments. The mean dimensions between increments are used in calculating flow values. An increment is defined in the following sketch:



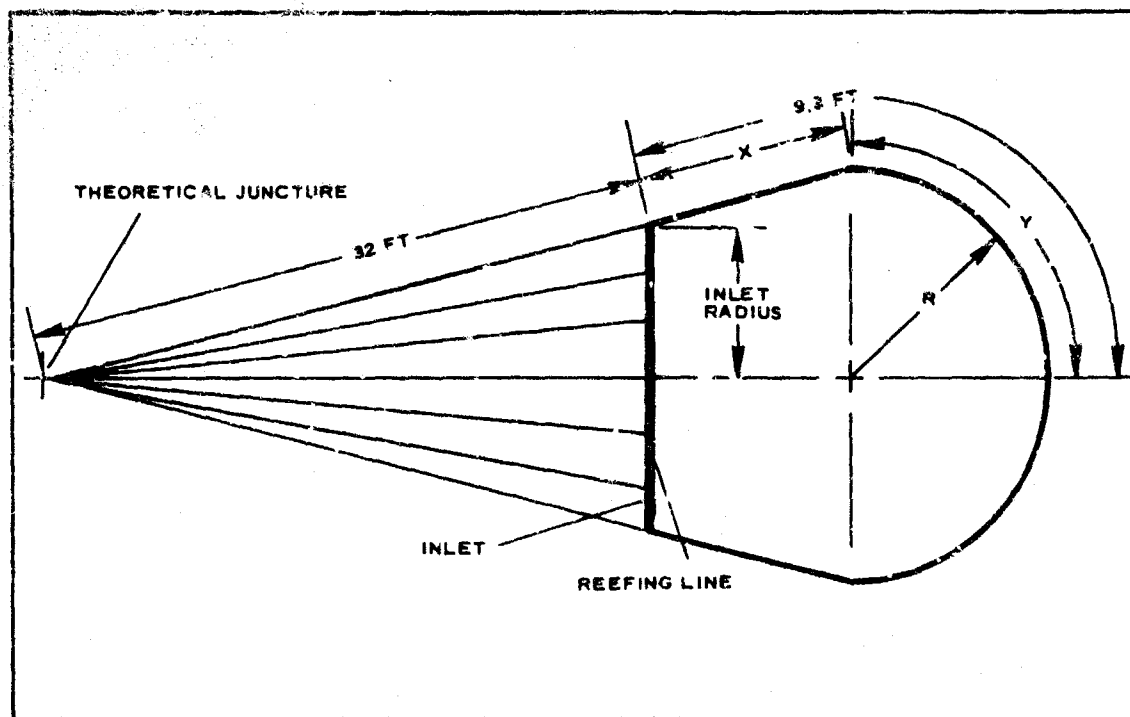
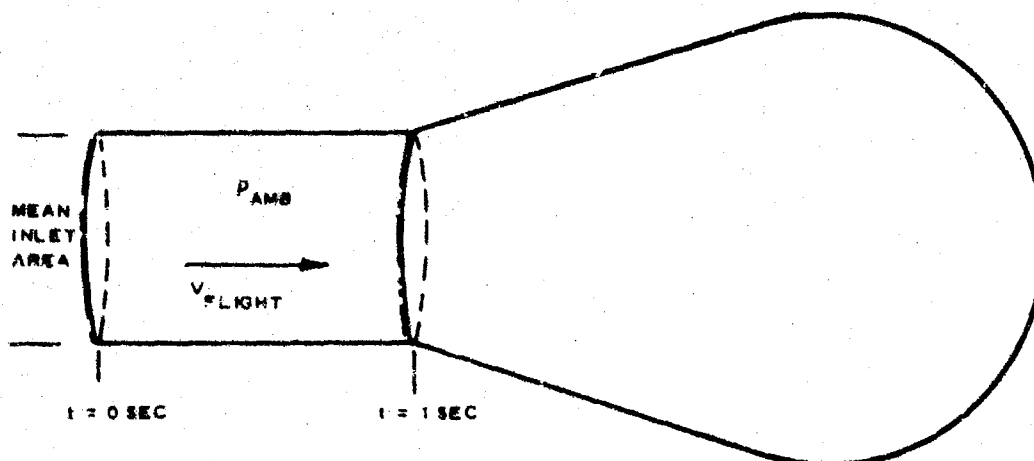


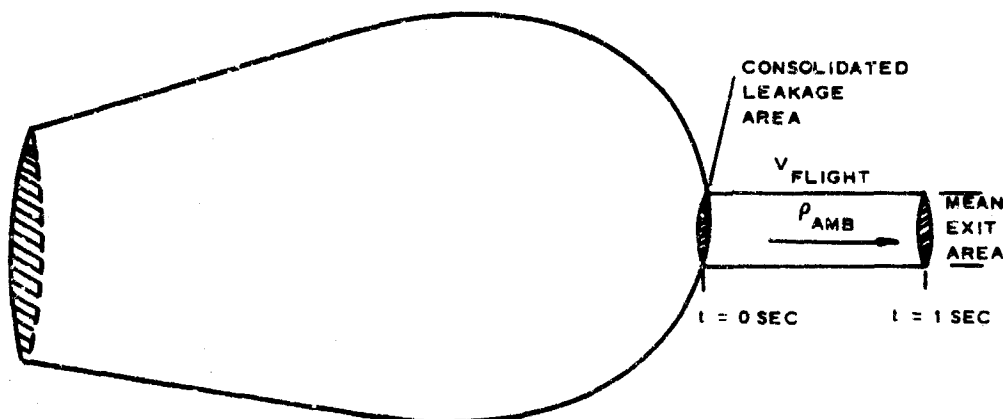
Figure 16 - Geometric Nomenclature

The aerodynamic shape-drag throughout one increment consists of the reefed shape-drag coefficient times the mean dynamic pressure and the mean projected inlet area during the increment. The net mass acquired during the increment consists of the mass-in minus the mass-out during the increment. The mass per second is considered to be in at the flight velocity at the beginning of the increment times the mean inlet area times the ambient mass density, as illustrated in the following sketch:



$$\text{Incoming mass per second} = \left(V_{\text{flight}}, \frac{\text{ft}}{\text{sec}} \right) \left(\rho_{\text{amb}}, \frac{\text{lb sec}^2}{\text{ft}^4} \right) \left(A_{\text{inlet}}, \text{ft}^2 \right) \quad (3)$$

The exciting mass per second is considered to be out at the flight velocity times the mean exit area times the ambient mass density, as illustrated in the following sketch:



$$\text{Exiting mass per second} = \left(V_{\text{flight}}, \frac{\text{ft}}{\text{sec}} \right) \left(\rho_{\text{amb}}, \frac{\text{lb sec}^2}{\text{ft}^4} \right) \left(A_{\text{exit}}, \text{ft}^2 \right) \quad (4)$$

Subtracting the exiting mass per second from the incoming mass per second yields net mass gain per second. Dividing the required mass increase in a volume increment by the net mass gain per second yields the filling time for the chosen increment. Multiplying the net mass per second by the increment initial velocity yields the force that is applied to the canopy in decelerating mass at this rate. Adding the shape-drag force yields the total force.

Forty-six steps were involved in calculating the loads during opening of LP-3, LP-4, and LP-5 for a range of inlet sizes at actual test conditions. Table XI shows the geometric considerations involved in Steps 1 through 23, and Table XII shows the environmental considerations involved in Steps 24 through 46. Figures 17, 18, and 19 show the calculated values from the tables and the measured force values. The values in Figure 17 are based on an assumed shape-drag coefficient used in Reference 23 and on shape-drag values calculated from early flight data after the parachute opened to the reefed shape. The values for Figures 18 and 19 use the shape-drag coefficient values from the early flight data only.

(2) Shape-Drag Calculations

A shape-drag calculation was made at the 12.622-sec point of the LP-5 trajectory. This point was selected for the trajectory because the canopy had opened to the reefed shape and the measured force is neither increasing or decreasing (Figure 20). Energy is not accumulating or being released from the suspension lines, and the canopy's velocity and acceleration match those of the vehicle. The top force line of Figure 20 shows

TABLE XI - OPENING LOAD CALCULATIONS FOR
LP-3, LP-4, LP-5 (GEOMETRIC)

Calculation step			Radius increment (ft)				
No.	Description	Source*	0 to 1	1 to 2	2 to 3	3 to 4	4 to 5
①	Mean hemisphere radius (ft)	Increment average	0.5	1.5	2.5	3.5	4.5
②	Mean great circle area (sq ft)	$\pi \times \textcircled{1}^2$ (Fig 16)	0.785	7.06	19.65	38.5	63.6
③	Mean hemisphere area (sq ft)	$2 \times \textcircled{2}$	1.57	14.12	39.30	77.0	127.2
④	Mean cylinder area (sq ft)	$0 \times \textcircled{2}$	0.0	0.0	0.0	0.0	0.0
⑤	Mean total leakage area (sq ft)	$\textcircled{3} + \textcircled{4}$	1.57	14.12	39.30	77.0	127.2
⑥	Effective leakage opening (sq ft)	$\textcircled{5} \times \lambda_g; \lambda_g = 0.14$	0.2193	1.979	5.50	10.79	17.82
⑦	Half mean hemisphere perimeter	$\textcircled{1} \times 0.5\pi = Y$ of Fig 16	0.785	2.36	3.93	5.50	7.06
⑧	Mean straight line distance (ft)	$41.3 - \textcircled{7}$ ($41.3 = X + Y + 2D_o$, Fig 16)	40.52	38.94	37.37	35.80	34.24
⑨	Mean skirt line distance (ft)	$9.3 - \textcircled{7}$ (Fig 16)	8.52	6.94	5.37	3.80	2.24
⑩	Ratio, suspension line to straight line	$2D_o / \textcircled{8}$	0.789	0.821	0.855	0.894	0.934
⑪	Mean inlet radius (ft)	$\textcircled{1} \times \textcircled{10}$	0.395	1.232	2.140	3.125	4.204
⑫	Mean inlet area (sq ft)	$\textcircled{11}^2 \times \pi$	0.490	4.775	14.40	30.75	55.5
⑬	Maximum hemisphere radius (ft)	Increment limit	1.0	2.0	3.0	4.0	5.0
⑭	Maximum hemisphere volume (sq ft)	$\textcircled{13}^3 \times 2.0944$	2.094	16.75	56.5	134.0	261.6
⑮	Half maximum hemisphere perimeter (ft)	$\textcircled{13} \times 0.5\pi$	1.571	3.146	4.71	6.29	7.85
⑯	Maximum straight line distance (ft)	$41.3 - \textcircled{15}$	39.73	38.15	36.59	35.01	33.45
⑰	Maximum skirt line distance (ft)	$9.3 - \textcircled{15}$	7.73	6.15	4.59	3.01	1.45
⑱	Ratio, suspension line to straight line	$2D_o / \textcircled{16}$	0.805	0.839	0.875	0.914	0.956
⑲	Maximum inlet radius (ft)	$\textcircled{13} \times \textcircled{19}$	0.805	1.678	2.625	3.656	4.78
⑳	Average maximum truncated cone radius (ft) [†]	$\frac{\textcircled{13} + \textcircled{19}}{2} C_f$	0.911	1.858	2.840	3.864	4.94
㉑	Maximum truncated cone volume (cu ft)	$\textcircled{20}^2 \times \pi \times \textcircled{17}$	20.18	66.7	136.2	141.4	111.0
㉒	Maximum total volume (cu ft)	$\textcircled{14} + \textcircled{21}$	22.27	83.45	172.7	275.4	372.6
㉓	Maximum total volume change (cu ft)	$\textcircled{22} - \textcircled{22}$ of previous increment	22.27	61.1	89.3	102.7	97.2

*Circled numbers in this column refer to step numbers in first column of table.

[†]Symbol C_f is an empirical factor to correct the average radius to a value that provides an average cross-sectional area; $C_f = 1.01$.

TABLE XII - OPENING LOAD CALCULATIONS FOR LP-3, LP-4, LP-5 (ENV

Calculation step			LP-3 radius increment (ft)					LP-4 radius increment		
No.*	Description	Source	0 to 1	1 to 2	2 to 3	3 to 4	4 to 5	0 to 1	1 to 2	2 to 3
24	Altitude (ft)	WSMR data	13,750	13,750	13,750	13,750	13,750	15,817	15,817	15,817
25	Ambient density (lb sec ² /ft ⁴)	WSMR data	0.001575	0.001575	0.001575	0.001575	0.001575	0.001453	0.001453	0.001453
26	Ambient pressure (psf)	WSMR data	1,252	1,252	1,252	1,252	1,252	1,175	1,175	1,175
27	Ambient temperature (R)	WSMR data	464.0	464.0	464.0	464.0	464.0	471.2	471.2	471.2
28	Ambient specific volume (ft ³ /lb)	WSMR data	19.70	19.70	19.70	19.70	19.70	21.43	21.43	21.43
29	Velocity (fps) [†]	29 - 42 of prev increment	1,440	1,437	1,429	1,417	1,414.3	1,632	1,629	1,626
30	Velocity squared (ft ² /sec ²) [‡]	29 ²	2,075,000	2,063,000	2,040,000	2,004,000	2,000,244	2,664,000	2,650,000	2,623,000
31	Inlet flow (ft ³ /sec) [†]	12 × 29	705	6,850	20,580	43,500	78,500	800	7,760	23,350
32	Exit flow (ft ³ /sec) [†]	6 × 29	316.4	2,840	7,850	15,280	25,200	359	3,220	8,900
33	Net flow-in (ft ³ /sec) [†]	31 - 32	389	4,010	12,730	28,220	53,300	441	4,540	14,450
34	Net mass rate-in (lb sec ² /ft sec) [†]	33 × 29	0.612	6.310	20.04	44.45	83.90	0.641	6.590	21.00
35	Fill time (sec) ^{†§}	29 × 29 / 34	0.0574 (0.574)	0.1527 (0.0727)	0.00700 (0.0797)	0.00364 (0.0833)	0.001281 (0.0841)	0.0505 (0.0505)	0.0135 (0.0640)	0.006 (0.07)
36	Fill mass rate (lb sec ² /ft sec) [†]	31 × 29	1.111	10.80	32.40	68.50	123.8	1.163	11.30	33.90
37	Fill mass (lb sec ² /ft) [†]	36 × 35	0.0636	0.1648	0.2270	0.2492	0.1585	0.0588	0.1525	0.205
38	Fill force (lb) [†]	37 × 29 × 35	1,600	15,500	46,300	98,900	174,900	1,930	18,400	54,900
39	Dynamic pressure (psf) [†]	0.5 × 29 × 30	1,632	1,625	1,608	1,580	1,576	1,938	1,924	1,900
40	Aerodynamic shape-drag (lb)	2.58 × 39 × 12 1.35 × 39 × 12 2.56 × 39 × 12	2,064 1,081 2,430	20,000 10,490 23,530	59,600 31,420 70,300	125,200 66,100 125,200	118,000 118,000 125,200	4,300 2,430 41,930	41,930 23,530 125,200	125,200 70,300 125,200
41	Total force (lb) [†]	40 + 38	3,664 2,681	35,500 25,900	105,900 78,020	222,100 164,900	292,900	4,300	41,930	125,200
42	Velocity decay (fps) [†]	0.0156 [¶] × 41 × 39	3.28 2.402	8.44 6.18	11.57 7.90	12.62 9.23	58.2	3.41	8.81	12.06
43	Reefed circumference (ft)	2π × 19	5.055	10.55	16.50	22.97		5.055	10.55	16.50
44	Reefed diameter (in.)	43 × 3.82 [¶]	19.30	40.30	63.0	87.7		19.30	40.30	63.0
45	Reefing line diameter (in.)	44 - 2	17.30	38.30	61.0	85.7		17.30	38.30	61.0
46	Reefing line circumference (ft)	45 × 0.262 [¶]	4.53	10.03	15.98	22.43		4.53	10.03	15.98

* Steps continue from Table XI.

† Circled numbers in this column refer to step numbers in first column of table.

‡ Double values for LP-3, where given, are based on 2.58 and 1.35 shape-drag coefficients in Step 40. Single values for LP-4 and LP-5 are based on 2.56 shape-drag coefficient of Step 40.

§ Total elapsed time in parentheses.

|| Increment values based on 2.58 shape-drag coefficient calculated from early LP-3 quick-look test data (2.58 based on mean inlet area).

¶ Increment values based on originally estimate presented by S. F. Hoerner (1.35 based on mean inlet area).

¶ Increment values based on 2.56 shape-drag coefficient test data (2.56 based on mean inlet area).

¶ Equal to (32.2 ft/sec²)/1991 lb.

¶ Value equal to (12 in./ft)/π.

¶ Value equal to π/(12 in./ft).

SECTION III - LARGE PARACHUTE DECELERATOR

AFFDL-TR-67-25

CALCULATIONS FOR LP-3, LP-4, LP-5 (ENVIRONMENTAL)

radius increment (ft)			LP-4 radius increment (ft)				LP-5 radius increment (ft)		
2 to 3	3 to 4	4 to 5	0 to 1	1 to 2	2 to 3	3 to 4	0 to 1	1 to 2	2 to 3
13,750	13,750	13,750	15,817	15,817	15,817	15,817	10,805	10,805	10,805
0.001575	0.001575	0.001575	0.001453	0.001453	0.001453	0.001453	0.001722	0.001722	0.001722
1,252	1,252	1,252	1,175	1,175	1,175	1,175	1,418	1,418	1,418
464.0	464.0	464.0	471.2	471.2	471.2	471.2	480.8	480.8	480.8
19.70	19.70	19.70	21.43	21.43	21.43	21.43	18.10	18.10	18.10
1,429	1,417	1,414	1,632	1,629	1,620	1,608	1,801	1,801	1,801
1,431.5	1,432.6	1,414.3	1,632	1,629	1,620	1,608	1,801	1,801	1,801
2,040,000	2,034,000	2,000,244	2,664,000	2,650,000	2,623,000	2,580,000	2,243,000	2,224,000	2,182,000
2,049,192	2,026,651	2,000,244	2,664,000	2,650,000	2,623,000	2,580,000	2,243,000	2,224,000	2,182,000
20,580	43,500	78,500	800	7,760	23,350	49,400	882	8,560	25,700
20,630	44,000	78,500	800	7,760	23,350	49,400	882	8,560	25,700
7,850	15,200	25,200	359	3,220	8,900	17,320	396	3,554	9,800
7,880	15,300	25,200	359	3,220	8,900	17,320	396	3,554	9,800
12,730	28,220	53,300	441	4,540	14,450	32,080	496	5,006	15,900
13,730	28,500	53,300	441	4,540	14,450	32,080	496	5,006	15,900
20.04	44.45	83.90	0.641	5.590	21.00	46.60	0.837	8.360	27.40
21.65	44.90	83.90	0.641	5.590	21.00	46.60	0.837	8.360	27.40
0.60700	0.00364	0.001281	0.0505	0.0135	0.00618	0.003196	0.0459	0.01221	0.00561
(0.0797)	(0.0833)	(0.0841)	(0.0505)	(0.0640)	(0.0702)	(0.0734)	(0.0459)	(0.0581)	(0.0637)
0.00649	0.00359	0.00359	0.00649	0.00359	0.00359	0.00359	0.00649	0.00359	0.00359
(0.0792)	(0.0828)	(0.0828)	(0.0792)	(0.0828)	(0.0828)	(0.0828)	(0.0792)	(0.0828)	(0.0828)
32.40	68.50	123.8	1.163	11.50	31.90	71.60	1.320	14.77	44.30
32.50	69.30	123.8	1.163	11.50	31.90	71.60	1.320	14.77	44.30
0.2270	0.2492	0.1535	0.0588	0.1525	0.2095	0.2292	0.0696	0.1802	0.2483
0.211	0.2490	0.1535	0.0588	0.1525	0.2095	0.2292	0.0696	0.1802	0.2483
46,300	96,900	174,900	1,900	13,400	54,800	115,200	2,740	26,500	78,900
46,600	98,800	174,900	1,900	13,400	54,800	115,200	2,740	26,500	78,900
1,608	1,580	1,576	1,938	1,924	1,908	1,874	2,795	2,750	2,740
1,615	1,598	1,576	1,938	1,924	1,908	1,874	2,795	2,750	2,740
89,666	125,200	118,000	1,938	1,924	1,908	1,874	2,795	2,750	2,740
31,420	66,100	118,000	1,938	1,924	1,908	1,874	2,795	2,750	2,740
105,900	224,100	292,900	4,300	41,930	125,200	262,700	6,240	60,520	180,000
78,020	164,900	292,900	4,300	41,930	125,200	262,700	6,240	60,520	180,000
11.57	17.62	58.2	3.41	8.81	11.08	13.10	4.455	11.53	15.77
7.90	9.23	58.2	3.41	8.81	11.08	13.10	4.455	11.53	15.77
16.50	22.97	58.2	5.055	10.55	16.50	22.97	5.055	10.55	16.50
61.0	87.7	58.2	19.30	40.30	61.0	87.7	19.30	40.30	61.0
61.0	85.7	58.2	17.10	38.10	61.0	85.7	17.10	38.10	61.0
15.98	22.43	58.2	4.53	10.03	15.98	22.43	4.53	10.03	22.43

¹ Increment values based on originally estimated 1.35 shape-drag coefficient for similar shapes presented by S. F. Hoerner (1.35 based on mean inlet area).

² Increment values based on 2.56 shape-drag coefficient calculated from early LP-3 quick-look test data (2.56 based on mean inlet area).

³ Equal to $(36.4 \text{ ft/sec}^2)/1991 \text{ lb.}$

⁴ Value equal to $(12 \text{ in./ft})/\pi$.

⁵ Value equal to $\pi/(12 \text{ in./ft})$.

icients in
Step 40.

quick-look

(Reverse is blank)

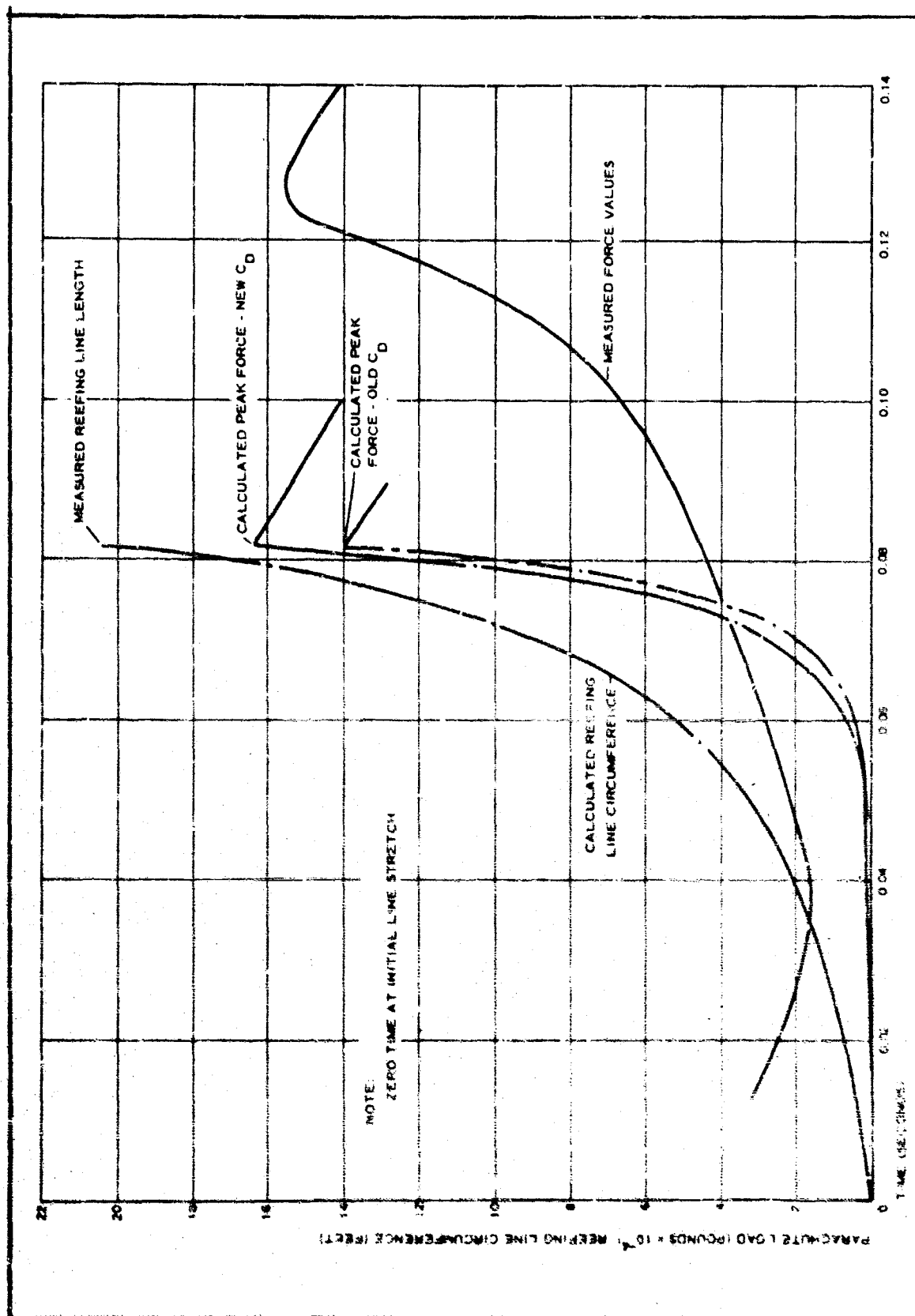


Figure 17 - LP-3 Deployment. Calculated and Measured Force-Time Relationship

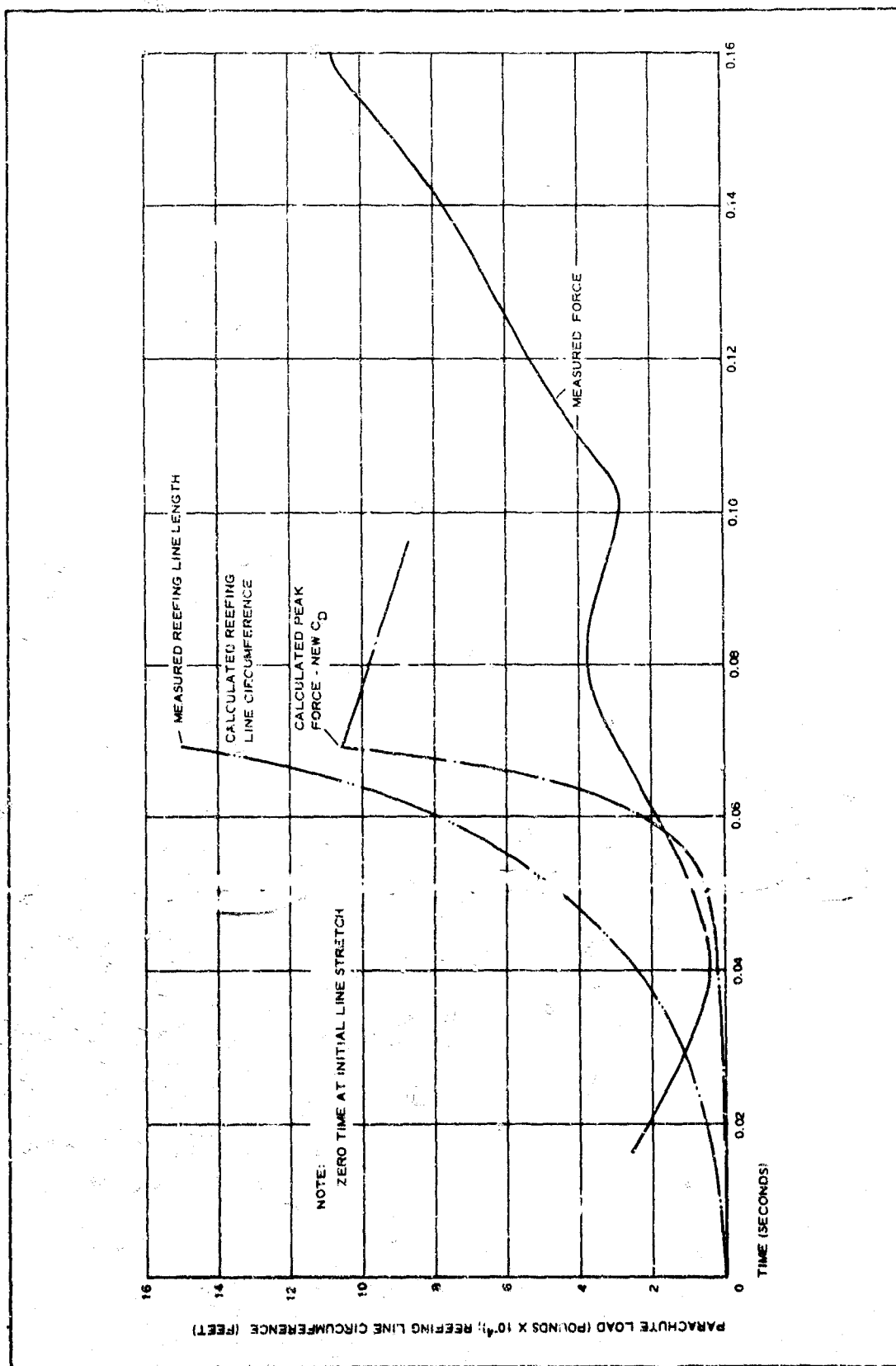


Figure 13 - LP-4 Deployment: Calculated and Measured Force-Time Relationship

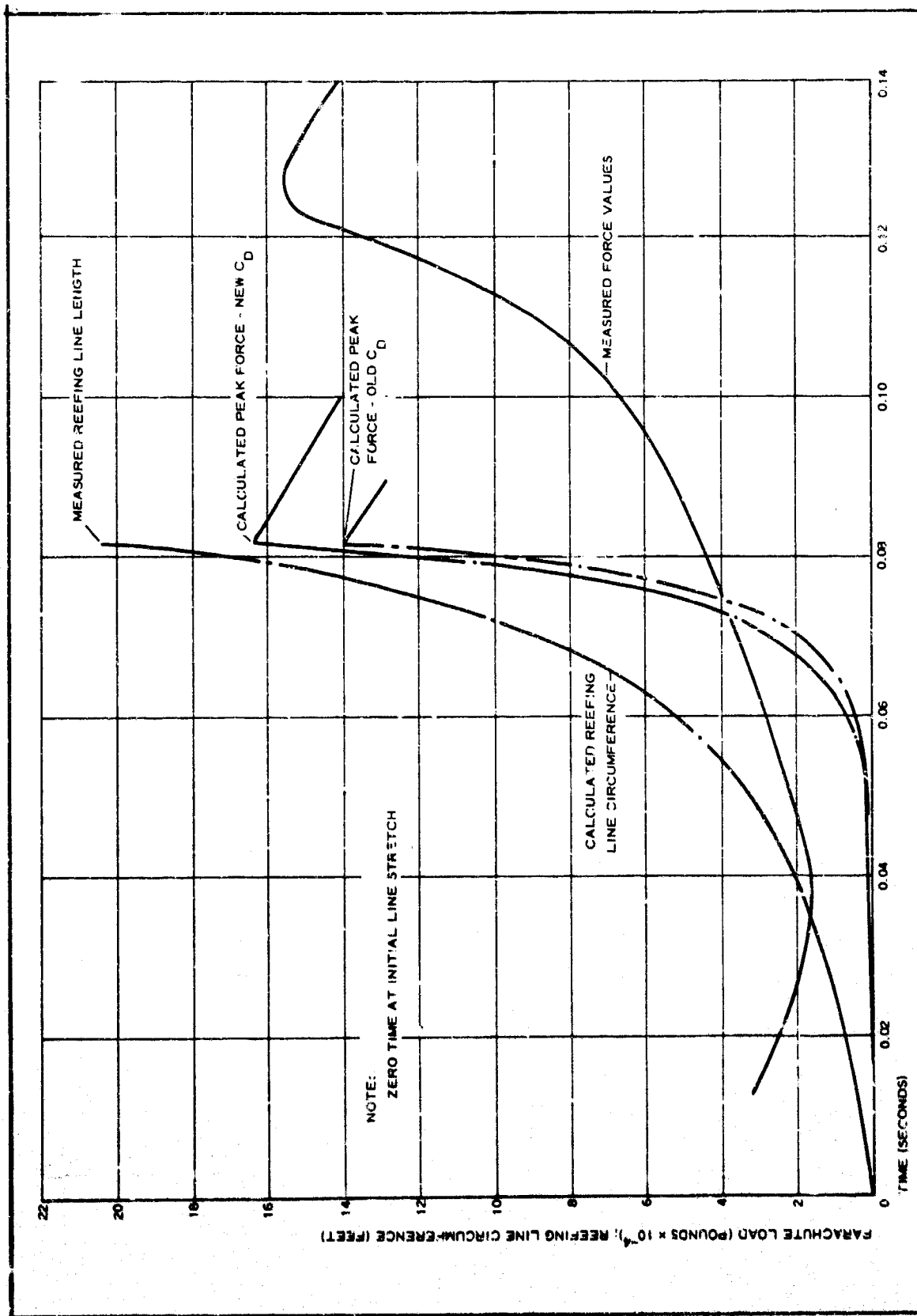


Figure 17 - LP-3 Deployment: Calculated and Measured Force-Time Relationship

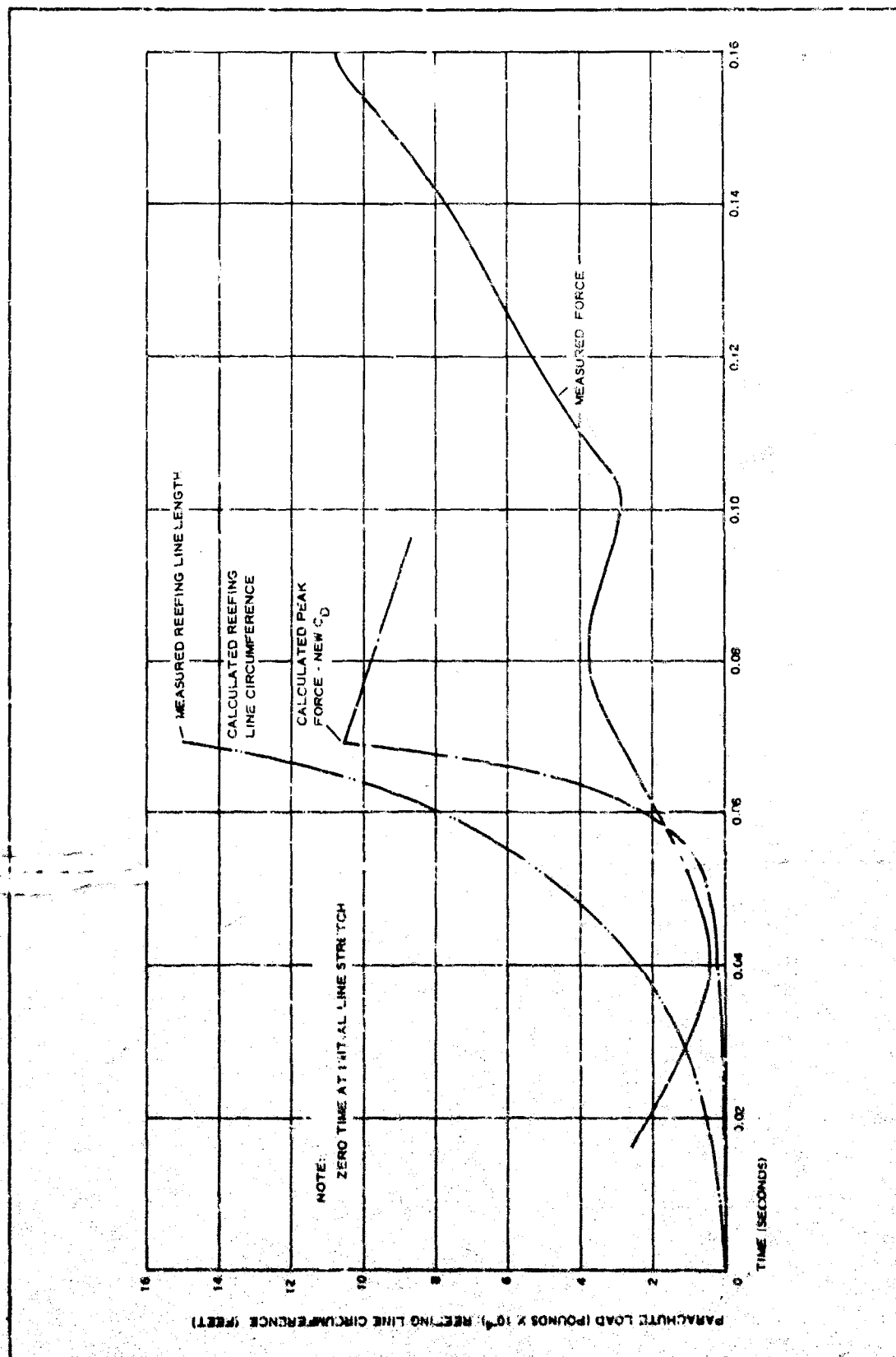


Figure 18 - LP-4 Deployment: Calculated and Measured Force-Time Relationship

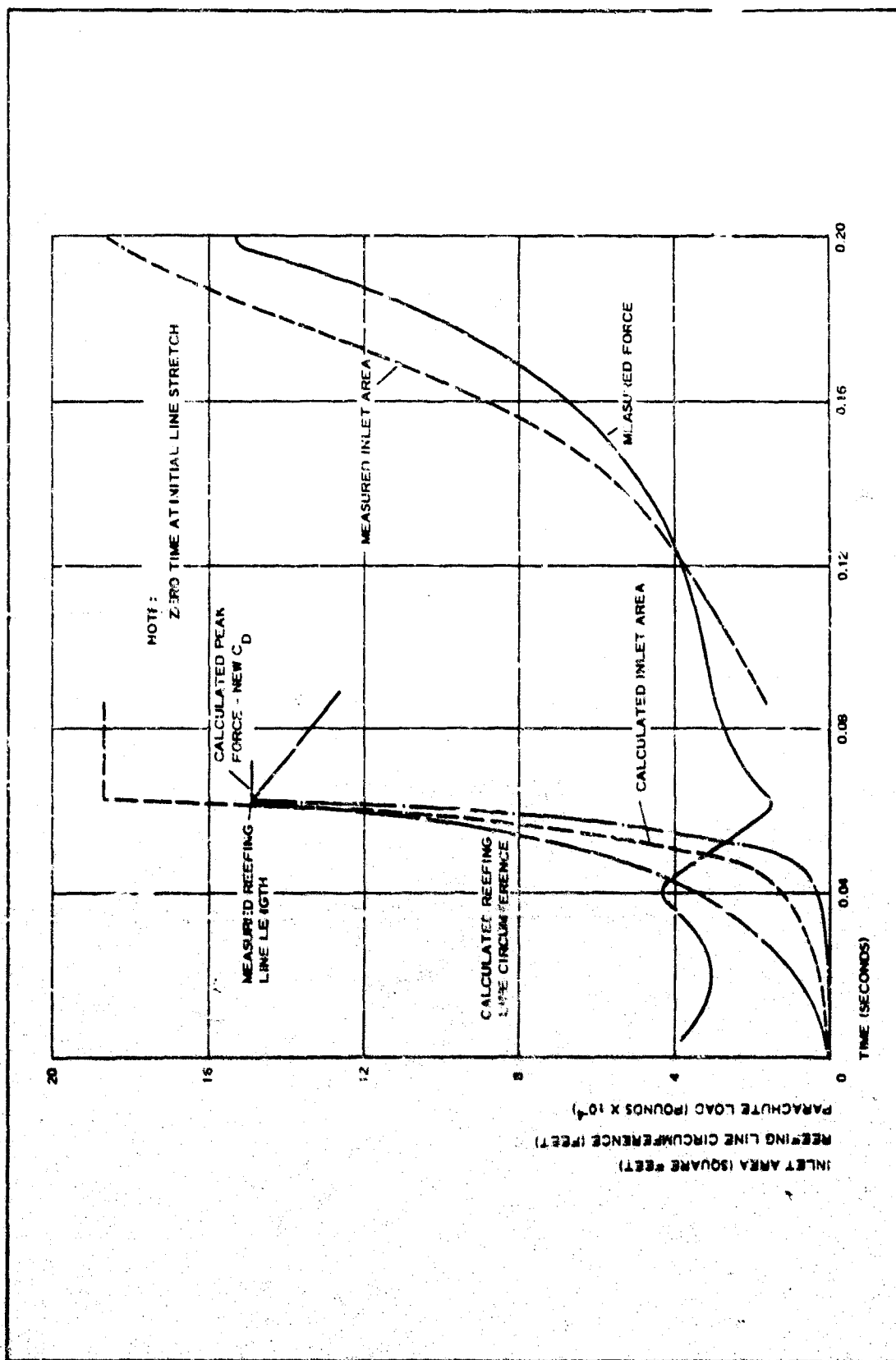


Figure 19 - LP-5 Deployment: Calculated and Measured Force-Time Relationship

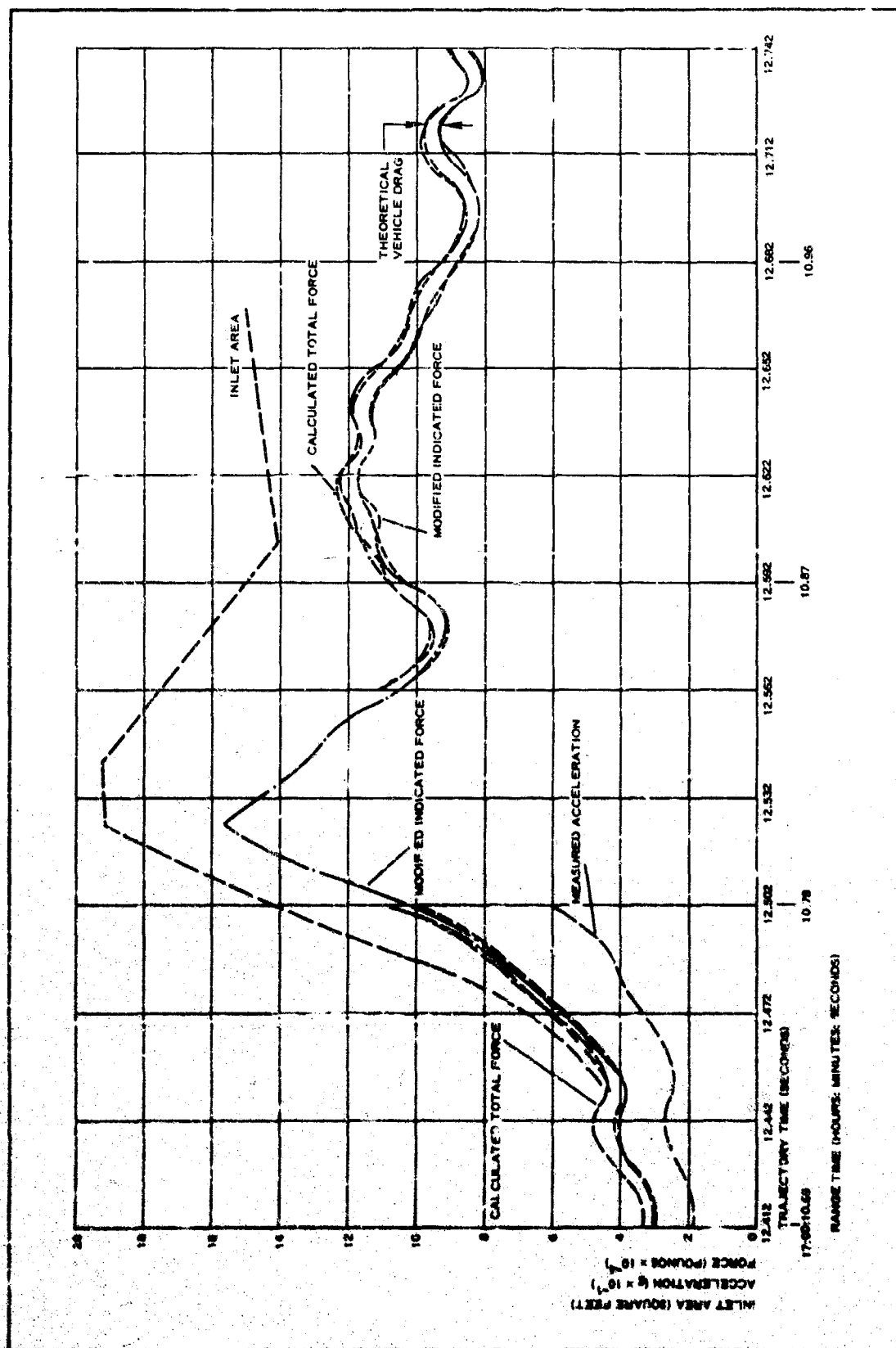


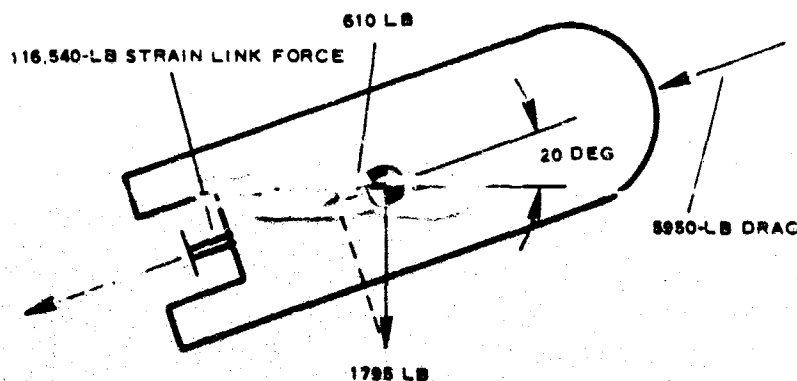
Figure 20 - LP-5: Inlet Area, Acceleration, and Force versus Time

the total longitudinal force acting on the vehicle, based on the accelerometer indication; this line, labeled "calculated total force," is obtained by multiplying the total vehicle weight acting ahead of the strain link by the measured acceleration (expressed in g). The lower force line of Figure 20 shows the average drag link load plus the longitudinal weight component of the 1795-lb weight; this line is labeled "modified indicated force."

Computation of the vehicle weight acting ahead of the strain link follows:

<u>Item</u>	<u>Net weight (lb)</u>
Total vehicle weight with test item	2062 (Reference 1)
Less test-container aft end (60 lb)	2002 (Reference 1)
Less test item (152 lb)	1850 (Reference 1)
Less attachment ring, aft of strain link (55 lb)	1795 (Reference 24)

For the 12.622-sec point, the acceleration is 68.57 g (from Reference 22). The total force from this value is 123,100 lb (1795 lb times 68.57 g). From Reference 22, the average of two drag link readings (116,540 lb) and the trajectory angle (20 deg) can be seen. The forces are summarized in the free-body diagram of the vehicle forward of the strain link, as shown in the following sketch:



The vehicle drag is the difference between the modified indicated force and the total force. An average value for the period from 12.562 to 12.752 sec is 5600 lb. Using this value, 5900 lb becomes 5600 lb, and missile g changes from 68.57 to 68.3, for $t = 12.622$ sec.

Next, that portion of the parachute attachment hardware aft of the strain link is considered. This aft hardware is assumed to be entirely immersed in the vehicle and its wake; thus, it does not experience aerodynamic drag. The parachute suspension line weights are assumed to be distributed one-half to the attachment hardware and one-half to the canopy.

The weight of one-half the parachute suspension lines is:

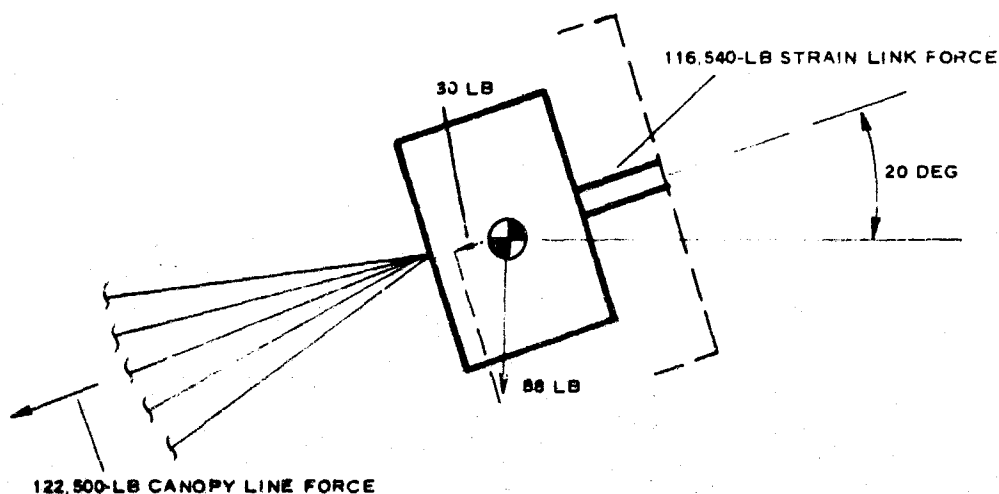
$$(32 \text{ suspension lines}) \frac{2 \text{ webs}}{\text{suspension line}} (15 \text{ ft/web}) \frac{1.65 \text{ oz}}{3 \text{ ft}} \frac{1 \text{ lb}}{16 \text{ oz}} = 33 \text{ lb} \quad (5)$$

Where:

(15 ft/web) is one-half the suspension line length plus an allowance for the loop

1.65 oz is from MIL-W-27657A (USAF) (Reference 25)

The effective weight of the rear attachment hardware, then, is 55 lb (from Reference 24) plus 33 lb of lines, or 88 lb. The free-body diagram of the rear member for the time $t = 12.622$ sec is shown in the following sketch:



The net unbalanced force acting on the 88-lb mass, using 68.3 as the accelerometer reading, is 6010 lb (89 times 68.3 g). The 122,500-lb canopy line force equals strain link force plus the unbalanced force from missile accelerations minus the longitudinal force component due to gravity. The canopy line force in this case consists of canopy drag less the force required to accelerate the canopy mass rearward (absolute values). In the following paragraphs, the canopy acceleration force is determined.

The parachute's total weight is 141 lb. The canopy's portion of the weight is 141 minus 33 or 108 lb. In addition to the canopy material weight, the associated air mass is also accelerated. This mass can be considered as a sphere of air at stagnation pressure.

From Reference 4, the reefing-line circumference is 178 in. The corresponding diameter is 56.6 in. The reefing rings place the skirt approximately 1 in. outside the reefing line. Thus, the skirt diameter is 58.6 in., and the skirt radius is 2.445 ft. The other dimensions are obtained from Reference 24 and are shown earlier in Figure 16.

The geometrical radius, R , was found as follows:

$$\frac{32}{2.445} = \frac{32 + X}{R} \quad (6)$$

$$X = 13.09R - 32 \quad (7)$$

$$Y = 1.572R \quad (8)$$

$$X + Y = 9.3 \quad (9)$$

$$13.09R - 32 + 1.571R = 9.3 \quad (10)$$

$$14.66R = 41.3 \quad (11)$$

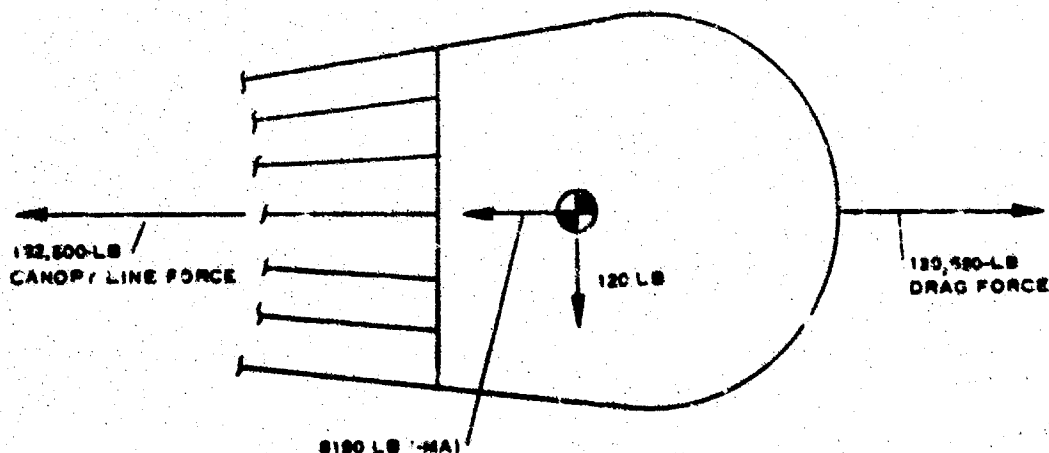
$$R = 2.818 \text{ ft} \quad (12)$$

The corresponding spherical volume is $(4.189)(2.818 \text{ ft})^3 = 93.5 \text{ cu ft}$. The density of the air volume was next established. Reference 22 shows the altitude above mean sea level at the 12.622-sec point to be 10,996 ft. From the Reference 22 air data, the conditions at this altitude were established. (Appendix I shows these calculations.)

The speed of sound is 1070 fps, and the ambient density is $0.001715 \text{ lb sec}^2/\text{ft}^4$. True air speed is 1557 fps, and Mach equals 1.454 (1557 fps divided by 1070 fps). Assuming the air is accelerated in a reversible adiabatic process to the canopy air speed and using values from Reference 26, the ratio of ambient to stagnation air density at Mach 1.454 is 0.4141.

Thus, the stagnation density is $(0.001715 \text{ lb sec}^2/\text{ft}^4)/(0.4141) = 0.004146 \text{ lb sec}^2/\text{ft}^4$. The local acceleration of gravity is 32.11 ft/sec^2 . The resultant specific weight is $(0.004146 \text{ lb sec}^2/\text{ft}^4)(32.11 \text{ ft/sec}^2) = 0.1331 \text{ pcf}$, and the weight of the sphere of air is $(93.5 \text{ cu ft})(0.1331 \text{ pcf}) = 12.45 \text{ lb}$.

The total canopy weight, assuming the virtual air weight is 12.45 lb, becomes 108 lb plus 12.45 lb, or 120 lb. The force on the canopy used to produce the canopy acceleration is $(120 \text{ lb})(68.3) = 8190 \text{ lb}$. The canopy free-body diagram is given in the following sketch:



The canopy drag coefficient, based on the cross-sectional area of the canopy inlet can be calculated as follows. Dynamic pressure was obtained from Reference 22. Inlet cross sectional area is $(2.445 \text{ ft})^2(\pi) = 18.82 \text{ sq ft}$. Based on the inlet area, the drag coefficient becomes:

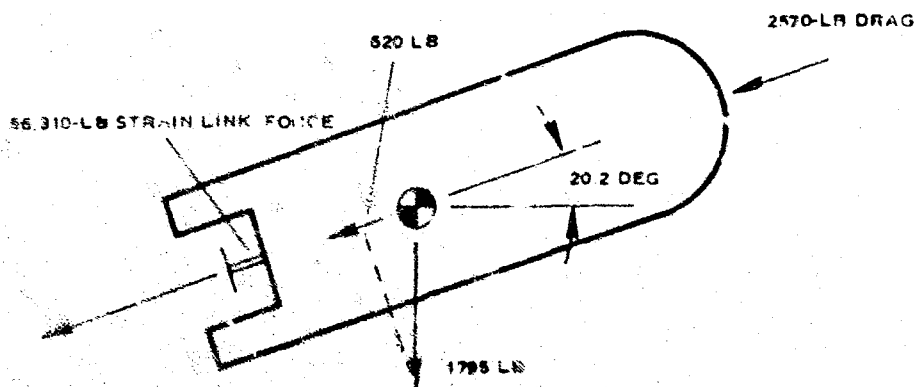
$$\frac{130,690 \text{ lb}}{(2068.6 \text{ psf})(18.82 \text{ sq ft})} = 3.350 \quad (15)$$

This value is higher than any of the canopy-shape drag coefficient values (i.e., 1.35, 2.56, and 2.58) used to calculate the loads in Table XII. Use of this value in the calculations will increase the canopy-shape portion of the drag by $3.35/2.56$ or 1.3.

(3) Canopy Opening Load Determination

An example of how the LP-5 canopy opening forces were determined follows: The opening time increment extends from 12.467 sec to 12.477 sec. This 0.01-sec interval is divided in half by a 12.472-sec point.

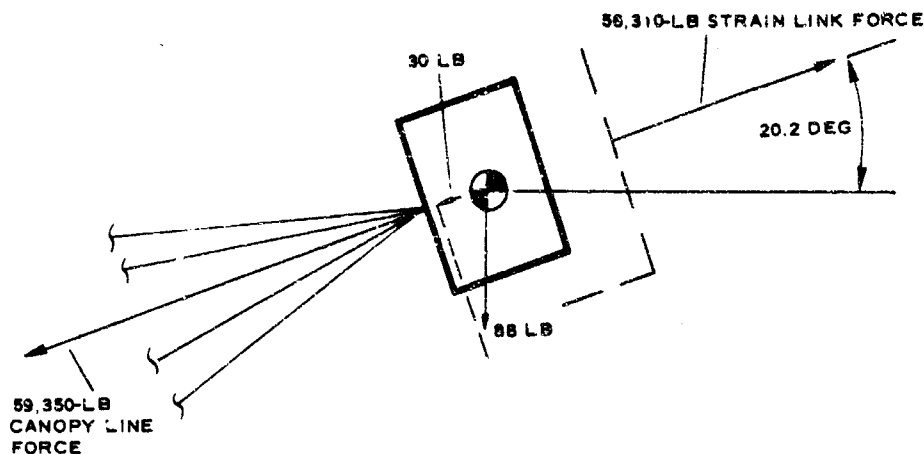
For the 12.472-sec point, the acceleration is 33.20 g (obtained from Reference 22). The total force from this value of that portion of the vehicle ahead of the strain link is $(1795 \text{ lb})(33.20)$ or 59,500 lb. The average of two drag readings (56,310 lb) and the trajectory angle (20.2 deg) can also be obtained. A free-body diagram of the vehicle ahead of the strain link is shown in the following sketch:



The true vehicle drag is considered 5600 lb instead of the apparent 2570 lb, because the vehicle's drag changes a negligible amount between 12.472 sec and the previously considered 12.622 sec. The error is considered due to accelerometer response, since the accelerometer reading is likely to lag the true value, and the drag link value is unlikely to lead its true value when the forces acting on the system are changing rapidly. Thus, the drag value goes from 2570 lb to 5600 lb, and the g value goes from the indicated value of 33.20 to 34.84. Figure 20 presents these values.

That portion of the parachute attachment hardware aft of the strain link is next considered. Repeating the shape-drag approach, it is assumed no drag forces are acting on the attachment hardware. As before, one-half of the parachute suspension line weight is assigned to the attachment

hardware and one-half to the canopy. The total weight of the attachment hardware plus one-half of the suspension lines weight is 88 lb. A free-body diagram of the attachment hardware is shown in the following sketch:



The net unbalanced force acting, based on the revised accelerometer reading, is $(88 \text{ lb})(34.84) = 3067 \text{ lb}$. The 59,350-lb canopy line force equals the strain link force, plus the 3067-lb unbalanced force, less the 30-lb longitudinal component of the gravity force.

The canopy line force consists of the canopy-shape drag force, added to the canopy mass acquisition force, less the force required to accelerate the canopy itself. Because the canopy force increases rapidly with time, the canopy moves rearward relative to the vehicle. This rearward velocity, which affects the canopy drag, opening force, and inertia force, is calculated in the following manner.

Because the velocity depends on force change, the force level is required at different times. Following the above procedure, the canopy forces at the 12.462- and 12.482-sec points are established to be 48,950 and 72,100 lb, respectively. Thus, the force change in the 0.02-sec interval centered on the 12.472-sec point is 23,150 lb. This load is distributed over 32 suspension lines of 2 webs per line. Hence, the load change per web is $23,150 \text{ lb}/64 = 362 \text{ lb}$. Reference 1 shows that the effective web length subjected to this load is 29 ft. Figure 21 shows the load-strain relationship of this webbing. The total load at the 12.472-sec point was previously determined as 59,350 lb. The corresponding load per web is $59,350 \text{ lb}/64 = 926 \text{ lb}$. Examination of the Figure 21 curve shows that the stress-strain relationship is linear up to the 1000-lb load point. At the 1000-lb load point, the strain is 0.051 ft/ft. From the foregoing, the differential displacement can be calculated as $(0.051 \text{ ft/ft})(362 \text{ lb}/1000 \text{ lb})(29 \text{ ft}) = 0.535 \text{ ft}$. The resultant rearward velocity of the canopy relative to the vehicle is $0.535 \text{ ft}/0.02 \text{ sec} = 26.8 \text{ fps}$.

From Reference 22, the vehicle air speed at the 12.472-sec point is 1727 fps. The corresponding canopy air speed is $1727 - 27 \text{ fps} = 1700 \text{ fps}$. From Reference 22, the vehicle dynamic pressure at the 12.472-sec point

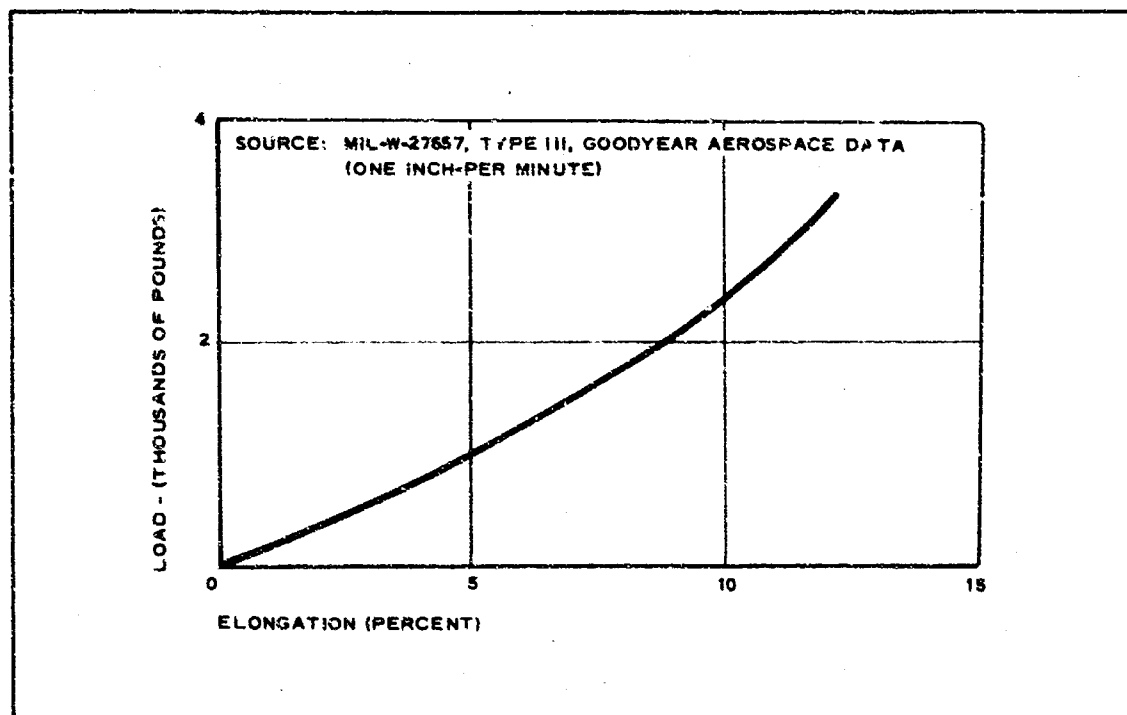


Figure 21 - Stress-Strain Relationships of Suspension Line Webbing (6000-Lb Rating)

is 2550 psf. The corresponding canopy dynamic pressure is:

$$\frac{(2550 \text{ psf})(1700 \text{ fps})^2}{(1727 \text{ fps})^2} = 2474 \text{ psf} \quad (14)$$

To calculate the canopy shape-drag, the inlet area of the canopy must be known, since the canopy shape-drag coefficient is based on this area. The canopy inlet area at the 12.472-sec instant was considered 6.75 sq ft based on the LP-5 onboard camera films. Thus, drag = $qC_D A = (2.474 \text{ psf})(3.350)(6.75 \text{ sq ft}) = 56,000 \text{ lb}$.

The shape-drag coefficient (3.350) is based on the value at 12.622 sec calculated earlier. The drag coefficient change between conditions at 12.472 sec and 12.622 sec is assumed to be small.

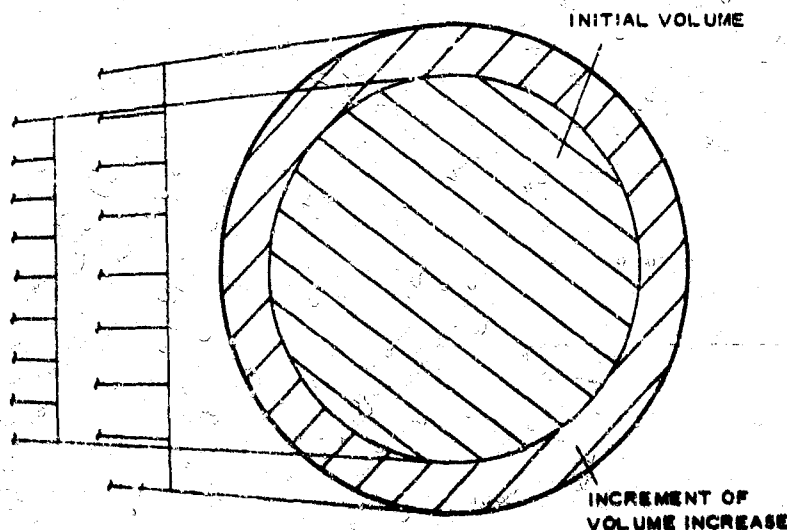
Next, the canopy inertia effect is calculated. The first portion of this calculation parallels the corresponding steady-state calculations. The spherical volume corresponding to the 1.769-ft R is 23.11 cu ft. The density of this gas volume is based on Reference 22 data. The altitude at the 12.472-sec point is 10,090 ft.

From Appendix II of this report, the speed of sound is 1070 fps. The true airspeed was previously calculated to be 1700 fps. The Mach number is $(1700 \text{ fps})/(1070 \text{ fps}) = 1.589$. Assuming the air is accelerated in a reversible adiabatic process to the canopy airspeed, then from Reference 26

the ratio of ambient to stagnation air density at Mach 1.589 is 0.3599. From Appendix II, the ambient density is $0.001719 \text{ lb sec}^2/\text{ft}^4$. Thus, the stagnation density is $(0.001719 - 0.3599 \text{ lb sec}^2/\text{ft}^4) = 0.00477 \text{ lb sec}^2/\text{ft}^4$. Appendix II shows the local acceleration of gravity to be 32.11 ft/sec^2 . The resultant specific weight is $(0.00477 \text{ lb sec}^2/\text{ft}^4) \text{ times } (32.11 \text{ ft/sec}^2) = 0.1532 \text{ pcf}$, and the weight of the sphere of air is $(23.11 \text{ cu ft})(0.1532 \text{ pcf}) = 3.54 \text{ lb}$. The total canopy weight, with the virtual air weight included, becomes $(108 + 4) \text{ lb} = 112 \text{ lb}$.

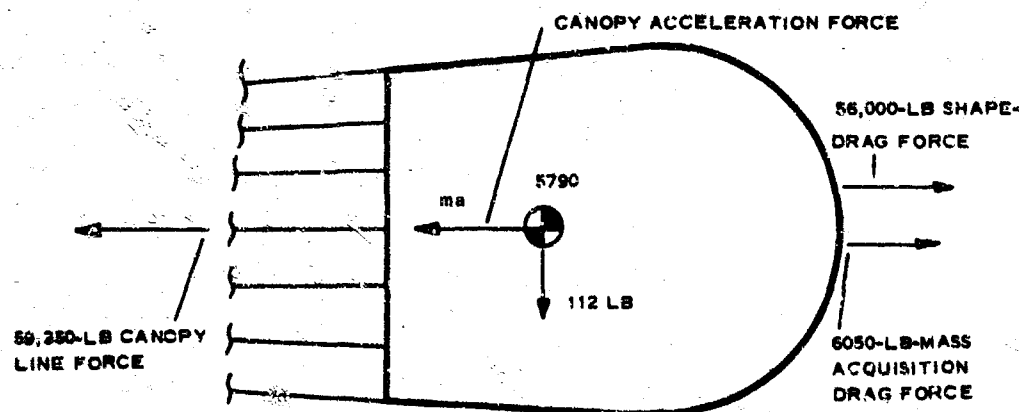
The canopy acceleration is different somewhat from the vehicle acceleration because of suspension-line elasticity. The acceleration of the canopy relative to the vehicle is calculated as follows: The calculated canopy loads at the 12.461-, 12.471-, and 12.482-sec points of Figure 20 are 48,950, 59,350, and 71,100 lb, respectively. Thus, the force changes in the two 0.01-sec intervals represented are 10,400 and 12,750 lb. As in previous practice, the corresponding load changes per web are $10,400 \text{ lb}/64 = 162.6 \text{ lb}$ and $12,750 \text{ lb}/64 = 199 \text{ lb}$. The corresponding displacements are $(0.051 \text{ ft/ft})(162.6 \text{ lb}/1000 \text{ lb})(29 \text{ ft}) = 0.2403 \text{ ft}$ and $(0.051 \text{ ft/ft})(199.0 \text{ lb}/1000 \text{ lb})(29 \text{ ft}) = 0.2940 \text{ ft}$. The resultant rearward velocities are $0.2403 \text{ ft}/0.01 \text{ sec} = 24.03 \text{ fps}$ and $0.2940 \text{ ft}/0.01 \text{ sec} = 29.40 \text{ fps}$. The velocity rate of change is $(5.37 \text{ fps})/(0.01 \text{ sec}) = 537 \text{ ft/sec}^2$. With the local acceleration of gravity 32.11 ft/sec^2 , the velocity rate of change is 16.75 g . The total canopy acceleration is the vehicle acceleration plus the canopy acceleration relative to the vehicle; or $(34.84 + 16.75) \text{ g} = 51.59 \text{ g}$. The force on the canopy required to produce this acceleration is $(112 \text{ lb})(51.59) = 5790 \text{ lb}$.

The canopy mass acquisition force is the remaining factor to be calculated that contributes to the suspension line force. This mass acquisition force results from acquiring air mass as the canopy opens. To avoid considering various airspeeds in the calculations, all the virtual mass air is treated as stagnant. The stagnant air volume is increased to the spherical shape to allow for the slow-moving air. An incremental volume change is shown in the following sketch:



As previously mentioned, the increment being used extends from 12.467 to 12.477 sec. The canopy inlet areas from Reference 6 are plotted in Figure 20. From the curves of Figure 20, the inlet areas for the increment end points are 6.04 and 7.60 sq ft. The corresponding radii are 1.388 and 1.588 ft. As in the previous procedure, the R dimensions are 1.678 and 1.867 ft, respectively. The corresponding spherical volumes are 19.75 and 27.22 cu ft. Thus, the volume of air accumulated in the increment is $27.22 - 19.75$ cu ft = 7.47 cu ft. In determining the density of this air mass, it is assumed that the air is brought to the canopy velocity in a reversible adiabatic process. The air has the same density that was calculated for the entire sphere: 0.00477 lb sec²/ft⁴. From the foregoing information, mass accumulation is calculated to be $(7.47 \text{ cu ft})(0.00477 \text{ lb sec}^2/\text{ft}^4) = 0.03565 \text{ lb sec}^2/\text{ft}$.

The force required to accelerate this mass to the canopy speed is $(dv)(M)/(dt)$. The velocity change (dv) is the canopy speed at 12.472 sec, which has previously been determined to be 1700 fps. The mass acquisition force, then, is $(1700 \text{ fps})(0.0356 \text{ lb sec}^2/\text{ft})/(0.01 \text{ sec}) = 6050 \text{ lb}$, acting to accelerate the canopy rearward. The canopy forces calculated in the preceding paragraphs are shown in the following free-body sketch:



By equating these forces, then $59,350 + 5790 - 56,000 - 6050$ should equal zero. However, a difference of 3090 lb occurs when either of the drag terms is low or either of the force terms is high.

An evaluation can be made of the methods used in Tables XI and XII for calculating inlet and exit flow rates. The mass-accumulated was calculated from flight conditions to be $0.0356 \text{ lb sec}^2/\text{ft}$. The mass-entering can be calculated from the mass-accumulated plus the mass-exiting. The mass-exiting can be calculated from the geometry and the environmental conditions.

The nominal geometric porosity is 14 percent. The porosity of the ribbons and webs is assumed to raise the total effective porosity to 15 percent. The gross leakage area is considered the surface area of the hemisphere at 12.472 sec. The leakage flow is considered isentropic and critical. The R dimension at the 12.472-sec point is 1.769 ft. The corresponding hemispherical area is $2\pi(1.769 \text{ ft})^2 = 19.65 \text{ sq ft}$. The leakage

area is $(19.65 \text{ sq ft})(0.15) = 2.946 \text{ sq ft}$. From Reference 26, the ratio of ambient to stagnation pressure at the previously determined canopy Mach number of 1.589 is 0.2391 for an isentropic compression. From Appendix II, the ambient pressure is 1412 psf. Thus, the stagnation pressure (P_s) is $(1412 \text{ psf})/(0.2391) = 5900 \text{ psf}$. From Reference 27, the critical pressure (P_c) is $(0.53)(5900 \text{ psf}) = 3132 \text{ psf}$. Also from Reference 27, the critical specific volume (v_c) may be found from the following relationship for isentropic flow: $(v_c)^{1.4} = (P_s/P_c)(v_s)^{1.4}$. From the previously determined w_s of 0.1532 pcf, v_s is determined. The v_c value is calculated to be 10.35 cu ft/lb.

The resultant air density is $(1)/(10.35 \text{ cu ft/lb})(32.11 \text{ ft/sec}^2) = 0.003014 \text{ lb sec}^2/\text{ft}^4$. From Reference 27, the speed of sound (c) is $(kP_c/c)^{1/2}$. Thus, the speed of sound at the orifices is:

$$\left[\frac{(1.4)(3132 \text{ psf})}{(0.003014 \text{ lb sec}^2/\text{ft}^4)} \right]^{1/2} = 1208 \text{ fps} \quad (15)$$

The mass flow rate out can now be calculated: $(1208 \text{ fps})(2.946 \text{ sq ft})/(0.003014 \text{ lb sec}^2/\text{ft}^4) = 10.71 \text{ lb sec}^2/\text{ft sec}$. In the 0.01-sec increment, 0.1071 lb sec²/ft will exit. Since mass-in equals mass-accumulated plus mass-exiting, the mass-in is $0.0356 + 0.1071 = 0.1427 \text{ lb sec}^2/\text{ft}$ in 0.01 sec or $14.27 \text{ lb sec}^2/\text{ft sec}$.

Another approach for calculating mass-in is to use free stream conditions and the inlet area. This was done in the calculations shown in Tables XI and XII. By using this approach, the inlet flow rate is $19.71 \text{ lb sec}^2/\text{ft sec}$, as compared with $14.27 \text{ lb sec}^2/\text{ft sec}$. It is apparent either that the calculated exit rate values used to calculate the $14.27 \text{ lb sec}^2/\text{ft sec}$ rate-in are low; or that the inlet flow rate values using free stream conditions are too high. The latter seems to be the more obvious, since wake and suspension line effects are not considered using free-stream conditions. Future efforts should consider these factors.

4. LARGE PARACHUTE GEOMETRY

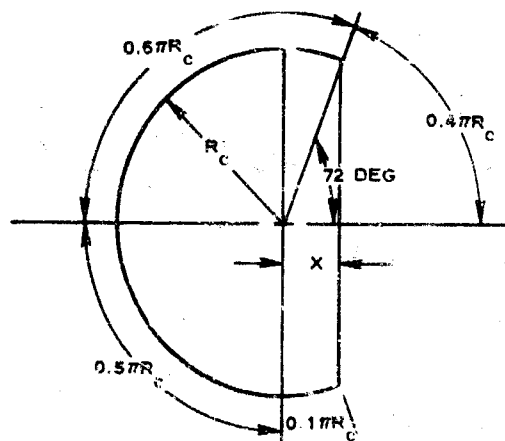
a. Parachute Dimensions

The basic configuration selected for Large Parachutes LP-3, LP-4, and LP-5 was a 16 foot D_0 hemisflo ribbon type with 10-percent extended skirt and a 14-percent porosity. The parachute detailed profile dimensions were derived by geometric computation:

$$\begin{aligned} D_0 &= 16 \text{ ft} \\ &= 192 \text{ in.} \end{aligned} \quad (16)$$

$$\begin{aligned} S_0 &= \frac{\pi(192)^2}{4} \\ &= 28,953 \text{ sq in.} \end{aligned} \quad (17)$$

With a spherical 10-percent skirt extension, the geometry is shown in the following sketch:



$$D_c = 2R_c$$

The canopy surface area (S_o) is equal to the total spherical area minus the open spherical area:

$$\begin{aligned} S_o &= \pi D_c^2 - 2\pi R_c(R_c - x) \\ &= \pi D_c^2 - 2\pi R_c(R_c - R_c \cos 72 \text{ deg}) \\ &= \pi D_c^2 - 2\pi R_c^2(1 - \cos 72 \text{ deg}) \\ &= \pi D_c^2 - \frac{\pi D_c^2}{2}(1 - \cos 72 \text{ deg}) \\ &= 2.057 D_c^2 \end{aligned} \quad (18)$$

$$\begin{aligned} D_c &= \sqrt{0.487 S_o} \\ &= \sqrt{0.487 \times 28,953} \\ &= 118.5 \text{ in.} \end{aligned} \quad (19)$$

$$R_c = 50.25 \text{ in.} \quad (20)$$

Then:

Equator-to-equator perimeter = $\pi R_c = 186.4$ in. (21)

$$\text{Skirt height} = 0.10R_c = 0.10 \times 186.4 = 18.64 \text{ in.} \quad (22)$$

Circumference at maximum diameter = $118.5\pi = 372$ in. (22)

$$\text{Circumference at inlet} = \frac{118.5}{2} \cos 18 \text{ deg} \times 2\pi = 355 \text{ in.} \quad (24)$$

$$\text{Inlet diameter} = \frac{355}{\pi} = 113 \text{ in.} \quad (25)$$

$$\text{Suspension line length} = 2D_o = 2 \times 16 = 32 \text{ ft.} \quad (26)$$

The parachute dimensions are shown in Figure 22.

b. Ribbon Arrangement for Desired Porosity

Layouts and calculations determined the ribbon arrangement and provided the desired 14-percent porosity. The ribbon arrangement is shown in Figure 23, and the ribbon dimensions and locations for a typical gore are presented in Table XIII. The space-area total between the ribbons, including the area blocked by the verticals and radials, is obtained by summing up the ribbon length and multiplying it by the gap. The length of Spaces 1 through 20 equals the sum of Ribbon Lengths 1 through 20; that is, the sum of lengths 73.87 through 310.07 = 4035.15-in. length. The area of space = length \times gap = 4035.15(0.465) = 1876.35 sq in.

The length of Spaces 21 through 41 equals the sum of Ribbon Lengths 21 through 41; that is, the sum of lengths 319.34 through 358.68 = 7521.79-in. length. The area of space = length \times gap = 7521.79(0.430) = 3234.37 sq in.

The total space areas, including the blocked area, are 1876.35 + 3234.37 = 5110.72 sq in.

The area blocked by the verticals is the number of spaces times the tape width times the gap length times the number of tapes:

$$13 \text{ spaces} \times 0.56 \times 0.465 \times 64 = 216.5 \quad (27)$$

$$21 \text{ spaces} \times 0.56 \times 0.430 \times 64 = 323.0 \quad (28)$$

$$\text{Total} = 539.5 \text{ sq in.} \quad (29)$$

The area blocked by the radials is the number of spaces times the radial width times the gap length times the number of radials:

$$20 \text{ spaces} \times 1.00 \times 0.465 \times 32 = 298.00 \quad (30)$$

$$21 \text{ spaces} \times 1.00 \times 0.430 \times 32 = 289.00 \quad (31)$$

$$\text{Total} = 587.00 \text{ sq in.} \quad (32)$$

The vent's open area is the total area of the triangles between the radials:

$$\frac{0.96(4.75)32}{2} = 73.00 \text{ sq in.} \quad (33)$$

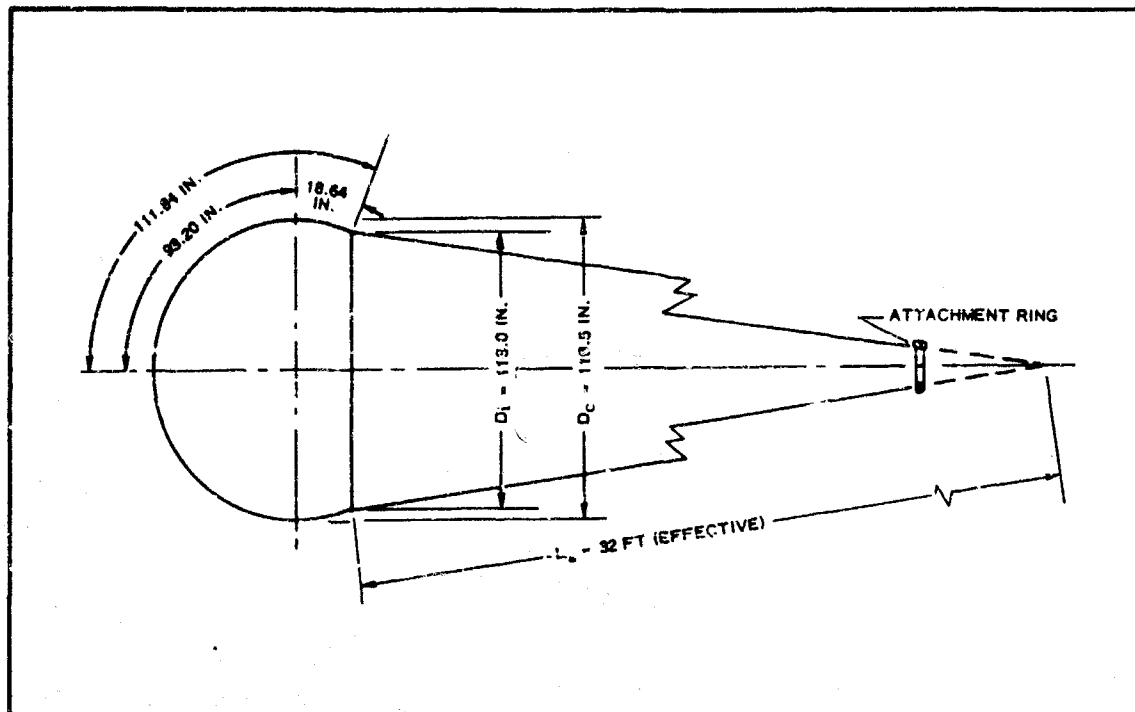
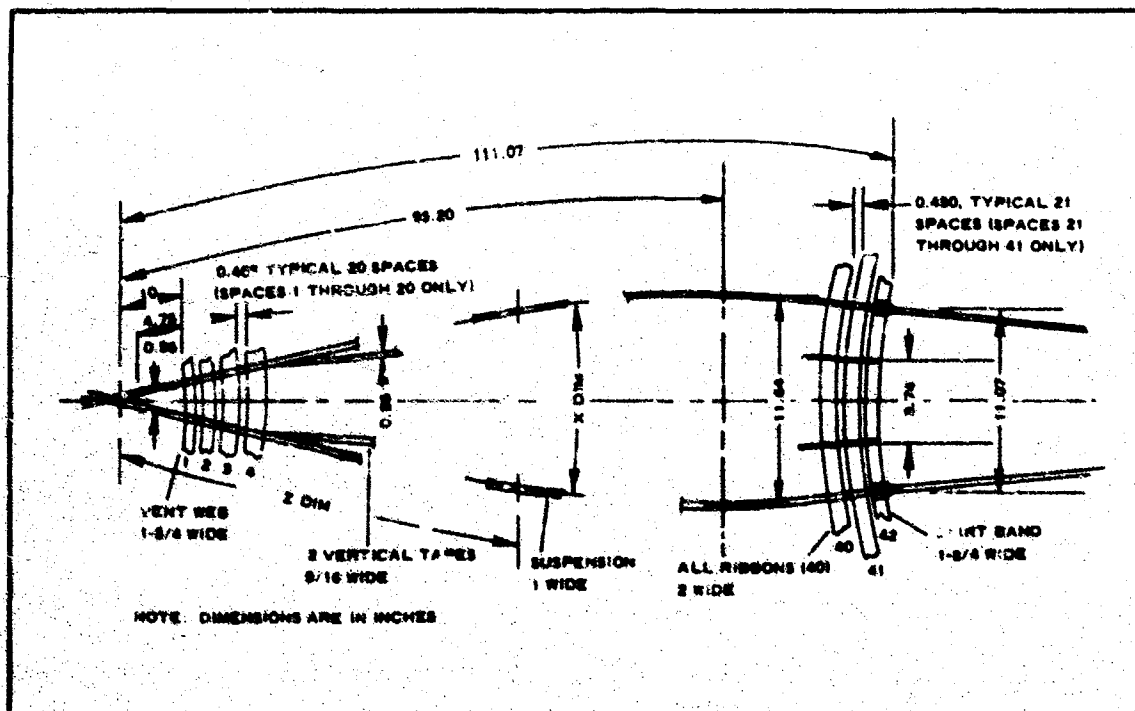
Figure 22 - Sixteen-Foot D_0 Hemisflo Profile Dimensions

Figure 23 - Ribbon Arrangement for Typical Core

TABLE XIII - RIBBON AND WEB DIMENSIONS FOR TYPICAL GORE

Ribbon	Z *	Circum- ference (32 x)	X *	Ribbon	Z *	Circum- ference (32 x)	X *
1	10.95	73.87	2.31	22	62.65	325.70	10.21
2	13.42	88.00	2.75	23	65.08	333.68	10.43
3	15.88	103.00	3.22	24	67.51	340.30	10.63
4	18.34	117.77	3.68	25	69.94	346.42	10.83
5	20.81	132.32	4.14	26	72.37	351.65	10.99
6	23.28	146.50	4.58	27	74.80	356.40	11.14
7	25.74	160.47	5.01	28	77.23	360.65	11.27
8	28.20	174.45	5.45	29	79.66	364.00	11.38
9	30.67	187.50	5.86	30	82.09	366.90	11.47
10	33.14	200.92	6.28	31	84.52	369.38	11.54
11	35.60	213.62	6.68	32	86.95	371.13	11.60
12	38.07	226.34	7.07	33	89.38	372.25	11.63
13	40.53	238.78	7.46	34	91.81	372.73	11.65
14	43.00	250.78	7.84	35	94.24	372.62	11.64
15	45.46	261.00	8.16	36	96.67	371.84	11.62
16	47.93	271.80	8.49	37	99.10	370.46	11.58
17	50.39	282.41	8.83	38	101.54	368.41	11.51
18	52.86	292.95	9.15	39	103.98	365.80	11.43
19	55.32	302.00	9.44	40	106.43	362.48	11.33
20	57.79	310.67	9.71	41	108.87	358.68	11.21
21	60.22	319.34	9.98	42 inner	111.07	354.45	11.08
				42 outer	111.07	338.45	...

* Canopy gore-shaping coordinates.

Thus:

$$\text{Total open area} = 5110.72 - 539.50 - 587.00 + 73.00 = 4057.22 \text{ sq in.} \quad (34)$$

The porosity = $(4057.22)/(28,953) = 14.0$ percent.

The following spot checks were made to determine local porosity (open space/total area):

For Space 6:

$$\frac{(146.50 - 32)0.465}{(146.50)2.465} = \frac{114.50(0.465)}{361.5} = 14.7 \text{ percent} \quad (35)$$

For Space 12:

$$\frac{[226.34 - (32 \times 2.12)]0.465}{(226.34)2.465} = \frac{(158.54)0.465}{557.5} = 13.2 \text{ percent} \quad (36)$$

For Space 16:

$$\frac{[271.80 - (32 \times 2.12)]0.465}{(271.80)2.465} = \frac{(204.00)0.465}{670.00} = 14.15 \text{ percent} \quad (37)$$

For Space 20:

$$\frac{[310.67 - (32 \times 2.12)]0.465}{(310.67)2.465} = \frac{(242.87)0.465}{767} = 14.72 \text{ percent} \quad (38)$$

For Space 24:

$$\frac{[340.30 - (32 \times 2.12)]0.430}{(340.30)2.43} = \frac{(272.5)0.43}{826.5} = 14.2 \text{ percent} \quad (39)$$

For Space 28:

$$\frac{[360.65 - (32 \times 2.12)]0.430}{(360.65)2.43} = \frac{(292.85)0.43}{876} = 14.35 \text{ percent} \quad (40)$$

For Space 34:

$$\frac{[372.73 - (32 \times 2.12)]0.430}{(372.73)2.43} = \frac{(304.93)0.43}{905.7} = 14.50 \text{ percent} \quad (41)$$

The porosities derived in the above calculations, from center line of ribbon to center line of ribbon, show an increase in porosity from Space 12 (near the top of the verticals) going forward to Space 20. At this point, the spacing dimension is changed from 0.465 to 0.430, resulting in a step to lower porosity, from which point it again increases toward the skirt.

5. STRUCTURAL LOADS AND MATERIAL SELECTIONS

a. General

Parachute structural elements, such as suspension lines, skirt band, ribbons, and reefing lines, were analyzed to determine the loads and select the materials.

b. Suspension Line

The parachute is reefed to limit the opening shock force or peak load (F_o) to a maximum of 200,000 lb. Then, assuming all lines are equally loaded:

$$F_{sl} = \frac{F_o j}{ZUC} \quad (42)$$

Where:

F_{sl} = suspension-line strength

F_o = 200,000 lb

j = safety factor = 1.5

C = confluence factor = $\cos Y_c = 0.98$

Y_c = confluence half angle

U = seam efficiency factor = 0.80

Z = number of gores = 32

Thus:

$$F_{sl} = \frac{200,000(1.5)}{32(0.80)(0.98)} \quad (43)$$

= 12,000 lb per line

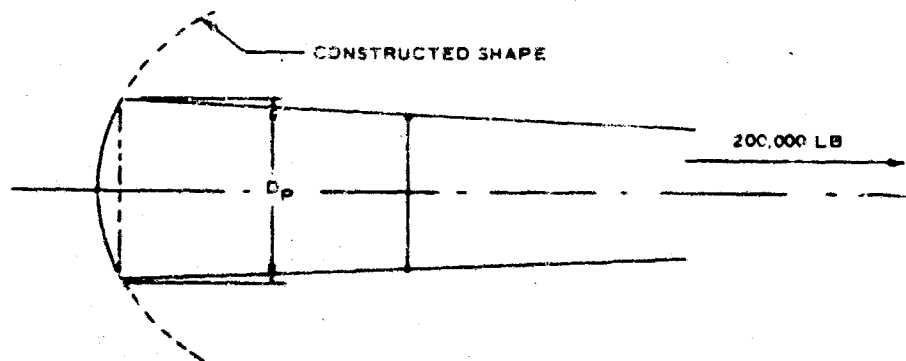
Considering the size of these lines and the rapid decay of vehicle velocity, heating effects will occur after the initial critical loadings (see Item 6 of this section). Thus, 12,000-lb suspension lines are required.

c. Ribbon Strength

No ribbon strength data were available for the Mach 3 and 10,000-psf dynamic pressure conditions. However, relationships between ribbons and lines are presented in Table 7-5 of Reference 23 (ASD-TR-61-579). In this table, 30f J-lb strength ribbon material is recommended for use with 12,000-lb suspension lines. Twice this ribbon strength was chosen to avoid ribbon breakage. The ribbon strength was reduced from apex

to skirt locations, as described in Reference 28. The strengths were reduced successively from 6000, to 4000, to 3000, and to 2000 lb. The location of the rear-most graduated step in strength, from 6000 lb to 4000 lb, is based on the canopy's inflated size at Mach 3. Similarly, the second step, from 4000 lb to 3000 lb, is based on the canopy's inflated size at Mach 2.2.

The canopy size at opening shock is based on that portion of the canopy inflated to the constructed contour. The contour matches the design opening shock force (F_o) of 200,000 lb. From the circumference of the bubble thus determined, the ribbon location is selected by using Table XIII (shown in Item 4, b of this section). To establish the constructed contour limits, note the following sketch:



From this sketch:

$$F_o = X C_{D_p} S_p q \quad (44)$$

Where:

$$X = \text{opening shock factor} \\ = 1.5$$

$$C_{D_p} = 1 \text{ (assumed value for design)}$$

$$S_p = \frac{\pi D_p^2}{4}$$

Then:

$$S_p = \frac{F_o}{X C_{D_p} q} \quad (45)$$

At Mach 3:

$$S_p = \frac{200,000}{1.5(1)9180} = 14.5 \text{ sq ft} \quad (46)$$

$$D_p = \sqrt{\frac{4S_p}{\pi}} = 4.3 \text{ ft.} \quad (47)$$

$$\text{Circumference} = 4.3(12)\pi = 162 \text{ in.} \quad (48)$$

$$\text{Last 6000-lb ribbon (Table XIII) = Ribbon 8} \quad (49)$$

At Mach 2.2:

$$S_p = \frac{200,000}{1.5(1)4940} = 27 \text{ sq ft} \quad (50)$$

$$D_p = \sqrt{\frac{4S_p}{\pi}} = 5.87 \text{ ft} \quad (51)$$

$$\text{Circumference} = 5.87(12)\pi = 222 \text{ in.} \quad (52)$$

$$\text{Last 4000-lb ribbon = Ribbon 14.} \quad (53)$$

Ribbon 28 is the last 3000-lb ribbon.

d. Reefing System: Static Loads

Based on geometry, the reefing line and the reefing ring static loads can be calculated for a 200,000-lb peak parachute drag load.

For the maximum reefing diameter, the static load solution is identical to the skirt-band strength. The calculation follows the method of the example for the minimum reefing diameter below. The angles based on constructed geometry are 18 deg for the skirt and 8.45 deg for the lines. The tension value calculated is $F_{RL} = 5580 \text{ lb}$.

For the smallest reefing diameter (Mach 3 and the highest condition), the suspension-line angle at the skirt is assumed to be 10 deg (note the sketch at the top of the next page).

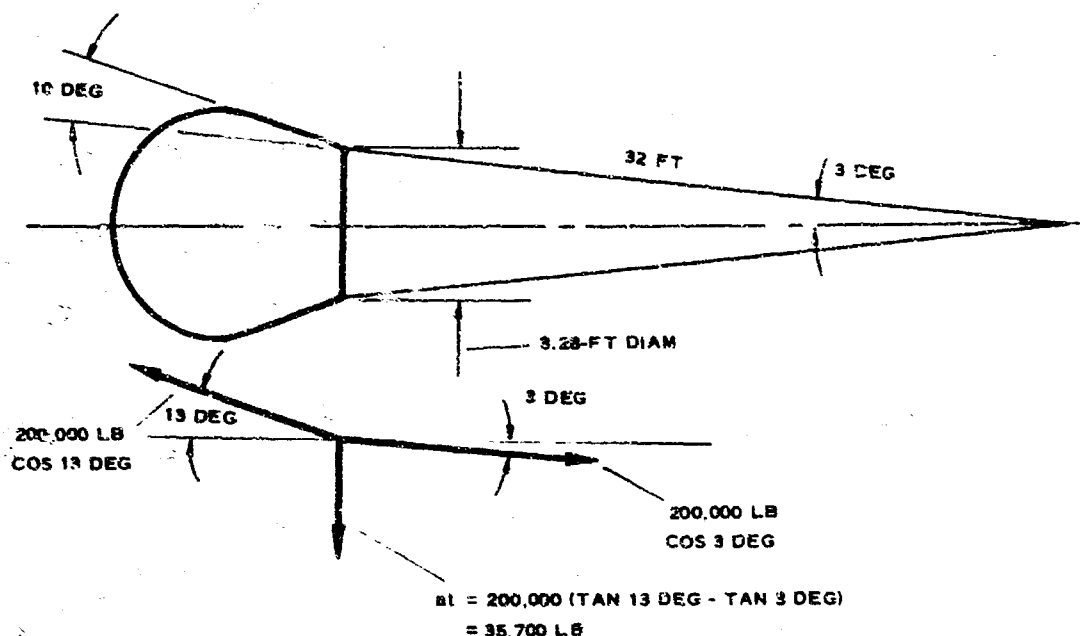
From this sketch:

$$T = \text{static hoop tension} = \frac{nt}{2\pi} = \frac{35,700}{2\pi} = 5700 \text{ lb} \quad (54)$$

Where:

n = number of line

t = radial force/line



Considering the dynamic loads as being several times more severe than the static loads, greater reefing line strength was chosen.

A 12,000-lb and a 6000-lb webbing were used together for LP-4 and LP-5 reefing lines. The reefing-line layout and construction are shown in Figure 24. The 6000-lb Type 4088 web was stitched to the larger web's inner surface and serves as a buffer by bearing against the reefing rings. The web's overall contribution to the reefing line's tensile strength was less than 100 percent because of the different elongations of the two webs.

The ultimate reefing ring load, based on an 18,000-lb reefing line, is calculated as follows:

$$T = \frac{nt}{2\pi} \quad (55)$$

$$t = \frac{2\pi T}{n} = \frac{2\pi 18,000}{32} = 3540 \text{ lb (ultimate)} \quad (56)$$

6. THERMODYNAMIC ANALYSIS

A thermal analysis was made for the conditions following parachute deployment at Mach 3 and 10,000 ft. Calculated trajectory results indicated that a large velocity decay occurs. Thermal analysis results indicate that, during the first 0.2 of a second, the edges of ribbons and the skirt band experience a temperature rise to about 500 F. The greater portion of a typical ribbon's mass is relatively unaffected during this 0.2 of a second. After this period of time, the adiabatic wall temperature falls to below 500 F.

A calculated trajectory for deploying this parachute is shown in Figure 25.

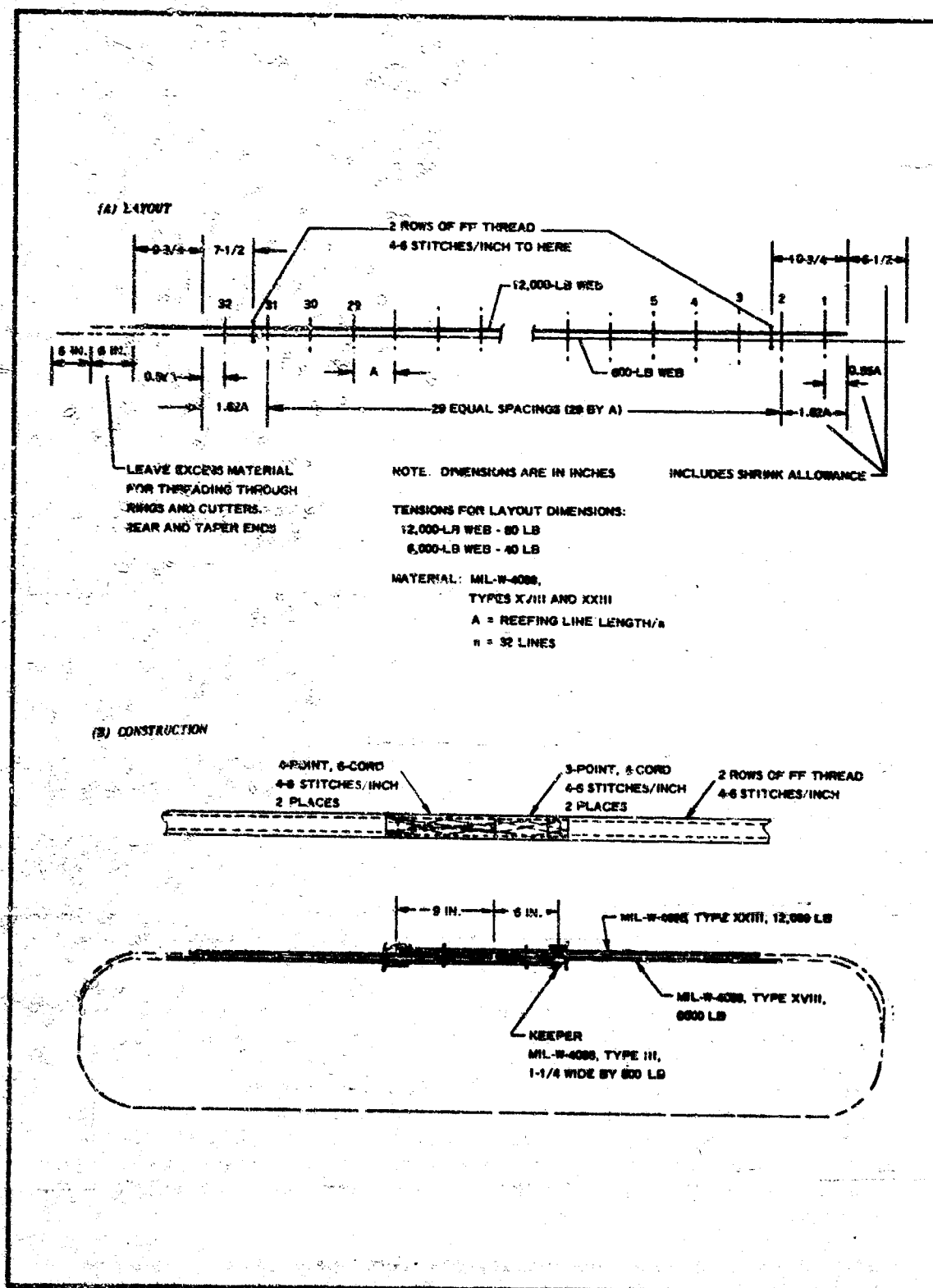


Figure 24 - Reefing Line Layout and Construction for LP-4 and Subsequent LP-5

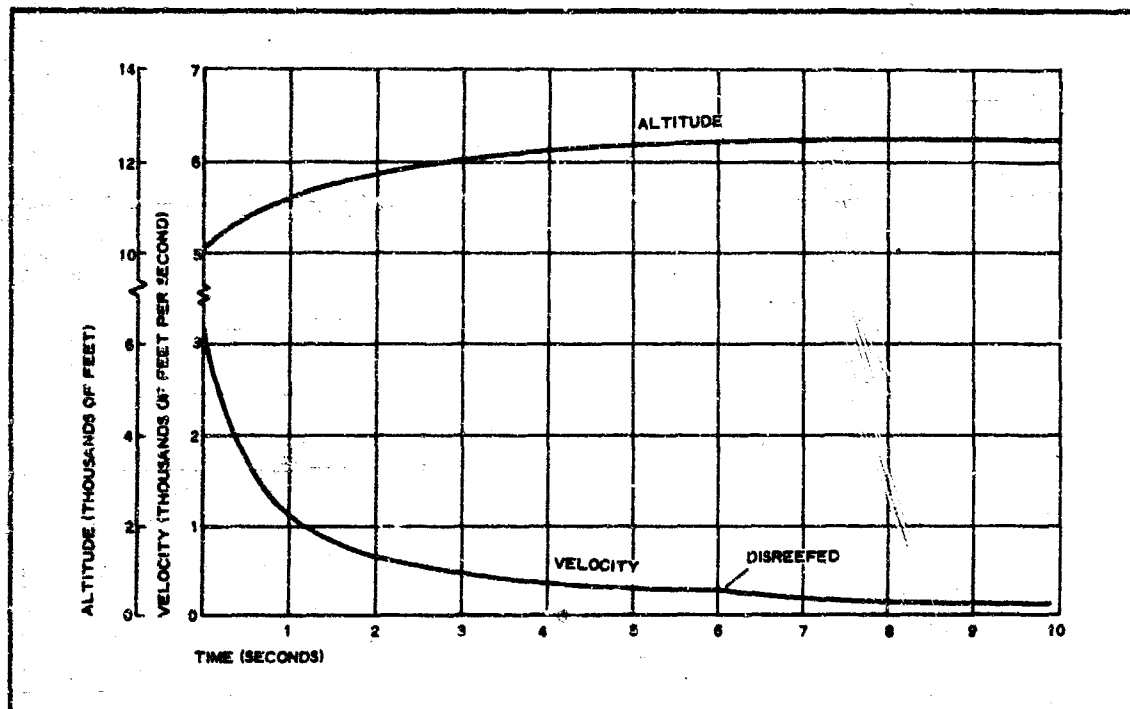
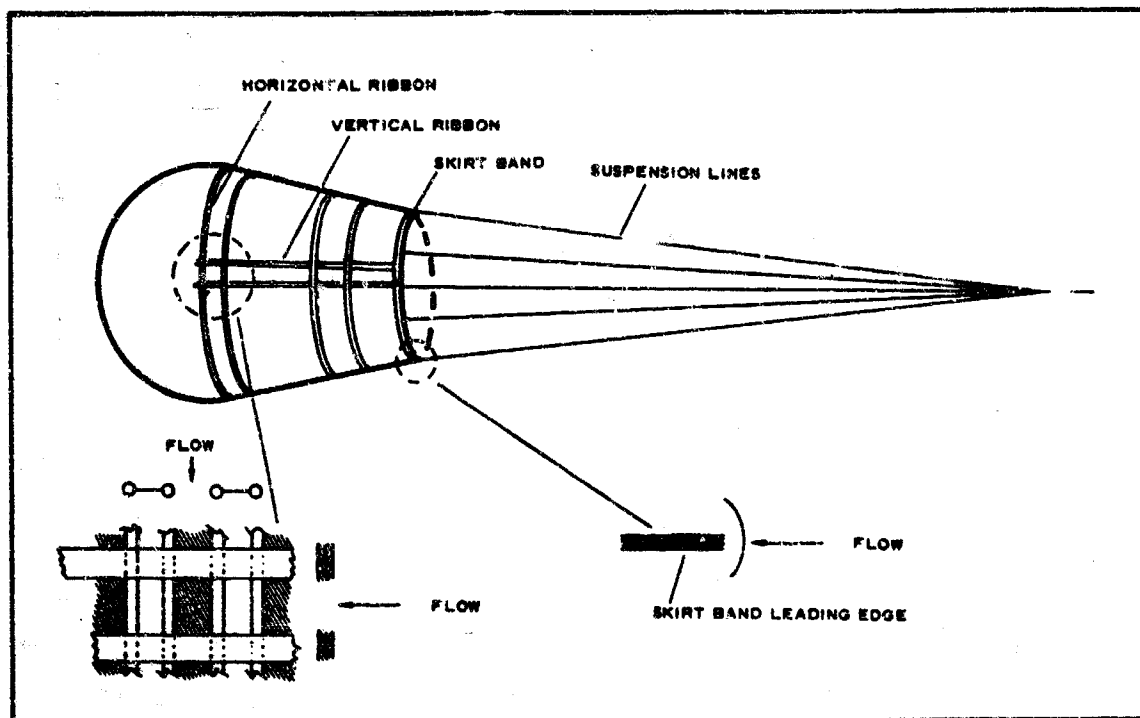


Figure 25 - Calculated LP-9 Trajectory from Deployment

Deployment conditions at time zero are (1) velocity = 3230 fps and (2) altitude = 10,000 ft. In one second, the velocity is shown to decay to about 1000 fps, accompanied by a slight rise in altitude. Subsequent deceleration reduces the velocity to a low value at an almost constant altitude.

A schematic of a reefed hemisflo parachute and its roof elements are shown in Figure 26. The roof elements are verticals and horizontal ribbons. The horizontal ribbons are beaded, while the verticals have a rectangular cross section. In the roof structure, the ribbons and verticals cross and are normal to each other. Rectangular openings are formed by these elements. Assuming that upon deployment the parachute envelope fills out as shown in Figure 26, then the flow through the parachute envelope is governed by the dimensions and by the number of these individual roof openings. When the flow is supersonic and the envelope is filled, a strong shock can be assumed to stand forward of the skirt inlet. The pressure inside the envelope approaches stagnation pressure. The ratio of envelope pressure to the pressure around the parachute envelope is greater than critical, and sonic flow exists at the openings.

Under these conditions, the heating of a roof opening's edges can be based on the flow through an orifice. The heat transfer coefficient can then be calculated as follows (see List of Symbols in preliminary pages of this report:

Figure 26 - Reefed 16-Ft D_0 Hemisilo Parachute

$$k = \left[\frac{0.026}{D_t^{0.2}} \left(\frac{\mu 0.2 C_p}{P_r^{0.6}} \right)_o \left(\frac{P_{tg}}{C^*} \right)^{0.8} \left(\frac{D_t}{r_e} \right)^{0.1} \right] \left(\frac{A^*}{A} \right)^{0.9} \sigma \quad (57)$$

This equation, obtained from Reference 29, represents the convective heat transfer coefficient for turbulent flow through a nozzle. Since the equation is derived for nozzle flow, the roof openings can be represented as circular orifices by using the hydraulic diameter of the rectangular openings and by treating the flow as that through an orifice. The radius of curvature (r_e) can be assumed to be the radius of curvature on the horizontal-ribbon bead.

Assuming the beads shown in Figure 27 are cylinders of infinite length surrounded by a gas at stream temperature at T_{aw} , a transient one-dimensional equation for surface-heat conduction can be written. For such a cylinder, the condition of heat input at the surface, neglecting any out radiation, is

$$h[T_{aw} - T(r_e, \tau)] = k \left[\frac{\partial}{\partial r} T(r_e, \tau) \right] \quad (58)$$

An approximate solution of the previous equation is available in Reference 30, assuming an average adiabatic wall temperature during a given

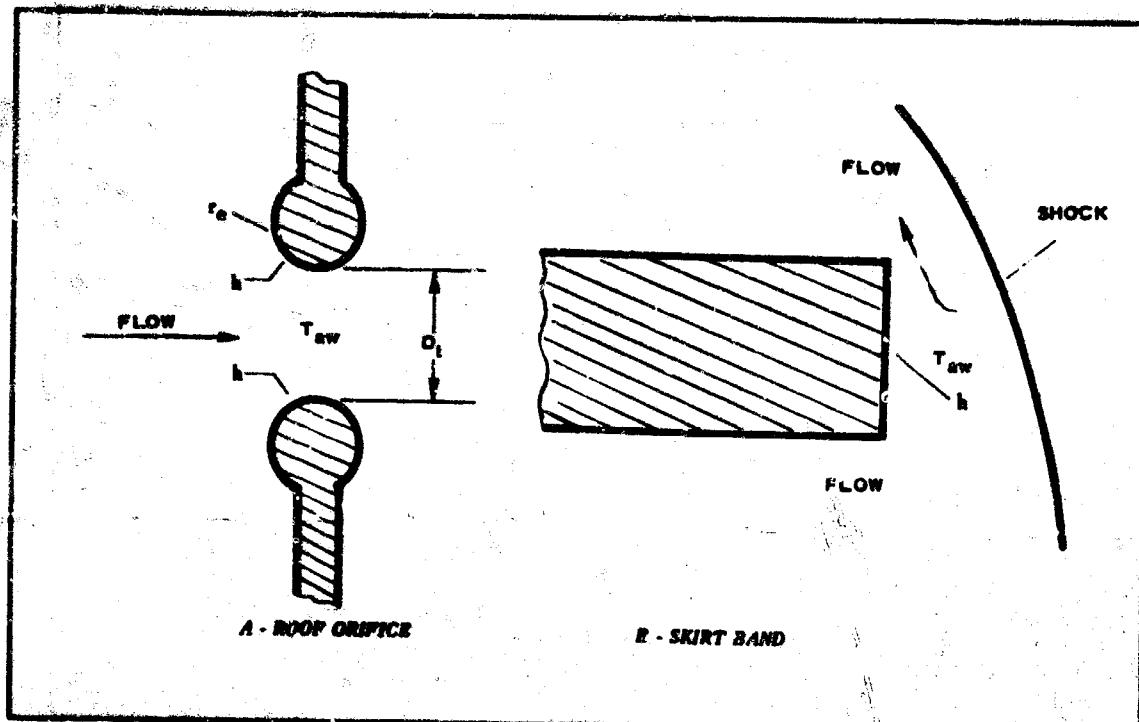


Figure 27 - Thermal Models

time interval exists. Since Figure 25 shows the critical deceleration time to be approximately one second, the average thermal environment for small increments of time during this period should be a good approximation for determining the thermal response of the bead material.

A similar approach can be described for the skirt band that forms the leading edge of the decelerator, assuming a strong shock exists at the skirt inlet. That such a shock is present in the immediate vicinity of the skirt band can also be assumed by looking at the skirt-band lip. An expanded sketch of this leading edge is shown in Figure 27. Assuming the air is compressed upon crossing the shock and then expands around the leading edge to the point where sonic velocity is reached, maximum heating should occur at this point. For turbulent boundary layer flow, the heat transfer coefficient can be calculated using:

$$h = \rho_{\infty} u_{\infty} C_p \frac{C_{f2}}{2} \left[G(x) \right]^{1/5} \quad (59)$$

This equation, taken from Reference 31, represents the heat-transfer coefficient to a blunt leading edge. The equation is evaluated at the stagnation point, and the factor $G(x)^{1/5}$ accounts for the degree of bluntness. Density and velocity evaluations are based on local flow conditions at the stagnation point.

Temperature response is calculated in a manner analogous to that used for the bead. However, a semi-infinite slab is assumed to be heated in the cylinder's place. The heat-input condition at the surface from a fluid at the adiabatic wall temperature (T_{aw}) is:

$$h[T_{aw} - T(0, \tau)] = -k \frac{\partial T}{\partial x} T(0, \tau) \quad (60)$$

An approximate solution of this equation is also available in Reference 30 if the same assumptions are made regarding the external thermal environment.

Thermal analysis results are shown in Figure 28. The adiabatic wall temperature assumes a turbulent boundary layer flow and is shown as a function of time. At the instant of deployment, the adiabatic wall temperature is about 800 F. In 0.2 of a second, the adiabatic wall temperature drops to about 450 F; in one second, the adiabatic wall temperature decreases to 100 F. Figure 28 also shows the temperature rise on the surface of a bead element fabricated from 90-mil diameter nylon yarn. The weight per unit area of the 2000-lb strength beaded nylon ribbon was established at 0.92 lb/sq yd. The thermal conductivity value was 1.7 Btu/hr-sq ft-F/in., and the specific heat value was 0.5 Btu/lb-F. The latter is an average value. The average heat transfer coefficient over the first 0.2-sec time interval was calculated to be 583 Btu/hr-sq ft-F. These values were used to evaluate the temperature rise in the bead using the temperature response charts contained in Reference 30. The surface temperature was calculated to rise very rapidly in the first 0.1 sec until it equaled the adiabatic wall temperature at about 0.15 sec after deployment. The temperature rise at the center of the bead was calculated to be zero over the same time interval. Since deceleration continues, the surface temperature will decline to the ambient level.

The temperature rise on the skirt band's leading edge is also shown in Figure 28 as a function of time after deployment. The surface-temperature rise at the sonic point of the skirt band's leading edge is calculated on the basis of a semi-infinite slab solution. The temperature-gradient inside a slab solution is practically nonexistent, except for the first few mils of depth from the leading edge. The surface temperature rises to about 540 F in the first 0.15 sec from deployment, then cools during further deceleration.

The thermal analysis of parachute materials indicates that the surfaces at the edge of the ribbons and at the skirt band's leading edge experience an initial rapid temperature rise. However, the velocity decays so rapidly that aerodynamic heating becomes nonexistent after the first second. Because of this rapid velocity decay, the interior of the materials experience little temperature rise. Nylon-edge surfaces may experience surface fusing during the first 0.1 sec following deployment. The temperature rise on the flat surface areas of the ribbons will be substantially less than the temperature of the edge surfaces due to a much lower heat transfer coefficient. Because of the extremely short time interval for high heating rates and the predicted absence of thermal damage, instrumentation for measuring free-flight thermal conditions was not recommended.

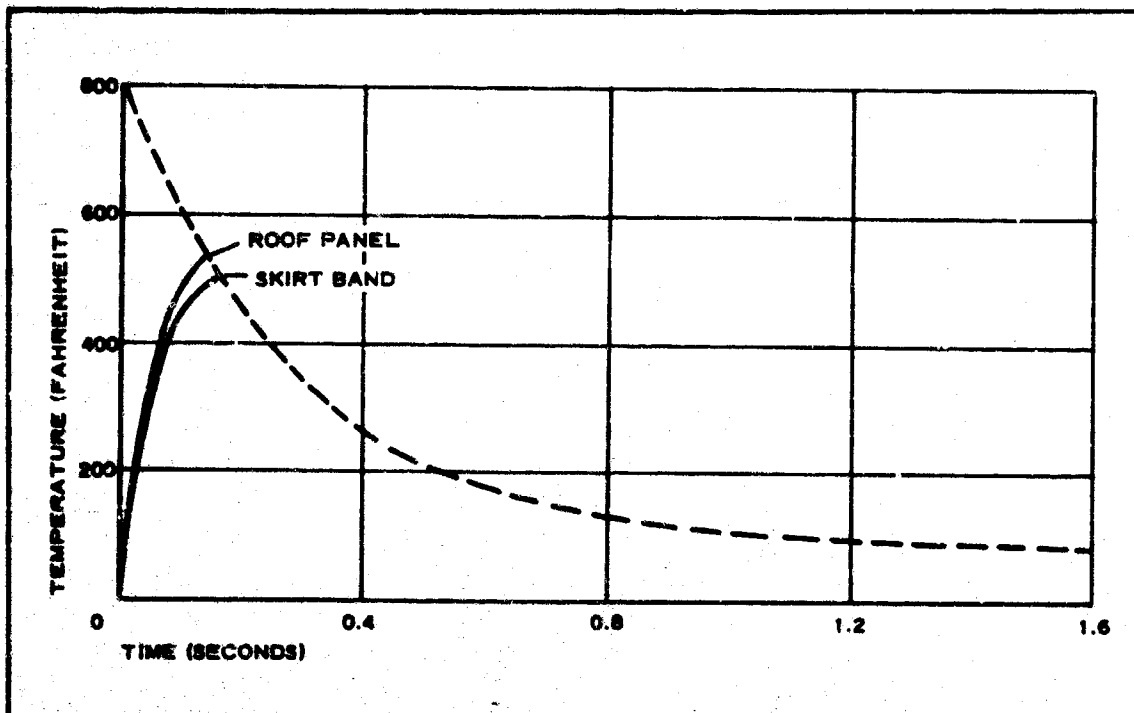


Figure 28 - Temperature versus Time from Deployment

7. MATERIAL, SEAM, AND JOINT TESTING

a. General

The basic material strengths of all webbing and ribbon types used in the design and construction of the canopies were determined by tests in accordance with Federal Specification CCC-T-191 (Reference 32). Critical joints and seams were also tested in accordance with this specification. The test results given in Table XIV indicate the actual strength of the basic material used in the canopy construction. The remainder of this discussion deals with seam and joint testing.

b. Seam and Joint Testing

(1) Skirt Band

The reference for the skirt band is Detail X of Drawing 530A005-016 (Reference 33). This band consists of two turns of MIL-W-27657 (Reference 25), Type VI, webbing with three thicknesses at the splice. The splice is two separate 5-point-cross-stitches, each 1.75 in. long. Number 6 cord is used with 5 to 7 stitches per inch. Between the cross stitches is the suspension line and related sewing.

The original design had a single turn of webbing joined by a 6-in. long, 4-point cross stitch; a tensile test of this earlier configuration indicated an ultimate strength of 8000 lb.

SECTION III - LARGE PARACHUTE DECELERATOR

AFFDL-TR-67-25

TABLE XIV - MATERIAL TESTS*

Specimen	Material	Width (in.)	Rated strength (lb)	Application	Specimen No.	Ultimate load (lb)	Failure type
MIL-W-27657 Type III Gage length = 6 in. Loading rate = 1 in./min	Nylon	1	6,000	Reinforced ribbon, reinforced web, suspension line	1	6230	Jaw failure
					2	6350	Jaw failure
					3	5980	Jaw failure
					4	6060	Jaw failure
					5	5840	Jaw failure
MIL-W-27657 Type IV Gage length = 6 in. Loading rate = 1 in./min	Nylon	1-3/4	8,700	Vent loop, ring retainer, vent band	1	4280	Jaw failure
					2	3700	Jaw failure
					3	3600	Jaw failure
					4	4480	Jaw failure
					5	4120	Jaw failure
MIL-W-27657 Type VI Gage length = 6 in. Loading rate = 1 in./min	Nylon	1-3/4	10,000	Skirt band	1	4260	Jaw failure
					2	4140	Jaw failure
					3	4770	Jaw failure
					4	4550	Jaw failure
					5	4490	Jaw failure
MIL-T-5038 Type IV Gage length = 6 in. Loading rate = 1 in./min	Nylon	1	1,000	Tie loops	1	1130	Jaw failure
					2	1230	Webbing failure
					3	1240	Webbing failure
					4	1190	Jaw failure
					5	1200	Webbing failure
MIL-T-5038 Type V Gage length = 6 in. Loading rate = 1 in./min	Nylon	9/16	500	Vertical ribbon	1	581	Jaw failure
					2	538	Jaw failure
					3	430	Jaw failure
					4	501	Jaw failure
					5	554	Jaw failure
MIL-T-5405 Type V Gage length = 6 in. Loading rate = 1 in./min	Nylon	2	600	Reinforced web	1	822	Webbing failure
					2	830	Webbing failure
					3	817	Webbing failure
					4	840	Webbing failure
					5	842	Webbing failure
Type 1746 Gage length = 6 in. Loading rate = 1 in./min	Nomen	2	4,000	Horizontal ribbon	1	3900	Jaw failure
					2	3930	Jaw failure
					3	3920	Jaw failure
					4	3870	Ribbon failure
					5	3910	Ribbon failure
Type 1747 Gage length = 6 in. Loading rate = 1 in./min	Nomen	2	3,000	Horizontal ribbon	1	3000	Ribbon failure
					2	3010	Ribbon failure
					3	3050	Ribbon failure
					4	3010	Ribbon failure
					5	3040	Ribbon failure
Type 1748 Gage length = 6 in. Loading rate = 1 in./min	Nomen	2	2,000	Horizontal ribbon	1	2200	Ribbon at top of pin
					2	2130	Ribbon failure
					3	2140	Ribbon failure
					4	2140	Ribbon failure
					5	2140	Ribbon failure
MIL-W-5425 Gage length = 6 in. Loading rate = 1/2 in./min	Nylon	1	4,000	Keeper	1	3690	Jaw failure
					2	3740	Jaw failure
					3	3735	Jaw failure
MIL-W-5425	Nylon	1/2	1,000	Around keep, web, keeper band			

* All tests performed with 2-in. -wide roll pin jaws.

(2) Horizontal Ribbon Seams

The reference for the horizontal ribbon seams is Detail J of Drawing 530A005-016. These seams are designed to approach the strength of the parent material. The sewing pattern for all the horizontal ribbons is a 3-in. -long, 5-point cross stitch, using Nomex Size FF thread with 7 to 9 stitches per inch. Static test results are presented in Table XV.

TABLE XV - RIBBON SPLICE TEST RESULTS

Ribbon type Nomex no.	Rated strength (lb)	Ultimate load* (lb)	Failure type
1746	4000	3500	Ribbon at stitching
1746	4000	3380	Ribbon at loop end
1746	4000	3550	Ribbon at loop end
1747	3000	2650	Ribbon at stitching
1747	3000	2800	Ribbon at stitching
1747	3000	2700	Ribbon at stitching

* Loading rate = 1 in./min

(3) Vent Band

The reference for the vent band is Detail A of Drawing 530A005-016. To achieve a seam strength approaching the 17,400-lb strength of MIL-W-27657, Type IV webbing doubled, the following procedure is used. Two three-point cross-stitch patterns, using Number 3 cord with 6 to 8 stitches per inch, are sewn across the webbing. These two patterns are separated by a suspension line whose sewing also goes through the vent band. This configuration replaced a 6-in. -long, 4-point cross-stitch seam of 6 cords, which tested at 15,250 and 15,650 lb for two samples.

(4) Suspension Line Loops

The source for the suspension line loops is Section P-P of Drawing 530A005-016. For these loops, MIL-W-27657A, Type III, webbing with a rated strength of 6000 lb is used in pairs to form the suspension lines. A 6-in., 3-point cross-stitch of Number 6 cord is used to form the end loops. Two seams are used to join each suspension line pair. The configuration tested is shown in Figure 29. The results of the tests are presented in Table XVI.

(5) Reefing Line Test Values

As already indicated, Table XVI shows the loop test values of a pair of

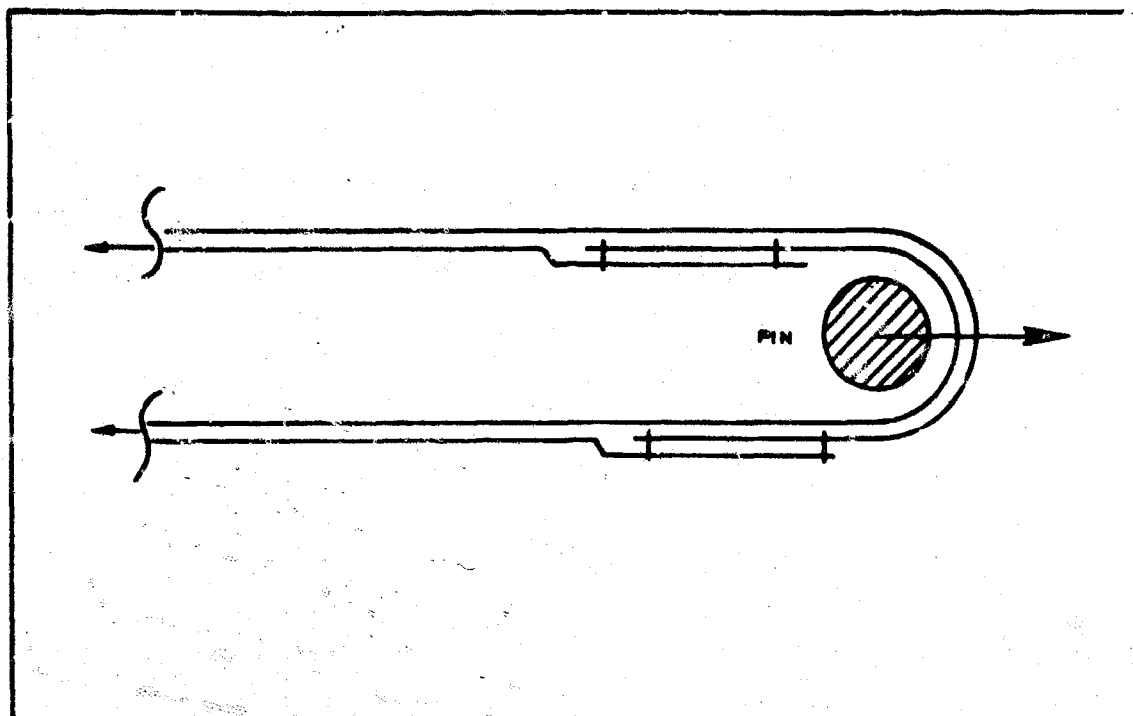


Figure 29 - Suspension Line Loops Test Specimen

TABLE XVI - SUSPENSION LINE LOOP TEST RESULTS

Webbing type	Rated strength* (lb)	Ultimate load** (lb)	Failure type
Nylon, MIL-W-27657, Type III	24,000	21,400	Webbing at stitching
	24,000	19,700	Webbing at pin
	24,000	21,200	Webbing at stitching

* Four webbings.

+ Loading rate = 1 in./min.

MIL-W-27657 Type III webbings on top of each other. These values are typical of the reefing line test values using 1.25-in. -diameter loading pins. The reefing line tension capability would be one-half of these values or $21,200/2 = 10,600$ lb.

Loop tests were made of a MIL-W-4088, Type XXIII, webbing on top of one MIL-W-27657, Type III, webbing, using 1.25-in. -diameter loading pins. An ultimate loop value of 25,200 lb was measured, with failure

occurring at the pins. Reefing line tension capability will be at least one-half of this value or $25,200/2 = 12,600$ lb.

(6) Suspension Line/Skirt Band Joint

The reference for the suspension line/skirt band joint is Detail L of Drawing 530A005-016. This specimen, which was fabricated according to the drawing, was tested by initially applying a 2000 skirt band load and then loading the suspension line in a 30-deg direction. Figure 30 depicts the basic specimen configuration. The results are as follows:

1. In Test 1, the stitching failed at a 2870-lb skirt load and a 3800-lb line load.
2. In Test 2, the stitching failed at a 2960-skirt load and a 4900-lb line load.

(7) Reefing Ring Attachment

The reference for the reefing ring attachment is Detail L of Drawing 530A005-016. Direct attachment of the reefing ring to the skirt band is made by means of (1) a MIL-W-27657, Type IV, nylon web (-35 of drawing) and (2) a keeper of MIL-W-5625 (Reference 34, -41 of drawing) of 4000-lb strength placed around each end of the -35 web. Each of these members is sewn to the skirt with a box-stitch pattern of Number 6 cord, with 5 to 7 stitches per inch. The test setup is shown in Figure 31. The test results are as follows:

1. For Specimen 1, the stitches pulled out at a 6685-lb load
2. For Specimen 2, the stitches pulled out a 6260-lb load

8. DESIGN AND FABRICATION

a. General

The test item parachute packed in its deployment bag, and the pilot parachute packed in its deployment bag form the test decelerator package as it is stowed into the test Vehicle A test container. The stowage arrangement is shown in Figure 2 (Section II).

b. Test Parachute and Deployment Bag

Drawing 530A005-016, Rev E (Reference 33), presents the test 16-ft hemisflo parachute assembly. The canopy consists of 32 shaped gores to produce a hemispherical contour, with a 10-percent extended skirt. The skirt is a continuation of the spherical contour, and it has an arc length equal to 10 percent of the meridional perimeter of the hemisphere. Each of the 42 horizontal ribbons is a continuous hoop with a single splice and a beaded edge. The horizontal ribbons are graded, and the strongest ribbons are near the top of the canopy. The splices of the ribbons are staggered from gore to gore in a spiral to minimize asymmetry of

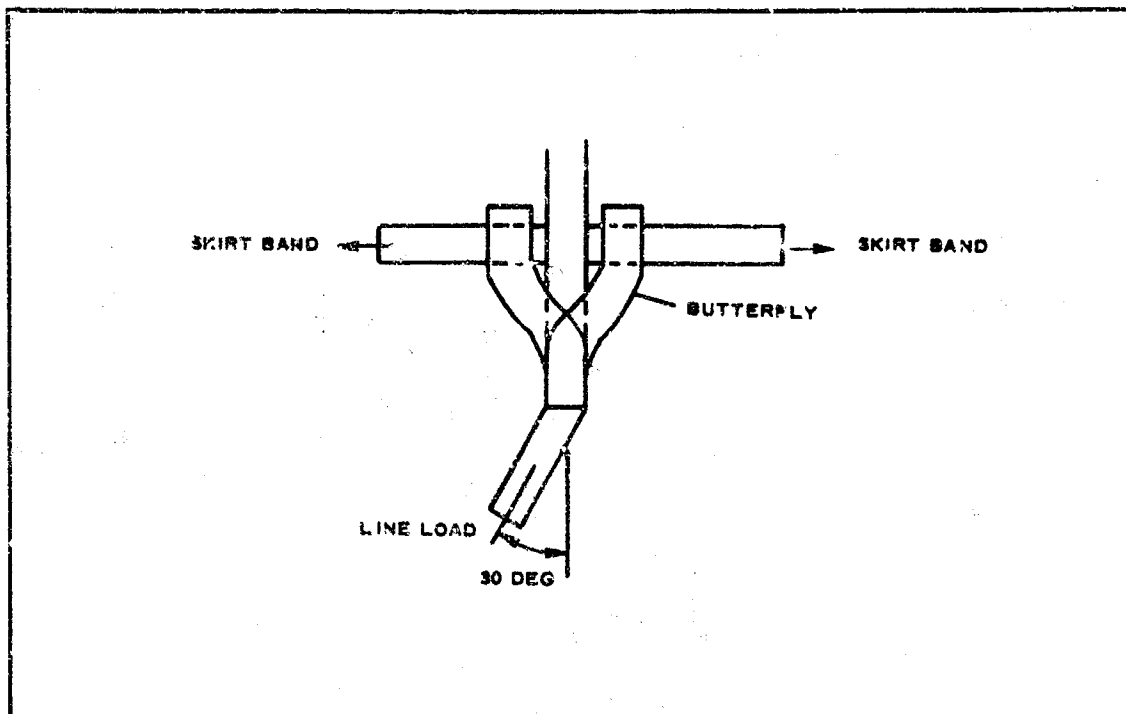


Figure 30 - Suspension Line Skirt Band Joint

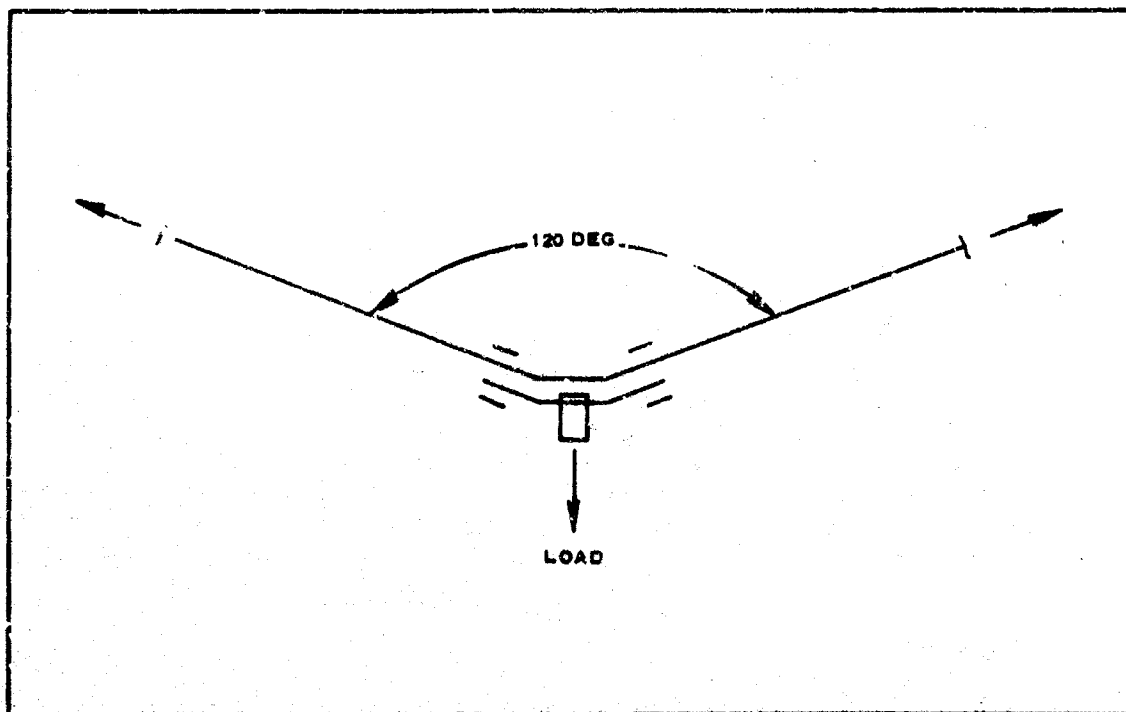


Figure 31 - Reefing Ring Attachment Test Configuration

material placement. The suspension lines consist of pairs of webbing that become the radials at the canopy, with the ribbons sandwiched between the lines. The 32 suspension lines are formed by placing across the canopy 16 continuous pairs of webbing from attachment loop to attachment loop.

The skirt band consists of two turns of webbing. The first turn of the band is Ribbon No. 42; the skirt band/suspension line joint is reinforced by a doubler web (-17 web) plus a butterfly arrangement of the -15 web. The second and outer turn of the skirt band webbing is not attached at the suspension lines but at midgore in conjunction with attaching the reefing rings; this turn is 16 in. shorter than the first turn and forms the pocket bands across alternate suspension lines.

Webbing loops are attached to the suspension lines (see Detail W of drawing) for tying the deployment break ties. Leather cuffs are added to protect the lines against scuffing damage from the rear edge of the test item container.

The reefing line strengths and lengths are determined by computation with respect to the desired test point deployment conditions. The reefing line is inserted into the reefing rings and then sewn together to final dimensions. Two Sandia heavy duty line cutters are used for disreefing. The canopy is folded in a conventional manner and placed in the aft end of the deployment bag (Drawing 530A005-017, Reference 35). Eight 500-lb break ties of MIL-T-5038, Type V, tape attach the canopy to the bag (Reference 36). Four ties are made at each of two levels on the canopy; each tie is made by gathering alternate suspension lines over a quarter of the canopy (4 lines) and passing the tie tape under these webs at a point immediately forward of the two intermediate reinforcing webs (-19 and -21 webs). The canopy is locked in position by a separate locking loop (Drawing 530A005-017-33), which is released only by extracting the last fold of the suspension lines. The suspension lines are gathered into two bundles, and each bundle is attached to its respective bag panel. Each fold is tied to the panel with a 250-lb break tie of MIL-T-5038, Type III, 0.5-in. -wide tape.

c. Pilot Parachute and Deployment Bag

The pilot chute (Drawing 530A005-303, Reference 37), a 48-in. -diameter hemisflo, is packed in its own deployment bag (Drawing 530A005-019, Reference 38). It is stowed on the back end of the main chute deployment bag, and its suspension lines are attached to eight points on the main chute bag. Two knives are employed for pilot chute deployment. One knife is actuated by the pilot chute bag bridle; it releases the pilot chute pack from the main chute deployment bag. The second knife cuts the locking cord at the front of the pilot chute bag; it is actuated by a lanyard to the back of the main chute bag.

d. Fabrication

All fabrication procedures requiring dimensional measurements and marking were accomplished in a room with ambient conditions maintained at a temperature of 75 F and a relative humidity of 50 percent. All layout

and marking of webs and ribbons were accomplished in the same room. Prior to marking, the webs and materials were unrolled from the raw material stocks and left "relaxed" for a minimum period of 24 hours. As a guarantee of final dimensional assurance once assembly was started, the material was kept in the controlled atmosphere except for brief periods as required for sewing operations. Templates were used for the large parachute vent band and gore layout to assure uniformity of parachute layout and fabrication.

9. DEPLOYMENT SYSTEM AND PACKING PROCEDURE

a. Deployment System

The sequence of the test item deployment system (Reference 39) is shown in Figure 32. In Sequence 1, a timer-actuated shaped charge begins final-stage booster separation. Its cutting action allows the opening of the spring loaded drag plates. The booster case is decelerated by the drag force acting on these drag plates and on the booster case. A small metal drag cone is attached to the rear half of the test item container by a riser line and to the booster assembly by three Number 10 screws.

In Sequence 2, drag cone riser line stretch has occurred, breaking the three Number 10 screws and freeing the cone from the booster assembly.

Sequence 3 is initiated by a shaped charge that cuts the cylindrical test item container at midsection. The drag cone then removes the rear half of the test item container.

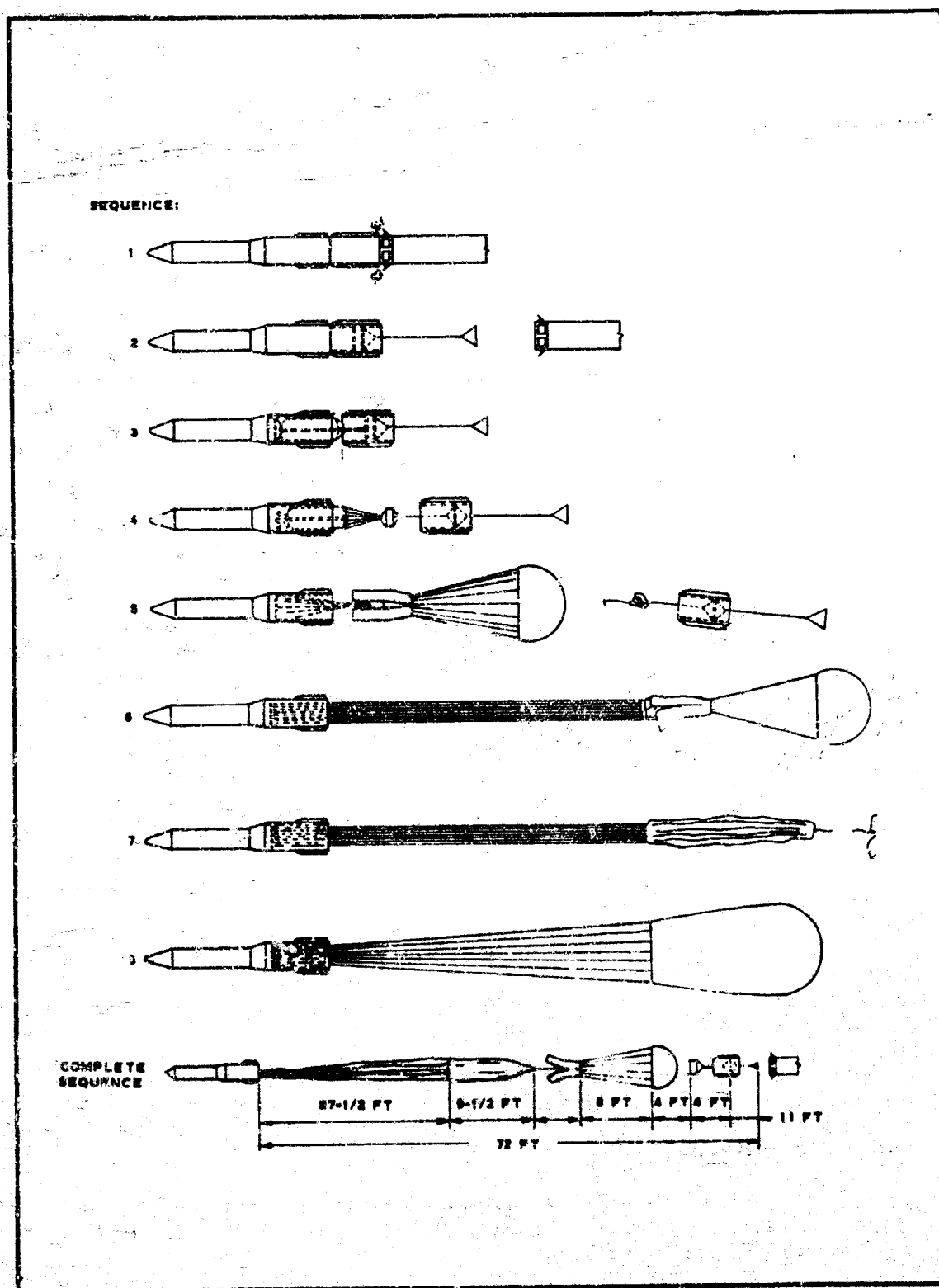
In Sequence 4, the movement of the rear half of the test item container has caused the first knife to release the pilot chute bag. This movement extracts the pilot chute. The position shown is at partial extension of the pilot chute suspension lines and where the second knife will cut the lock cord on the pilot chute bag, thus releasing the remainder of the suspension lines and the canopy.

In Sequence 5, several events have occurred. The pilot chute has been deployed, and the canopy-to-deployment bag break line is broken. The pilot chute is extracting the test item deployment bag. The bag lacings have been cut, and the test item suspension lines are being extracted. Break ties of 250-lb tape are broken at regular spacings along the lines to ensure orderly line deployment.

In Sequence 6, the lines are at full extension, and the canopy lock is unlocked. Eight 500-lb break ties (4 each at 2 levels along the canopy) between the canopy and the bag will be broken to stretch the canopy and arrange it for filling.

In Sequence 7, the test item is shown at line stretch, following breaking the two apex-to-bag lines. The first 4000-lb line is 4 ft long, and the second 4000-lb line is 8 ft long.

Sequence 8 shows the test parachute inflated in the reefed condition.

Figure 32 - Deployment Sequence of 16-Ft D₀ Hemisflo Test Parachute

b. Packing Procedure

The canopy is folded in pleats as shown in Figure 33. Temporary ties are made in eight places. Each tie is around four suspension lines in each quadrant as shown. Four ties are just forward of each ribbon reinforcing web (Ribbons 15 and 29). MIL-T-5038, Type V, ribbon (500 lb) is used for the ties. Temporary bow knots are tied.

Lines are tacked into four-line groups, one four-line group to each of the eight attachment loops, as follows:

1. A group of 4 adjacent lines are laid on a long table, and a light tension is applied (approximately 20 lb) to the group, keeping the skirt ends lined up.
2. The first tack is made 66 in. from the skirt. Additional tacks are made to the loop end at 20-in. spacings.

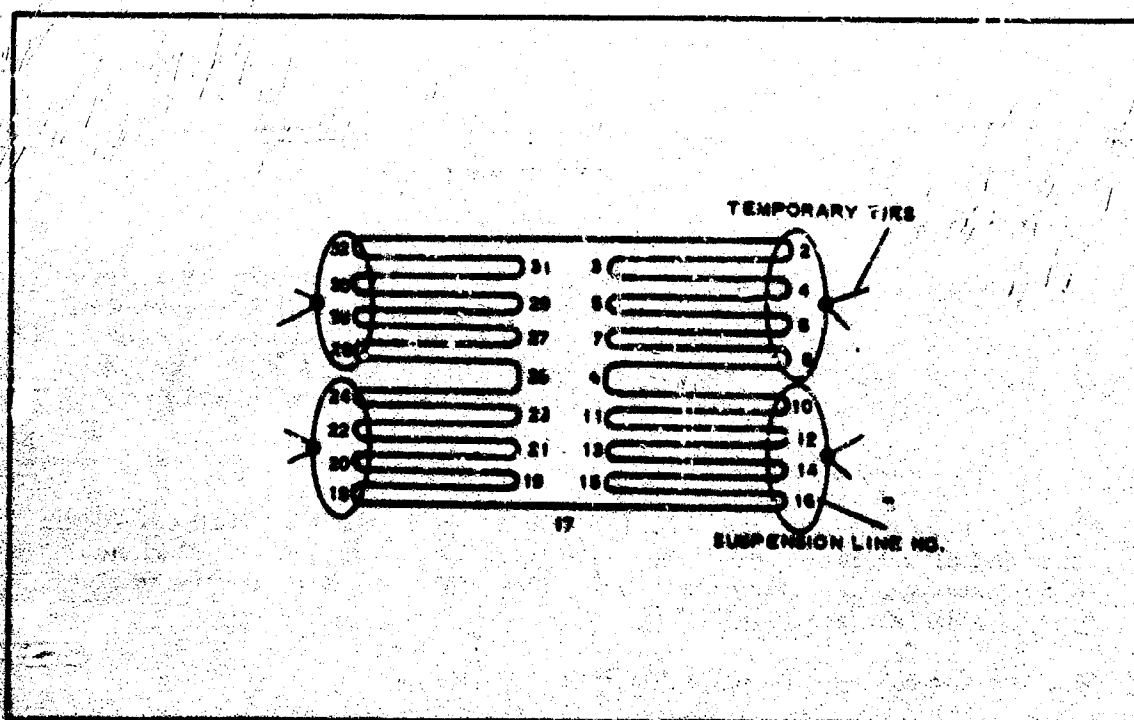
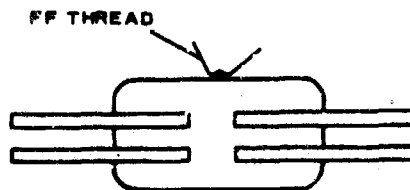


Figure 33 - Folding Canopy

3. Black nylon size FF thread is used, making a single turn through the four lines, as shown in the following sketch:



4. The above steps are repeated on each of the seven remaining line groups of four suspension lines.

Attachment loops are arranged as follows:

1. The eight loops are laid in line as shown in Detail W (13-D) on Drawing 530A005-016.
2. A one-inch-diameter metal tube is inserted through the first four-loops (No. 4, 3, 2, 1), and another tube is inserted through loops No. 8, 7, 6, and 5.
3. The first four loops are raised (No. 4, 3, 2, 1), and the second group of four loops (No. 8, 7, 6, 5) is rotated into the position shown in Figure 34A. A temporary tie is made in this position with heavy cord.
4. The line groups are stacked as shown in Figure 34B. Temporary ties are made around each of the 16-line stacks with colored cord or ribbon. The ties are spaced at approximately three-foot intervals along the lines.

(3) Installing Reefing Line

The reefing line is laid out as shown earlier in Figure 24A and stitched together using two rows of FF thread. Ring locations and line numbers are on the stenciled inner web. The line is inserted into the canopy reefing rings and spliced as shown in Figure 24B. The lines are tacked to each ring using two six-cord tacks through the line and around the ring.

(4) Preparing Canopy Vent

A temporary 4-ft length of 500-lb cord is tied to the vent loop and to the back end of the deployment bag. The vent loop is tacked together near the suspension line using six-cord. The vent is tucked into the folded canopy approximately one foot.

(5) Facing Canopy into Deployment Bag

The bag panels are laced together loosely with MIL-W-5625 9/16-in. -wide web (1500 lb). The end panel is not installed as yet, and the tucked vent

is placed at the bottom of the bag. The canopy is folded to the first four canopy ties, Item (1), above. The temporary bows are removed, and each break ribbon is installed into its respective loop in the first tier of tie loops in the bag panels. The canopy is folded to the second group of four canopy ties, repeating the above steps, then tying into the second tier of loops (see Figure 35A). Folding of the canopy into the bag is continued until the skirt is in a circular bundle with the skirt plane perpendicular to the bag centerline and the cutter pockets folded 90 deg inward.

(6) Arming Reefing Cutter

The shear pin, charge, firing mechanism, and arming lanyard are installed in each cutter. The lanyard is MIL-W-5625, 9/16-in. -wide-web (1500 lb). A very short bowline loop is tied in each end to make its total length 5.5 in. The fold in the corresponding suspension line is placed over the cutter pocket and tacked to the cutter pocket in two places with six-cord so that the lanyard is slack.

(7) Installing Canopy Lock

The Drawing 530A005-017-33 locking loop is positioned in one of the large web loops in the deployment bag by hand-stitching with a minimum of six stitches of six-cord. The reefing cutters are positioned axially in the skirt bundle and approximately midway between the center and the outside of the bundle. A short length of the suspension lines is laid over the skirt bundle and toward the open side of the bag. The canopy locking loop is installed through the remaining three large web loops in the bag and through itself to form a second loop through which the bundle of suspension lines is to be inserted. Note that the first (cinching) turn of the locking loop is placed over the suspension lines and not around them. The loop of suspension lines is then inserted through the second loop of the canopy locking loop and adjusted so that the lines are all aligned. The upper portion of the locking loop is visible in Figure 35B.

(8) Stowing Suspension Lines

The line groups are divided so Lines 1 through 16 go to one bag panel and Lines 17 through 32 go to the other. Line bundles are folded into the bag (without twisting) forming 20-in. loops. Each bundle loop is tied to the bag panel tie loops, as shown in Figure 35B. A single turn of MIL-T-5038, Type V, tape (500 lb) is used for each tie, and each tie is passed through the loops provided on the suspension lines. A surgeon's knot is used.

(9) Tucking Attachment Loops

The attachment loop splices are tucked between the bag and the line loops as shown in Figure 35C. Each loop is tacked to the bag with the knots placed outside. Doubled black six-cord is used.

(10) Lacing Bag

Laces are pulled up successively, using a hoist.

(A) INSTALLING CANOPY TIES



(B) STOWING
SUSPENSION LINES



(C) TUCKING
ATTACHMENT LOOPS



Figure 35 - Parachute Packing Procedure

(11) Installing Vent Break Cords and End Panel

Two break cores are installed, one with a finished length of eight feet and the other with a finished length of four feet. Both cords are of MIL-W-5625 1-in. -wide webbing (4000-lb rated strength). The ends of each cord are tied separately into the vent loop and into the bag end panel with bow-line loops. The vent loops are tacked in the same manner as in Item (4), above. Cords are folded into place, and the end panel is laced into the bag using the 1500-lb web for lacing.

(12) Installing Knife Lanyards

The bag lacing is removed down to Grommet 11. The knives of the lanyard (Drawing 530A005-017-107) are tacked at Grommets 1 and 10 on each panel in the fold of the flap. White six-cord is used. The excess length of the lanyard is tucked over the end of the flap and into the pack. The loops of the lanyards are placed over the nearest attachment loop and tacked in place with FF thread (see Figure 36A).

(13) Installing Spreader Loops

Twelve-inch loops are made of MIL-W-5625, 9/16-in. -wide webbing (1500 lb) through Grommets 2 and 11. A four-inch lap splice with 3-cord is hand-stitched (see Figure 36A). The excess is tucked into the pack.

(14) Installing Drogue Chute

The drogue parachute suspension lines are attached to the main bag using eight MS24553-1 links. The bag-opening knife lanyard is attached to the center of the main bag end panel with a bowline loop. The drogue bag is placed in position on the main bag, and a MIL-C-5040, Type III, cord (550 lb) is passed through the loops of the main bag, as shown in Figure 36B. The cord is passed through the cutter knife as shown and tied with a surgeon's knot.

(15) Installing Front Packing Plate

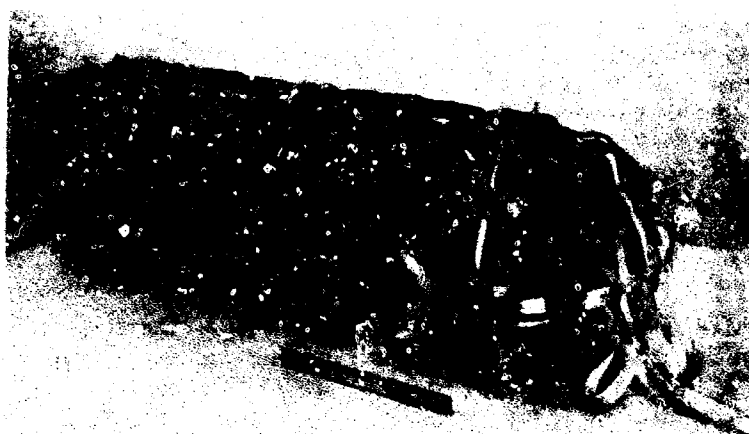
The front packing plate is installed as shown in Figure 36C, using doubled 6-cord. Note that this plate is removed during installation of the test item into the Vehicle A test container.

10. SUMMARY AND CONCLUSIONS**a. Configuration**

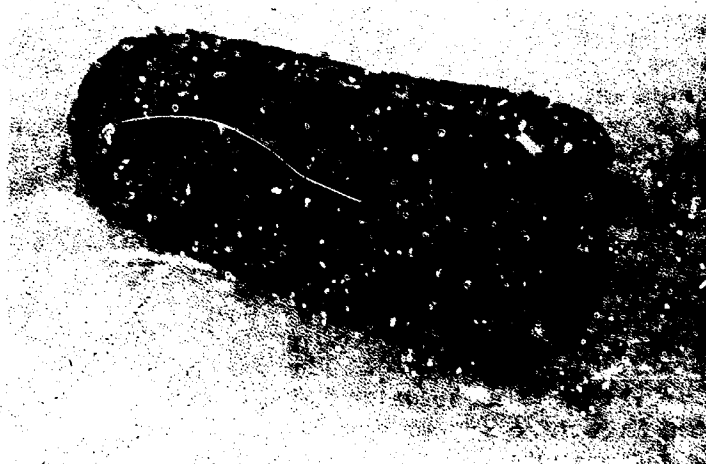
Three free-flight tests were conducted on large parachute (LP) decelerator models whose basic configuration had been selected previously by wind-tunnel tests. The free-flight tests confirmed the earlier wind-tunnel conclusion that this configuration has the inflation stability needed for use as a reusable transonic and supersonic parachute. Moreover, review of the test films and load traces indicated that the free-flight inflation and system stability of the free-flight test models were superior to those of the wind-tunnel test models despite the high deceleration rates



(A) SPREADER LOOPS AND KNIFE LANYARD



(B) DROGUE CHUTE INSTALLATION



(C) FRONT PACKING PLATE INSTALLED

Figure 36 - Packed Parachute

associated with the flight tests. The flight tests also disclosed excellent system and inflation stability when the parachutes were disreefed in the transonic and subsonic regimes.

b. Aerodynamic Loadings

Three approaches were considered for determining the reefing dimensions needed to attain a maximum opening load of 200,000 lb:

1. Using wind-tunnel steady-state drag values and applying an anticipated opening shock factor
2. Using an analytical approach consisting of a drag term based only on shape and a mass-acquisition force term
3. Using flight test data as they become available for empirical predictions

The first approach could not be used with confidence because the steady-state drag values varied markedly between different size wind-tunnel models of the same configuration. Therefore, the second approach was undertaken to calculate the reefing line lengths (Item 3, d of this section). This simplified approach included only two basic terms. The first term used an estimated shape-drag coefficient based on inlet area, and the second term was based on the rate of mass acquired by the parachute during opening.

As flight test data became available, reefing line lengths were predicted empirically. These values were used in conjunction with the values predicted by the analytical approach to select the reefing line length for the next test.

Evaluation of the simple analytical approach using the flight test data indicates a good opening drag force correlation (Figures 17, 18, and 19). However, inspection of the two basic terms making up the predicted drag force indicates the shape drag term value is low and the mass acquisition force value is high compared to the corresponding flight test values. The flight data indicated a shape drag value of approximately 3.35 based on the inlet area, compared to 2.56 or 2.58 used in the analytical approach. The predicted mass acquisition force value was high because the predicted filling time was too high - approximately one-tenth of the actual filling time. Since mass acquisition force is directly related to filling time, the predicted mass acquisition force was an order of magnitude high.

This high filling results from the difference between the calculated inlet rate and the calculated exit rate. The inlet rate is based on free stream values. Correction to these values should consider the vehicle wake effects and the parachute suspension lines. The exit calculations consider only geometric porosity and the surface of the hemispherical portion of the canopy. These assumptions require further consideration.

A phenomenon not considered in the analytical approach is the stretch of

the reefing line at peak load. This was most apparent from the LP-3 results, where the reefing line parted near peak load. An inlet area increase of approximately 12 percent is apparent from inspection of Figure 7B.

Based on these evaluations a more complete analysis is required to predict with accuracy the values of the terms that make up the opening load equation. Such an analysis should consider:

1. More accurate drag coefficient for the shape of a reefed parachute based on its inlet area
2. Reductions in inlet flow rates due to the forebody wake and the parachute suspension lines
3. Increases in load due to the stretching of the reefing line under load

The empirical approach (Item 3, c of this section) indicated a reasonable correlation for opening load coefficients based on either reefing line length or inlet area (Figure 15). The values based on inlet area remained approximately constant despite increasing Mach number and smaller inlet sizes.

c. Geometry

Review of the free-flight films indicated a firm shape of the reefed skirt and the canopy ribbons. Based on these observations, no change is recommended for changing the canopy porosity, distribution of porosity, or configuration.

d. Structure

Inspection of the parachute after each test confirmed the lack of thermal effects on the structure (Item 6, above, of this section) and the adequacy of the canopy to withstand the loadings (Item 5). Failures were associated only with some suspension lines during deployment of LP-4 and LP-5 and the reefing line on LP-3. The Nomex ribbons and verticals withstood the opening shock loadings without apparent damage. Where the light verticals were attached to the heavy skirt band, some fraying had begun locally. The nylon skirt band, reefing ring attachments, and butterflyes were undamaged. The reefing line, which was broken on LP-3, was increased in strength for LP-4 and LP-5 and suffered no damage in the tests.

e. Deployment System and Packing Procedure

The deployment system and packing procedure (Item 9 of this section) was satisfactory with two exceptions: (1) in the last 2 tests, 4 of the 32 lines were broken during deployment; (2) in the LP-5 test, the packing position prevented the lanyards from initiating the cutters prior to lanyard failure.

Based on these results, the following steps are recommended to reduce

SECTION III - LARGE PARACHUTE DECELERATOR AFFDL-TR-67-25

line damage: increase the length of suspension line folded on the canopy side of the locking loop, and locally add Teflon sleeves to the lines. Repositioning of the packed cutters to produce a straight pull for initiation of the cutters is also recommended.

The drogue design and the approach of reefing the drogue for similar deployment acceleration in each test provided smooth deployments with a constant set of line and canopy ties.

SECTION IV

TEXTILE BALLUTE DECELERATOR

1. GENERAL

a. History

The objective of the BALLUTE effort under ADDPEP (Aerodynamic Deployable Decelerator Performance-Evaluation Program) is to establish the configuration, loadings, design, and structural materials for an ascending 400-lb payload, for an application domain ranging from Mach 2.7 at 73,000 ft to Mach 10 at 210,000 ft, and for dynamic pressures to 500 psf. The textile BALLUTE (TB) decelerator effort discussed in this section encompasses work involving TB-1, TB-1A, TB-1B, TB-2, TB-3, TB-4, TB-5, and TB-6.

Textile BALLUTES TB-1, TB-1A, TB-1B, and TB-2 were designed and fabricated during ADDPEP Phase I (described in Reference 1, Technical Report AFFDL-TR-65-27). The TB-3, TB-4, TB-5, and TB-6 test items were designed and fabricated during Phase II. A Phase II attempt to deploy TB-1 was unsuccessful. However, TB-1A, TB-1B, TB-2, TB-3, and TB-4 were deployed and performance-evaluated during Phase II.

The design, fabrication, and free-flight tests of BALLUTES were investigated in Mach number increments to Mach 9.7. Problems involving inlet basic design and location were resolved and proved by data obtained from wind-tunnel and free-flight tests. Excellent results were obtained in investigating the use of liquids to cool Nomex BALLUTES so as to extend their performance capability.

b. Test Point Conditions

The anticipated test environment was established by trajectory analysis within the capabilities of the test BALLUTES and the test vehicle/booster combinations (see Figures 1 and 2, Section II). Each trajectory considered the aerodynamic, thermodynamic, and structural flight environment required for validation of theoretical design techniques and for comparison with wind-tunnel test data. The desired initial deployment conditions to be achieved by Test Vehicle C and its booster combinations are presented in Table XVII. The parameters after deployment are shown in Figures 37, 38, and 39.

c. BALLUTE Configurations

During ADDPEP Phase I, two textile BALLUTE shapes, TB-1 and TB-2, were generated based on the results of wind-tunnel tests and isotensoid requirements. The basic shapes of TB-1 and TB-2 are described and defined in Section IV of Reference 1, the ADDPEP Phase I report. While these basic shapes remained unchanged for Phase II, the inlet and fence geometries and positions were changed for higher Mach number operation. Essentially, the flight test textile BALLUTES have had four different configurations (list starts next page):

TABLE XVII - TEXTILE BALLUTE: DESIGN TEST POINTS BASED ON
PREDICTED TRAJECTORIES

Config- uration	Mach no.	Altitude (ft $\times 10^3$)	Dynamic pressure (psf)	Flight path angle (deg)*	Ballistic coeffi- cient (psf) [†]	Reynolds no. ($\times 10^6$) [‡]	Booster combi- nation [§]
TB-1A	2.40	84	200	70.0	20	2.80	HJ-N
TB-1B	2.78	71	484	70.0	20	5.00	HJ-N
TB-2	3.80	104	197	72.0	30	1.60	HJ-N-N
TB-3	3.70	98	250	73.0	30	2.80	HJ-N-N
TB-4	4.95	200	20	48.5	30	0.08	"
TB-5	6.70	131	200	71.1	30	0.80	HJ-N-L
TB-6	5.66	122	198	75.0	30	0.08	HJ-N-L

* Degrees ascent from horizontal

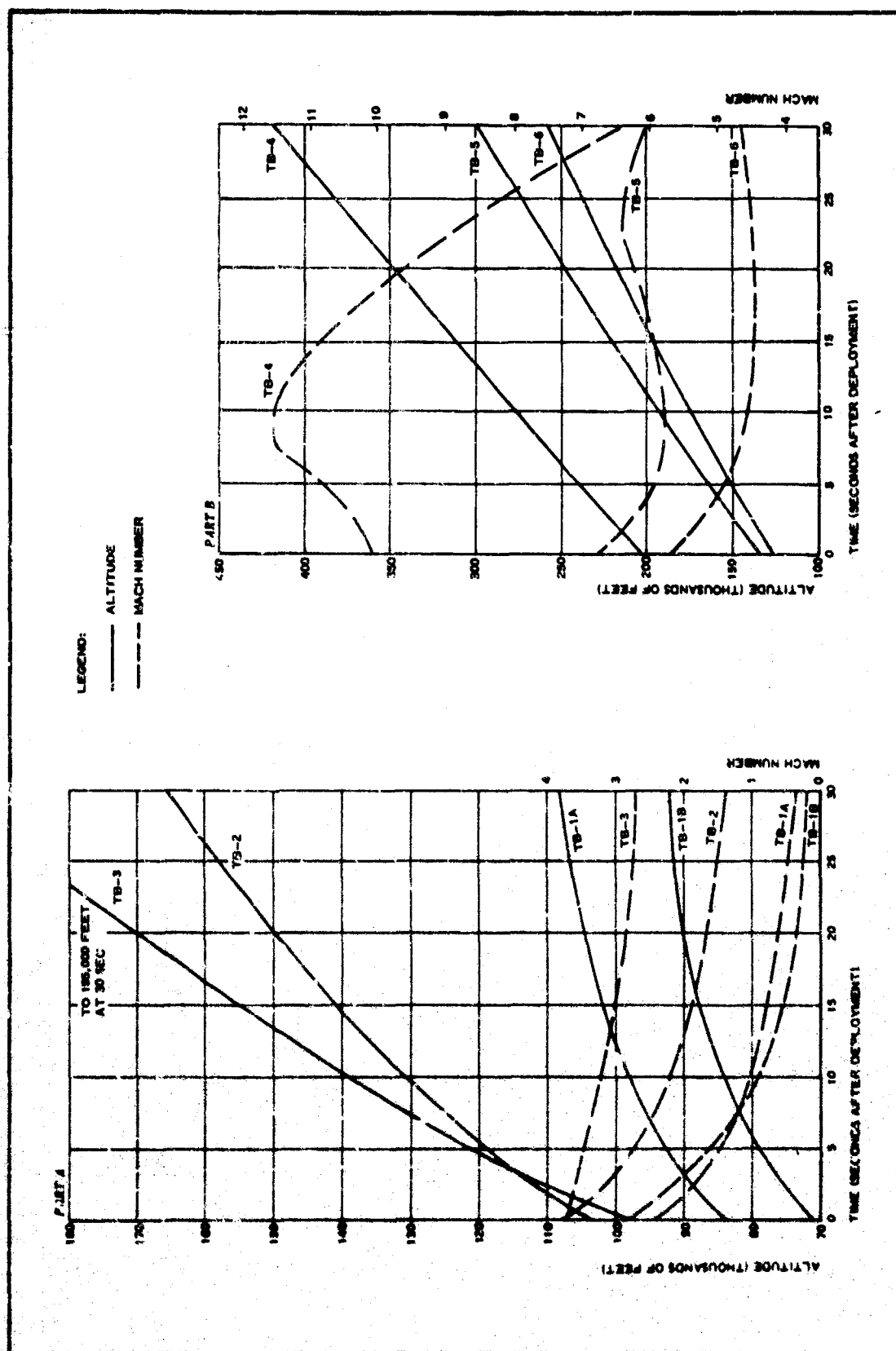
[†] Ballistic coefficient of missile and booster combination

[‡] For Reynolds number, l = five-foot diameter.

[§] Booster definitions: HJ = Honest John; N = Nike; L = Lance.

^{||} XM-33/2XM-19-L.

1. Configuration One - TB-1, TB-1A, TB-1B, and TB-1WT - is a five-foot nylon BALLUTE with a fence that increases its projected diameter, (see Figure 40A). The dimensions are detailed in Figure 82 of Reference 1. A modification of TB-1 was made for wind tunnel tests; the dimensions for this item, designated TB-1WT, are shown later in this section (Figure 51D).
2. Configuration Two - TB-2 - is described in References 1 and 40 and is shown in Figure 40B. It was designed for higher Mach numbers than the configuration one series. The inlets were located further aft than for TB-1 in an attempt to reduce the values of the inlet pressure and, thus, strength and weight requirements. To accomplish the inlet location change, the burble fence was removed rearward. Also the size was reduced to prevent the fence from affecting flow approaching the inlets. The B-2
(list continues page 91)



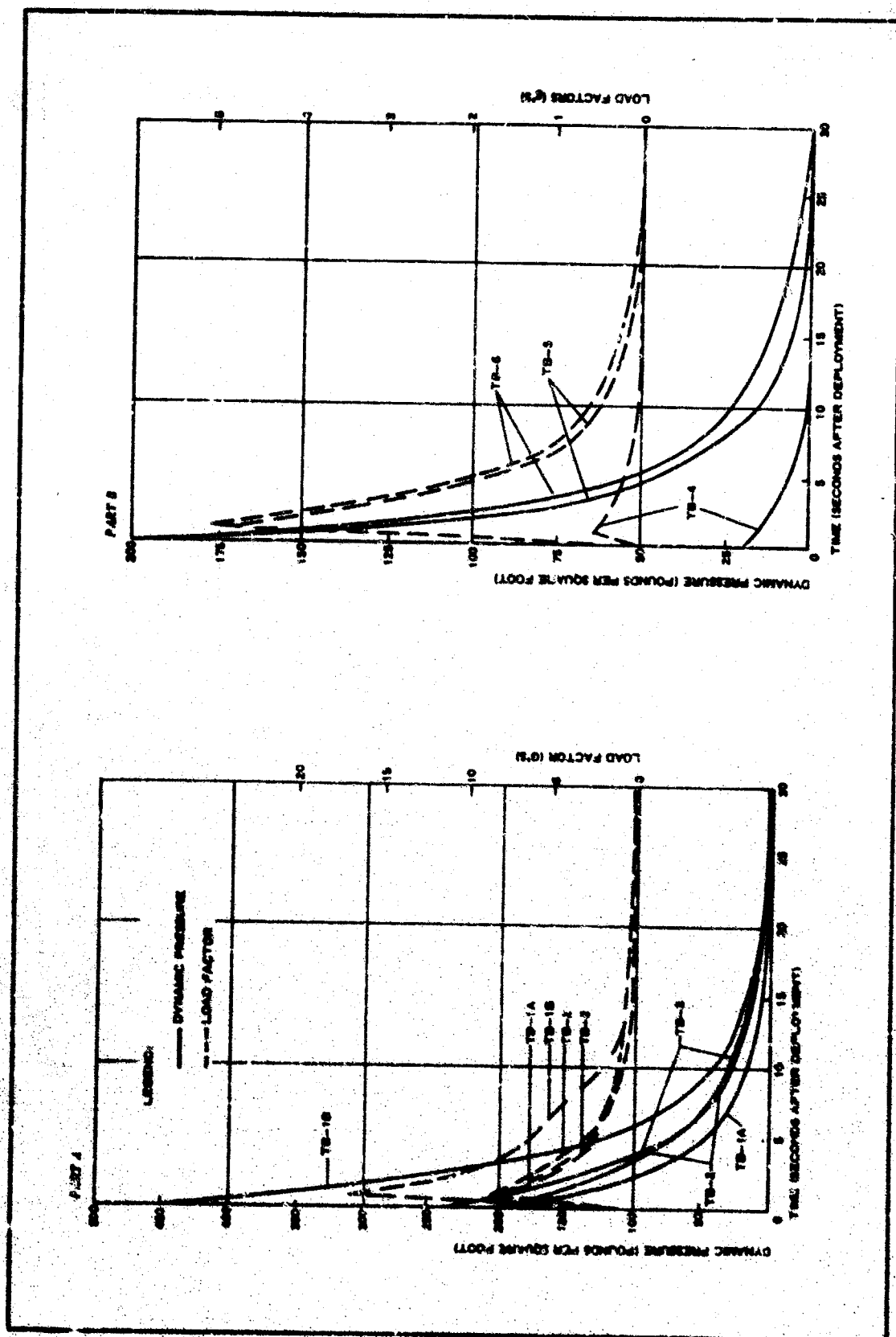


Figure 38 - Textile BALLUTES: Dynamic Pressure and Load Factor versus Time (Predicted for Design)

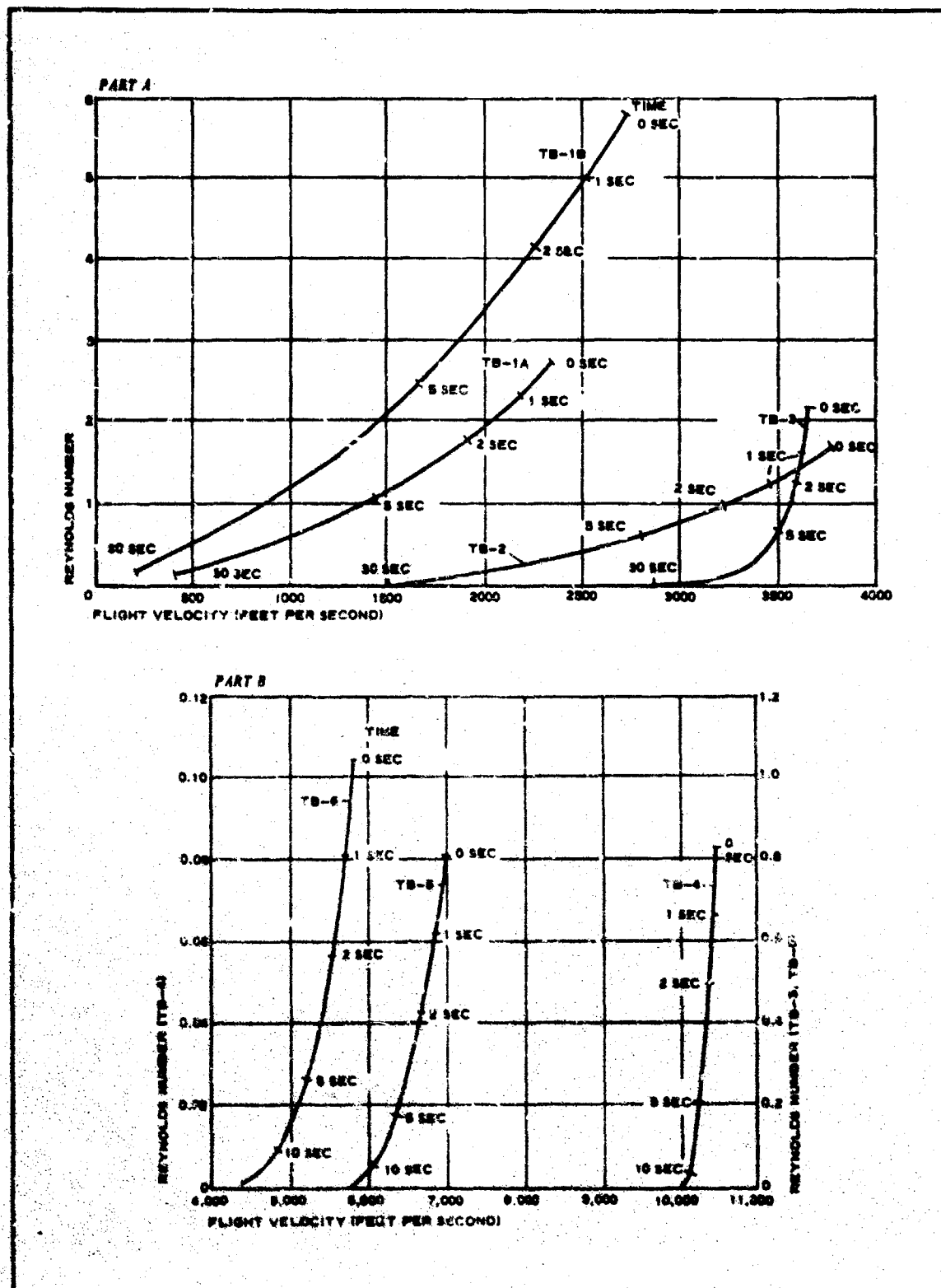
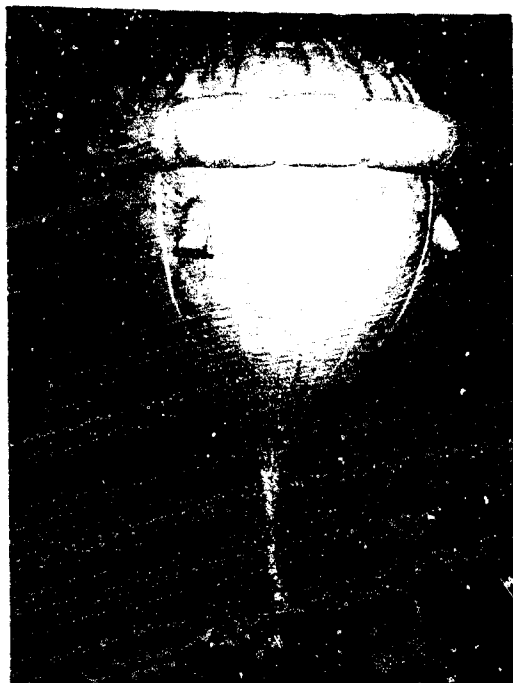


Figure 39 - Textile BALLUTE: Reynolds Number versus Free-Flight Velocity (Predicted for Design)



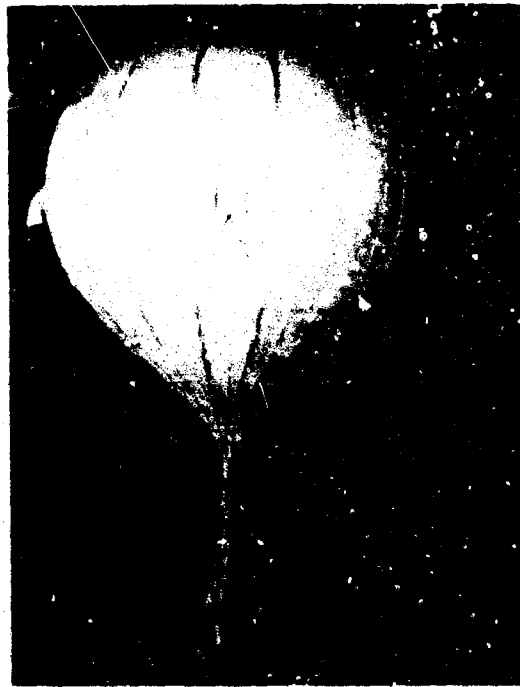
(A) TB-1A



(B) TB-2



(C) TB-3



(D) TB-4

Figure 40 - Textile BALLUTE Decelerators

Nomex BALLUTE has a five-foot diameter and a fence that does not increase its projected diameter. Dimensions are presented later in this section (Figure 51A).

3. Configuration Three - TB-3, TB-3WT - is a five-foot diameter BALLUTE without a fence (described in Reference 41 and shown in Figure 40C). It was generated during Phase II to represent the configuration of the metal BALLUTE designs. The TB-3 configuration resembles TB-2 except that the burble fence is removed and a liquid pressurizing system is added for attaining initial shape. Two Nomex test items were fabricated to the TB-3 design: the first, a modification of TB-2 for wind-tunnel testing, was designated TB-3WT; and the second was a new TB-3 free-flight test unit. The TB-3 and TB-3WT dimensions are presented later in this section (Figures 51B and 51E).
4. Configuration Four - TB-4, TB-5, TB-6, and TB-4WT - is a five-foot diameter BALLUTE without a fence (described in Reference 42 and shown in Figure 40D). It was generated during Phase II to validate inlet frame and location design changes from TB-3 and the liquid initial pressurizing system. Four Nomex test items were generated to the Configuration Four design: the first, TB-4WT, was a modification of TB-3; and the other three were new flight test items. Dimensions are presented later in this section (Figure 51C).

2. WIND-TUNNEL AND FREE-FLIGHT TESTS

a. General

The wind-tunnel and free-flight tests of BALLUTE decelerators supported three basic disciplines: aerodynamics, thermodynamics, and structures. These tests were used to obtain decelerator performance data to validate the design of a specific decelerator.

b. Wind-Tunnel Tests

(1) TB-3WT

The TB-3WT wind-tunnel test model was created by modification of recovered flight test item TB-2 (Reference 43). The burble fence was removed and one set of inlets was made taller and relocated to the rear. Pressure tubes were installed in each inlet and in the envelope to measure inlet pressure recovery and envelope flow losses. The objective of the wind-tunnel test was to obtain data for the final design of TB-3.

Item TB-3WT was tested at the Arnold Engineering Development Center (AEDC) on 21 December 1964. Deployment was at Mach 3.0 and a q of

120 psf (Reference 44). Observation of the test and analysis of the data indicated that the BALLUTE inflated fully and had a final internal pressure coefficient of approximately 3.74. Observations also indicated that the lower set of inlets was fully erected and that the taller set of inlets was not completely erected. The wire used for the inlets and springs was piano wire for the shorter set and work hardened stainless steel for the taller set. Steady state drag measured 1620 lb. Wind-tunnel data were reflected in the approval package for TB-3 (Reference 41).

(2) TB-1BWT and TB-4WT

The inlet frame failures and resulting softness of TB-2 and TB-3 during flight test indicated a low probability of full inflation for TB-4, TB-5, and TB-6 unless the inlet structural design was improved. Therefore, it was desirable to prove the structural capability of the new inlet design. Two BALLUTES, recovered from previous flights, were modified to investigate this factor and other design changes including liquid partial inflation under wind-tunnel conditions.

Recovered flight test item TB-1B, a 60-in. BALLUTE with fence, was modified by incorporating the TB-4 inlets and liquid inflation-aid system; it was designated TB-1BWT. Item TB-3, a 60-in. BALLUTE without a fence, was modified by incorporating the TB-4 inlets and liquid inflation-aid system; it was designated TB-4WT.

The TB-1BWT and TB-4WT BALLUTES were tested at AEDC in May 1966, with excellent results. The test parameters and results are documented in Reference 45. Deployment for both decelerators was at Mach 2.8 and at a 120-psf dynamic pressure. Item TB-1BWT attained full inflation in approximately 0.77 sec after full line stretch. Figure 41A plots drag force and internal pressure coefficient versus time. Item TB-4WT attained full inflation in 0.69 sec after full line stretch and had excellent stability. Figure 41B plots the drag force versus time. The performance of both wind-tunnel models was excellent, with no sign of construction failures.

c. Free-Flight Tests

(1) General

Free-flight tests of BALLUTE decelerators were made with Test Vehicle C and various booster combinations. Table XVIII summarizes key conditions for each decelerator. The deployment details of each flight test are presented in a flight summary manner.

(2) TB-1A

The objective of the TB-1A flight test was to demonstrate the accuracy of the analytical design for a neoprene-coated nylon BALLUTE decelerator. A design factor was chosen for a test point dynamic pressure of twice the predicted nominal value for this first BALLUTE test.

BALLUTE TB-1A was flight tested on 8 June 1964 (References 46, 47). All flight events occurred as programmed. The test item was deployed

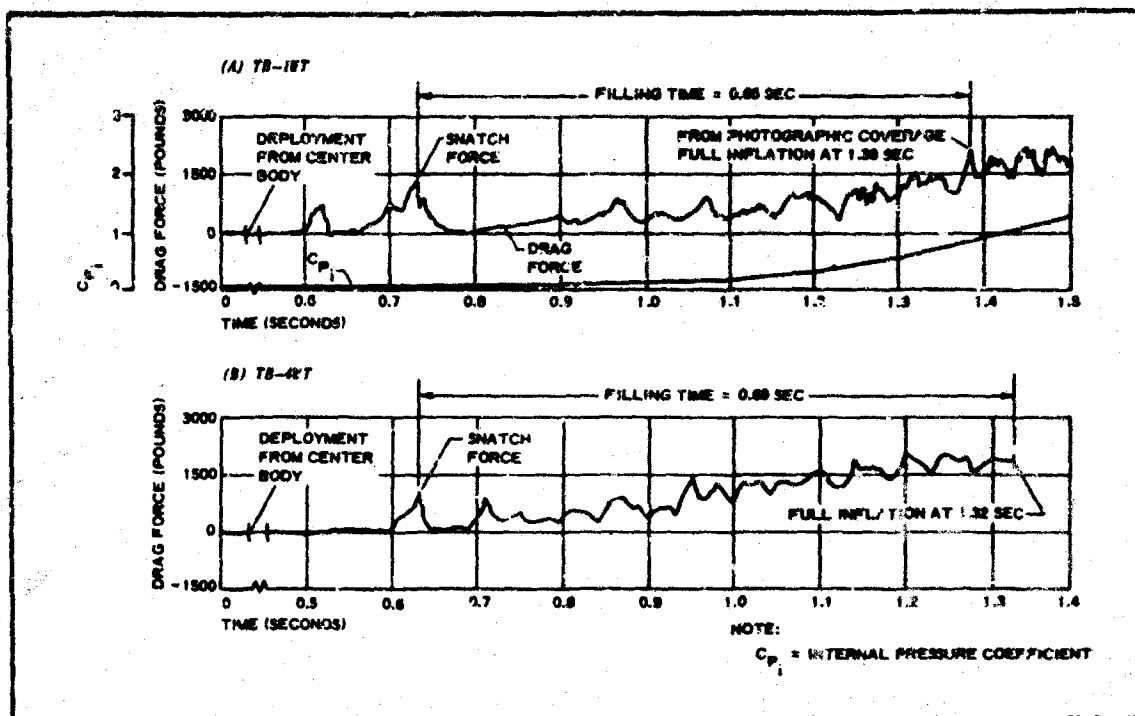


Figure 41 - Wind-Tunnel Deployment Characteristics:
(A) TB-1BWT; (B) TB-4WT

satisfactorily at design conditions and at dynamic pressure (q) test loading of 270 psf. The decelerator inflated and performed as anticipated. However, as a result of vehicle telemetering system failure, the shock, drag, acceleration, static pressure, and dynamic pressure portions of the telemetering data were not provided after TB-1A deployment.

The Air Proving Ground Center (APGC) supplied radar plots and digitized computed data. Test vehicle onboard camera film footage were used as a basis for computing decelerator performance characteristics relative to Mach number, dynamic pressure, altitude, and acceleration. The inflation time of TB-1A, as calculated from film observation, was 1.06 sec after line stretch.

Figure 42 shows the performance curves of TB-1A beginning at container separation for 30 sec. Information for the performance curves was obtained from the APGC-supplied digitized data, which are records of the vehicle telemetry and ground tracking radar outputs (References 3, 46, 47). The test results established the stability, deployment and inflation characteristics of the BALLUTE system. An inspection of the test item after recovery, as well as data films, indicated that no heating or structural damage occurred under the load. Also, no evidence of seam raking could be found.

SECTION IV - TEXTILE BALLUTE DECELERATOR

AFFDL-TR-67-25

TABLE XVIII - TEXTILE BALLUTES: SUMMARY OF TEST CONDITIONS

Test item	Event	Range time (hr:min:sec)	Load (10 ³ lb)	Mach no.	Dynamic pressure (psf)	Altitude (10 ³ lb)
TB-1A: 5-ft nylon with 10-percent fence	Test item container separation	13:54:35.00	. . .	2.50	270.0	84.0
	Initial line stretch	13:54:36.29	1.75	2.30	230.0	86.0
	Maximum load	13:54:37.35	3.96	2.10	160.0	87.5
TB-1B: 5-ft nylon with 10-percent fence	Test item container separation	14:30:32.68	. . .	2.20	355.0	75.0
	Initial line stretch	14:30:33.08	1.70	2.10	330.0	75.5
	Maximum load	14:30:34.18	5.10	1.88	215.0	77.5
TB-2: 5-ft Nomex with fence, zero projected area	Test item container separation	18:39:34.05	. . .	3.25	248.0	96.0
	Initial line stretch	18:39:34.32	0.70	3.20	230.0	97.0
	Maximum load	18:39:35.00	2.05*	3.12	196.0	99.0
TB-3: 5-ft Nomex with no fence	Test item container separation	15:17:33.30	. . .	4.05	287.0	100.0
	Initial line stretch	15:17:33.62	3.0	4.12	284.0	101.0
	Maximum load	15:17:33.81	3.4*	4.13	279.0	102.0
TB-4: 5-ft Nomex with no fence	Test item container separation	15:00:56.2	. . .	9.70	9.2	227.0
	Initial line stretch	15:00:56.14	1.2	9.75	8.3	230.0
	Maximum load					
TB-5 and TB-6: 5-ft Nomex with no fence		Not flight tested				

* Test item not fully inflated.

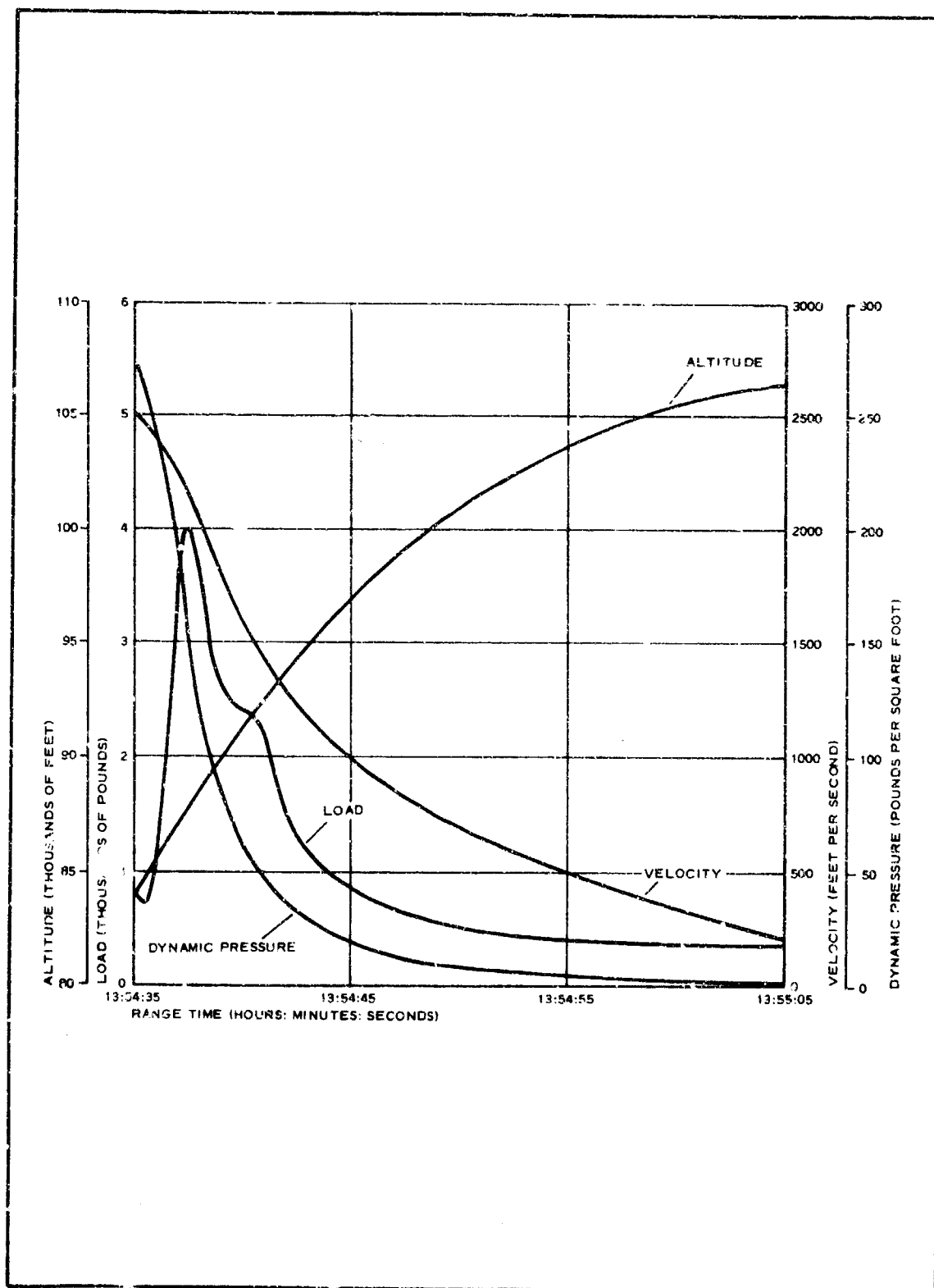


Figure 42 - TB-1A Performance

(3) TB-1B

The objective of the TB-1B flight test was to demonstrate the analytical design of a high-pressure, high-temperature Polyurethane CUR71A-coated nylon BALLUTE decelerator. The overload design factors were reduced to increase the probability of obtaining data relative to the imposed loading for comparison with TB-1A free-flight, wind-tunnel, and TB-1B design calculations.

BALLUTE TB-1B was flight-tested on 29 July 1964 (Reference 48). All flight events occurred as programmed. The test item was deployed satisfactorily near the design conditions at a 355-psf dynamic pressure (q). Both onboard cameras provided complete coverage of the test item during and after the inflation period. Deployment, inflation, and stability of TB-1B was shown to be very good. Inflation required approximately 1.1 sec for completion. A sound telemetry signal was obtained, and recording provided complete information for data reduction.

Figure 43 shows the performance curves of TB-1B beginning at container separation for 30 sec. The data from which the plots were formed were taken directly from the APGC-supplied digitized output sheets, which were records of the telemetry and radar outputs. The decelerator was recovered in excellent condition.

(4) TB-2

The objectives of the TB-2 test were to obtain data to evaluate the validity of the design methods for a BALLUTE at a high Mach number and at aerodynamic heating conditions compatible with Silastic 131-coated Nomex materials. Data were also required for the results of a change in inlet location incorporated into the TB-2 design to limit the internal pressure to a more optimum value.

BALLUTE TB-2 was flight-tested on 17 August 1964 (Reference 49). Radar data indicated that the trajectory up to the test point was very close to the predicted flight path even though all events occurred about three seconds early. The test item was deployed satisfactorily at a 248-psf dynamic pressure (q). Both onboard cameras functioned very well and provided excellent coverage of the BALLUTE's performance. Telemetry performance was satisfactory, although decelerator internal pressure data were not obtained due to a faulty transducer.

Examination of onboard camera film-footage indicated that the BALLUTE never inflated fully. Inspection of the fabric after the tests indicated (1) the coating had changed state under the test environment and (2) the material porosity increased beyond acceptable limits. Investigations of the coating indicated it had not been cured completely prior to the test. Methods were established in conjunction with the manufacturer to assure obtaining a cure with higher reliability. These included more exact environmental control than originally indicated and the addition of a chemical wash.

Figure 44 shows the performance curves of TB-2 beginning at container separation for 30 sec. The data from which the plots were formed were

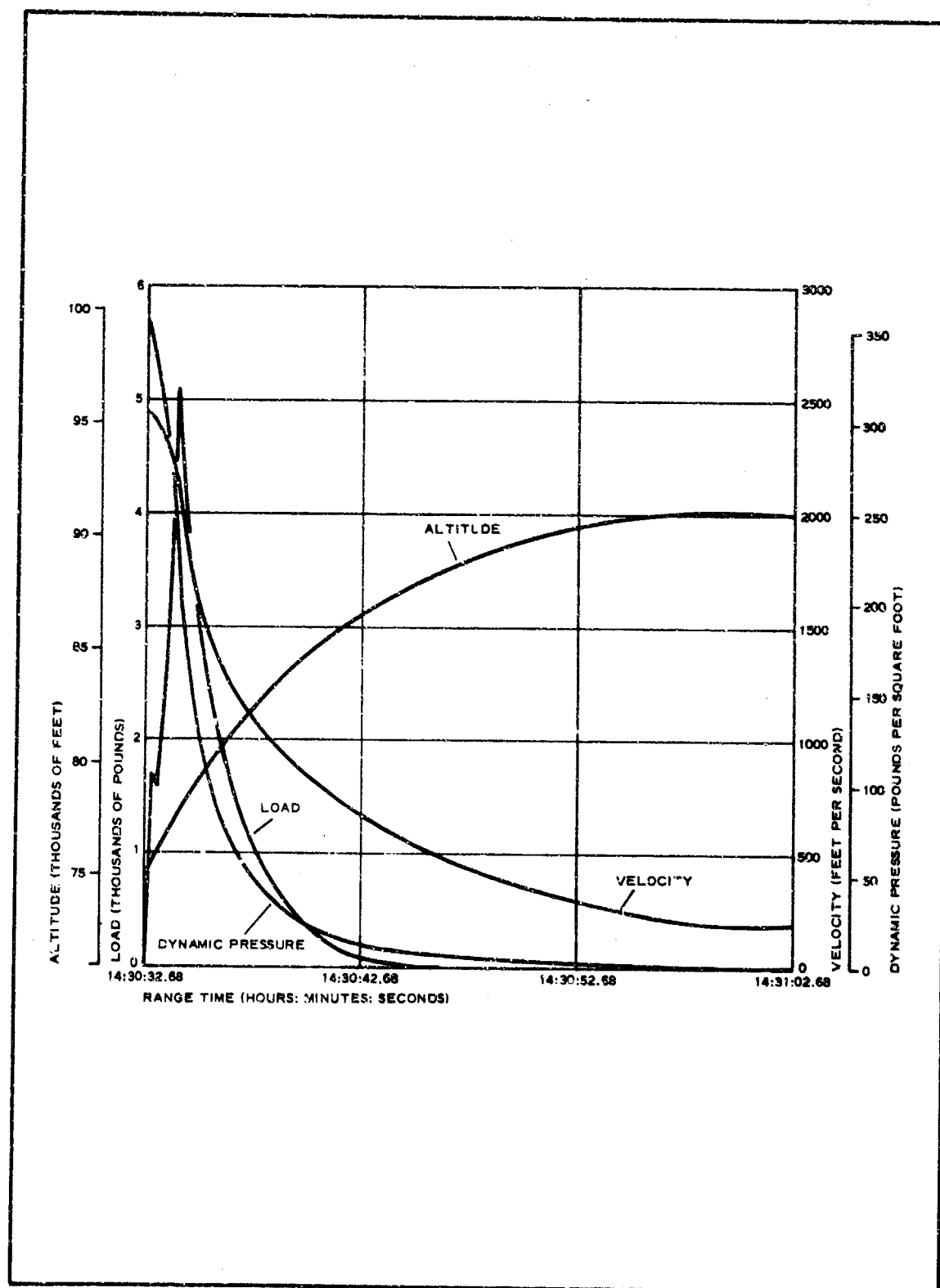


Figure 43 - TB-1B Performance

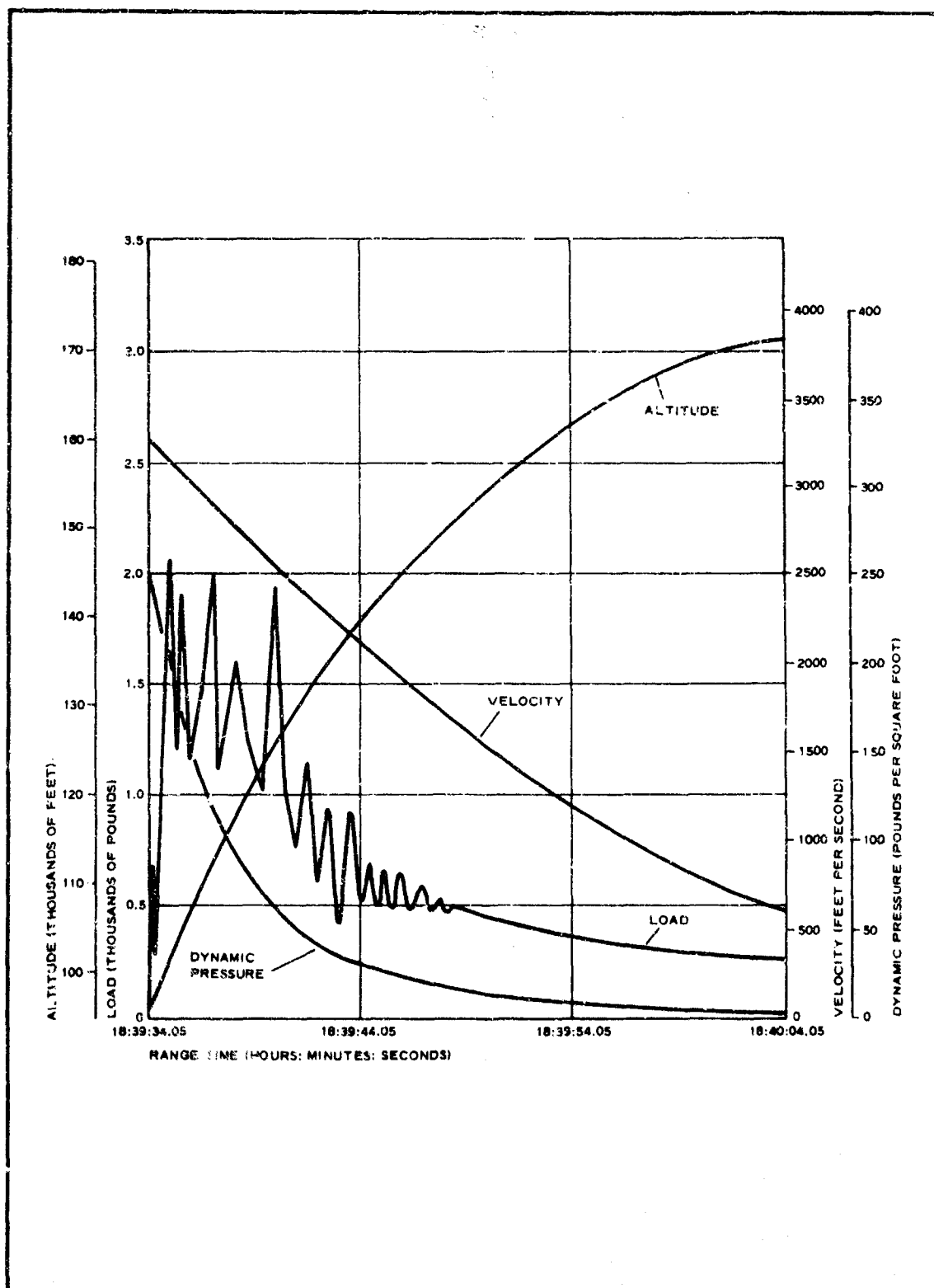


Figure 44 - TB-2 Performance

taken from the APGD-supplied digitized output sheets, which were records of telemetry and radar outputs. The decelerator was recovered in excellent condition.

(5) TB-3

The main objective of the TB-3 flight test was to obtain data for the technique for early envelope pressurization by means of a low vapor pressure liquid approach. The BALLUTE was fabricated from Nomex materials and coated with Silastic 131 elastomer.

BALLUTE TB-3 was flight-tested on 18 June 1965 (Reference 50). All flight events occurred as programmed. The BALLUTE was deployed satisfactorily near the test conditions at a 287-psf dynamic pressure (q). Both onboard cameras provided excellent coverage of the BALLUTE's performance before and after the inflation period.

Telemetry performance was satisfactory, although static and differential pressure data were not obtained. Examination of the onboard camera film-footage indicated that the early pressurization technique functioned properly and provided the initial inflation to one-third to one-half size. However, based on the onboard films, failure of the metal inlet frames began approximately one-fourth of a second after line stretch, and all the metal frames were failed within one-half second after line stretch. The BALLUTE configuration remained in this partially inflated shape. The forward portion of the metal frames and the first gore of the inlet fabric were lost within two to five seconds after deployment. Postflight inspection revealed that the gore fabric seams and webbing were undamaged; there was no evidence of heating. Examination of the inlets indicated gross failure of the metal inlet springs and frames. Examination of the coating indicated it performed satisfactorily.

Figure 45 shows the performance curves of TB-3 beginning at container separation for a 30-second period.

(6) TB-4

The main objective of the TB-4 flight test was to obtain thermodynamic and aerodynamic data for a textile BALLUTE at hypersonic speeds. The BALLUTE was made of Nomex materials and coated with Dyna-Therm D-65 elastomer. Partial inflation/cooling aids were incorporated to determine their effects in cooling textiles and in aiding the inflation of the metal BALLUTES.

BALLUTE TB-4 was flight tested on 22 August 1966 (Reference 51). All decelerator test events occurred as programmed. The BALLUTE was deployed near the test conditions, at a 9.2-psf dynamic pressure (q). Telemetry performance was excellent over the long flight path. Strain gage drag data and BALLUTE internal pressures were not obtained. Telemetry data covered not only the exiting test point as anticipated, but also the re-entry flight down to 30,000 ft. Since the test vehicle was not located, the onboard camera films were not recovered. BALLUTE temperature data for the complete flight were obtained from thermocouples woven into the BALLUTE gore material.

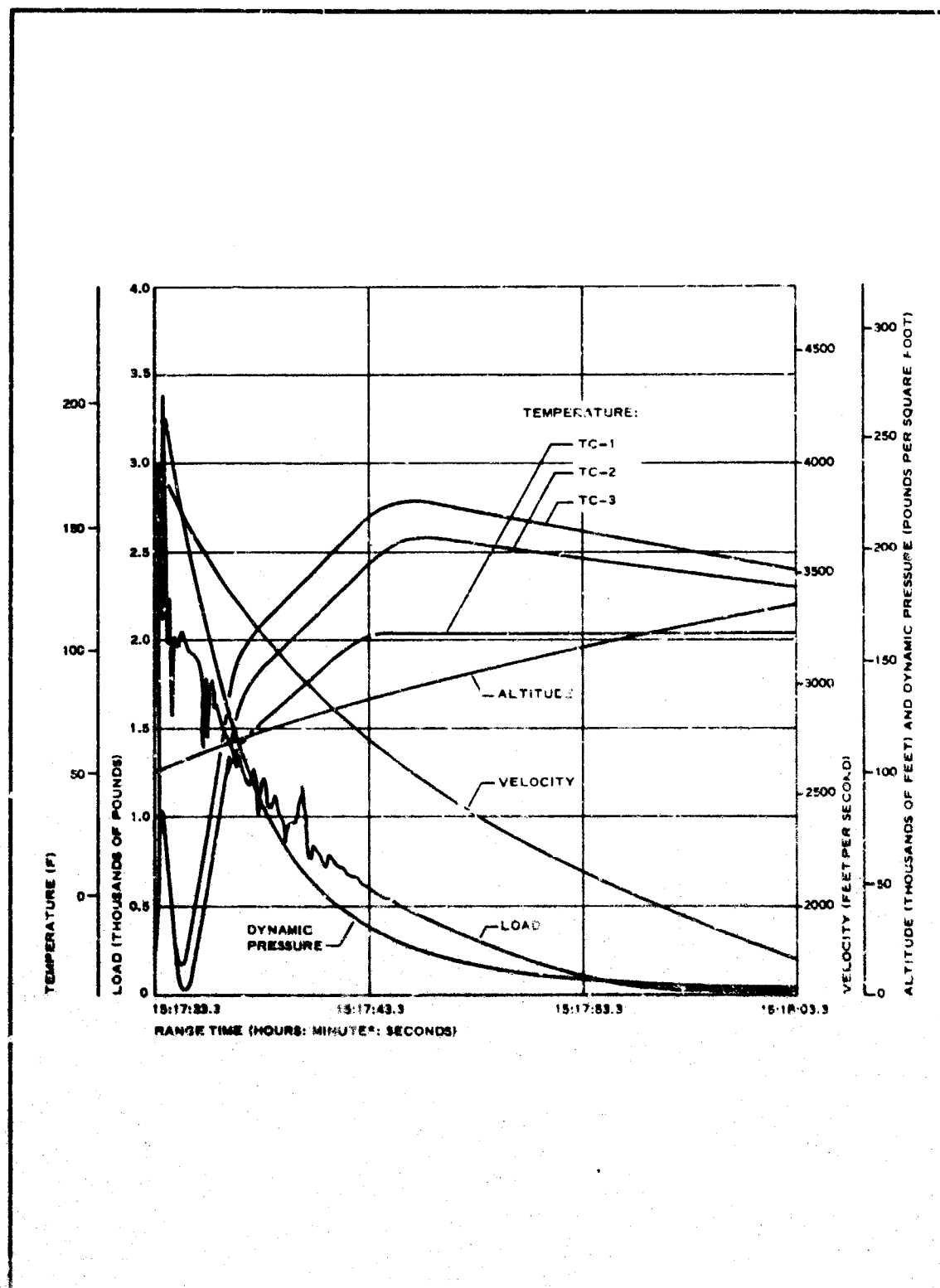


Figure 45 - TB-3 Performance

Figure 46 shows the performance curves of TB-4 beginning at container separation and later at re-entry. The re-entry trajectory parameters are based on vehicle static pressure readings (two different transducers).

(7) TB-5 and TB-6

The TB-5 and TB-6 units are available for flight testing.

(8) Free-Flight Test Summary

One of the most useful parameters for design is $C_D A$ (drag area) versus Mach number (see Figure 47). The values of this parameter are affected by the relative accuracy of the load readings and the predicted ambient pressures as the vehicle ascends. The load readings become a smaller percent of full scale, and the percent of ambient pressure variation increases with altitude. Because of these factors, the values are accurate near the test point and become less accurate with increasing altitude, which corresponds to decreasing Mach number for any given curve in Figure 47. This can account for a portion of the apparent large changes in values with decreasing Mach number along a given curve.

BALLUTES TB-1A and TB-1B are identical configurations that were fully inflated to very firm shapes. The flight conditions near Mach 1.6 for both units are above a Reynolds number of one million and only approach a half million below Mach 1. It is anticipated that these data should correspond. The lower values for TB-2 and TB-3 are due to two factors: (1) the zero projected area of the fence on TB-2 and the lack of a fence on TB-3, and (2) the lack of complete inflation of either unit. The corresponding drag and projected area ratios are presented in Figure 47 for reference.

3. AERODYNAMIC ANALYSIS

a. General

The aerodynamic analysis supports the design of the BALLUTE by estimating the (1) shape required for aerodynamic stability, (2) external pressures over the body, (3) inlet pressures, and (4) air-flow rates through the inlet. The values of these parameters are used in determining BALLUTE aerodynamic performance, the shape and stresses of an isotenoid-pressurized membrane structure, and the local-flow conditions over the BALLUTE surface for thermodynamic calculations.

In the ADDPEP Phase I report (Reference 1), both analytical and empirical methods are presented for determining the values of these aerodynamic parameters and establishing shapes of minimum weight membrane structures. During Phase II, these methods were used to determine the values of the aerodynamic parameters at higher performance deployment conditions and for other inlet and fence locations.

b. BALLUTE Shape Required for Aerodynamic Stability

The BALLUTE shape selected was based on the results of wind-tunnel tests at supersonic velocities and isotenoid requirements (Reference 52).

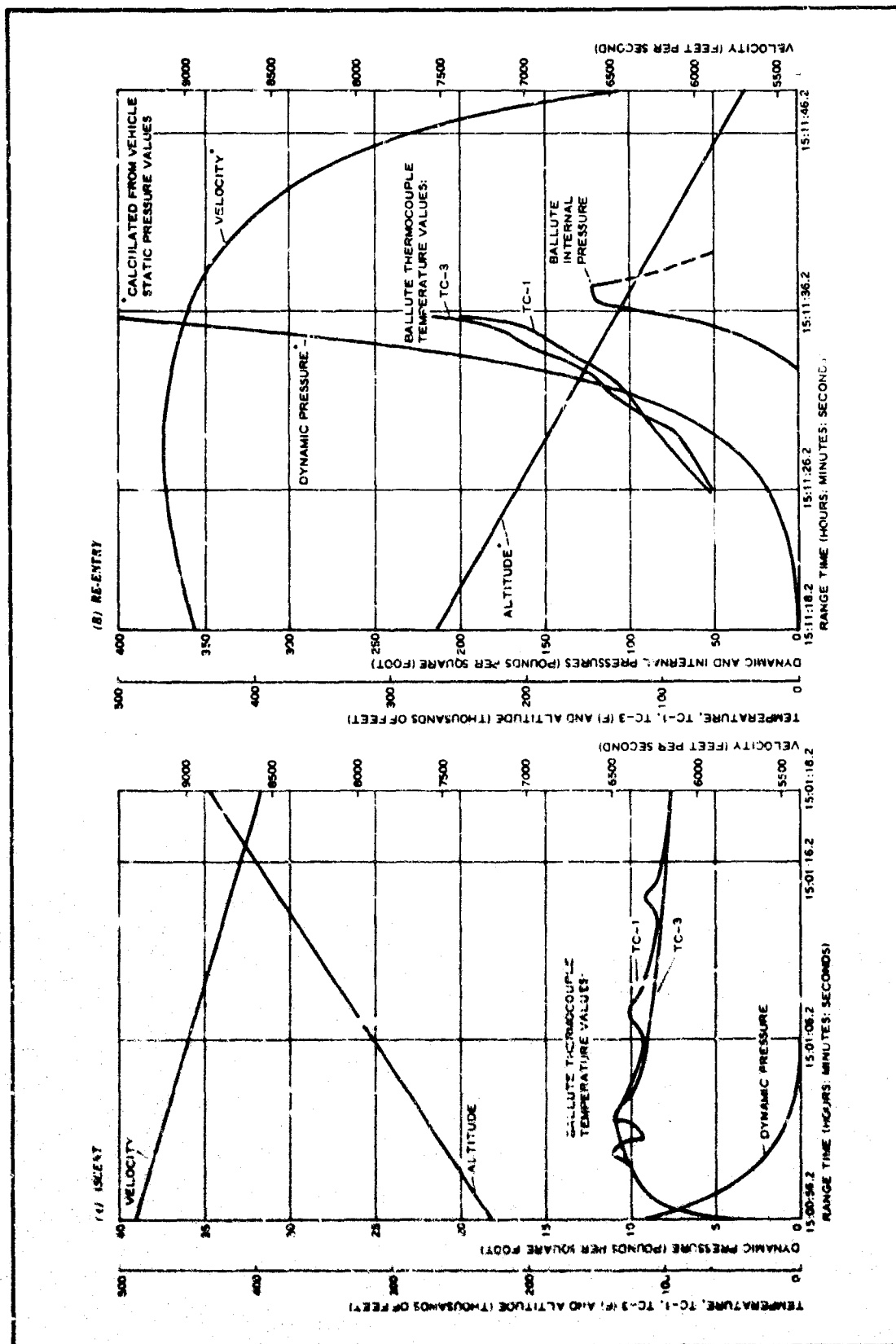


Figure 46 - TB-4 Performance

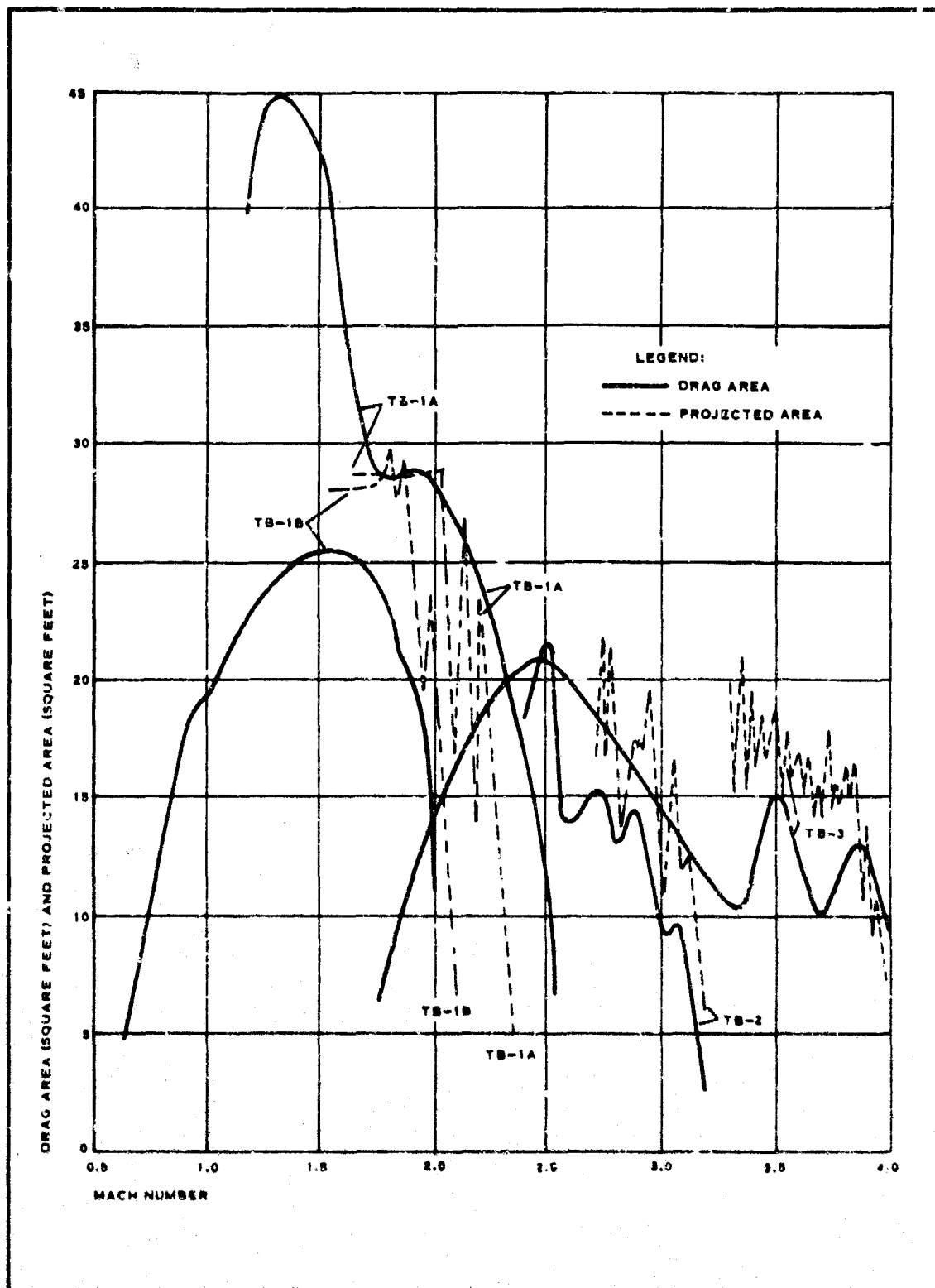


Figure 47 - BALLUTE Flight Tests: Drag and Projected Areas versus Mach Number

Additional data from RTD wind-tunnel tests conducted at AEDC and ADDPEP free-flight tests confirmed the high degree of aerodynamic stability obtained with this family of decelerators (References 13, 45, 53). The Gemini, ALARR, and PRIME programs have also established the high-degree of BALLUTE stability (References 54, 55, 56).

c. Pressure Distributions

The static pressure estimates over a BALLUTE are used for estimating the drag and, in conjunction with the internal pressure, the envelope shape and stresses. Analytical approaches and test data for estimating surface pressure and inlet pressures are presented in Reference 1. Comparisons of estimated surface pressure coefficients (C_p) using analytical and testing methods are presented in Figures 48A and B for higher Mach number conditions than presented in Reference 1. (Figures 48A and B are based partially on wind-tunnel data from References 52 and 57). Forebody wake effects indicated on the first part of the curves are based on empirical data.

Inlet locations were investigated in greater detail to establish approaches for reducing the inlet pressure coefficients of trailing BALLUTES at flight Mach numbers greater than two. Early wind-tunnel test data presented in References 13 and 54 indicated that, for a wide range of inlet sizes and locations, inlet pressures exceed the values required for a stable structural shape. The inlet pressure coefficient values for specific inlets on these hard models varied at a given free-flight Mach number; however, somewhere within the test Mach number range of between 3.5 and 6, the inlet pressure coefficient value for each inlet tested became almost twice that required. The height and the height-to-width ratio varied between inlets; however, all inlets had a semicircular top with parallel sides tangent to the top and perpendicular to the BALLUTE's surface.

Postulations for the higher than anticipated inlet pressure coefficient values, approximately twice the values measured without a forebody, included:

1. The forebody shock waves decelerate the flow approaching the inlets efficiently, thus reducing the Mach number and the total head loss across an inlet bow shock.
2. The thicker boundary layer over the BALLUTE, due to the forebody wake, provides a better path for transmitting inlet pressures forward, causing an efficient oblique shock system to form forward of each inlet.
3. The fence pressures feed forward in the thicker boundary layer and effectively modify the shape of the BALLUTE approaching the fence. This change reduces the amount of flow acceleration following the position of maximum BALLUTE slope and limits the effectiveness of placing the inlets in a more

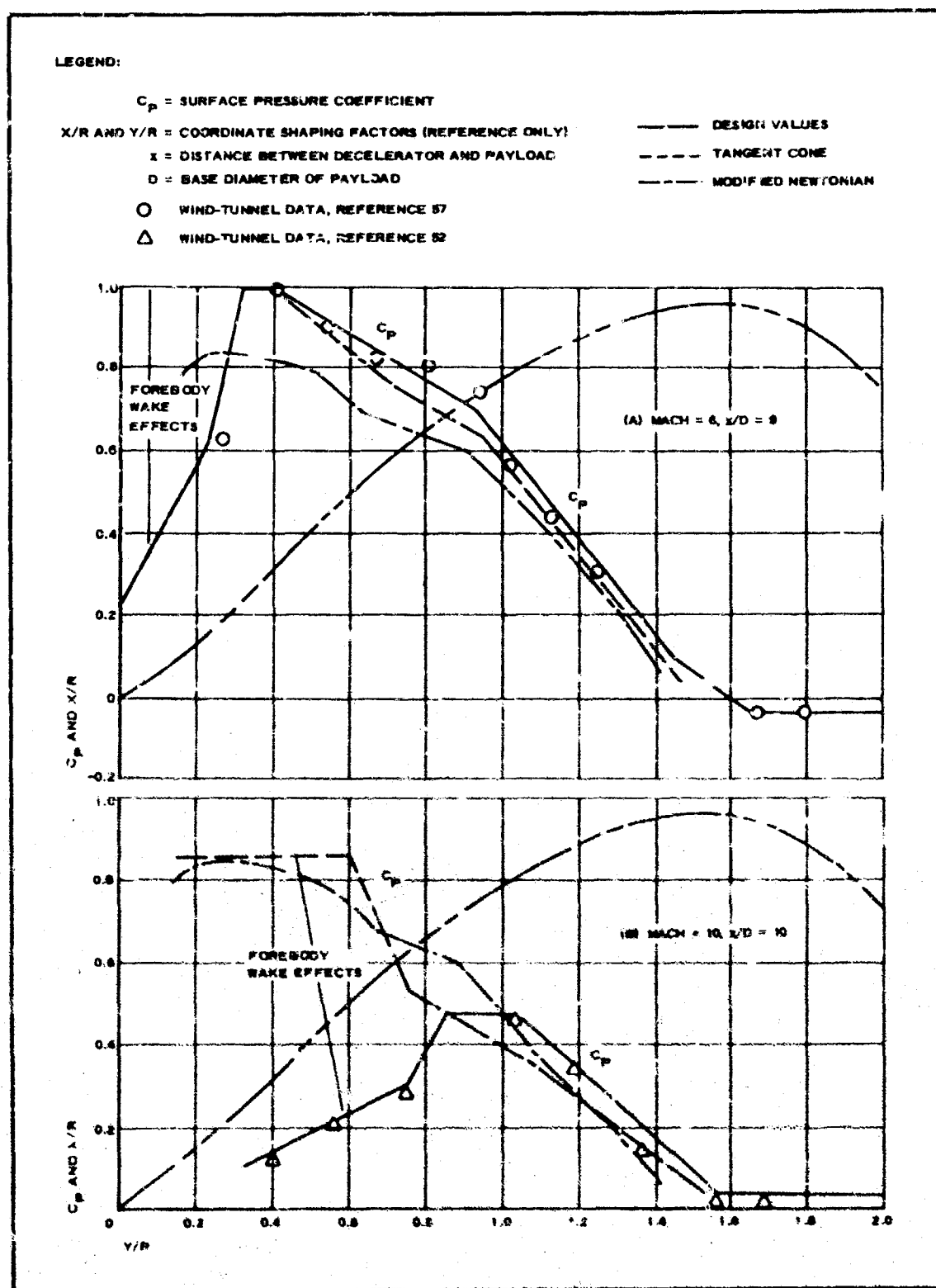


Figure 48 - BALLUTE Surface Pressure Distribution: (A) Mach = 6, $x/D = 9$; (B) Mach = 10, $x/D = 10$

rearward position, where anticipated higher Mach numbers and higher inlet bow shock losses would occur.

In an attempt to reduce the effect of the BALLUTE fence on the flow forward, the fence was reduced in size and moved more rearward in the TB-2 design. Also, the inlets were moved more rearward ($Y/R = 1.572$) and into a position of calculated higher Mach number flow. The inlet mouth was circular following past practices for pressurized structures. Instead of positioning the inlets directly adjacent to the surface as in the hard models, they were positioned $3/4$ of an inch from the surface in an attempt to reduce the inlets' effect on the BALLUTE boundary layer and the flow approaching the inlet.

To further determine the inlets' effect, TB-2 was modified, after flight test, to become TB-3WT for wind-tunnel testing. The fence was removed, and a pair of high inlets with the lower edge two inches from the surface were interchanged with an original pair. Tests in the AEDC facility indicated somewhat less recovery with the high inlets shown in Figure 49 (References 13, 45, 48, 52, 57, 58, 59); however, structural integrity of the high inlets was less than acceptable. There was structural incompatibility between the BALLUTE fabric and the (1) metal inlet frames, (2) metal inlet springs, and (3) gore reinforcement metal frames; this led to eliminating all metal in the BALLUTE except for a flexible cable hoop within the inlet's lips. Top and bottom webs, running forward, were added to the inlet for initial erection of the inlet. Once erected, the pressure within the inlet maintained its structural integrity.

BALLUTES with these inlets were tested for the design of TB-4 in the AEDC facility. Reference 45 presents some of the results. Internal pressures were measured using a single pressure tube into the BALLUTE. Values at Mach 2.8 and at a 120 psf dynamic pressure were 180 psf for the MB-1 metal BALLUTE (see Section V), with rearward positioned inlets; and 218 psf for TB-1B with more forward TB-4 type inlets. Leakage in the pressure-measuring tube prevented determining the pressure within TB-4WT, which had the same inlet type and location as the modified TB-1B. The corresponding C_{p_i} (inlet pressure coefficient) value for MB-1 was:

$$C_{p_i} = \frac{180 - 21.8}{120} = 1.32 \quad (61)$$

For TB-1B as modified, the C_{p_i} value was:

$$C_{p_i} = \frac{218 - 21.8}{120} = 1.64 \quad (62)$$

These values are considerably below either set of the hard model data, the TB-3WT wind-tunnel data, or the TB-1B flight-test data (Figure 49). Inlet locations correspond to the TB-1B flight-test unit. No definite reason can be established for these low C_{p_i} values.

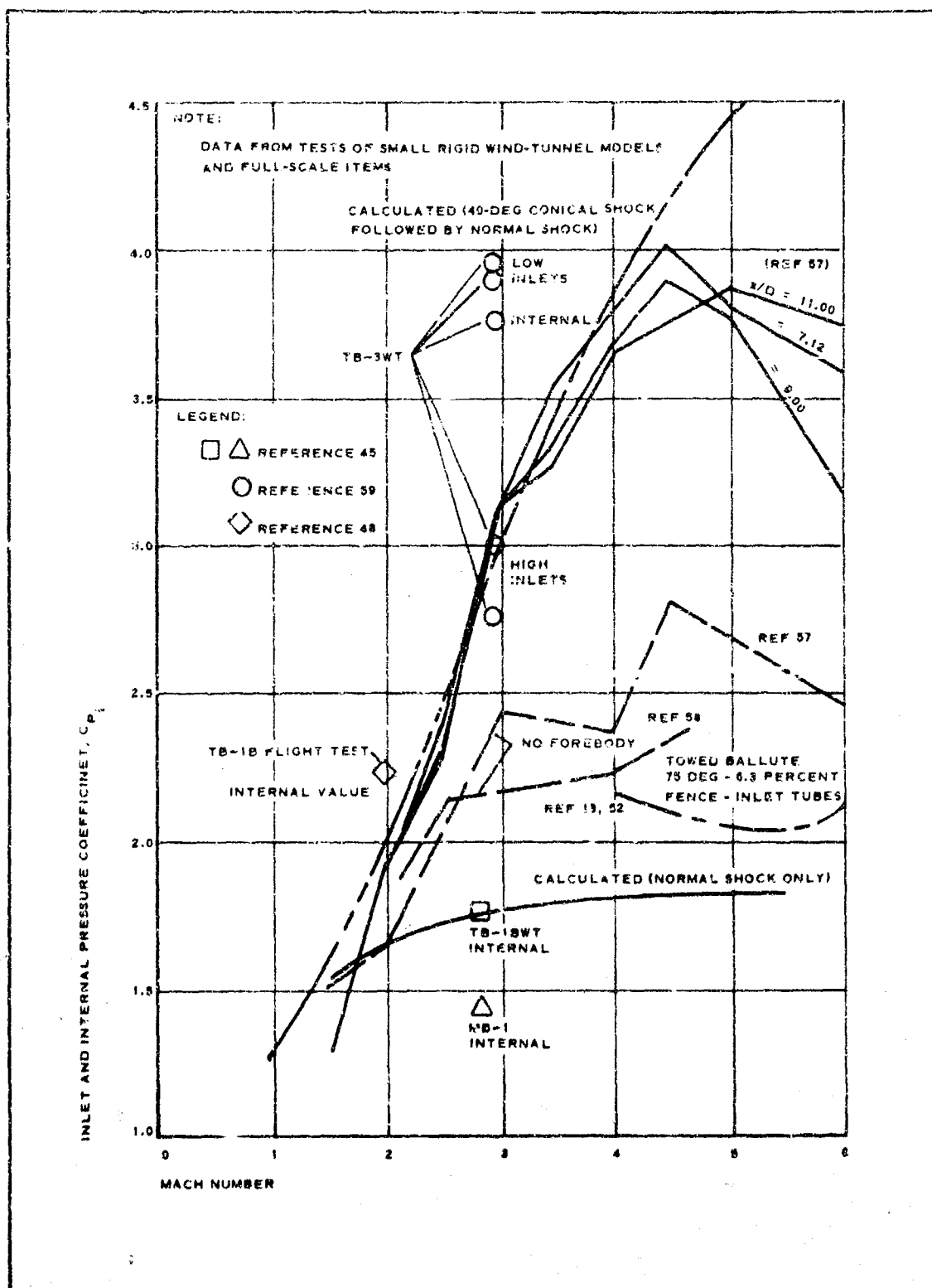


Figure 49 - Textile and Metal BALLUTES: Inlet and Internal Coefficient Pressure Coefficient Data

d. Drag and Filling Times

Drag data were consistent between large scale wind-tunnel tests and flight testing. The drag coefficient (C_D) values are shown in Figure 50 (References 45, 48, 54, 59). The higher set of values are associated with BALLUTEs having a 10-percent fence. All C_D 's were calculated using the envelope diameter for determining the reference areas.

4. BALLUTE GEOMETRY

a. General

During ADDPEP Phase II, two basic configurations were added to the two established in Phase I. All told, two envelope shapes, two fence sizes, two fence locations, and four inlet positions are the variables that make up the four ADDPEP flight-test configurations. These were flight-tested during Phase II. Wind-tunnel models of these and other configurations also were tested during Phase II. The work was done at AEDC by R1D personnel.

b. Flight-Test Units

The Configuration One TB-1, TB-1A, and TB-1B flight-test configurations, having the same envelope shape, fence size, fence location, and inlet location, are described in Figure 82 of the ADDPEP Phase I report (Reference 1). The construction is described in Reference 1 and in Item 8 of this section.

The Configuration Two TB-2 flight-test configuration, having a different envelope shape, fence size, fence location, and inlet location, is shown in Figure 51A.

The Configuration Three TB-3 flight-test configuration, having the same envelope and inlet shape as TB-2, has no fence (see Figure 51B, foldout page 111). Design details are presented in Item 8 of this section.

The Configuration Four TB-4, TB-5, and TB-6 flight-test configurations, having the same envelope shape as TB-2 and TB-3, have no fence and new inlet construction and location, (see Figure 51C). Design details are presented in Item 8 of this section.

c. Wind-Tunnel Units

The TB-1BWT wind-tunnel configuration consists of TB-1B with TB-4 inlets located at the TB-4 position (see Figure 51D).

The TB-3WT wind-tunnel configuration consists of TB-2 with the fence removed and a new pair of high inlets replacing one pair of the original size flight-test inlets (see Figure 51E).

The TB-4WT wind-tunnel configuration consists of TB-3 with all the flight-test inlets removed and four new TB-4 inlets located at the position of TB-4. Its configuration is identical to that of TB-4 (see Figure 51C).

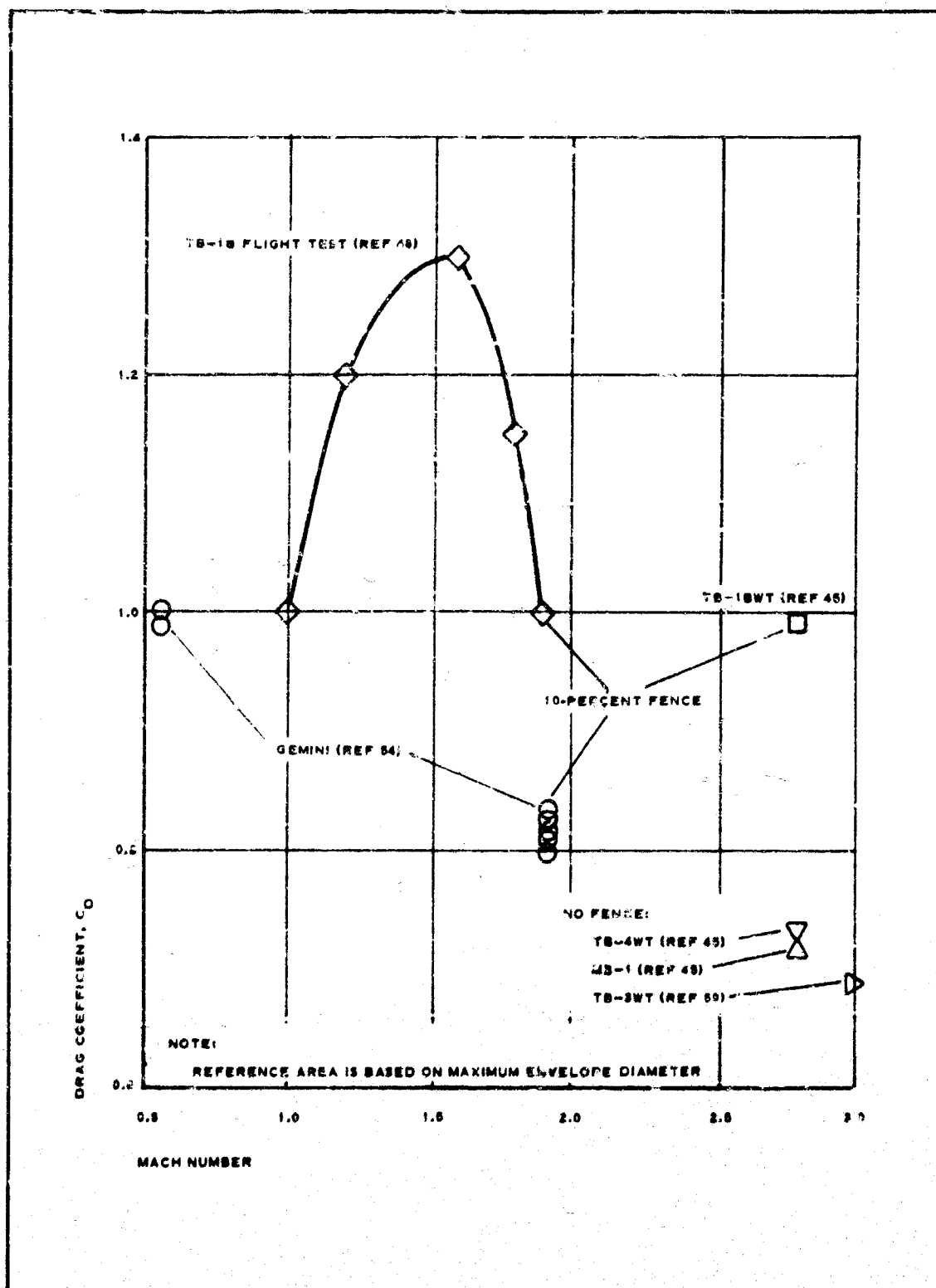


Figure 50 - Textile and Metal BALLUTES: Drag Coefficient versus Mach Number

Deployment of trailing decelerators generally creates two distinct large forces that have been identified as "snatch force" and "opening shock force." Snatch force is the initial force imposed on the test vehicle by the riser in returning the deployed decelerator mass to the same velocity as the vehicle. The opening shock force follows the snatch force and is caused by the sudden inflation of the decelerator to its full shape. The period of time between these two forces is the "filling time."

BALLUTES do not exhibit an opening shock force as such because of the amount of filling time required to inflate the BALLUTE with the small inlets. Inflation times are discussed in Appendices VI and VII of Reference 1. Data are presented in References 45, 54, and 56 for full-scale wind-tunnel tests and in the ADDPEP free-flight tests. Internal pressures greater than required are available with the inlet locations. Hence, the BALLUTE attains its final shape before the internal pressure reaches the maximum value. Internal pressures equivalent to an external pressure coefficient of approximately one causes a full BALLUTE shape and maximum drag coefficient. Values greater than one cause the BALLUTE to become very firm and slightly more spherical. BALLUTES with a partial inflation aid system are discussed in Section V of this report.

5. STRUCTURAL LOADS

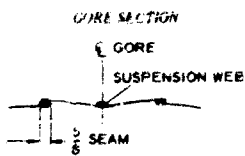
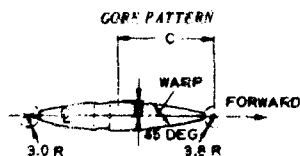
a. General

The BALLUTE configuration can be based on estimated internal and external pressure loadings using a computer program to define the shape for an isotensoid structure. This type of structure takes the calculated shape and becomes the most efficient structure when the ratio of pressures across the fabric are equal to those estimated. At other ratios of pressures, the gore fabric tends to rack because it is bias, and the BALLUTE takes a slightly different shape. When the ratios of pressures become more extreme, the fabric becomes limp in one direction (start of wrinkles), with maximum stresses occurring in a direction parallel to wrinkles.

Applicable background for a structural analysis is presented in the ADDPEP Phase I report, Item 4, Sections III and IV. (Reference 1). Appendix II of the same reference presents the general isotensoid design approach for inflatable drag devices.

b. Isotensoid Shapes

Because a BALLUTE travels through a range of flight conditions and ratios of pressures, the BALLUTE configuration normally is selected to obtain the highest structural efficiency at the highest loadings, thus having minimum weight. Since the ADDPEP program uses ascending trajectories, the highest loadings usually occur shortly following deployment. After this point, especially for higher altitude test ascents, the aerodynamic loads decrease much faster than the heating decreases the structural efficiency.



COORDINATES FOR (A), (B), (C), (E)

GORE				PROFILE	
C	B	C	B	X	Y
6.00	0.62	60.00	3.94	3.0	4.95
12.00	1.38	66.00	6.66	9.0	12.08
24.00	2.98	72.00	8.04	15.0	18.70
36.00	3.78	78.00	4.18	21.0	25.52
48.00	4.54	84.00	7.15	27.0	34.41
42.00	5.22	90.00	2.01	30.0	47.40
48.00	5.88	96.00	0.47	27.0	58.80
54.00	5.53	98.00	0.22	0	67.05
57.00	5.98	100.12	0.00	12.0	68.45
				0.0	70.53

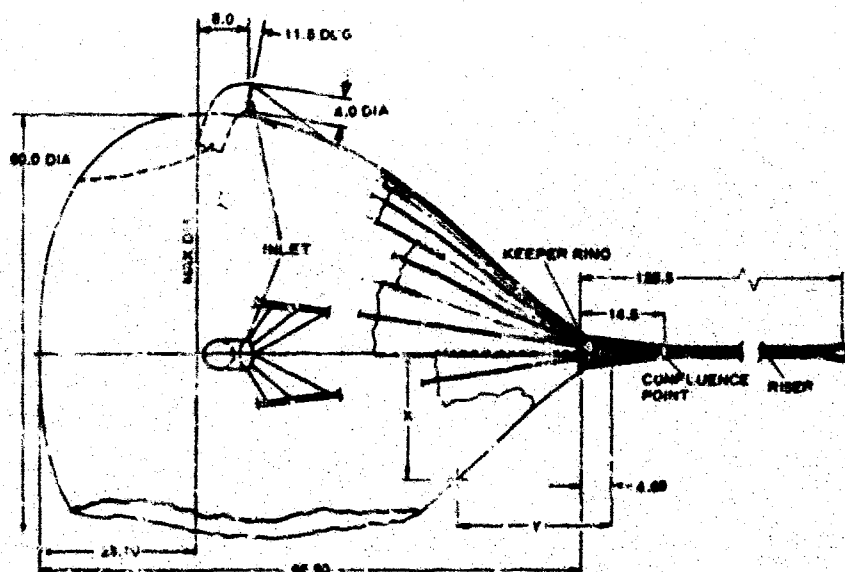
COORDINATES FOR (D)

GORE				PROFILE	
C	B	C	B	X	Y
6.00	0.63	61.63	5.95	3.0	4.79
12.00	1.34	63.00	5.84	9.0	12.44
24.00	2.88	68.00	5.75	15.0	19.54
36.00	3.66	69.20	5.84	21.0	27.23
48.00	4.33	72.00	5.89	27.0	36.22
42.00	4.95	79.00	5.06	30.0	55.50
48.00	5.43	84.00	4.15	27.0	65.73
54.00	5.77	90.00	3.10	18.0	73.80
60.00	5.94	102.00	0.76	12.0	75.50
				0.0	76.32

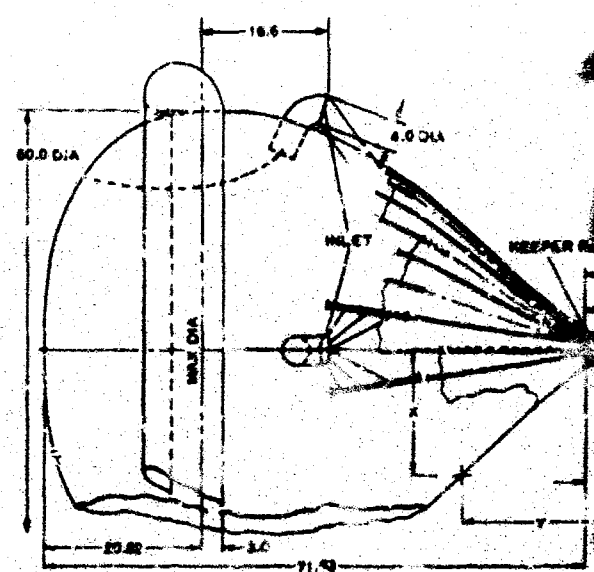
NOTES:

- ALL DIMENSIONS ARE IN INCHES
- THERE ARE 16 GORES

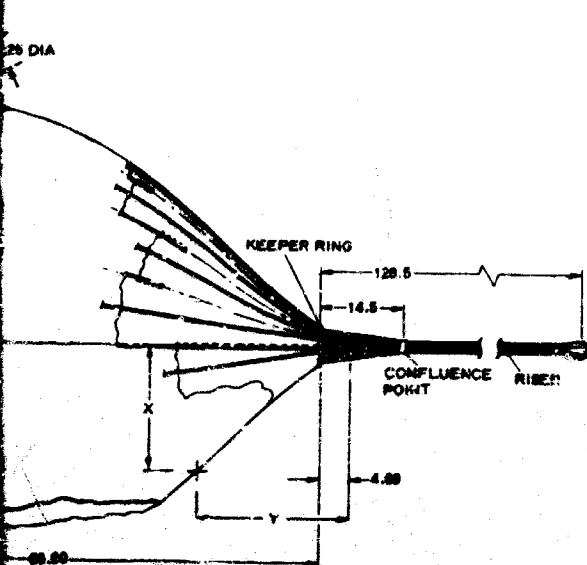
(C) FLIGHT-TEST CONFIGURATION FOUR: TB-4, TB-5, TB-6, TB-4BT



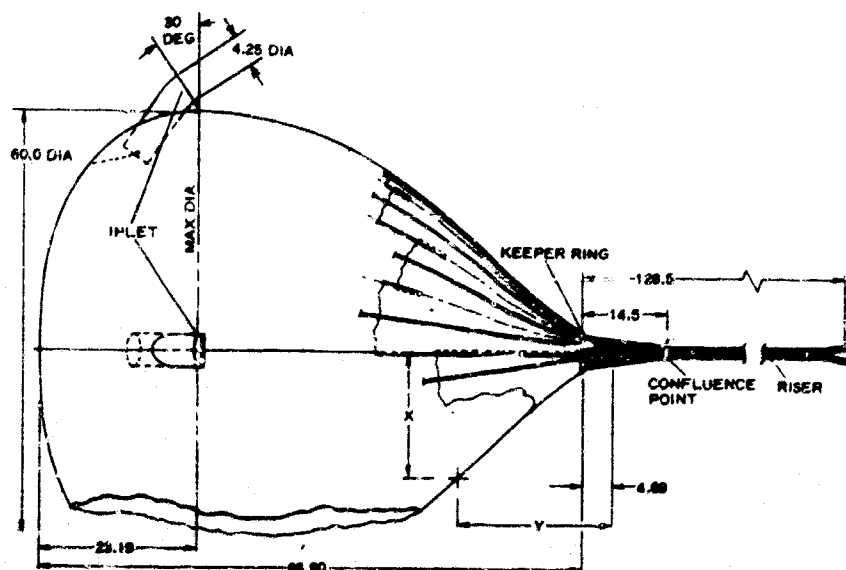
(D) BIND-TUNNEL CONFIGURATION: TB-4BT



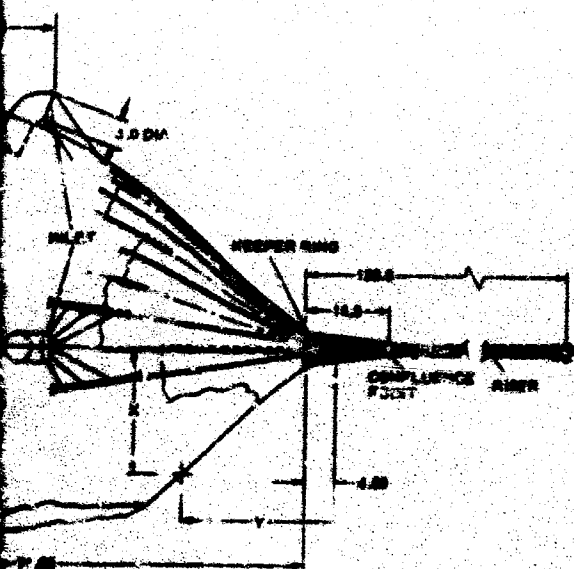
(A) FLIGHT TEST CONFIGURATION TWO: TB-2



(B) FLIGHT TEST CONFIGURATION THREE: TB-3



(C) WIND-TUNNEL CONFIGURATION: TB-1WT



(D) WIND-TUNNEL CONFIGURATION: TB-3WT

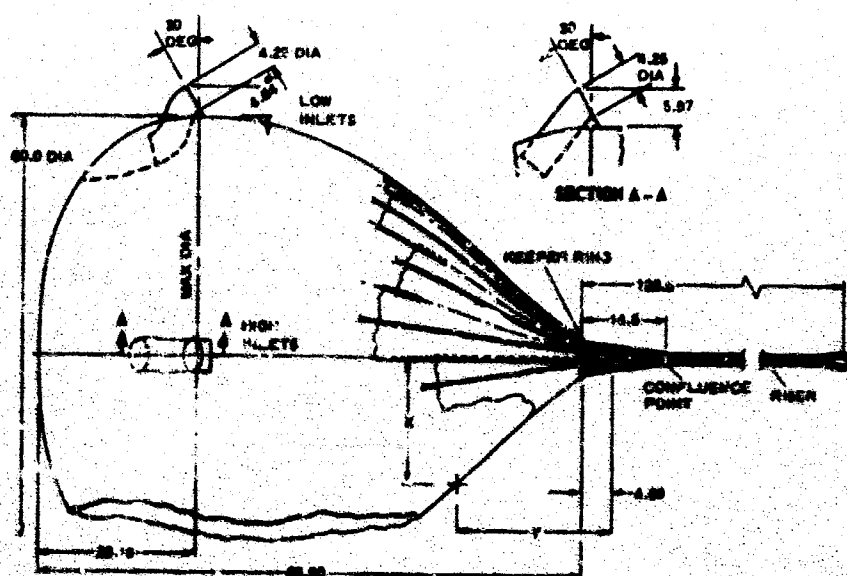


Figure 51 - Flight-Test and Wind-Tunnel Configurations

(Reverse is blank)

Data are available for the external loadings for shapes similar to TB-1, TB-2, TB-3, and TB-4. The tangent cone method also has been shown to predict the external distribution within design limits and can be used to predict pressures on other BALLUTE shapes. The wake effects on the external distribution are estimated based on empirical data. Figures 48A and B, (in Item 3 of this section) present the estimated external pressure coefficients (C_p) for conditions near the deployment points for advanced ADDPEP Phase II flights.

ADDPEP Phase I test data for small, hard models in wind tunnels at Mach numbers above 3 indicated that inlet pressures were above isotenoid limits for 80- to 90-deg BALLUTES and that these pressures meet the limits for 110- to 130-deg BALLUTES. Tests of TB-3WT and TB-1B further confirmed the high inlet pressures; tests of TB-1BWT and MB-1 at Mach 2.8 had close to the desired internal pressure coefficients for 80 to 90-degree total-angle BALLUTES. Figure 52 shows isotenoid shapes for two internal pressure coefficient values and several values of K (the ratio of the pressure load carried by the meridians to the total pressure load).

Although inlet pressures are available for inflating these much blunter BALLUTES at high Mach numbers, the total-flight Mach number regime must be considered along with the effect of high apex angles on BALLUTE stability. For these reasons the BALLUTE envelope angle of TB-2 was retained for TB-3 through TB-6.

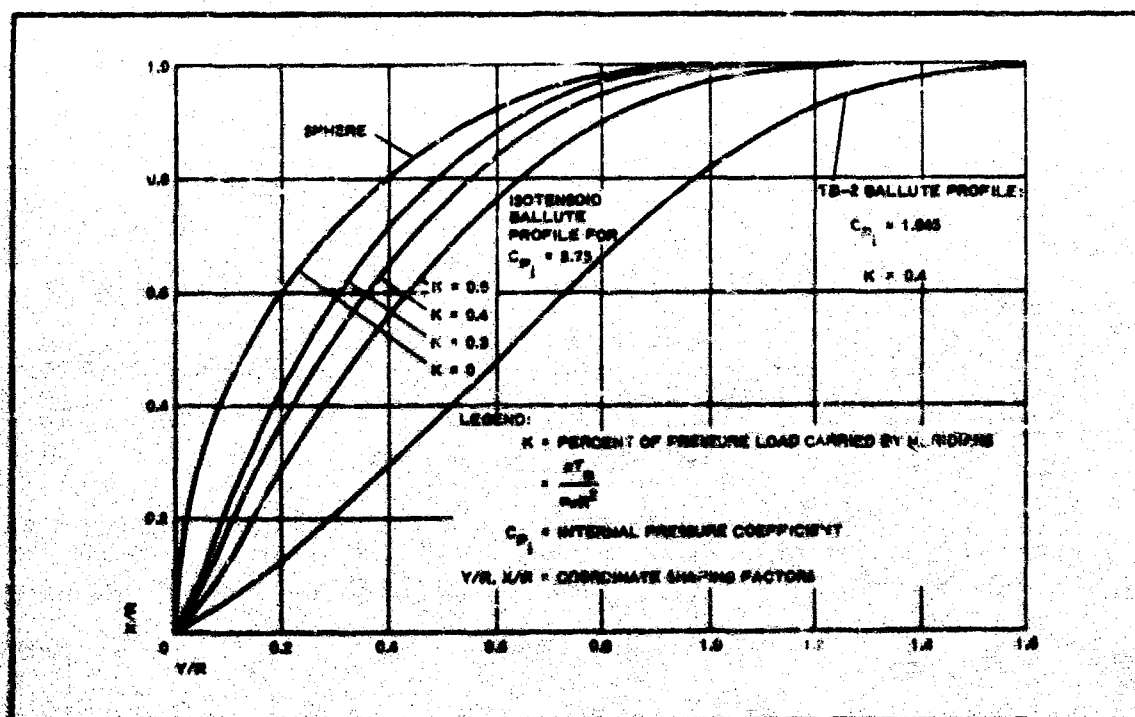


Figure 52 - Isotenoid BALLUTE Shapes for C_{p1} and K Values

c. Structural Considerations Based on Static Loads

The first step of the structural analysis was to determine the static loads on the major components and subassemblies to begin material selection and candidate assembly approaches. Factors initially considered were: (1) gore-fabric static stresses, (2) meridian static loads, (3) inlet fabric static stresses, (4) riser line static load, (5) keeper-ring static load, and (6) keeper-ring tie-loop static load.

With respect to gore-fabric static stress, the selection of TB-2 envelope shape and inlet location results in a structure that is only optimum to a flight Mach number of approximately three. At higher Mach numbers and higher internal pressure coefficients, the shape attempts to change to meet the off-design pressure loadings, and the value of K varies from 0 to 0.6 depending on the position on the BALLUTE. Under these off-design conditions, the maximum static fabric stress occurs at a BALLUTE position where the meridian stresses are minimal:

$$\text{Maximum gore-fabric static stress} = \frac{[(1-K) PR]_{\max}}{2} \quad (63)$$

where

K = 0 to 0.6 depending on position

P = pressure across the fabric

R = BALLUTE radius

The meridian static load is based on K_{\max} , which occurs in the base portion of the BALLUTE (Reference 1).

$$\text{Meridian static load} = \frac{K_{\max} P \pi R^2}{n} \quad (64)$$

Where K_{\max} is approximately 0.4 at high Mach numbers and 0.6 at Mach numbers approaching 2.

The inlet fabric static stress is based on the pressure difference across the inlet and the inlet tube radius (Reference 1):

$$\text{Inlet fabric static stress} = PR \quad (65)$$

The riser line static load in the riser line equals the maximum BALLUTE line force (Reference 1). Since BALLUTES do not exhibit an opening shock force, the maximum line force is equal to the BALLUTE drag:

$$D = C_D q S \quad (66)$$

Where:

C_D = steady-state drag coefficient

q = dynamic pressure

$S = \pi R^2$

$R = 2.5 \text{ ft}$

The keeper-ring static load is determined from the amount of force required to change the meridian/riser line direction from approximately 10 to 38 deg at the BALLUTE apex under maximum drag conditions.

The keeper-ring tie-loop static loads are calculated on the basis of preventing the keeper ring from sliding under maximum drag conditions.

1. Structural Considerations Based on Dynamic Loads

(1) General

The static loads were used as a basis to establish shape and static margins after the BALLUTE is fully inflated. Tests have demonstrated that, once the BALLUTE is fully inflated, its inflation and system stability are such that life-times in the wind tunnel are on the order of hours (References 56, 60).

Free-flight tests that contributed to minimum weight design of BALLUTES also established that failures are associated with the early portions of the inflation process only (Reference 61). Several events in the deployment and inflation process can result in critical loads compared to the static loads. Methods for controlling the values of these critical dynamic loads are available and are discussed below in Items (2), (3), and (4).

(2) Snatch Load

The snatch load is the result of the energy associated with pyrotechnic deployment and air loads acting on the decelerator as it travels from its stored position to line stretch where the snatch load occurs. By the use of a carefully sized deployment bag and a lines-first deployment, minimum energy is added and the snatch load becomes less than the maximum static drag load. This technique has been used for all ADLPEP free-flight tests, and the snatch load values measured have been less than the maximum static drag load.

(3) Inflating Loads

Critical loads affect the selection of gore materials, the fence, and the inlets during the inflation process. These loads are the result of high dynamic pressures and free-stream velocities acting on relatively large areas of light weight cloth tailored to the inflated BALLUTE shape. The extra high-speed cameras on the ADLPEP vehicle provided considerable data for inspecting this partially inflated condition.

The observed early whipping action can result in split envelope gores.

fence gores, inlet gores, or broken inlet frames, unless dynamic factors are added to the static load values or methods are used to limit the dynamic load values. This early whipping action ceases as soon as a "ball" of air is within the BALLUTE. The size of the ball can be as small as one-third to one-half the diameter of the BALLUTE. At high altitudes, this volume can be filled quickly by a simple partial inflation source, such as a liquid, that vaporizes at low ambient pressures. At low altitudes and high dynamic pressure, other energy sources (i.e., pressure bottles, gas generators, steam generators, and pyrotechnics) can fulfill this function. Larger inlet areas to BALLUTE volumes and reinforcement ribbons are other tradeoffs to be considered.

After the BALLUTE is partly inflated, there is a less violent motion that affects only structures mounted to the BALLUTE. This motion is a local wave or rippling action of the envelope fabric. The motion is well within the bias fabric limits; however, it causes flexing of the inlet metal parts at visual frequencies and amplitudes beyond spring wire limits.

The latter problem was solved by eliminating the metal frames that were directly secured to the envelope. The only metal retained was a cable within the inlet lip, where it is isolated to a large degree from the motions of the gore fabric.

(4) Opening Shock

Opening shock is associated with the violent filling and above-static drag values obtained with supersonic parachutes. Such shock does not occur with BALLUTES because of the small inlet size relative to the size of the BALLUTE. The opening loads on the BALLUTE envelope and fence are considered to be of the same order as the static values because of the inflation time. Full internal pressure loads actually occur at a measurable time period (1/4 to 1/2 sec) after the BALLUTE has attained maximum size and drag.

Each inlet, however, fills very rapidly because (1) its mouth diameter is essentially the same as any other section of the inlet tube or sock and (2) its mouth is held fully open by the wire cable hoops. Under these conditions, large dynamic load factors similar to those for fast-opening, small, supersonic parachutes can occur.

Factors for the inlet were evolved empirically from bomb drops at high subsonic velocities and high dynamic pressures using TB-1A and TB-1B after the ADDPEP flight tests. Under the most severe tests (820-psf dynamic pressure at Mach 0.84), TB-1B was undamaged except for the four inlet socks that act as check valves. The inlet socks were developed during the Gemini program to establish and maintain a firm BALLUTE shape by preventing (1) outflow through any inlet in the low energy unsymmetrical wake directly behind the man or (2) outflow through a damaged inlet. The socks also damped any tendency for the BALLUTE to pulse due to possible resonance at some point along the flight path.

The socks were made by using a 200-lb/in. -seam in 322/337-lb/in. cloth. The seams split in all socks. The same damage occurred to an identical construction when TB-1A was tested to a 760-psf dynamic pressure at

Mach = 0.805. The damage to the socks did not affect performance of the BALLUTE behind the symmetrical bomb. Based on the subsonic bomb drop test results, a factor of approximately 20 is needed on the inlet static stress values calculated using the simple OR formula where the pressure across the fabric is approximately equal to the dynamic pressure.

To better understand the need for this large factor of 20 times the static inlet stress, the possible physical happenings were investigated analytically. Assumptions were made of a firm inlet shape and a pressure wave opening the inlet fabric from either a centerline position radially outward or from a flat position outward. The energy into the inlet fabric was considered to be absorbed by elongating the fabric while in the shape of a hoop. Fabric stress values of the same magnitude as the empirical values were calculated. Fabric stress/strain values from inplant tests at low loading rates were used in the calculations. Accepting this large dynamic factor for designing the small inlets was a small weight penalty for this size BALLUTE compared to adding devices for controlling the mouth size of the inlets during opening.

e. Other Structural Considerations

In addition to considerations of static and dynamic loads for design, other factors were required in selecting materials for the BALLUTE as an ADDPEP flight-test unit. These included:

1. The possibility of the test unit being deployed earlier and at higher than the design dynamic pressure
2. Seam and joint efficiencies
3. Seam leakage if it occurs before ultimate capability
4. The effect of temperature on strength
5. Safety factor

These factors, discussed below, were used initially in conjunction with the room temperature "quick break" strengths to select material for further analysis (Reference 1).

With respect to deployment at higher than design conditions: based on the ratio of the anticipated to the actual deployment loads for the many ADDPEP flights (see Table IV, Section II), a factor of 1.5 was considered sufficient for design. A factor of 2 was originally used, based on the results from earlier test vehicle systems.

Seam and joint tests were made of all critical portions of the BALLUTE to establish the actual efficiencies. However, initial selection of candidate material values was assumed based on tests of similar construction. Eighty-percent seams were used to aid in material selections. The factor was one/efficiency.

Seam leakage is more peculiar to BALLUTES than parachutes. Some

cloths rake under loads considerably below the ultimate seam strength. Raking occurs when the cloth yarns running in one direction are pulled locally by the sewing threads into a bunch leaving small local voids in the cloth. Values were initially assumed as 80-percent of the seam ultimate loads based on tests of standard cloths. It was determined from tests of cloths woven for the BALLUTE gores that this factor (one/efficiency) could be eliminated if tightly woven cloth were specified.

With respect to the effect of temperature on strength, the strength of Nomex versus temperature is shown in Figure 53 (References 62, 63). To establish an exact factor relative to room temperature strength for a given flight, iterations had to be conducted. The iterations considered the load dropoff and the decrease in fabric strength associated with evaluated material temperatures, which vary with the weight of the Nomex cloth selected. The value of the factor was originally chosen as 1.3 for beginning the iterations (Reference 1). For some flights (TB-4), the factor became 1.0 since the load dropoff was more rapid than material strength loss with rising material temperatures. Here the critical loads occurred initially when the fabric was still at room temperature.

A standard 1.5 safety factor was retained.

f. Loads, Design Factors, and Material Requirements

The load values and factors used for material selections and joints for the BALLUTES flight tested are given in Reference 1 and shown in Table XIX.

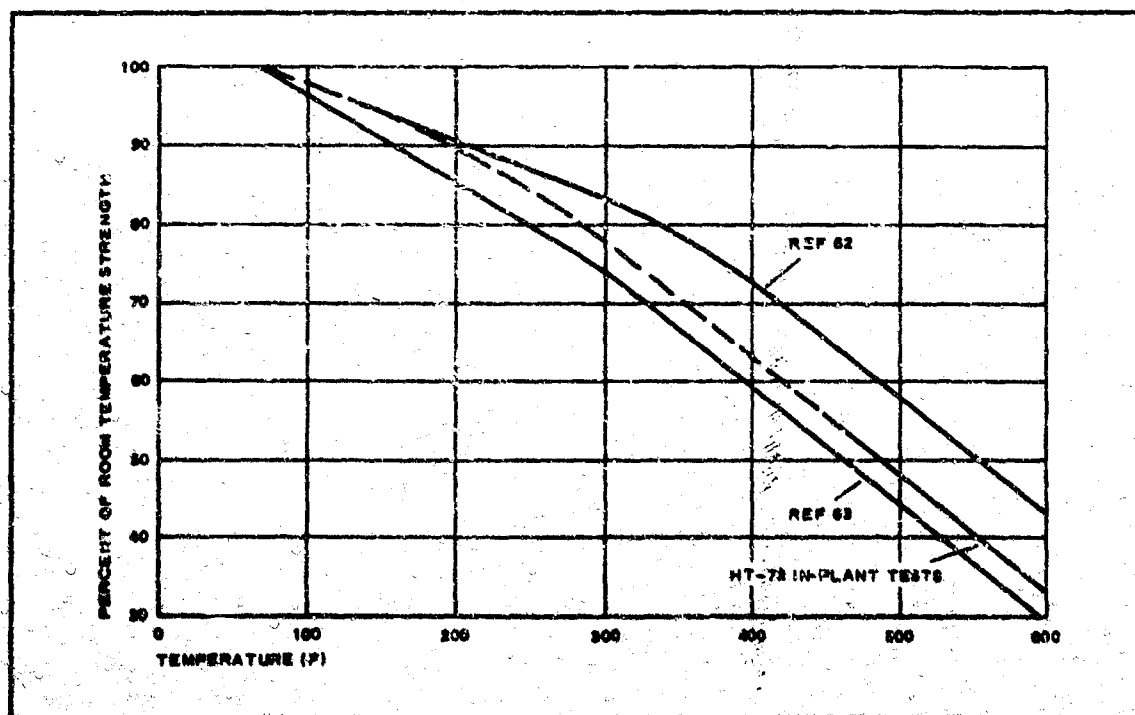


Figure 53 - Nomex Strength (Percent of Room Temperature Strength) versus Temperature

SECTION IV - TEXTILE BALLUTE DECELERATOR

AFFDL-TR-67-25

TABLE XIX - TEXTILE BALLUTE LOADS, DESIGN FACTORS, AND
MATERIAL REQUIREMENTS PREDICTED

Textile BALLUTE	Item	Gore fabric (lb/in.)	Inlet fabric (lb/in.)	Meridian webs (lb each)	Keeper ring (lb)	Keeper ring loops (lb each)	Riser (lb total)
TB-2	Static load for $q = 218$ psf and Mach 3.8	39	6.4	240	243	39	2,640
	Design factors						
	Overload	2	2	2	2	2	2
	Dynamic	2	2	2	2	2	2
	Seam efficiency	1.2	1.2	1.2	1.2	1.2	1.2
	Temperature	1.5	1.5	1.5	1.5	1.5	1.1
	Raking	1.2	1.2	1.0	1.0	1.0	1.0
	Safety	1.5	1.5	1.5	1.5	1.5	1.5
	Product of factors	12.96	12.96	10.8	10.8	10.8	7.92
	Material strength requirements						
	Basic	505	83	2590	2620	421	20,919
	Seam	421	69	2160	2190	351	16,800
	Raking	351	58
TB-3	Static load for Mach 3.7 and:						
	$q = 171$ psf at inflation	89	...	420	220	54.5	2,350
	$q = 250$ psf at deployment	...	19.5
	Design factors						
	Overload	1.25	1.25	1.25	1.25	1.25	1.25
	Dynamic	1.5	2.0	1.5	1.5	1.5	1.5
	Seam efficiency	1.2	1.2	1.1	1.1	1.1	1.2
	Temperature	1.5	1.8	1.2	1.2	1.2	1.2
	Raking	1.2	1.2
	Safety	1.5	1.5	1.5	1.5	1.5	1.5
	Product of factors	6.08	9.73	3.72	3.72	3.72	4.1
	Material strength requirements						
	Basic	540	190	1560	820	203	9,500
	Seam	450	158	1420	745	185	7,925
	Raking	375	132
TB-4, TB-5, TB-6	Static load for $q = 200$ psf and Mach 4	104	13.9	488	264	45.6	2,752
	Design factors						
	Overload	1.5	1.5	1.5	1.5	1.5	1.5
	Dynamic	1.5	27	1.5	1.5	1.5	1.5
	Seam efficiency	1.2	...	1.1	1.15	1.15	1.2
	Temperature	1	...	1	1	1	1
	Raking	1
	Safety	1.5	...	1.5	1.5	1.5	1.5
	Product of factors	4.05	40.5	3.71	3.88	3.88	4.05
	Material strength requirements						
	Basic	421	...	1810	1024	177	11,018
	Seam	351	560	1648	890	154	9,188
	Raking	352

6. THERMODYNAMIC ANALYSIS

a. General

In the ADDPEP Phase I report (Reference 1), several methods are presented for estimating the heat flux rates and subsequent temperature rise in a material for BALLUTE type decelerators subjected to aerodynamic heating. The calculation of the heat flux rate and heat transfer coefficient when using these methods was based largely on the assumption that the leading body ahead of the decelerator body does not affect the flow over the decelerator body. For example, the analytical approach outlined in Reference 1 suggested estimating the heat transfer coefficient at the BALLUTE surface on the basis of free stream flight conditions. Once this assumption is made, the calculation of the heating criteria may proceed in a manner similar to analyzing a conical body or blunt nose body in a high velocity stream.

An empirical approach, also outlined in Reference 1, advanced the following method for estimating the local heat flux rate on the decelerator body: utilize a reference heat flux rate at (1) the leading edge of the decelerator body in the case of laminar flow and (2) a distance $S/R = 2$ from the leading edge for the case of turbulent flow. The reference heat flux rates used in this method provide an index from which the local heat flux rates on the decelerator body can be obtained from a set of convenient heat flux rate distribution curves presented in Reference 52 for two different decelerator bodies.

The reference heat flux rates were convenient to calculate since they were to be evaluated on the basis of free stream flight conditions existing ahead of the leading body using the geometry of the decelerator body. On the other hand, the heat flux rate distribution data were obtained from an experimental wind tunnel heat transfer evaluation of a BALLUTE decelerator at Mach 10. Thus, the proposed empirical approach takes into account, in a limited manner, the effect of a leading body on the heat transfer characteristics at the decelerator surface.

In subsequent analyses of BALLUTE heating, a variation in the method of analysis was introduced. The basis for the introduction of this variation was the results of additional studies conducted on the flow phenomena that occur between a leading body and a decelerator body that trail in the wake of the leading body. A simple model of the wake flow resulting from the interaction between the leading body and the trailing decelerator was formulated through the use of available experimental data and was published in Reference 64. More recently, some additional work was conducted on this flow phenomena, and these data were presented in Reference 65.

As a result of these investigations, it was decided to modify the thermal analysis methods presented earlier for calculating BALLUTE heating to take into account the formation of the wake resulting from the flow interaction between the leading body and the trailing decelerator body. The proposed method of analysis does not invalidate previous methods; however, it is based on a more comprehensive flow definition and shows

promise for understanding the flow phenomena involving a decelerator body trailing in the wake of a leading body.

b. BALLUTE Thermal Analysis Methods

One of the important conclusions drawn from the investigation of wake phenomena between an aerodynamic decelerator trailing in the wake of an axisymmetrical leading body was the concept of a cylindrical viscous wake existing between the two bodies (Reference 64). However, no criteria were available to establish whether the wake would be laminar or turbulent, although it was shown that the diameter of a viscous turbulent cylindrical wake between the two bodies would be approximately twice the diameter of a laminar type wake. Since for most practical engineering applications it is required to predict whether the material chosen for the decelerator body will sustain the most severe environment encountered, a decision must be made as to whether the flow over the decelerator body is laminar or turbulent. One approach is to test the boundary layer on the leading body. If this boundary is turbulent, the cylindrical wake will be turbulent. A simple method of determining whether transition has occurred on the leading body is to use the following equation for calculating a momentum Reynolds number (see List of Symbols in preliminary pages of this report):

$$Re_{\theta} = \frac{\rho_1 V_{\infty} \theta}{\mu_1} = 0.695 \left(\frac{\rho_w \mu_w}{\rho_1 \mu_1} \right)^{0.114} \left(\frac{\rho_1 V_{\infty} x}{\mu_1} \right)^{0.5} \quad (67)$$

This equation was derived from data presented in Reference 66. The transition Reynolds number is usually taken as occurring in the 400 to 600 range.

If the preceding analysis reveals that the flow over the leading body is laminar, then a wake transition analysis must be conducted to determine its state. Since wake transition data for a flow between two bodies are practically nonexistent, free wake data must be used. In general, the unified wake transition correlation data in Reference 67 are very simple to use. Predicting the transition of the wake using the correlation parameter from Reference 67 requires an evaluation of the following grouping:

$$\left(Re_{x_{TR}} \right)_{\infty} \left(M_{\infty} / M_e \right)^2 = \left(\frac{\rho_{\infty} V_{\infty} x_{TR}}{\mu_{\infty}} \right) \left(M_{\infty} / M_c \right)^2 \quad (68)$$

A plot of this wake transition parameter is presented versus free stream Mach number along with the range of transition data taken from Reference 67 in a subsequent discussion of wake characteristics.

With the type of boundary layer type established, the heat flux criteria at the decelerator surface can be calculated. At this time, one may proceed with the methods outlined in Reference 64 for calculating the properties of the wake and then using these wake flow properties for estimating the heat transfer rates at the decelerator surface as a function of

these upstream flow properties. For a laminar boundary layer, the heat transfer coefficient on a decelerator surface can be calculated from the following equation (Reference 65):

$$\frac{h}{h_{\text{cone}}} = \frac{\left(\frac{p'}{p_{\infty}}\right)\left(\frac{r'}{D_0}\right)\left(\frac{x'}{D_0}\right)^{1/2}}{\sqrt{3} \left(\frac{p_{\text{cone}}}{p_{\infty}}\right)^{1/2} \left[\int_0^{x'/D_0} \left(\frac{p'}{p_{\infty}}\right)\left(\frac{r'}{D_0}\right)^2 d\left(\frac{x'}{D_0}\right) \right]} \quad (69)$$

The prime notation indicates these properties must be evaluated at conditions existing at the edge of the boundary layer and at the particular station under consideration. The pressure distribution over the decelerator surface may be calculated using the tangent-cone method, since the flow properties of the wake and the geometry of the decelerator are known. The decelerator and the cone must be compared at equal distances from their respective noses.

In case it is determined that the boundary layer is turbulent, the heat transfer distribution over the decelerator surface can be calculated using the following heat transfer equation (as suggested in Reference 65):

$$\dot{q}_w = \frac{0.0296}{\left(\frac{\rho^* u' x}{\mu^*}\right)^{0.2} \left(P_r\right)^{2/3}} \rho' u' (H_1 - h_w) \quad (70)$$

The prime notation again indicates that the appropriate properties must be evaluated for conditions at the edge of the decelerator boundary layer. The starred quantities on the other hand must be evaluated using the local pressure and reference enthalpy (h^*) where this latter quantity is evaluated by the following equation:

$$h^* = h' + 0.45 (h_w - h') + 0.20 (h'_{aw} - h') \quad (71)$$

As in the laminar flow case, the evaluation of the turbulent flow heat flux rates depends on the evaluation of wake flow properties ahead of the decelerator body. The calculation of these wake flow properties is outlined in References 64 and 65.

The above methods may be simplified somewhat if, in the interest of expediency, it is required to calculate the maximum expected temperature rise in the decelerator material during flight along a prescribed trajectory path. In such a situation, the flow parameters at the decelerator surface usually vary with time. Thus, it is required to define the flow conditions at the decelerator surface as a function of time prior to calculating the heat transfer characteristics.

The heat flux rate for turbulent flow, for example, can be calculated

using Equation 70. Evaluation of this equation requires a knowledge of the local velocity, temperature, and pressure. These flow properties at the decelerator surface may be estimated with fair accuracy by the methods described in the following discussion.

Consider the flow model proposed in Reference 65 and shown in Figure 54. The flow in front of the decelerator is composed of a viscous cylindrical core and an inviscid outer region. Mach number M_e near the junction of these two wake flow regions may be approximated by considering a single expansion of the flow from the stagnation pressure region at the nose of the leading body to ambient pressure in the wake region. This isentropic expansion freezes Mach number M_e to values less than five. In the region away from the junction of the inner viscous wake and the outer inviscid wake, the Mach number of the flow behind the bow shock approaches free stream conditions (M_∞) as the trailing portions of the bow shock are approached.

Considering Mach number M' of the flow at the decelerator surface, it is evident that the flow must cross a weak oblique shock that forms in front of the decelerator forebody in the range of upstream Mach numbers described. The effect of this weak shock gives rise only to a small variation in Mach number M' at the decelerator surface if one considers the possible variation in the Mach number range resulting from the upstream variation in Mach number M_e . Thus, it is possible to assume that Mach number M' at the edge of the decelerator surface boundary layer is that resulting from the flow crossing an oblique shock at Mach number M_e . Once this assumption is made, Mach number M' variation at the decelerator forebody forebody surface may be readily calculated using the compressible flow data contained in Reference 68.

The local enthalpy of the stream may now be calculated at the edge of decelerator surface boundary layer from the following relationship:

$$h' = \frac{H_1}{1 + 0.5 (\gamma - 1)(M')^2} \quad (72)$$

where H_1 is the total enthalpy of the stream, a constant and equal to free stream enthalpy; and M' is the local surface Mach number described above.

The remaining property that must be evaluated is the surface pressure acting on the decelerator forebody. It has been found experimentally, as reported in Reference 52, an approximate linear increase occurs in the surface pressure as the distance from the BALLUTE apex increases. In support of these experimental data, theoretical pressure distribution methods presented in Reference 1 have been shown to predict these values with a reasonable amount of accuracy using a modified tangent-cone approach. Therefore, the pressure associated with the local velocity and temperature can be readily estimated.

For purposes of heat transfer calculations, however, it is the peak pressure acting on the decelerator surface that is of interest because this position should give rise to the maximum heating rate to the decelerator material. Examination of the experimentally determined pressure

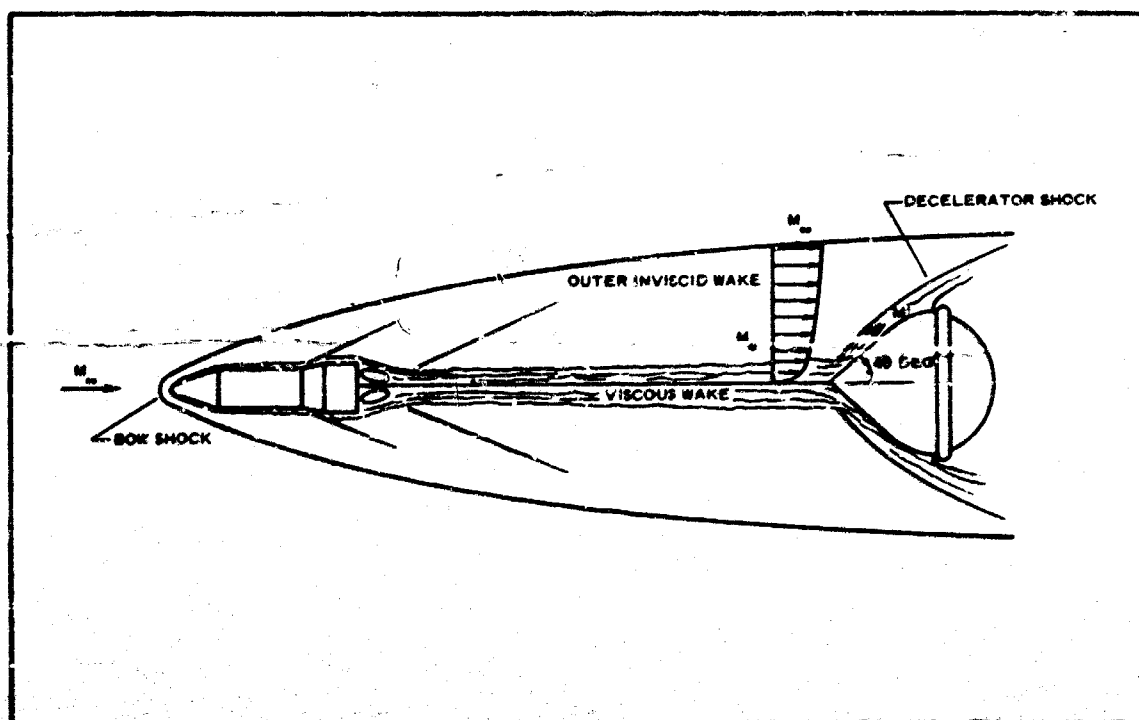


Figure 54 - Payload and BALLUTE Flow Field Schematic

distribution over a BALLUTE decelerator trailing in the wake of a leading body (reported in Reference 52 and shown in Figure 55) revealed that the maximum pressure can be predicted by the following technique. First, consider a BALLUTE in the free stream Mach number (M_∞) flow. Using cone theory for Mach 10.2, the ratio of local pressure to free stream pressure can be calculated to be about 63, as shown in Figure 55. This value grossly overpredicts the maximum pressure acting on the BALLUTE.

Second, calculate the local Mach number (M_0) resulting from a compression across a normal shock and then expanding to free stream pressure. This yields Mach 3.91. Using this Mach number (M_0) and the cone data of Reference 66, the pressure coefficient may be estimated.

The local pressure-to-free stream pressure ratio may now be evaluated on the basis of local upstream flow. This results in a 10.75 pressure ratio, as shown in Figure 55. While the 10.75 value predicts the local pressure on the BALLUTE surface quite well for an S/d' of -0.65, it underpredicts the maximum value by more than a factor of 3. However, by averaging the two calculated values, the maximum pressure can be predicted quite accurately. Thus, in lieu of a complete pressure distribution evaluation, the above technique can be applied readily.

Since all the flow properties required above can be quite easily determined from a knowledge of the trajectory path, the evaluation of the

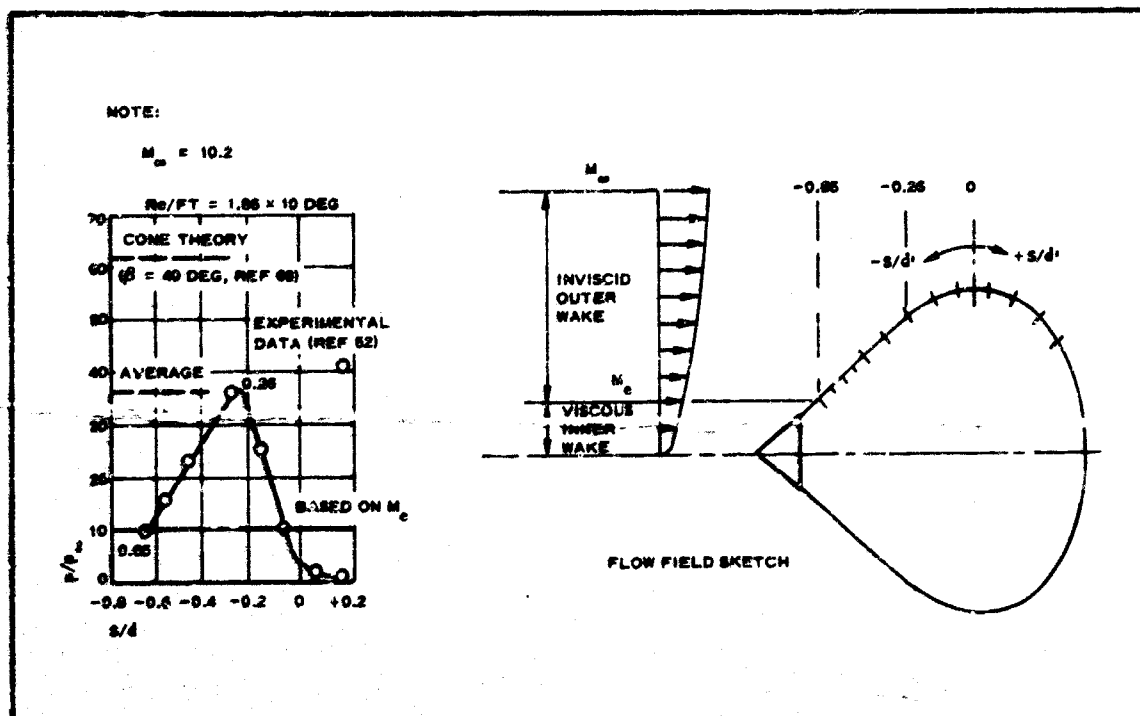


Figure 55 - Pressure Distribution over BALLUTE

turbulent heating rates as a function of time may be conducted expediently using Equation 70.

c. Heat Conduction Methods

The temperature response of the decelerator material can be calculated as a function of the aerodynamic heating rates experienced during the critical periods of a trajectory path once the heating rates are defined. Reference 1 describes two types of methods of heat conduction solutions leading to the temperature response rate. Due to the highly transient nature of the heating problem during deceleration along a trajectory path, the following method was adapted for solving the temperature response of decelerator materials.

Basically, the heating of the decelerator material can be considered as a transient one dimensional heating problem due to the material thermal properties, which class them as poor conductors. Hence, one may apply the partial differential equation for heat conduction in a slab:

$$\frac{\partial T}{\partial t} = c \frac{\partial^2 T}{\partial y^2} \quad (73)$$

This equation may be converted to a finite difference equation and put in the form of a heat balance, so that the heat-in minus the heat-out is equal to the heat-stored. For any i th layer, if one assumes that the material

is divided up into a number of layers, the heat balance can be written as:

$$\frac{k}{\Delta y} (T_{i-1} - T_i) - \frac{k}{\Delta y} (T_i + T_{i+1}) = \frac{\rho c \Delta y}{\Delta \tau} (T_i' - T_i) \quad (74)$$

At the outer surface, the following heat balance can be written:

$$h(T_{aw} - T_1) - \epsilon \sigma (T_1^4 - T_s^4) - \frac{2(T_1 - T_2)}{\frac{\Delta y_1}{k_1} - \frac{\Delta y_2}{k_2}} = \frac{\rho c \frac{\Delta y_1}{2} (T_1' - T_1)}{\Delta \tau} \quad (75)$$

The inner surface may be considered an adiabatic wall in most cases. However, if a heat transfer occurs at this surface, the appropriate boundary condition equation can be specified.

If one considers the previous calculations of the heat flux rates uncoupled from the heat conduction problem, then these must be adjusted to fit the proposed heat conduction solution. If one assumes that the heat flux rates were calculated on a cold wall basis, then the following modification may be made to adjust the external heat in terms in Equation 75:

$$\begin{aligned} h(T_{aw} - T_1) &= \dot{q}_w \\ &= \dot{q}_{cw} \left(\frac{T_{aw} - T_1}{T_{aw} - T_{cw}} \right) \end{aligned} \quad (76)$$

These equations are readily adaptable to a digital computer language. A description of an example solution follows.

d. TB-4 Calculated and Measured Values

BALLUTE fabric temperature values were calculated using the thermal analyses methods presented above for the actual TB-4 BALLUTE flight conditions. The purpose was to make a comparison with measured values.

The deployment point of the BALLUTE decelerator was established from radar tracking data as taking place at a 226,700-ft altitude and a 9126-fps velocity. On the basis of the wake transition criteria presented, an evaluation of Equation 68 shows that, during the exit flight phase of the trajectory, the decelerator should be in a laminar wake. Thus the evaluation of the heat transfer coefficient was based on Equation 69. The cold wall heat flux rate for the most critical position on the decelerator surface is shown in Figure 56A as a function of time of flight.

The re-entry phase of a calculated re-entry trajectory was examined next. Again, the wake transition criteria was applied, and the results of this analysis are shown in Figure 57. Transition criteria showed that the re-entry flight begins with the decelerator in a laminar wake. At about 695 sec from launch and along the calculated re-entry trajectory, the wake transition point apparently begins to move forward toward the

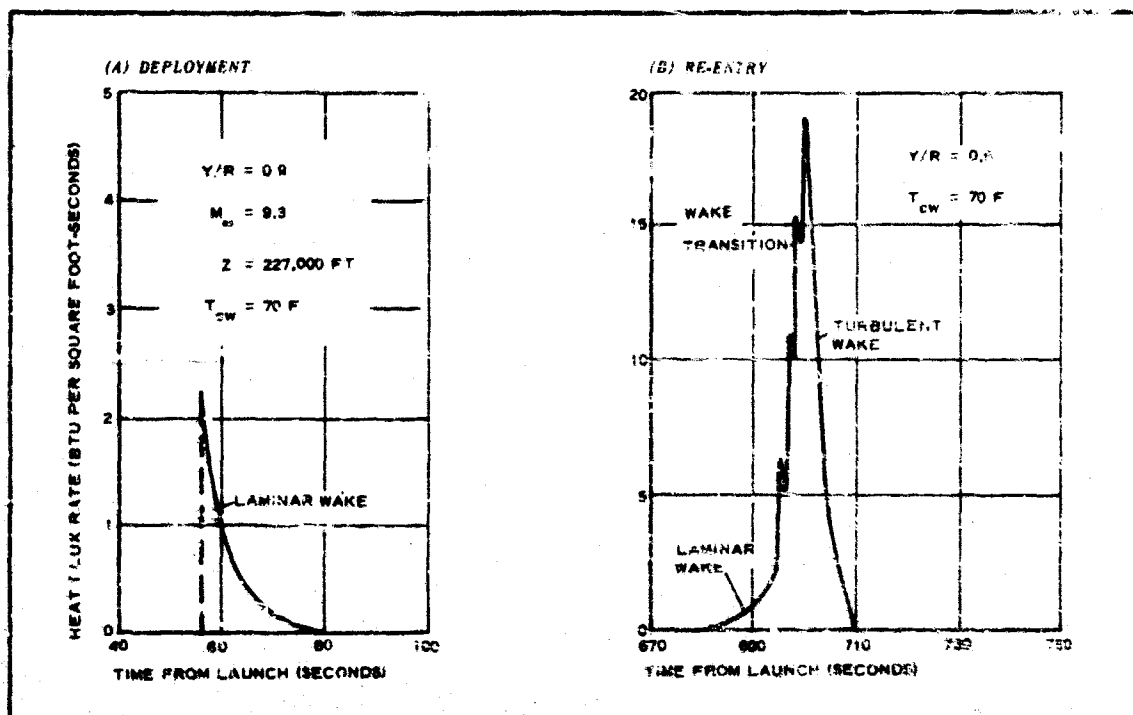


Figure 56 - Cold Wall Heat Flux Rate: (A) Deployment; (B) Re-entry

leading body. Until about 700 sec, the decelerator is encompassed in a turbulent wake with transitions either on the leading body or immediately behind the body.

As a result of this criterion, the heat input into the decelerator material must be calculated partially by using Equation 69 for the laminar wake case and then using Equation 70 for the turbulent wake case. The results are shown in Figure 56B. The laminar cold wall heat flux rates rise rather slowly as the bodies re-enter the atmosphere and gradually reach a heat flux rate of about 2 Btu/ft²-sec at 695 sec from launch. The heat flux rates increase on the critical position on the decelerator surface until a cold wall turbulent heat flux rate of about 19 Btu/ft²-sec is reached at 700 sec from launch. Thereafter, the heat flux rate decreases quite rapidly.

The temperature response of the decelerator material was calculated next on the basis of the cold wall heat flux rates and the transient heat conduction equations presented earlier. The results are shown in Figure 58 as a function of time of flight along with the telemetered temperature data. The leading vehicle total temperature probe data are presented for reference. Since the total temperature probe is not designed to read temperatures in excess of 2000 F, no correlation is attempted between the probe values and the BALLUTE thermocouple values. In the case of re-entry flight, the probe total temperature data was programmed to be terminated near apogee.

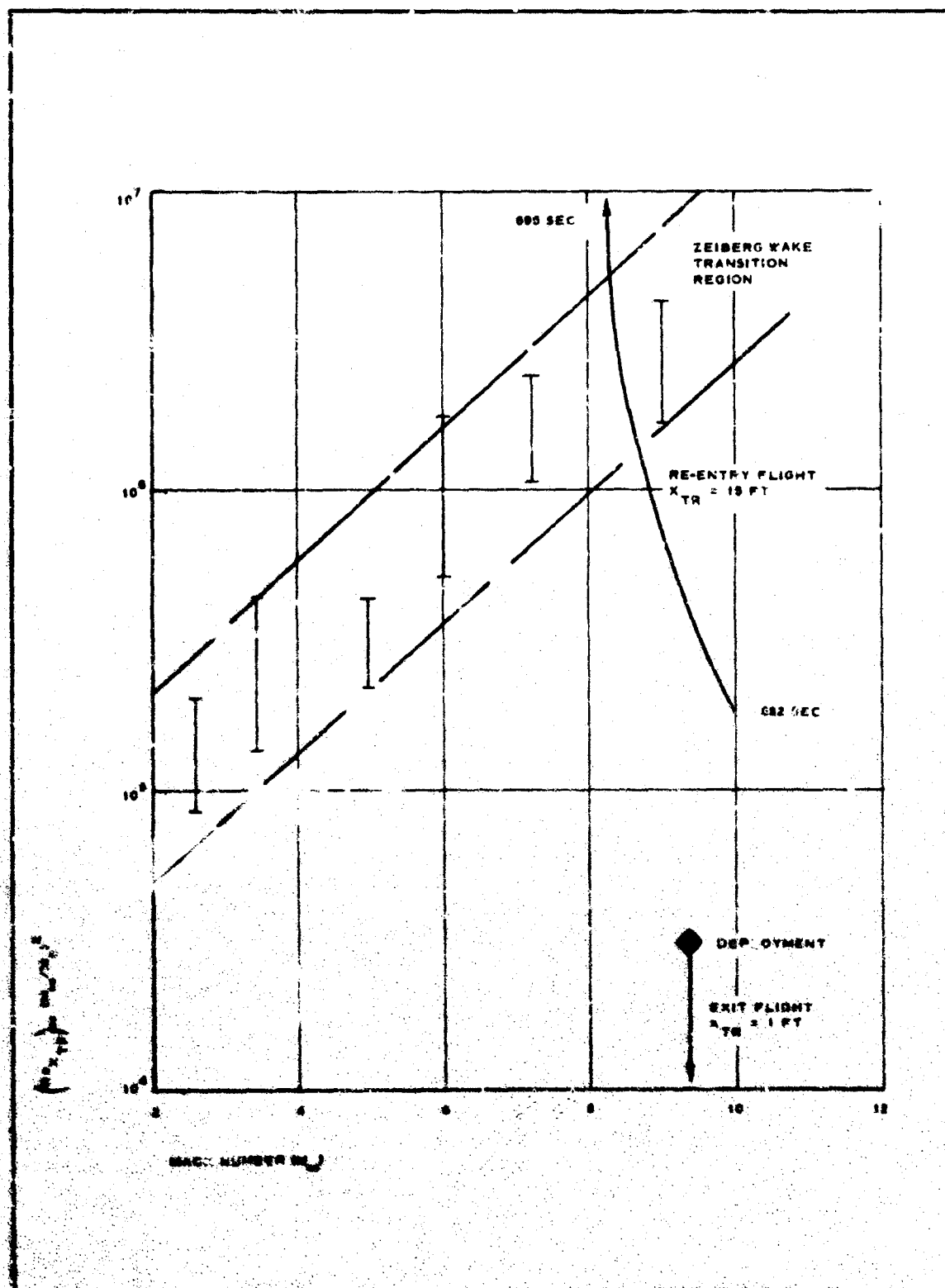


Figure 57 - Unified Wake Transition Criterion

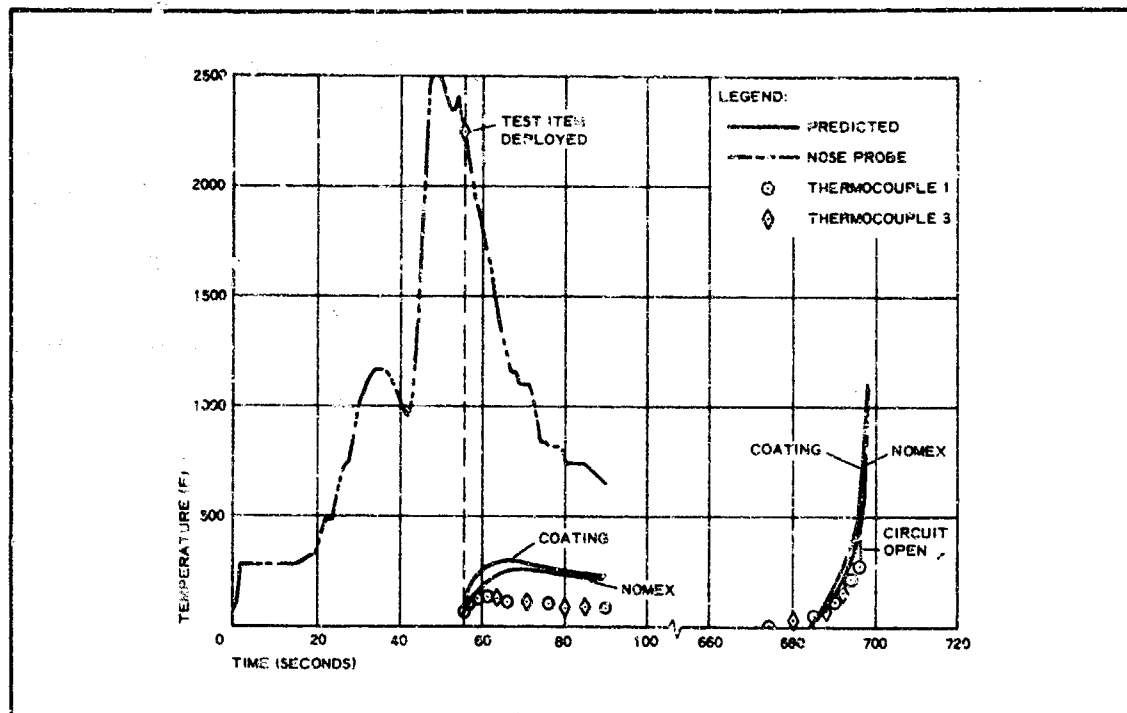


Figure 58 - Flight-Test TB-4: Predicted and Measured Temperature

Looking at the decelerator material temperature response during the exit flight phase, the telemetered results show a quick rise to about 137 F and a subsequent cooling to about 80 F as the upper rarified atmosphere is reached. The predicted surface temperature, as well as outer Nomex surface temperature, is presented for this portion of the estimated trajectory path. This predicted temperature is based on the heat transfer coefficients obtained using Equation 68. The surface temperature in this case is predicted to reach about 280 F in about 10 sec and then cool as the test items continue to gain altitude. Thus, the predicted temperature evidently overestimates the telemetered temperature by about 150 F during the exit flight phase.

Turning to the re-entry flight phase, the same comparison is made. The telemetered results show that the material temperature had cooled to less than 0 F during the 10 min of flight in the rarified atmosphere. An estimate of this radiation cooling effect indicates that, for an absorption-to-emittance ratio of less than one, this is admissible. Although no test data are available on the absorption or emittance characteristics of the coating material, the material type shows a trend in the direction of a ratio less than one.

As the test vehicle re-enters the denser atmosphere, the BALLUTE material temperature response indicates a slight rise initially and then rises to about 270 F at 696 sec from launch, whereupon telemetry signals from these circuits cease. In the predicted case, the temperature is

assumed to be 14 F at 684 sec from launch along a calculated trajectory; the temperature response of the material is calculated from this temperature level.

The initial predicted temperature rise is based on a laminar wake and shows the temperature rising to about 400 F in 11 sec. The comparable rise in the telemetered data is about 270 F. At the end of this period, the wake is predicted to undergo a transition to a turbulent type. Thus, the heating rates at the BALLUTE surface rise quite significantly as shown in Figure 56A. The predicted temperature shows a rise to a value greater than 700 F in less than 5 sec from the onset of transition to turbulent. This is in excess of its load-carrying capability at an elevated temperature, and apparently it correlates with the cessation of telemetry readings for material temperatures.

Comparison of the predicted and experimental data for this test flight demonstrates that the methods developed for analyzing BALLUTE decelerators in the wake of a leading body yield a fair degree of accuracy in establishing environmental thermal effects and temperature response of the material.

Typical thermal properties of the materials used in this test flight are shown in Table XX. The properties of the D-65 coating material were obtained from the Dyna-Therm Chemical Corporation, while the Nomex data were extrapolated from the data presented in Reference 69. On the basis of these properties, as well as information regarding the properties of the materials utilized and the simple methods of analysis developed, it is concluded that the thermal design of BALLUTE decelerators may be conducted within the limits of applied engineering accuracy.

e. Liquid Cooling Considerations

During the establishment of a rapid partial inflation technique, several vacuum-chamber, wind-tunnel, and free-flight tests were made. In the TB-3 tests, the effect of vaporation on the material temperature was very pronounced because of the relatively low aerodynamic heating rates compared to the rapid heat absorption capability of the liquid and its vapor. Flight test results of the effect for TB-3 are shown earlier in Figure 40. For the metal BALLUTE, the effect is given in Reference 45 and is shown later in Figure 65 of this Phase II report (Section V).

TABLE XX - TEXTILE BALLUTE: THERMAL PROPERTIES OF
MATERIALS IN FLIGHT TEST

Material	Position	Thickness (mil)	Density (lb/ft ³)	Specific heat (Btu/lb F)	Thermal conductivity (Btu/ft-hr F)
D-65	Outside surface	7	63.6	0.25	0.053
Nomex	Fabric 11.84 oz/yd ²	23	42.0	0.35	0.032
D-65	Inside surface	3	68.6	0.25	0.053

Both sets of data indicate that a rapid transfer of heat occurred between the BALLUTE fabric and the vapor. The flight-test conditions were Mach 4 at 98,000 ft in an ascending trajectory of approximately 80 deg. Three thermocouples measured the cloth temperature. They were located along a gore, with a third thermocouple located at a position corresponding to one-half the BALLUTE diameter and maximum surface slope. The values versus time starting at deployment are shown in Figure 40. The liquid solution used was 12 oz methyl alcohol and 4 oz water.

Since the flight was short and the BALLUTE was packed in a dual wall container, it was anticipated that the contained fluid would maintain its temperature until deployment. The energy available for vaporization is (1) the sensible heat in the solution itself as a liquid and with the water becoming ice, (2) heat in the fabric, and (3) heat in the incoming air. The heat required to vaporize the methyl alcohol is 482 Btu/lb, or $12/16 \times 482 = 362$ Btu. To vaporize the water, 1000 Btu/lb are required, or $4/16 \times 1000 = 250$ Btu. While the exact sequence of vaporization has not been established, the following action sequence is postulated (see Figure 59):

1. Alcohol vaporizing absorbs heat from alcohol liquid (A toward B)
2. Alcohol vaporizing and alcohol liquid absorb heat from water (A to B)
3. Alcohol vaporizing and alcohol liquid absorb heat from water freezing (A to B to C)
4. Vapor and liquid absorb heat from the fabric by convection (B-C to D); all alcohol is vaporized at 70 F
5. Convection heats 12 oz of alcohol vapor, and BALLUTE pressure becomes 560 psf at 600 F

7. MATERIAL, SEAM, AND JOINT TESTING

a. General

The criteria and procedures for TB-1 and TB-2 material selection, material qualification, and fabrication techniques were generated during ADDPEP Phase I. A tabular comparison of test result data for in-plant testing of fabrics, seams, webbing, and sewing threads is presented in Section IV of the Phase I report (Reference 1).

The selection and qualification of the materials and the generation of fabrication techniques applicable to textile BALLUTES was continued during ADDPEP Phase II. The data from tests of materials, seams, and joints were reviewed, and the values for the major structural members applicable to TB-3, TB-4, TB-5, and TB-6 were abstracted for use in the selection of materials for BALLUTE fabrication.

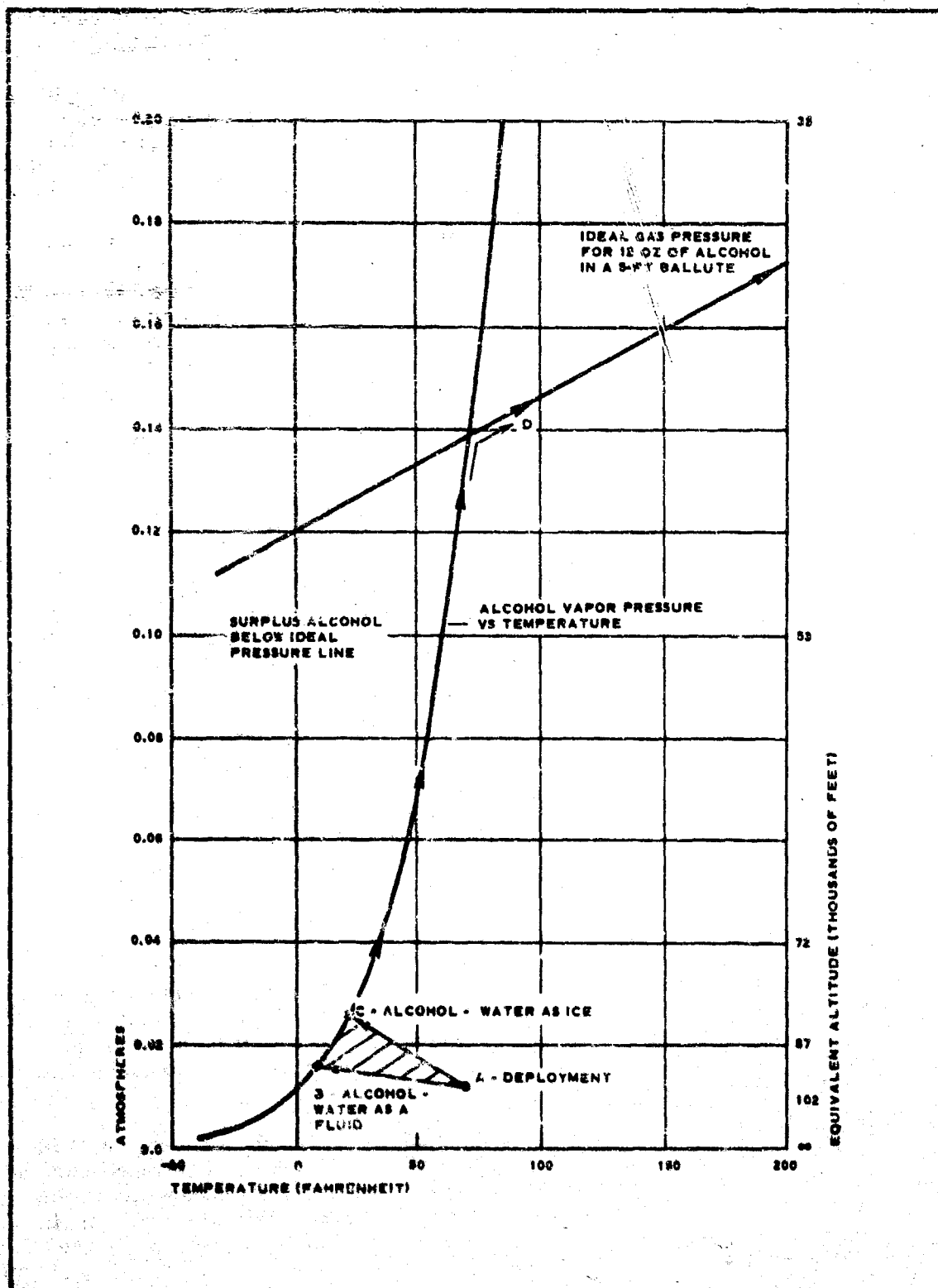


Figure 59 - Calculated BALLUTE Internal Pressures and Temperatures Based on TB-3 Flight Test Conditions

b. Material Selection

In view of the TB-3 and TB-4 loads, design factors, and material requirements, Stern and Stern HT-122-45 11.84 oz/yd² Nomex cloth was selected to fabricate TB-3, TB-4, TB-5, and TB-6.

c. Materials Test Data

The HT-122 Nomex cloth used for the gores, inlets, meridians, and risers was tensile tested; the test results are shown in Table XXI, Part A. Test result data for gore and riser seams are presented in Table XXI, Part B. The characteristics of the sewing threads used in BALLUTE fabrication are given in Table XXI, Part C.

Exact static margins for the inlet attachments, keeper rings, and loops have not been established by static tests. However, full-scale wind-tunnel tests for as long as five hours have established their structural strength and acceptability (Reference 45).

Permeability tests were conducted using helium at a pressure of 3 cm of water across specimen coated with Dyna-Therm elastomer to the design values; i. e., one light coat each side, plus an additional heavy coat inside and two additional heavy coats on the outside. The values measured under these conditions on the Cambridge permeameter varied from equivalent to 0.001243 ft³/ft²/min to 0.01368 ft³/ft²/min.

Nomex strength variation with respect to varying thermal conditions is shown earlier in Figure 53 as percent of room temperature strength versus temperature.

Materials were heat-tunnel tested to determine their response to heating conditions similar to the TB-4 flight conditions. The Goodyear Aerospace heat tunnel is a continuous flow facility that uses heated high pressure gas expanded to Mach 8. The samples were mounted in a controllable holder downstream of the nozzle. The holder was within a large test chamber evacuated by a four-stage ejector pump system. Heat flux rates were controlled by the stagnation temperature (to 1400 F) and by the stagnation pressure (to 150 psi) of the gas. Heat flux rates to 20 Btu/ft²-sec were accomplished easily with the heated gas system. The stagnation and chamber pressure ratio was set to match the Mach 8 nozzle pressure ratio requirements. The diameter of the exiting flow under these conditions was approximately two inches.

A list of the better candidate coatings and the test conditions are presented in Table XXII. The coated specimen were tested at 40 deg to the flow, which corresponds to the BALLUTE surface at the maximum heating conditions. Lower angles also were used for uncoated samples as a control. All specimen were two inches wide and were preloaded. Preload values were used in conjunction with Figure 53 to obtain a gross check of the average fabric temperature at failure. All the coatings gave a considerable increase in the time to failure, from 6 to 20 times.

**TABLE XXI - NOMEX TEST RESULTS AND
CHARACTERISTICS**

Part A - General Tensile Test Results

Material	Width (in.)	Rated strength	Application	Ultimate load (lb)
Nomex HT-122, 11.84 oz/yd ² , λ = 45.7 ft ³ /min.	Cloth 1-in. wide ravelled	. . .	Gore and inlets	Warp: 538, 33 per- cent elongation Fill: 548, 31.2 percent elongation
Nomex, similar to MIL-W-5626	1-in. wide	3000	Meridian and risers	High: 3100 Low: 3050

Part B - Webbing Seam Tensile Tests

Specimen	Width (in.)	Stitching	Application	Average load
Nomex HT-122, 5/8-in. wide double felled seam	2	4 rows, F thread, 10 to 11 per inch	Gore seam	450 average per inch
Nomex webbing MIL-W-5625, double 3 point seam	1	Two 2-1/4-in. , 3 point spaced, 1 in. apart, 3 cord, 190 stitches	Riser seam	2850 average

Part C - Characteristics of Sewing Threads

Size	Tensile strength (lb)	Loop strength (lb)	Weight (gm/ft)	Diameter (mil)
E	7.46	11.69	0.0197	7.25
F	16.68	24.46	0.0453	13.50
F-F	23.00	35.58	0.0631	16.75
3 cord	23.50	35.98	0.0607	14.75
6 cord	44.44	68.54	0.1248	24.75

TABLE XXII - TEST RESULTS OF MATERIALS USING
HEAT TUNNEL*

Item	Angle to flow (deg)	Preload (percent of room temperature quick break)	Time to failure (sec)	Heat flux (Btu/ft ² -sec)
Bare	10	10	No failure after 60 sec	2.8
Bare	20	10	No failure after 60 sec	3.1
Bare	30	10	No failure after 60 sec	6.1
Bare	40	10	15.60	12.9
Bare	40	10	11.50	12.9
Coated with 11-12 mils D-65 (Dyna-Therm)	40	5	95.20	12.9
Coated with 11-12 mils D-65 (Dyna-Therm)	40	5	70.45	12.9
W/9 mils 92-009 silicone (Dow-Corning)	40	5	78.50	12.9
W/9 mils 92-009 silicone (Dow-Corning)	40	5	129.50	12.9
W/11-15 mils GE RTV 511 (General Electric, Silicone Products Dept.)	40	5	115.60	12.9
W/11-15 mils GE RTV 511 (General Electric, Silicone Products Dept.)	40	5	217.70	12.9

* Using Nomex HT-72 (8.67 oz/sq yd and a 398 lb/in. room temperature warp strength) and Mach 8.

8. DESIGN AND FABRICATION

a. General

During ADDPEP Phase II, two basic textile BALLUTE designs of similar construction but of slightly different configuration were designed and fabricated:

1. Configuration One: TB-3
2. Configuration Two: TB-4, TB-5, TB-6

The test BALLUTE, packed in its deployment bag, formed the test decelerator package as it is stowed into the Test Vehicle C. The stowage arrangement is shown in Figure 4, Section II, of this report. BALLUTE TB-3 was fabricated to the detail requirements of Drawing 530A005-022 and is described in detail in Reference 41. A complete description of the BALLUTE decelerators is presented in Section IV of the Phase I report (Reference 1). Significant details of only TB-4, TB-5, and TB-6 are included in the following discussion.

b. BALLUTES TB-4, TB-5, TB-6**(1) Design**

Sheets one and two of Drawing 530A005-201 (Reference 70) show the Configuration Two BALLUTE assembly and gore patterns. The configuration of TB-4, TB-5, and TB-6 is shown earlier in Figure 40; characteristics are defined in Figure 51. The BALLUTE is without a fence, and the envelope contour is the same as TB-2 and TB-3 (also shown in Figure 40).

The BALLUTE has 16 gores and 16 meridian webs. The bias gores are patterned to provide the correct lobe radius for this structure. The 16 meridian webs and the riser are formed by placing 8 webs continuously around the envelope and into the riser, forming the 16 riser webs. The webs end at the riser attachment loop. At the front of the BALLUTE the webs are brought through a 6-in. -diameter keeper ring. This ring is constructed of 12 turns of cord made from 6 Nomex 6-cord twisted together at a point 14.5 in. forward of the keeper ring. This arrangement is intended to keep the meridians oriented and loaded equally and to decrease the angle change at the keeper ring.

All the cloth used in the construction of the BALLUTE envelope is Stern and Stern Textiles, Inc., Pattern Number HT-122 plain weave Nomex, weighing 11.84 oz/sq yd. The Nomex webbing in the meridians and riser is similar to MIL-W-5625; it is 1 in. wide and has a rated strength of 3000 lb.

For cloth strength, all seams are sewn before final coating. Envelope gore seams are double-felled with 4 rows of stitches. After BALLUTE assembly, additional coats of D-65 are applied to the entire envelope surface (see Appendix III). The coating serves a two-fold purpose: (1) decreases the porosity of the fabric for proper inflation and (2) protects the cloth during aerodynamic heating (see Appendix IV).

Changes were made to improve the reliability of the inlet structure. This was done by moving the inlets more forward into a region where there is less movement and a much more flexible inlet structure. Thus, the movement of the fabric during the early inflation process does not result in critical loads in the frames or inlet structure. The inlet design is presented in drawing 530A005-G33 (Reference 71).

The inlet position on the envelope is approximately the same as that of TB-1A and TB-1B shown earlier in Figure 51. The mouth of the inlet is normal to the contour of the envelope, which differs from the 30-deg slope angle of TB-1 and TB-2. The metal inlet frames, springs and base, which were used in prior units, were eliminated. The only metal now used is a flexible seven-wire hoop incorporated into the inlet lip itself. Webs are provided for initial erection and support of each inlet. Material and coating thickness were added to the inlet lips and regions of small radii to sustain the local high heating rates.

The method of erecting and supporting the inlets using folded 0.5-in. webbing is detailed in Drawing 530A005-201 (Reference 70). A top center and bottom center attachment to the inlet hoop was selected to allow

the inlet to align itself laterally to the flow. The inlets were provided with socks to prevent reverse flow.

A preinflation system using liquids is used to attain an early inflated shape and to cool the structure during the initial high heating rates. The liquid is a solution of 12 oz methyl alcohol and 4 oz water; this liquid is contained in two latex bladders both placed end to end within a 2-piece cloth cylinder (bag) that was held together with lacing.

The fluid bag assembly is shown in Drawing 530A005-111 (Reference 73). As presented in Drawing 530A005-036 (Reference 73), one end of the cylinder is attached to the nose of the BALLUTE, and the other end is attached to the rear of the BALLUTE/deployment bag. As the BALLUTE is stretched during deployment, the lacing is broken and the cylinder is pulled into a forward and a rearward half. The rear latex bladder is attached to the forward half of the cylinder, and the forward latex bladder is attached to the rearward half of the cylinder; thus, the bladders are broken and the fluids dispersed during the separation of the cylinder. Vaporization of the fluid results in envelope initial pressurization and cooling.

Five chromel-Alumel thermocouples are woven into the envelope cloth prior to coating. The wires from each thermocouple lead over to adjacent meridians and then forward to the riser and connection to the test vehicle. The thermocouple location and installation technique is shown in Detail R of Drawing 530A005-201. (Reference 70).

A hose from the forward portion of the BALLUTE envelope transmits the pressure to the test vehicle. The hose consists of a latex tube with a continuous wire spring inserted within to prevent tube collapse. The latex tube is within and is supported by a tubular web from the BALLUTE to the pressure transducer in the test vehicle.

(2) Fabrication

Fabrication has been done according to the detail design requirements of Drawing 530A005-201. Prior to dimensional marking and cutting, heat-set and scoured Nomex cloth is stretched and clamped on frames with warp and fill linearity established. The cloth is then primed with a thin coat of Dyna-Therm D-65 elastomer. Templates dimensioned to Drawing 530A005-201 are used as a guide for marking and cutting the stable Nomex fabric. Prior to closing the final gore seam, a thin coat and a full coat are applied to the total envelope inside surface. An additional full coat is then applied locally to the stitched areas. Next the BALLUTE is closed, and two full-coats are applied to the outside of the fabric. After the BALLUTE is completely fabricated, the liquid initial pressurizing system is installed.

c. Deployment Bags TB-4, TB-5, TB-6

The deployment bag for TB-4, TB-5, and TB-6 is presented in Drawing 530A005-050 (Reference 74). The deployment bag is fabricated from nylon materials and is approximately 20 in. in length, 15.5 in. in diameter, and shaped to fit the test item container. The bag is reinforced

with six equally spaced webs and three lateral webs, one around each end and one at the center. The six external longitudinal webs are attached to the bag rearward half and become the bridle to the test item container. BALLUTE storage requires two bag compartments. Compartmentation is accomplished by loops of webbing sewn longitudinally to the inside of the bag. The rearward portion is used to retain the envelope, and the forward portion is used to stow the riser lines.

9. DEPLOYMENT SEQUENCE AND PACKING PROCEDURE

a. Deployment Sequence

The BALLUTE deployment system is shown in Figure 60. This system is illustrated by a sequence of six steps that represent various times and events from the start of container separation to BALLUTE partial inflation.

b. Packing Procedure

(1) Installing Fluid Bag

Prior to packing the BALLUTE into the deployment bag, the fluid bag containing the initial pressurization liquid is installed into the BALLUTE envelope. The method of filling and installing the fluid bag is presented in Drawings 530A005-036 and 530A005-111 (References 72, 73). The fluid bag installation is accomplished through an envelope inlet.

(2) Folding BALLUTE Envelope into Longitudinal Pleats

The envelope is folded into pleats as shown in Figure 61. The folds are laid out to keep the final pleated arrangement approximately 12 in. wide. The inlets are positioned so that they are arranged in two groups of two-high each. The folding is started by orienting the envelope portion containing the forward fluid bag lanyard within the first (bottom) pleat. The fluid bag is positioned at 90 deg to the BALLUTE axis and at a point approximately 15 in. in front of the inlets.

(3) Folding Pleated Pile

The first fold is made as close possible to the front of the inlets, so that a full-folded pile can be created between the fluid bag and the inlets. The envelope folding is continued using serpentine folds. When the BALLUTE is completely folded, it forms a stack approximately 12 in. square.

(4) Attaching Apex Cord

A single MIL-C-5040 Type III Cord (550 lb) is used for the apex cord installation (Reference 73). The end of the cord is doubled back in the knot area, and a bowline is tied in the doubled cord around the top four webs at the envelope apex using a bowline in the single cord. The effective length of the line should be approximately 18 in. long.

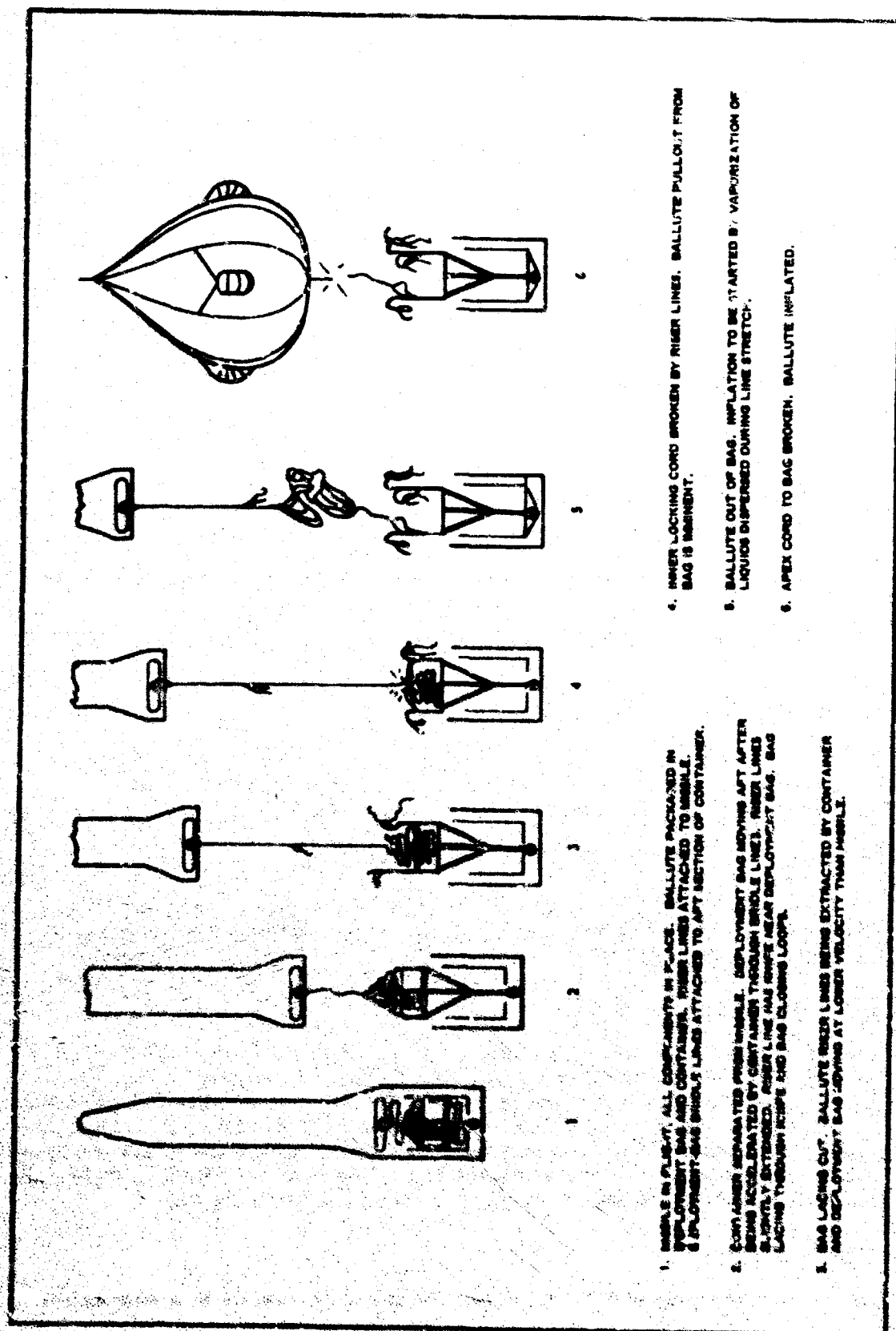


Figure 60 - BALLUTE Deployment Sequence

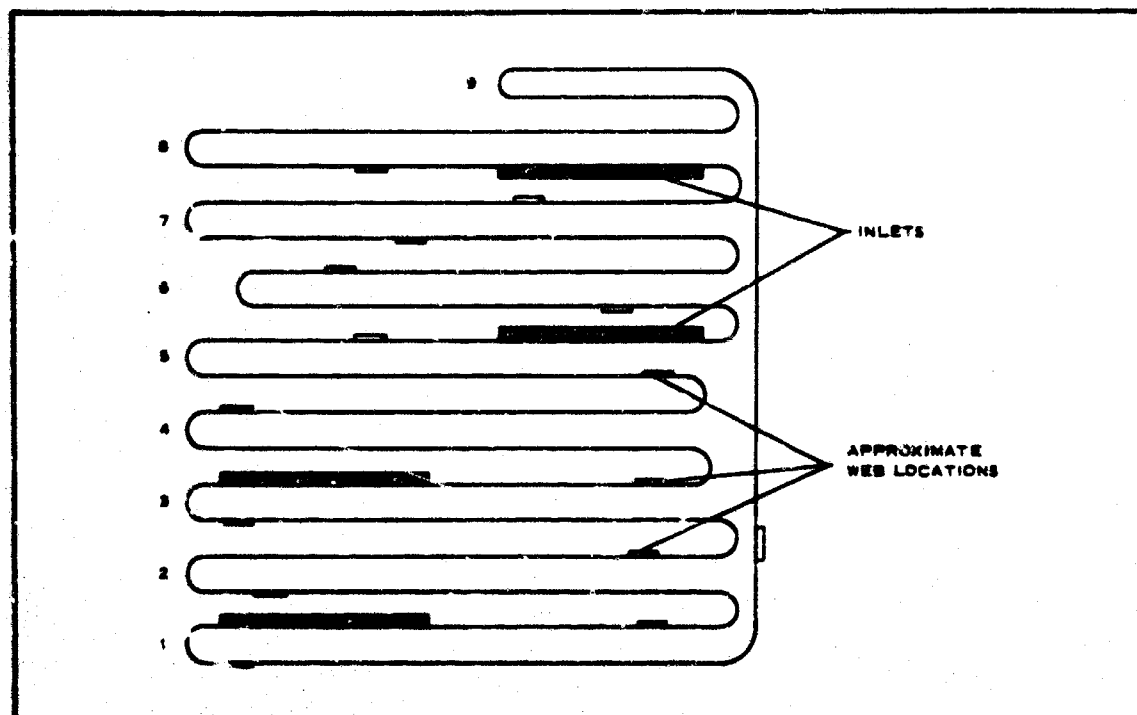


Figure 61 - TB-4 Longitudinal Pleating Arrangement

(5) Attaching Fluid Bag Lanyard

The aft fluid bag lanyard is attached to the same loop to which the apex cord was attached. A bowline is tied, locating the mark specified in Drawing 530A005-036 within the loop (Reference 73).

(6) Placing BALLUTE Envelope into Deployment Bag

The folded BALLUTE envelope is placed into the deployment bag by inserting one fold at a time. Apex chords are placed, free of tangles, at the bottom of the deployment bag.

(7) Installing Inner Lock Cord

One turn of MIL-C-5040 Type III (550 lb) cord is made through the three locking loops in the deployment bag and through the breaking loop provided on the BALLUTE (530A005-261-29 Web). The cord is installed so that it passes around all the BALLUTE webs except three: the one web supporting the breaking loop and the two webs on which the pressure tube and the thermocouple leads are attached. The cord is drawn up tight and tied with a surgeon's knot plus an over-hand knot in each tail.

(8) Stowing Riser Line

The risers are placed into the deployment bag by means of a serpentine

folding technique, keeping the end loops oriented and free from twists with respect to the deployment bag. Each fold is tacked to an inner lock cord, with one turn of three-cord sewing through all webs except the wire-carrying webs. Caution is exercised during the stowage to prevent puncturing the pressure sensing tube, and care is taken that the tack cord is not placed around the pressure sensing tube.

(9) Closing Deployment Bag

The forward deployment bag material is gathered into pleats around the riser at a point just below the cutter knife. The pleats are stitched to the riser with F thread in such a manner that, when the riser breaks the thread, all stitching pulls out freely.

The closing cord is installed by making three turns of MIL-C-5040 Type III cord (550 lb) through the six outer deployment bag loops and through the cutter knife provided on the BALLUTE riser. The ends of the cord are continued into the grommet lacing at the sides of the bag, one cord end to each side of the bag.

A single-cord pattern is laced as shown in Figure 62 and is terminated at a bottom grommet with two half-hitches and an overhand knot in the tail. The cords are tied away from the cutter's edge with two pieces of F thread, as shown in Figure 63.

10. SUMMARY AND CONCLUSIONS

a. Configuration

In generating four flight-test configurations, two textile BALLUTE envelope shapes were used with variations in inlet locations, fence sizes, and fence locations. Free-flight or wind-tunnel tests showed all configurations to be stable, inflated shapes at supersonic velocities.

Internal pressure coefficient control was attempted by inlet position; this was the basic reason for the many variations of inlet and fence positions. Internal pressure coefficients were of fundamental interest since the most efficient BALLUTE structure design considers the internal and external pressures. Wind-tunnel and free-flight test data revealed that, at Mach numbers greater than 2.5, the internal pressures for a trailing BALLUTE were greater than needed for a BALLUTE with an included angle of 80 to 85 deg. The test data also showed that, for the many inlet locations tested, the values increased and reached a plateau above Mach 4 (Figure 49).

All the data presented as symbols in Figure 49 are ADDPEP free-flight tests or wind-tunnel versions of former flight-test units. The curves are based on the results of measured values over the complete Mach number range. Hard models utilizing many inlet configurations are used with and without a missile-type forebody. Two analytical curves are presented for reference - one based on a one-shock system from free-stream conditions and the other on a two-shock system from free-stream conditions. The two-shock system provides good correlation with test data to Mach 4

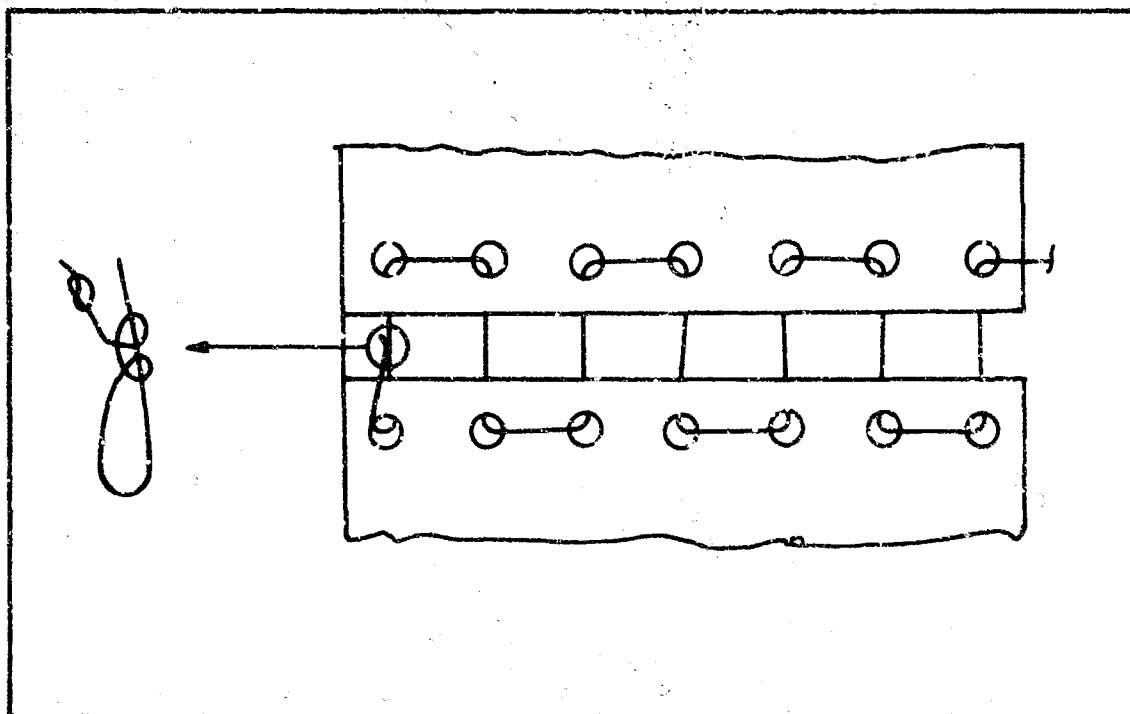


Figure 62 - Deployment Bag Lacing Technique

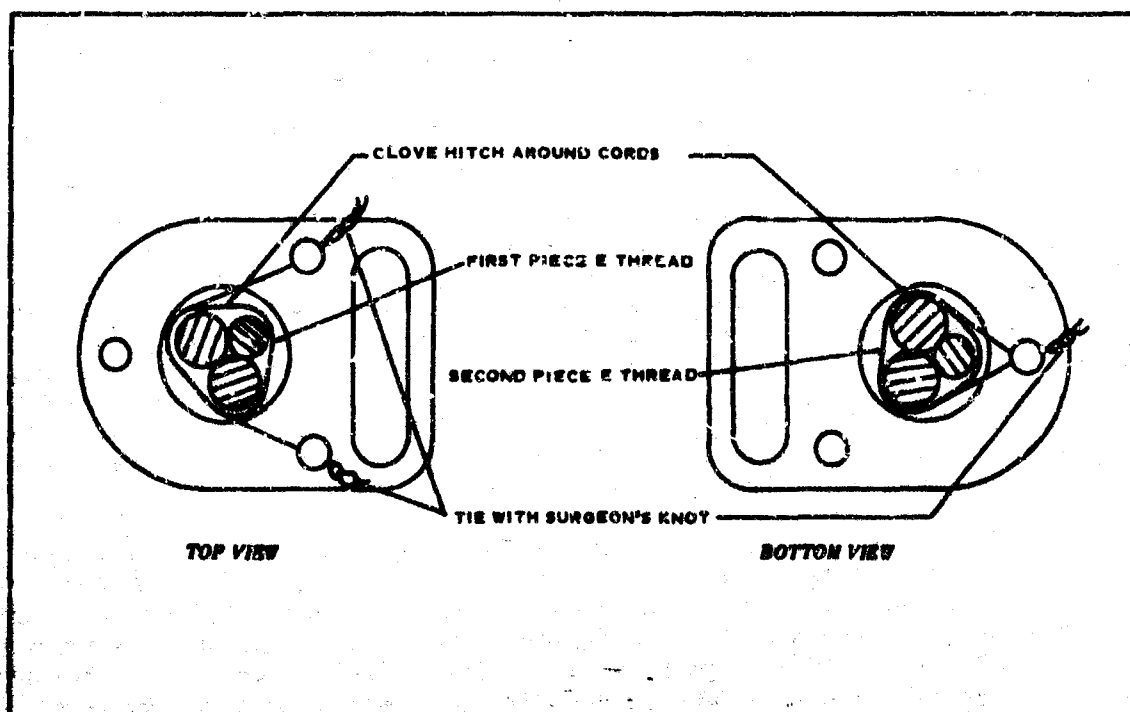


Figure 63 - Closing Cord and Cutter Arrangement

for towed units. For units without a forebody, the values are lower but above the one-shock system values.

It is not known why there was a large variation in measured internal pressure coefficient near Mach 3 in the wind-tunnel tests using flight-type units. The high inlets were expected to have less recovery than the low for test item TB-3WT; however, the values for TB-1BWT and MB-1 were far below anticipated values. Based on these results, it is concluded that the instrumentation approach and the flow phenomena approaching the inlets need further investigation.

b. Aerodynamic Loadings

On the basis of the free-flight and wind-tunnel test results, the selected configurations did take their predicted shapes while under load. These shapes were determined from estimated internal and external pressure distributions. Analytical approaches for determining the external pressure distribution are presented in Reference 1, and distributions for higher Mach numbers are presented in Figure 48. The correlations between analytical and wind-tunnel values are sufficiently accurate for engineering use of the analytical methods up to hypersonic Mach numbers (greater than five). In the hypersonic regime, the forebody wake reduced external pressure coefficient values near the central portion of the BALLUTE below those predicted ignoring the wake.

The drag values measured in the wind-tunnel correlate with the free-flight test data (Figure 50). The wind-tunnel values are more consistent with each other because of the more accurate knowledge of the test conditions. Based on these results, it is concluded that the wind tunnel is an excellent tool for BALLUTE drag and stability measurements.

Filling times are normally defined as the period from snatch load to maximum load. With a BALLUTE, this occurs when the internal pressure coefficient is approximately one. Free-flight and wind-tunnel tests indicate this occurs in approximately one second (References 47, 48, 54). Filling time to this condition can be calculated using methods presented in Appendix VI of the ADDPEP Phase I report (Reference 1). Normally at free-stream Mach numbers greater than two, the pressure ratio across the inlet is sufficient for sonic flow within the inlet until an internal pressure coefficient of one is attained. Figure 49 presents typical pressure coefficient values at the inlet.

Methods to reduce filling times were also investigated. Wind-tunnel tests were conducted using 12 oz alcohol and 4 oz water as an inflation aid. This measure decreased the time to maximum drag to two-thirds of the time without an inflation aid (Figure 41). The effect of the liquid on the filling time can be determined by calculating that portion of the total BALLUTE volume filled by the liquid under the temperature conditions existing within the BALLUTE at an internal pressure coefficient of one.

c. Geometry

Review of the wind-tunnel data films indicates that firm envelope shapes

can be obtained with all the configurations (Mach 2.6 to 3.0). Based on these observations, it is concluded that no changes are required for geometry analysis.

d. Structure

Inspection of the BALLUTES after each test confirmed the structural adequacy of the envelope, fence, and meridians for the design conditions. Problem areas were limited to the inlet structure on TB-3 and the coating on TB-2. The inlet structure was improved for TB-4, TB-5, and TB-6 by eliminating all metal parts except the hoop in the inlet mouth. This hoop was changed from a single wire to a multiple wire cable type structure to allow greater flexibility.

The TB-2 coating was applied to TB-3 techniques, and it performed satisfactorily. No problems were associated with the other coatings. Pressure instrumentation was associated with all flight tests. A tube carried the pressure from inside the BALLUTE to the vehicle transducer. On the TB-3 and TB-4 flights, five thermocouples were also imbedded in the envelope fabric along a gore. Light wire woven into the fabric and over to the meridians carried the readings forward to the vehicle instrumentation. Based on the tests, the pressure tube and the thermocouple approaches were structurally adequate for obtaining data.

e. Thermodynamic Analysis

A thermodynamic analysis was performed to (1) compare the predicted material temperature values with the measured temperature values for the TB-4 flight test and (2) evaluate the predicting technique. Based on the evaluation, the prediction technique is considered acceptable for engineering design. One reason for some conservatism during the ascent phase is omission of the heat absorbed by the liquid vaporizing. This amounts to approximately 700 Btu or 100 F in BALLUTE material temperature.

The effect of fluids on the BALLUTE material temperatures can be seen more clearly on the TB-3 test, where the heating rates are lower and the cooling action is more obvious (Figure 45).

f. Materials

The materials selected performed as required and included (1) nylon coated with neoprene, (2) nylon coated with polyurethane CUR 71A, (3) Nomex coated with Silastic 131, and (4) Nomex coated with Dynatherm D-65. No appreciable differences were found between nylon and Nomex as the structural cloth or webbing for accepting the loads. High efficiency, gas-tight seams were established in both materials by using tightly woven, plain weaves. Cloth was heat-set and scoured by the supplier to reduce shrinkage and to clean the material before coating.

Neoprene and polyurethane CUR 71A proved satisfactory coatings for nylon. The polyurethane was more flexible and penetrating than the neoprene. Silastic 131 and Dynatherm D-65 were used satisfactorily with Nomex cloth.

g. Design and Fabrication

The basic changes to the BALLUTE designs that evolved during Phase II were for accepting higher heating rates and/or higher loadings than the designs presented in the Phase I report (Reference 1). Aside from material changes, the design changes were associated with the inlets, the fence, and the partial inflation and cooling aid. Based on the program results, it was concluded that the final inlet designs are structurally superior to the metal-supported designs. The wind-tunnel tests confirmed that a BALLUTE is stable without a fence at supersonic speeds. The inflation and cooling aid approach appears to be practical for high altitude use and should be considered in the design of a BALLUTE recovery system.

h. Deployment System and Packing Procedure

The deployment and packing procedure was satisfactory for all tests. No changes are recommended for further tests.

SECTION V

METAL BALLUTE DECELERATOR

1. GENERAL

a. History

The analysis of BALLUTE decelerators at the higher Mach numbers and associated aerodynamic heating pointed to theoretical limits in the use of textile cloths and the need for a BALLUTE fabricated from metal cloth materials. During ADDPEP Phase II, the investigation of the design and fabrication of a metal BALLUTE (MB) decelerator was concurrent with the task of textile BALLUTE (TB) development. The goal for the metal BALLUTE was Mach 10 at 200,000 ft.

Three metal cloth BALLUTE decelerators were designed and fabricated. Two were wind-tunnel models, designated MB-1WT1 and MB-1WT2. Both were tested in wind tunnels for progressive study and evaluation of the design and construction requirements for a flight test model. The third metal cloth BALLUTE, designated MB-1, was a prototype flight test model, and was tested satisfactorily in the wind tunnel. The design and fabrication of two other metal cloth flight test BALLUTE decelerators, designated MB-2 and MB-3, were considered but delayed pending evaluation of the performance limits of coated Nomex cloth BALLUTES.

b. Conditions

The test environment for the metal BALLUTES was originally intended to extend the BALLUTE decelerator applications into the areas where aerodynamic heating would preclude use of Nylon or Nomex fabrics. The test item deployment conditions at the beginning of each trajectory are presented in Table XXIII. The changing parameters after deployment for MB-1, MB-2, and MB-3 are similar to the curves for TB-4, TB-5, and TB-6 (Figures 37, 38, and 39, Section IV). Therefore, the MB curves are not given in this section.

c. Configuration Selection

All considerations for the evolution of textile BALLUTE configurations are applied to the configuration selection for the metal BALLUTE series. The basic isotenoid shape and configuration of TB-3 (Reference 75) was selected for MB-1. The MB-1 configuration is shown in Figure 64. The geometry does not include the usual burble fence attachment found on TB-1 and TB-2 since it was not deemed necessary for hypersonic stability at the selected altitude. This approach simplified the construction for this initial test condition, and the TB-3 free-flight test proved feasibility. Dimensions of configuration are given in Item 4 of this section.

2. WIND-TUNNEL TESTS

a. Wind-Tunnel Models

The purpose of metal-BALLUTE wind-tunnel testing was to establish a

TABLE XXIII - METAL BALLUTE INITIAL FLIGHT
PARAMETERS AT DEPLOYMENT

Condition	Design configuration		
	MB-1	MB-2	MB-3
Mach number	5.7	7	11
Altitude (10^3 ft)	120	130	220
Dynamic pressure (psf)	220	215	15
Flight path angle (deg ascent)	75
Ballistic coefficient of system (psf, missile plus BALLUTE)	30	30	30
Reynold's number ($l = 5$ -ft diameter)	1×10^6
Booster combinations*	HJ-N-L	HJ-N-L	XM-33/2XM-19-L

* Definitions: HJ = Honest John; N = Nike; L = Lance

final design for the flight test item, MB-1. The first metal cloth BALLUTE design selected for wind-tunnel testing, MB-1WT1, has a 60-in. diameter and the configuration of the textile BALLUTE TB-3. The MB-1WT1 unit was fabricated from Cloth B-304S stainless steel fabric and state-of-the-art for joining to the detail design requirements of Drawing 530A005-021 (Reference 76).

The MB-1WT was tested at AEDC on 22 December 1964 (References 3, 15). Deployment was at Mach 3 and a free-stream dynamic pressure of 118.9 psf. Deployment was normal, with the BALLUTE going to line stretch and the inlets aligning into the airstream. Normal inflation cycles began and after several oscillations of filling the envelope separated from the meridians and moved intact to the rear of the meridian cage. Observation of the deployment indicated that normal inflation did not occur.

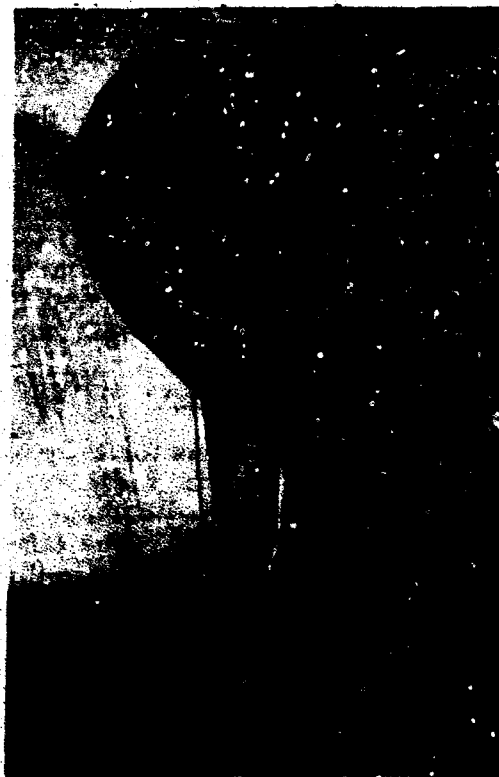


Figure 64 - MB-1 Metal BALLUTE

A further investigation of the metal BALLUTE fabrication techniques was undertaken to determine the loads the structure was capable of carrying under the events that occurred during the wind tunnel tests (Reference 15). Additional samples of candidate methods of attachment were fabricated and tested, both statically and dynamically (flag flutter models) for the design of MB-1 (References 9, 15). The modifications deemed necessary for the structural integrity of MB-1 were incorporated into the design of a second wind-tunnel model, MB-1WT2 (References 4, 9). In addition to improvements in the attachments between the meridians and the envelope fabric, thermocouples for the measurement of envelope temperature were added to MB-1WT2 to establish structural suitability under the deployment and inflation cycle loads. Pressure tubes were located to measure inlet and internal pressures.

The MB-1WT2 model was also fabricated from Cloth B-304S stainless steel fabric to Drawing 530A005-023 (Reference 77). It was tested at AEDC in April 1965 (Reference 75). The test results indicated normal deployment with the BALLUTE going to line stretch and the inlets aligning into the airstream. Normal inflation cycles began with the BALLUTE 1/4 to 1/3 full when a tear developed. This was caused either by a high inlet tearing off or by a stress concentration in the envelope material behind an inlet. The tear progressed, and the BALLUTE deflated.

b. MB-1 Wind-Tunnel Test

Previous failures of MB-1WT1 and MB-1WT2 pointed to a possible low probability of successful deployment for these metal BALLUTES. Therefore, MB-1 with structural improvements incorporated (see Section V) was tested under wind-tunnel conditions. The liquid initial inflation aid system utilized in TB-4, TB-5, and TB-6 was also installed into MB-1.

The MB-1 flight-test item was tested at AEDC on 11 May 1966 (Reference 45). Deployment was at Mach 2.8 and at a free-stream dynamic pressure of 120 psfa. The BALLUTE attained full inflation in approximately 0.46 sec after full line stretch. When fully inflated, MB-1 was stable and exhibited no oscillation. The thermocouple attachment approach was established by continuity being preserved during the tests.

Figure 65A plots the MB-1 pressure and temperature times. The temperature drop within the BALLUTE is the result of the vaporization of the alcohol-water solution contained in the liquid inflation aid system. Drag force versus time is shown in Figure 65B.

3. AERODYNAMIC ANALYSIS

The aerodynamic analysis and how it supports the design of the BALLUTE is presented in Section IV, Item 3 of this report and in the ADDPEP Phase I report (Reference 1). The configuration selected for the metal BALLUTE is shown in Figure 64. The pressure coefficient distribution used for design for Mach 10 design is presented in Figure 48 (Section IV). Internal pressure values based on those measured using TB-3WT were anticipated for design to be three or higher. Actual measurements during MB-1 wind-tunnel test at Mach 2.8, using a single internal tube, gave an approximate value for internal pressure coefficient, C_{p_i} :

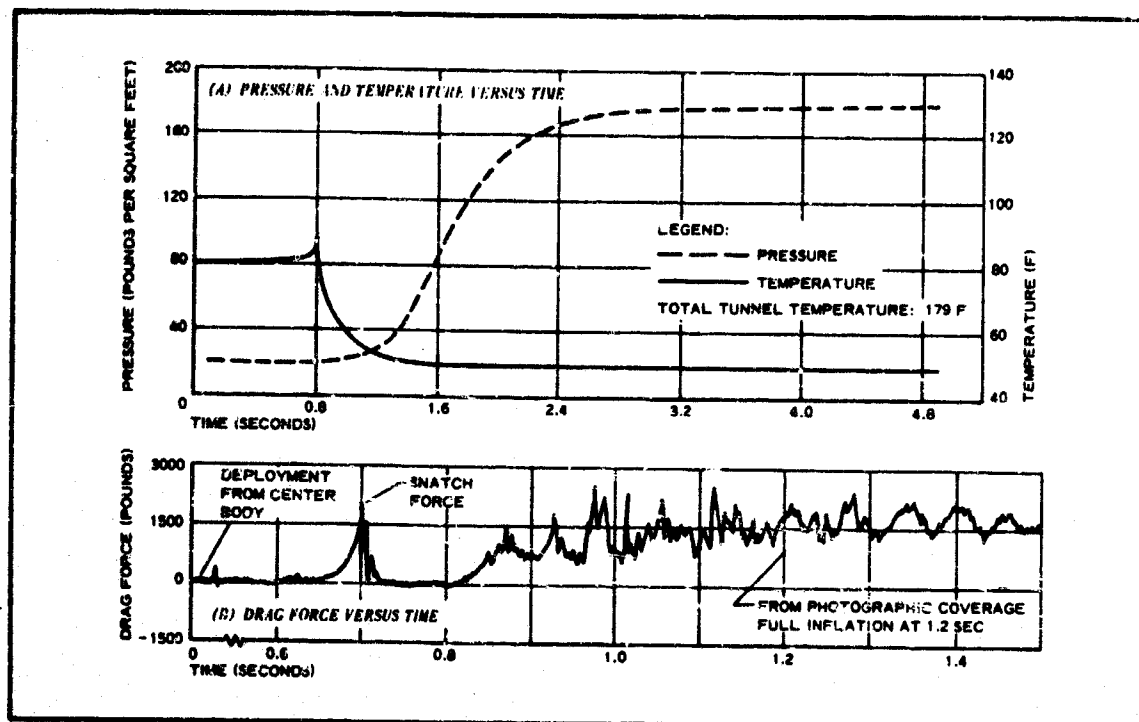


Figure 65 - MB-1 Wind-Tunnel Deployment: (A) Pressure and Temperature versus Time; (B) Drag Force versus Time

$$C_{P_i} = \frac{180 - 21.8}{120} = 1.32 \quad (77)$$

This value is much lower than values previously measured using similar configurations under the same test conditions (Figure 49, Section IV). The drag coefficient was 0.716, which compares with 0.733 for TB-4WT having the same envelope shape (Figure 50, Section IV).

4. BALLUTE GEOMETRY

The metal BALLUTE design used the same basic envelope shape as TB-2 through TB-6 (Figure 51, Section IV). No fence was required because the test regime was totally supersonic. Therefore, the fence was deleted to save fabrication costs.

The MB-1 flight-test configuration evolved from a series of tests to establish a structurally sound metal fabric design. Figure 64 shows a photograph of the completed unit ready for test. Its dimensions are presented in Figure 66. The method of construction is described in Item 8 of this section. The wind-tunnel configurations, MB-1WT1 and MB-1WT2, have the same shape, and inlet locations, and dimensions as MB-1.

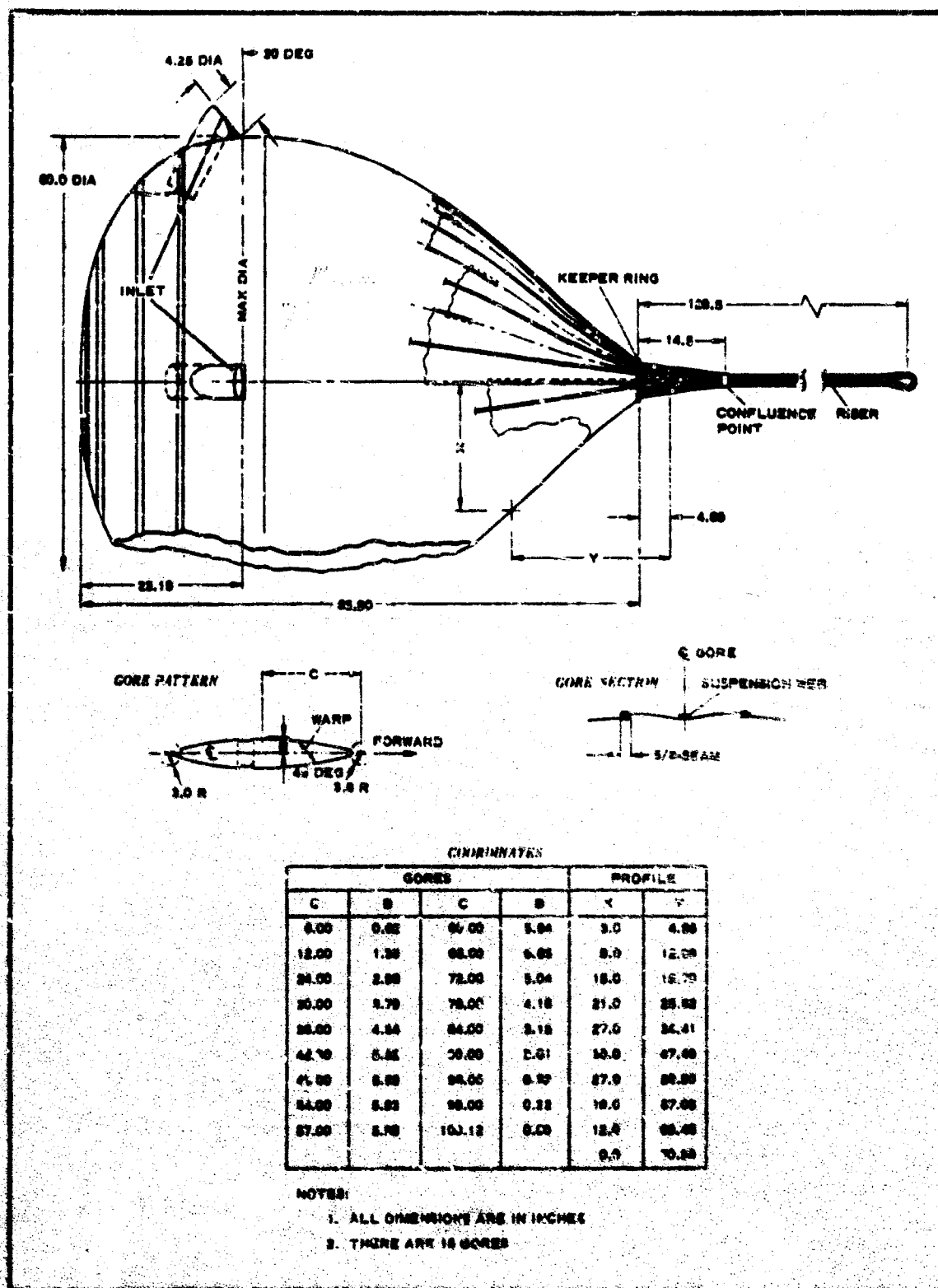


Figure 66 - MB-1 Configuration

5. STRUCTURAL ANALYSIS

a. General

The structural analysis for establishing BALLUTE shape and minimum fabric stresses has been based on static loads since it had been anticipated that maximum overall stresses will occur at full BALLUTE pressurization after the BALLUTE attains its final shape. Figure 67 presents data from two wind tunnel tests and one flight test supporting the assumption that a full shape is attained early in the pressurization cycle and that the shape changes very gradually during the final pressurization and maximum loadings.

Deployment tests of both textile and metal BALLUTES indicated that dynamic or flagging loads can cause local critical stresses that start small failures leading to larger failures before pressure loads become important. This was observed to occur shortly after line stretch and before any three-dimensional inflated shape is attained. No failures were observed once the BALLUTE became nearly filled. The base remained partly spherical without becoming flat or bowl-shaped (Reference 61).

Based on these test results, it became imperative, for a lightweight design, to establish a method that would partly fill the BALLUTE quickly. A liquid mixture with a vapor pressure greater than the ambient pressure was chosen as a simple, reliable approach for high altitude tests.

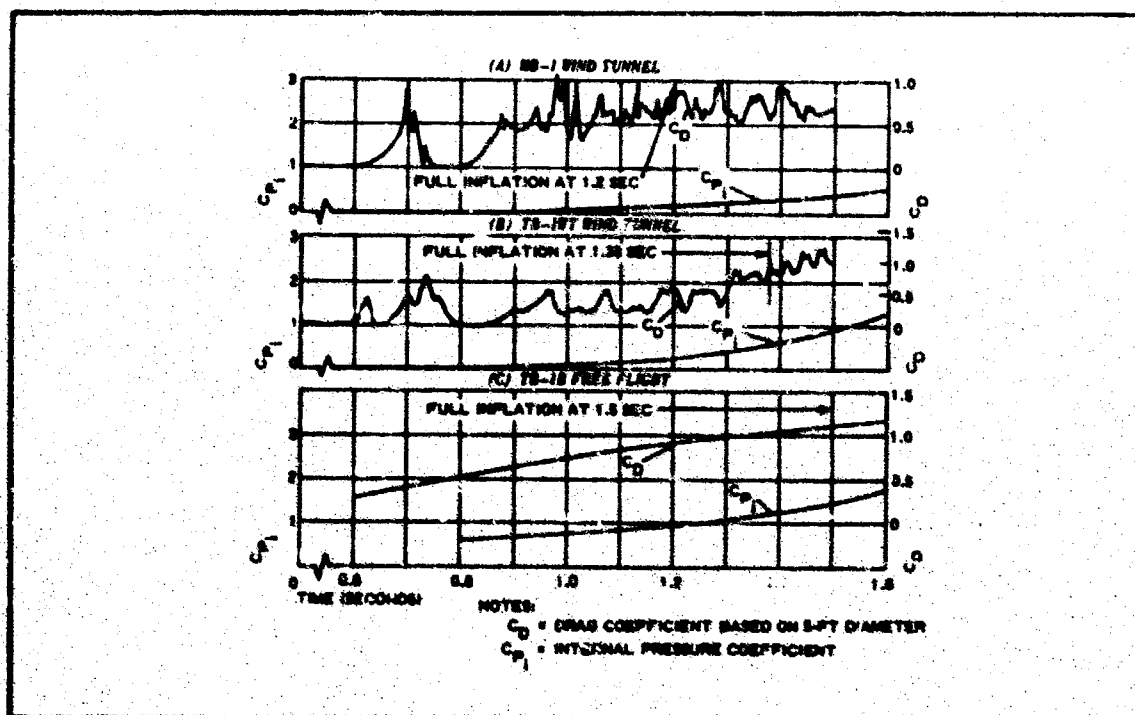


Figure 67 - BALLUTE Wind-Tunnel and Free-Flight Test Data (C_D and C_P versus Time)

With this approach, local pressures were limited to the vapor pressures of liquids, which are much less than final ram-air pressures and, therefore, were not considered critical in the design.

The static stress analysis described below was based on the assumptions that (1) with the addition of the fluids, the static pressure loads are the critical envelope loads; and (2) the loads occur when the BALLUTE is fully pressurized. The design was based on the internal pressure coefficient extrapolated from solid model wind-tunnel data, TB-1B free-flight data, and TB-3WT wind-tunnel data. The value of the internal pressure coefficient for Mach numbers greater than 4 became approximately 4 based on small models; and approximately 5 based on the full-scale models (Figure 49, Section IV). The envelope stress analysis was conducted in the same manner as for the textile BALLUTES (Section IV, Item 5).

b. Design Factors

The design factors to be imposed on the nominal test point and on the room-temperature, quick-break strength of the basic materials for a fabricated unit were:

1. Probable test point overload over nominal: 1.25
2. Probable increase in local static stress due to rapid loading: 2.00
3. One over seam or joint efficiency: 1.16
4. Room temperature strength per loading to strength per loading at critical loading: 1.00
5. Raking (strength when seam leakage becomes excessive to ultimate seam strength): 1.00
6. Standard factor of safety: 1.50
7. Product of the above factors: 4.35

The values for the separate factors follow the same reasoning as with the textile BALLUTES:

1. Factor 1 was reduced gradually toward the nominal test point as successive tests established that the Test Vehicle C booster combinations consistently deployed the test item very near the test point.
2. Factor 2 was left at 2.00 because some degradation was expected to the metal fabric as a result of rapid loadings and repeated shock type loadings.
3. Factor 3 was the result of welded seam tests.

4. With respect to Factor 4, Figure 68 shows the cloth strength as a percent of its room temperature strength. It is apparent that the load initially drops off as the material strength decreases due to temperature increase. Thus, a temperature factor of one is used in conjunction with the initial loadings for design.
5. With respect to Factor 5, tests showed that welded metal cloth seams maintain their yarn positioning up to the ultimate seam strengths. A raking factor of one was chosen based on these data.
6. For Factor 6, a standard safety factor of 1.5 was applied.

c. Test Point Consideration

The envelope cloth was tested over a range of temperatures to establish its physical properties. The results are shown in Figure 69. Based on these strength values, the design factors, and new internal pressure coefficients, the test points were reviewed. Since the configuration is not isotenoid at high Mach numbers:

$$\text{Static fabric stress}_{\max} = \frac{F'_{\max} P' R}{2} \text{ lb/ft} \quad (78)$$

Where:

F'_{\max} approaches 1

P' is $q(C_{P_{\text{internal}}} - C_{P_{\text{rear}}})$

P' is approximately $5q$

q is dynamic pressure

Substituting:

$$\begin{aligned} \text{Static fabric stress}_{\max} &= \frac{1(5q)2.5}{2} = 6.25q \text{ lb/ft} \\ &= 0.52q \text{ lb/in.} \end{aligned} \quad (79)$$

Then:

$$\begin{aligned} q_{\max} &= \frac{140}{(0.52) \text{ design factors}} = \frac{269}{\text{design factors}} \\ &= \frac{269}{4.35} = 62 \text{ psf} \end{aligned} \quad (80)$$

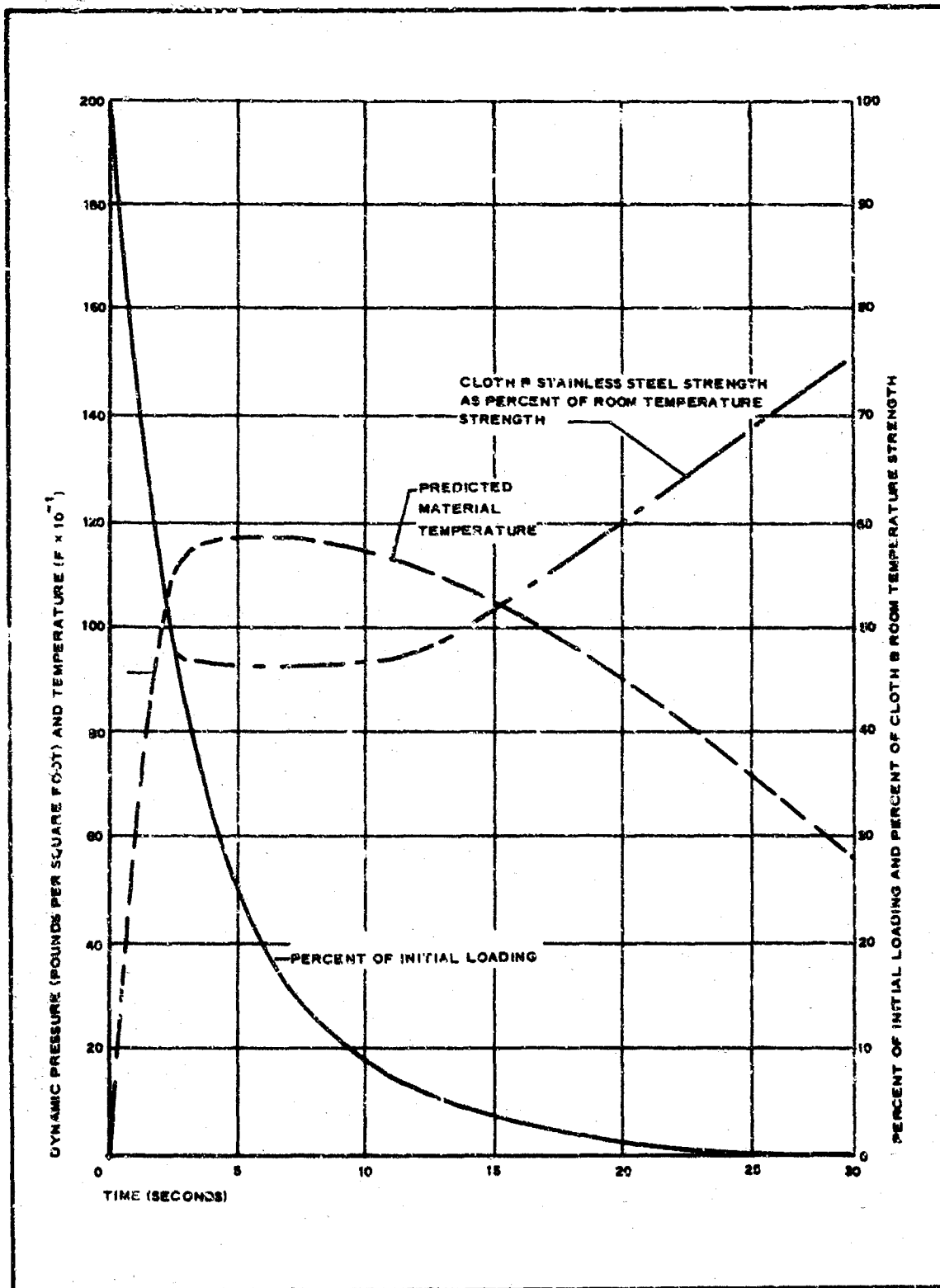


Figure 68 - Cloth B Strength and Loading versus Time

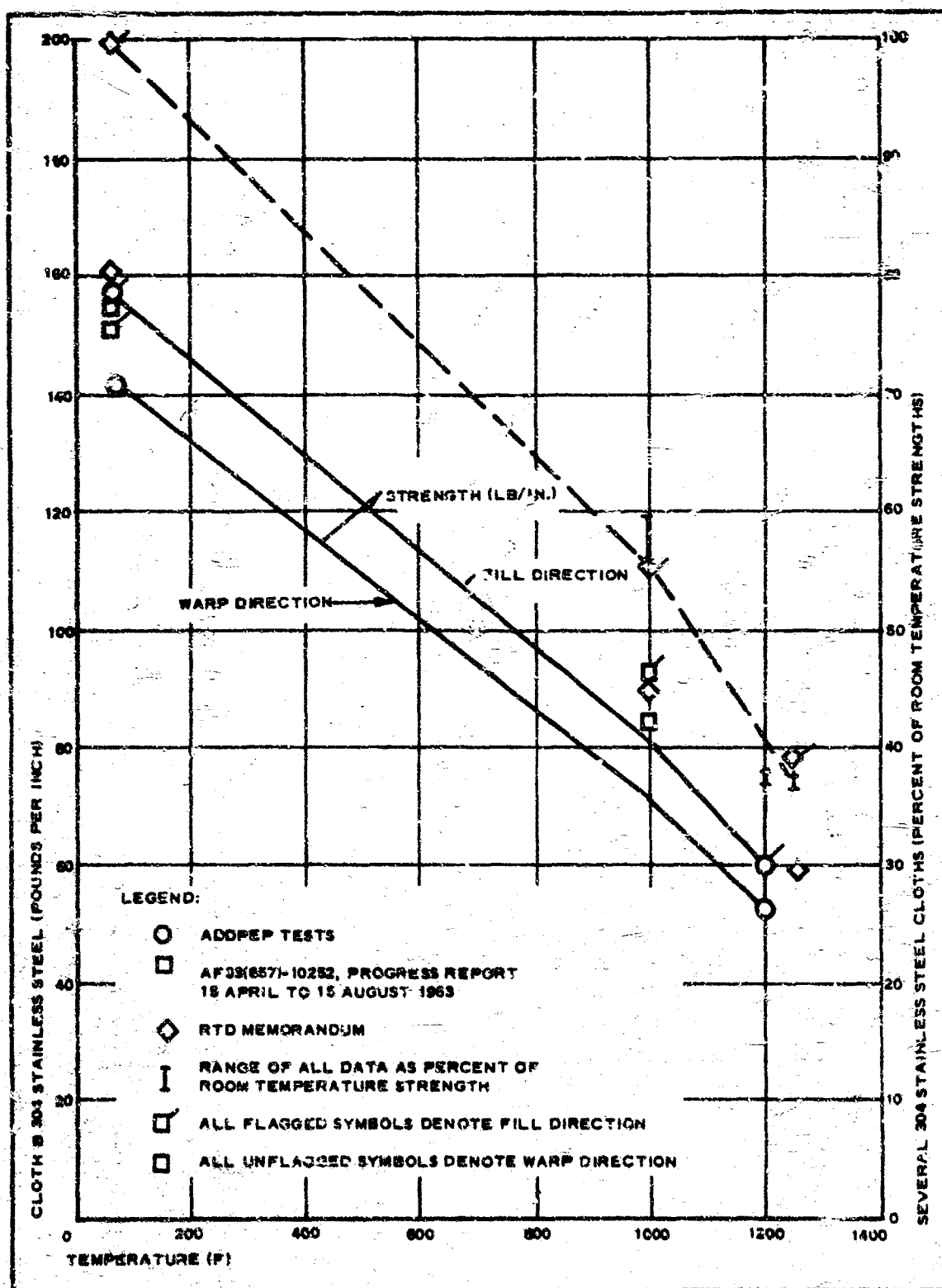


Figure 69 - Cloth B Strength versus Temperature

d. Design Stresses

By using a value of 62 psf for deployment, the stress for the components is as given in the following analysis.

With respect to envelope fabric, the q at full pressurization is approximately 60 percent of the 62 psf value or 50 psf. Using 50 psf:

$$\begin{aligned} \text{Fabric strength}_{\max} &= \frac{F'_{\max} P' R}{2} = \frac{1(5)50(2.5)}{2} \\ &= 312.5 \text{ lb/ft} = \frac{312.5}{12} = 26 \text{ lb/in.} \end{aligned} \quad (31)$$

Where.

$$F'_{\max} = 1$$

$$P' = 5q$$

$$R = 2.5 \text{ ft}$$

The inlet fabric tension equals the pressure differential times the radius. For 62 psf and $\Delta P = 5q$, this becomes:

$$\begin{aligned} \text{Inlet fabric tension} &= 5q(2.125) = \frac{5(62)}{144} 2.125 \\ &= 4.6 \text{ lb/in.} \end{aligned} \quad (82)$$

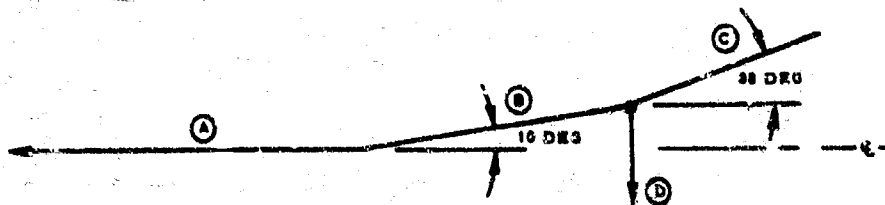
The meridian strap tension is as follows, based on attaining $K = 0.4$ in the base portion of the BALLUTE at $\Delta P = 5(60)$ psf:

$$\frac{K \Delta P \pi R^2}{n} = \frac{0.4(250)\pi 6.25}{16} = 122 \text{ lb} \quad (83)$$

The keeper ring tension is based on the maximum drag force when fully inflated ($q = 50$ psf) and the geometry. The drag force is equal to:

$$C_D q S = 0.7(50)(19.64) = 688 \text{ lb} \quad (84)$$

The geometry at each line is as shown in the following sketch:



Tensions within each line are as listed on the next page:

$$A = \frac{688}{16} = 43.0 \text{ lb}$$

$$B = \frac{43.0}{\cos 10 \text{ deg}} = 43.6 \text{ lb}$$

$$C = \frac{43.0}{\cos 38 \text{ deg}} = 54.3 \text{ lb}$$

Σ = vertical reactions at intersection of B, C, and D

$$C \sin 38 \text{ deg} - B \sin 10 \text{ deg} = D$$

$$54.3(0.615) - 43.6(0.1735) = D$$

$$D = 33.4 - 7.6 = 25.8 \text{ lb}$$

Thus:

$$\begin{aligned} \text{Tension in hoop} &= \frac{\text{force} \times \text{radius}}{\text{unit length}} \\ &= \frac{25.8R}{2\pi R} = \frac{25.8 \times 16}{2\pi} = 66 \text{ lb} \end{aligned} \quad (35)$$

The keeper ring tie loop is designated E on the 38-deg incline (see sketch below):



$$E \leq 25.8 \sin 38 \text{ deg} \leq 25.8(0.615) \leq 15.9 \text{ lb} \quad (86)$$

The riser static load is equal to the drag load at 50 psf, which is equal to $C_D q S$, where $C_D = 0.7$ and $0.7(50)(19.64) = 688 \text{ lb}$.

In addition to the static loadings, the dynamic loadings must be considered for each component. The gore fabric is discussed earlier in this section based on subsonic deployment test results and anticipated amplifications during the latter part of the inflation cycle. These load values and the corresponding factors for design are presented in Table XXIV.

6. THERMODYNAMIC ANALYSIS

The performance of a textile fabric BALLUTE in a hypersonic flight environment is described in Section IV. As a point of interest, a metal fabric BALLUTE was investigated to determine its capability under the same

TABLE XXIV - MB-1 LOADS, DESIGN FACTORS, AND
MATERIAL REQUIREMENTS

Item	Gore fabric (lb/in.)	Inlet (lb/in.)	Meridian webs (lb, each)	Keeper ring (lb)	Keeper ring loops (lb, each)	Riser (lb, total)
Static load (dynamic pressure)						
q = 50 at full pressurization	26.00	. . .	122.00	66.00	15.90	588.00
q = 62 at deployment	. . .	4.60
Design factors						
Overload	1.25	1.25	1.25	1.25	1.25	1.25
Dynamic	2.00	27.00	1.55	1.55	1.55	1.50
Seam efficiency	1.16	. . .	1.10	1.15	1.15	1.20
Temperature	*	*	1.00	1.00	1.00	1.00
Raking	1.00
Safety	1.50	. . .	1.50	1.50	1.50	1.50
Product of factors	4.35	33.80	3.20	3.34	3.34	3.28
Material strength requirements						
Basic	113.00	. . .	390.00	220.00	53.10	2320.00
Seam	97.50	155.00	355.00	191.00	46.10	1930.00
Raking	97.50	155.00

* See Figure 68

flight conditions. Using the same methods of analysis and the set of thermal properties listed in Table XXV, a temperature rise in the fabric was calculated using the heating data generated for the case of the textile fabric BALLUTE.

The results are shown in Figure 70 for a surface position on the coated metal BALLUTE. During exit flight, the surface temperature rises to a peak of about 200 F and then begins to cool as altitude is gained. As the payload-BALLUTE system re-enters the sensible atmosphere, aerodynamic heating is encountered. The surface temperature rises quickly, peaking at 1150 F in about 10 sec after encountering aerodynamic loading. The surface then cools as the system decelerates to terminal conditions.

It thus appears that a metal BALLUTE could have sustained the thermal environment of such a flight, since the CS-105 coating has an upper limit capability of about 1400 to 1500 F. This limiting range was experimentally

TABLE XXV - THERMAL PROPERTIES OF MATERIALS FOR
FLIGHT-TEST METAL BALLUTE

Material	Position	Thickness (mil)	Density (pcf)	Specific heat (Btu/lb-F)	Thermal conductivity (Btu/hr-ft-F)	Emissivity
CS-105	Outside surface	3.8	172.5	0.30	0.0453	0.9
SS-304	Fabric	10.0	142.0	0.13	0.0453	...
CS-105	Inside surface	2.0	172.5	0.30	0.0453	...

determined as reported in References 69 and 78. At the same time, fabric temperatures in the temperature range up to 1200 F should be within the capability of stainless steel alone. Therefore, the composite characteristics of the fabric and coating materials look attractive for use in this flight regime.

7. MATERIAL TESTING

a. General

The primary environment considered in the selection of materials for

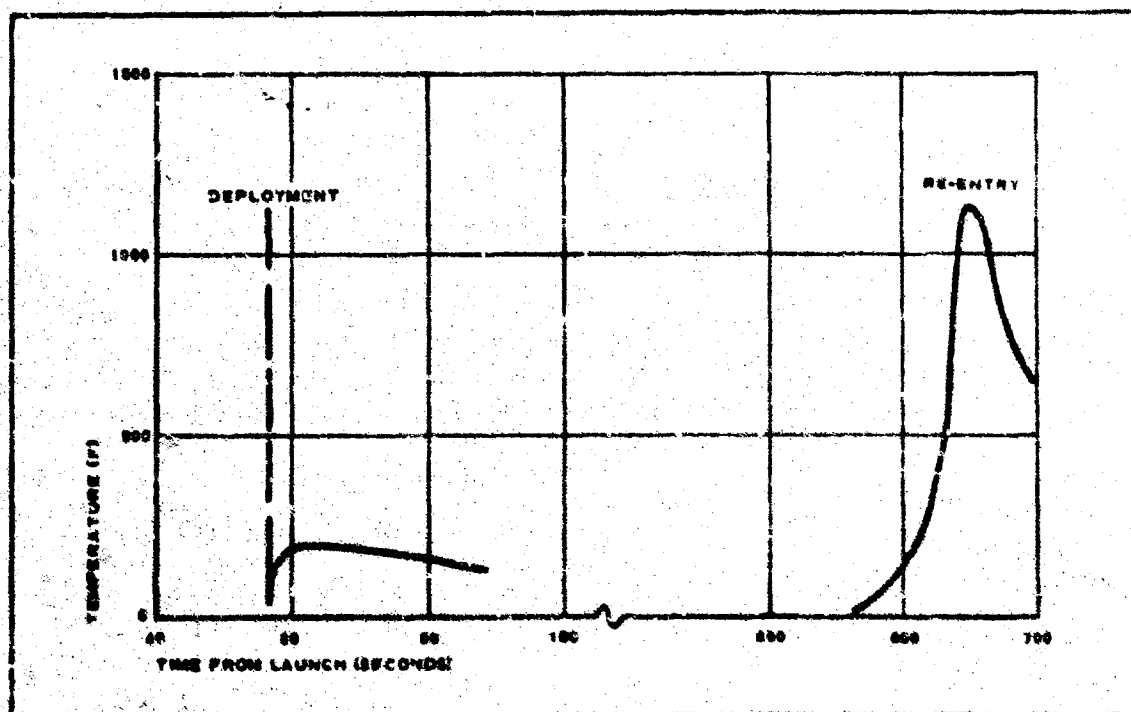


Figure 70 - Flight Test MB-1: Predicted Surface Temperature Data

BALLUTE applications in the hypersonic regimes was temperature calculated to be a maximum of 1500 F. The material-selection criteria were:

1. The material has to exhibit the necessary structural strength for the thermal situation associated with incremental deployment conditions for MB-1, MB-2, and MB-3 (see Table XXIII, earlier in this section).
2. The material must be flexible, thus permitting the fabricated BALLUTE to be packaged in a relatively small deployment bag and subsequently deployed without damage to the envelope or other components.
3. The envelope of the BALLUTE be capable of containing its pressurizing gas, thus ensuring its isotenoid shape could be maintained.

On the basis of these criteria, it was determined that a metallic woven cloth would be required for the structural material primarily because the cloth material exhibits considerably more flexibility than does sheet metallic material. In order to approach the maximum temperature requirement, it was evident that a superalloy material would be required while a cloth woven from stainless steel yarn could be used satisfactorily for the low hypersonic range. In each case a suitable elastomer would be applied to the envelope.

b. Initial Material Investigation

Much of the basic investigation into metal cloth weaving, welding, coating, and strength testing was accomplished under Contract AF33(600)-8015; the results are documented in ASD-TDR-62-702 (Reference 52). In addition, the characteristics of two types of metallic cloth weaves were investigated, designated Cloth A and B. Cloth A was woven from monofilament wire yarn 200 per inch in both the warp and fill directions. Cloth B was woven from stranded wire yarn woven 100 per inch in both the warp and fill directions. The Cloth B test data indicated more flexibility, strength, uniformity, and tear resistance than Cloth A (Reference 75). Both stainless steel and Rene 41 were woven satisfactorily into the Cloth B fabric.

Joining techniques were investigated and reported in References 9 and 15. Weld efficiencies approaching 90 to 100 percent were obtained by resistance welding techniques.

Goodyear Aerospace Code CS-105 coating material was evaluated for application to the BALLUTE envelope (Reference 79). Four specimens were tested, as indicated in Table XXVI. Except for some outer coat flaking, coating appeared continuous after testing. It was not necessary to adjust the pressure during test, indicating that leakage was less than the accuracy of the equipment.

TABLE XXVI - CS-105 HOT ROC TESTS

Test no.	Type of cloth	Number of coats*	Backup pressure (psi)	Temperature (F)	Time at temperature (min)
1	A	12	4	1275	2
2	A	12	4	1275	10
3	B	12	4	1275	2
4	B	12	4	1275	10

*One coat of CS-105 approximates one ounce per square yard.

Six specimens were permeability tested in the environmental laboratory, as shown in Table XXVII. Leak rates are shown in Figure 71.

TABLE XXVII - CS-105 PERMEABILITY TESTS

Test no.	Type of cloth	Weld or control	Number of coats	Backup pressure (psi)	Temperature (F)	Time at temperature (min)
3	A	Control	12	2	1500	20
1	A	Welded	10	2	1500	20
5	A	Welded	10	4	1275	20
8	B	Control	12	4	1275	20
6	B	Welded	10	4	1275	...
2	B	Welded	10	2	1500	60

c. MB-1 Materials and Joints

A material strength of 150 lb/in. was chosen early in the program, based on the selected initial test point environment, an early estimated internal pressure, and estimated design factors. Other factors considered in selecting the cloth were elongation, folding endurance, and state-of-the-art for joining. Cloth B stainless steel (100 X 100 yarns per inch of 7 X 0.0016 stranded wire yarns) was chosen to meet the strength requirement and the considerations for good elongation, folding endurance, and state of the art for joining.

Tensile tests were made of the fabric using 1 in. wide specimens in both the warp and fill directions at room temperature and at 1200 F. For room temperature (74 F) the loading rate, with 10-in. jaw spacing, was 0.5 in./min. The results were:

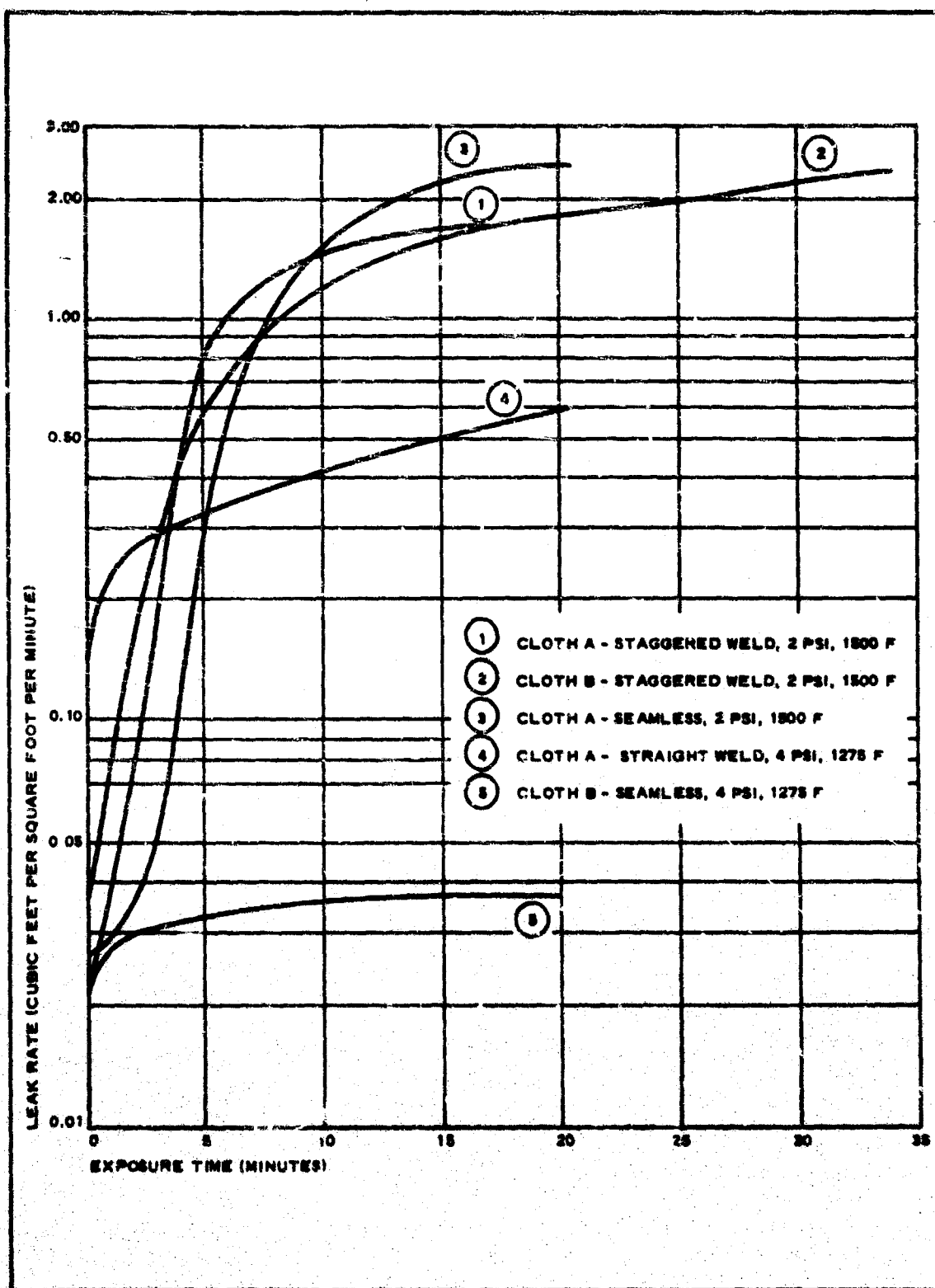


Figure 71 - Leak Rates for CS-105 Coating

1. Warp - 139 to 144 lb/in. (3 samples)
2. Fill - 156 to 160 lb/in. (3 samples)

For elevated temperature (1200 F), heated to 1200 F in two minutes, the values were:

1. Warp - 57.5 to 60 lb/in. (loading rate 0.3 in./min)
2. Fill - 50 to 63 lb/in. (loading rate 0.15 in./min)

The 1500-lb meridian web consists of 5-mil 304 stainless steel wire that is flat braided using 29 flat braided 13×2 wires. The meridian web braid and wire size was chosen to obtain flexibility and a nominal ultimate strength of 1500 lb. This material was tested (3 samples), and the average ultimate strength was 1470 lb at room temperature.

The 1000-lb meridian web consists of 5-mil 304 stainless steel wire that is flat braided using 21 flat braided 13×2 wires. This lighter meridian web braid was chosen to replace the 1500-lb strength braid and thus reduce the weight of the assembly. The strength reduction is compatible with the reduced loads. The thickness and construction are identical to the 1500-lb web except 21 wires are flat-braided instead of 29.

The 500-lb light web consists of 5-mil 304 stainless steel wire tubular braided using 36 carriers of 7 unbraided wires each. The web was used for attachments and reinforcements. This material was tested (3 samples), and the average ultimate strength was 450 lb.

An 80-mil stainless steel spring wire was chosen for the inlet lip, the inlet erecting spring, and cross wires in the inlet throat.

d. Seams and Splices

In establishing suitable gore seams, several spot welding parameters were considered, including probe size, power settings, probe pressure, number of rows of spots, and spacing between rows. Of the many combinations tested, the highest consistent efficiencies were obtained using two rows at 15 spots per inch per row, with the spots staggered and the rows spaced $1/8$ in. apart.

Test results ranged from 120 to 135 lb/in. at room temperatures using 0.5-in. specimens. The selected attachment is shown in Figure 72A. The gore seam tack weld was accomplished by means of a Unitek Weldmatic Model 1059 power supply adjusted to 11-w-sec and a HP-3030 heavy duty, probe, hand piece set, with an EP-1002 RWMA-2 electrode. The probe was set to 9 lb of weld force.

Since the meridian web-to-gore fabric attachment failed in the first wind-tunnel test, several series of tests were made statically and then dynamically of candidate methods for attaching the web to the gore fabric (References 9 and 15). The dynamic tests indicated that (1) the gore material should be reinforced to be two thicknesses at the spotwelds; (2) the

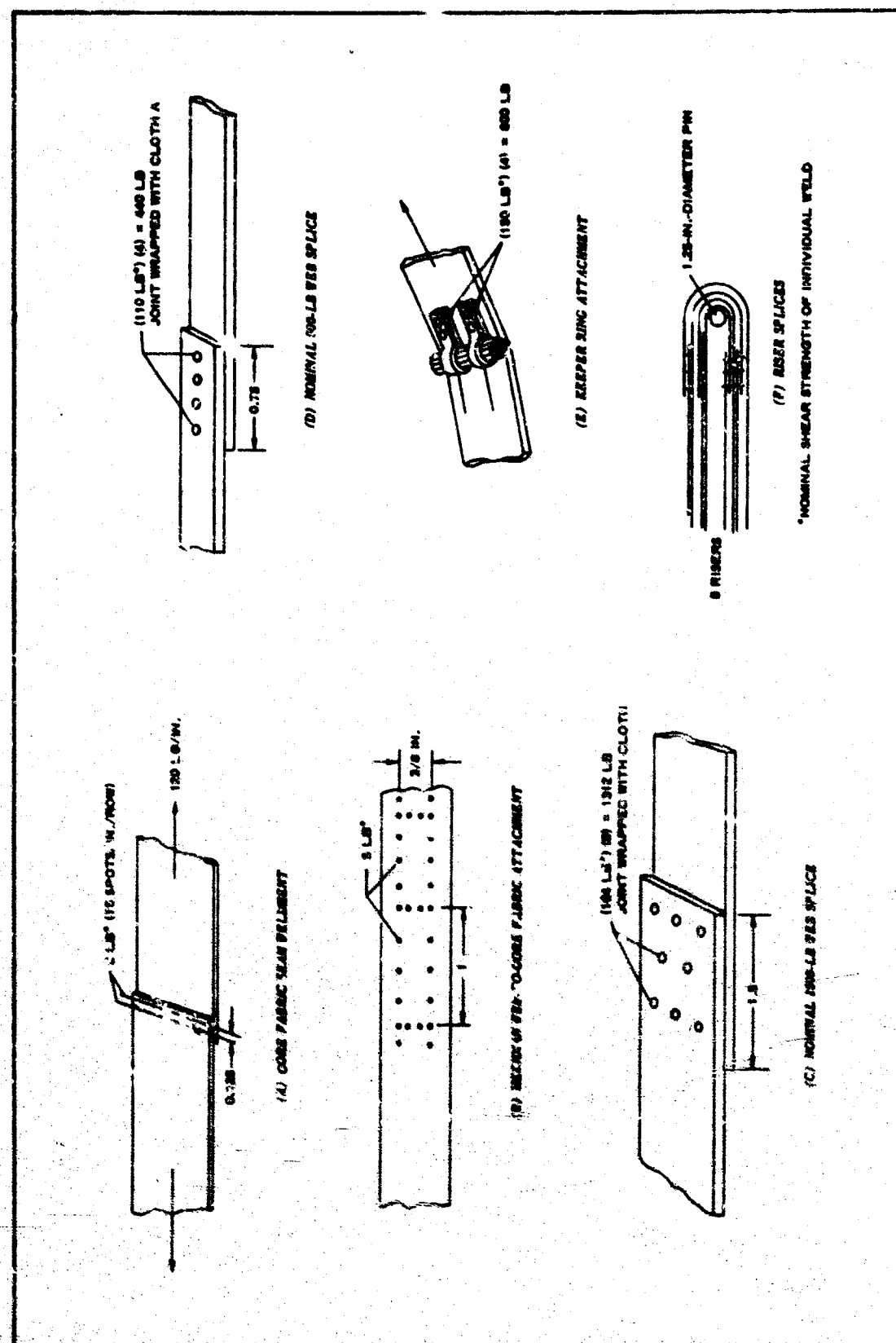


Figure 72 - Material Testing: Seams and Splices

welds should be sufficiently far apart to allow the yarns in the meridians to slide relative to each other during flexing of the meridians.

The selected attachment is shown in Figure 72B. The attachment tack welds were accomplished by use of a Unitek weldmatic 1034 power supply and a HP-3030 heavy duty, probe, hand piece set, with an EP-1002 RWMA-2 electrode. The power supply setting was 50 w-sec, and the probe set to 9 lb of weld force.

With respect to the meridian web-to-meridian web splice (1500-lb web), static tests were made of a series of joints to splice the meridian webs together. The spot size and spacing was varied with the web unwrapped and wrapped and with cloth material in the weld area. Wrapping the web provided significantly higher strength welds. The test results showed an average splice strength of 1310 lb. The selected splice technique is shown in Figure 72C.

The tack welds for the meridian web-to-meridian web splice and for other metal BALLUTE tack welds discussed below were accomplished by use of a Federal APA-2-42 spot welder, with the operating controls set as follows:

<u>Control</u>	<u>Setting</u>
Weld pressure	20 psi
Forge pressure	15 psi
Squeeze time	30 sec
Forge time	30 sec
Hold time	15 sec
Top setting	Parallel 2
Initial heat time	5 sec
Initial heat	55 percent
Weld time	13 sec
Weld heat	85 percent
Negative slope delay	14 sec
Negative slope	8 sec
Negative slope heat	55 percent

The top and bottom electrodes in this device have a 2-in. face radius, are 3 in. long, and have a 5/8-in. diameter reduced to 1/4 in. at the contact end. The throat depth is 45 in., and the spacing is 14 in.

The selected splice for the meridian web-to-meridian web splice, (nominal 500-lb web) is shown in Figure 72D. The static test results indicated a splice strength of 440 lb.

The keeper ring carries the tension load required to change the direction of the meridians from parallel to the envelope to 10 deg from the missile

centerline. A circular cross-section and flexibility are desired to minimize stress concentration and to facilitate packaging. The selected material was 1/16 in. flexible stainless steel cable, with a rated strength of 480 lb. Six turns were used and the ends were welded together.

The keeper ring loops carry the loads and tend to slide the ring forward. The joint used to carry these loads is a pair of 500-lb webs folded around the ring and welded to the meridian. The joint details are shown in Figure 72E.

The riser carries the drag load and consists of two groups of eight meridians, each with one-half of the meridians passing around the pin loop before being joined to an opposite meridian using the meridian-to-meridian splice. The riser splices are shown in Figure 72F.

8. MB-1 DESIGN AND FABRICATION

a. General

During ADDPEP Phase II, two designs of similar configuration but with different fabric materials were investigated. The MB-1 design specified Cloth B-304S stainless steel; and the MB-2 and MB-3 design specified René 41 cloth. Of the three, only MB-1 was fully designed and fabricated. The design and fabrication criteria presented, therefore, apply only to MB-1. The test BALLUTE, packed in its deployment bag, forms the test decelerator package as it is stowed into Test Vehicle C. The stowage arrangement is shown in Figure 2, Section II.

b. Design and Fabrication

(1) Design

Sheets 1 and 2 of Drawing 530A005-024 (Reference 80) present the complete MB-1 BALLUTE assembly and gore patterns. The BALLUTE contour, which is the same as TB-2 and TB-3 (Figure 40, Section IV), has 16 gores and 16 meridian webs located at the gore centerlines. The 16 meridian webs and the riser are formed by placing 8 webs around the envelope. Characteristics of MB-1 are shown in Figure 66. The web ends are joined together individually after passing around the riser attachment loop. At the front of the BALLUTE, the webs are constrained to a 6-in. diameter by a keeper ring. The keeper ring is constructed of 6 turns of 1/16-in. stainless steel cable lightly twisted together with the two ends welded together. The riser webs are served together at a point 14.5 in. forward of the keeper ring. This arrangement is intended to (1) keep the meridians oriented and loaded equally and (2) decrease the angle change at the keeper ring.

All the cloth used in the construction of the BALLUTE envelope was Cloth B 304 stainless steel (100 × 100 yarns per inch of 7 × 0.0016 stranded wire yarns) weighing 16 oz/sq yd. A lighter cloth (Cloth A 304 stainless steel, 200 × 200 per inch of 0.0016 filaments) was used to wrap webbing joints and thus improve the weld strength values. The webbing in the meridians and riser is 5-mil 304 stainless steel wire that

is flat-braided using 21 flat-braided 13 X 2 wires. The webbing nominal strength is 1000 lb.

All seams are welded before the cloth is impregnated with CS-105 elastomer. A lapped seam with 2 rows of spot welds spaced at 15 or 30 per inch total is used to join the gores. After BALLUTE assembly, the entire envelope surface is coated on both sides with CS-105 elastomer at a 12-oz/sq yd rate and cured at 500 F. The coating decreases the porosity of the fabric for proper inflation, and it reduces the heating rates into the cloth.

The BALLUTE has four inflation inlets located near the maximum diameter of the envelope. Each inlet has a stainless steel spring wire form attached to its lip and the inlet's sheet metal base.

A sheet metal base was used in place of a wire base to prevent the racking type actions occurring in the gore cloth during the inflation process from breaking the inlet support wires. Because the sheet metal base presents a marked rigidity change from the basic gore cloth, several layers of cloth were used to taper the change in stiffness from the base to the gore cloth. Webbs also were added between the base and the meridians to reduce the magnitude of deflections between the inlets and the gore cloth. The partial inflation system was used to reduce the magnitude and duration of the early inflation movements.

Although the inlet is essentially a stable pressure body, the spring wire frame is used for initial positioning and reacting the drag force. The torque of the inlet spring is approximately 20 lb/in. when the inlet is totally erected. Each inlet assembly has a sock-type valve for preventing outward flow. This is accomplished by the sock collapsing against the BALLUTE envelope or the wires across the inlet throat when outward flow is attempted.

The cross-sectional area of the inlet is approximately 14 sq in. The aft portion of the inlet sock converges to approximately 12 sq in. at the exit. The purpose of the convergence is to ensure that the sock is fully inflated during the initial high flow rates by maintaining the highest velocity and lowest pressure at the exit. The sock is constructed of coated Cloth B 304 stainless steel having a strength of 140 lb/in.

As in TB-4, TB-5, and TB-6, five Alumel-Chromel thermocouples for sensing temperatures are installed on the envelope, a pressure sensing line is carried on the risers, and a liquid initial pressurizing system is used.

(2) Fabrication

Fabrication was accomplished to the detail design requirements of Drawing 530A005-024 (Reference 80). Metal templates were utilized for the marking and cutting of the gores from the metal cloth. Correct matching of the welded gore seams was accomplished by providing match-marks along the centerline of the seam lap during the gore marking process. The marks were aligned over a contoured welding bar, and temporary spot welds were placed. With the seam located, the weld was completed.

Correct location of the meridional webs was obtained by premarking the webs with station marks while the webs were in a straight and lightly tensioned position; this arrangement matched corresponding station marks on the gores.

Quality control of the welded seams and splices was accomplished by visual inspection to detect improper penetration and to ensure proper spacing and quality of the weld spots. Dimensional control and inspection were maintained throughout fabrication. Before installing all textile and rubber parts, the BALLUTE was coated with Goodyear Aerospace CS-105 high temperature coating per detail requirement of Drawing 530A005-024. The BALLUTE was completely fabricated prior to installing the liquid initial pressurizing system.

c. Deployment Bag

Although no metal BALLUTES were flight-tested, it should be noted that the deployment bag used for TB-4, TB-5, and TB-6 could also be used for MB-1. The design of the deployment bag is presented in Drawing 530A005-050 (Reference 74) and is described in Section IV of this report.

9. DEPLOYMENT SEQUENCE AND PACKING PROCEDURE

The packing technique and deployment system for the metal BALLUTES are similar to those utilized for TB-4, TB-5, and TB-6 (described in Section IV).

10. SUMMARY AND CONCLUSIONS

a. Configuration

In generating the metal BALLUTE configurations, one envelope shape without a fence was selected. This shape corresponded to TB-4, TB-5, and TB-6. The inlets were placed at the position of maximum BALLUTE diameter. The wind-tunnel test of MB-1 at Mach 2.8 and a 120-psf dynamic pressure demonstrated that it had a stable, inflated shape at supersonic velocities. The internal pressure coefficient was very low compared to other test values (Figure 49). How much can be attributed to inlet location is unknown, as TB-1BWT was also very low with forward positioned inlets in the same test series (Reference 45).

b. Aerodynamic Loadings

Based on the wind-tunnel test at Mach 2.8, the selected configuration assumed its predicted shape while under load; this correlation indicates that analytical approaches for predicting shape are sufficiently accurate for engineering use. Moreover, the drag value was consistent with other drag values measured for similar configurations (Figure 50). The short filling time reflected the use of the partial inflation liquid mixture (Figure 65).

c. Structure

Inspection of the wind-tunnel films indicated the improved structure of

MB-1 over earlier units, and the partial inflation technique provided an adequate structural margin at Mach 2.8 and a 120-psf dynamic pressure for both the dynamic loads and the static pressurization loads. The metal inlet opening springs and inlet hoops were structurally adequate using a solid sheet metal base and the partial inflation system. The CS-105 coating and woven metal material withstood the test environment for the test period, approximately five minutes. Pressure and thermocouple instrumentation was carried on the test units. The MB-1 test indicated that the thermocouple and the pressure tube approach are structurally adequate for obtaining data.

d. Thermodynamic Analysis

Since no flight tests were made using a metal BALLUTE, no evaluation of the thermal analysis was made. However, the wind-tunnel test did demonstrate the effect of the liquids in lowering the BALLUTE material temperatures (Figure 65).

e. Materials

In-plant and wind-tunnel tests were used to establish a structurally adequate configuration for flight use. In-plant tests included the normal static type tests and subsonic wind-tunnel flag models to check joining techniques under dynamic loadings. The flag models were particularly useful for establishing meridian-to-envelope cloth attachments. Supersonic wind-tunnel tests were used to evaluate the total structure. The final structural configuration and coating were found to be adequate for the wind-tunnel test conditions (Mach 2.8 and a 120-psf dynamic pressure).

f. Design and Fabrication

The basic design changes during the metal BALLUTE effort were directed toward increasing its structural capability. Approaches were established that reduced the dynamic loadings and increased its overall, structural integrity to withstand the design load.

g. Deployment System and Packing Procedure

The deployment and packing procedure was similar to the textile BALLUTE. No changes are recommended.

SECTION VI

CONCLUSIONS

1. GENERAL

The wind-tunnel and free-flight test results of Phase II of ADDPEP (Aero-dynamic Deployable Decelerator Performance-Evaluation Program) were used to evaluate decelerator design methods and testing techniques. The main conclusions stemming from these evaluations are drawn together in this section.

2. FREE-FLIGHT TEST CAPABILITY

From tests of the free-flight test vehicle/booster systems, it is concluded that:

1. The performance of Test Vehicle A/Booster can be predicted with confidence. The data system is adequate. Recovery and reusability meet design goals.
2. The performance of Test Vehicle C/Booster also can be predicted with confidence. The data transmittal range is excellent. Beacon dropout occurs some of the time. When recovered, the vehicle meets design goals for reusability.

3. LARGE PARACHUTE DECELERATOR

From tests of a large, supersonic, hemisflo parachute design, it is concluded that:

1. The flight tests confirm the use of wind-tunnel tests for establishing a stable configuration.
2. Free-flight stability is excellent in the reefed and disreefed shapes.
3. Free-flight drag values are significantly higher for the parachute in free-flight tests than for similar models in wind-tunnel tests (see values in Figure 15).
4. Further refinements to the presented analytical approach are required for calculating opening drag loads with confidence.
5. An analytical approach is needed to predict reefing line loads.
6. The canopy structure and materials withstand the shock and heat loadings associated with the test conditions. (Nomex materials were used for ribbons and verticals.)

7. The deployment approach is satisfactory, as demonstrated by the fact that the snatch loads are significantly less than the opening loads.

4. TEXTILE AND METAL BALLUTE DECELERATORS

From the wind-tunnel and free-flight tests of textile BALLUTES and the wind-tunnel tests of metal BALLUTES, it is concluded that:

1. Both the textile and metal BALLUTE configurations have predictable and stable inflated shapes at supersonic velocities.
2. External surface pressure coefficients of textile and metal BALLUTES can be predicted within engineering requirements for shape determinations.
3. Drag and stability data for textile and metal BALLUTES can be determined by the use of wind-tunnel models.
4. Partial inflation techniques significantly reduce the degree of material flagging during inflation of the textile and metal BALLUTES. Initially, the partial inflation system significantly lowers the BALLUTE material temperature.
5. A satisfactory metal BALLUTE structure can be established for test conditions of Mach 2.8 at a 120-psf dynamic pressure, using the partial inflation system. Metal inlet opening springs and inlet hoops are structurally adequate using a solid sheet metal base and the partial inflation system.
6. Textile BALLUTE structural problems are limited to one type of coating on test item TB-2 and to the metal wire inlet springs and inlet hoops on TB-3. The inlet structure is improved by eliminating all metal except a cable type hoop in the inlet lip.
7. The textile and metal BALLUTE deployment system is adequate, based on snatch loads less than inflation loads.
8. For both the textile and metal BALLUTE decelerators, additional efforts are required to establish means of controlling the internal pressures for optimum weight.

APPENDIX I
 AMBIENT CONDITIONS AT 12.622-SEC POINT OF
 LP-5 TRAJECTORY

From the data reduction report (Reference 22, page H-4), the altitude from mean sea level is 10,996 ft. The interpolation steps, from Appendix B of Reference 22, are given in Table XXVIII.

TABLE XXVIII - INTERPOLATION OF FLIGHT CONDITIONS (12.622 SEC)

Interpolation steps	Altitude from MSL (ft)	Pressure (millibars)	Specific weight (gm cu m)	Temperature (deg C)	Wind direction (deg from true N)	Wind speed (knots)	Density X speed of sound, ρ_c (lb-sec/cu ft)
Conditions at	10,500	686.6	891.9	-5.3	275	36	1.865
Conditions at	11,000	672.8	878.3	-6.4	275	35	1.833
Increment	500	13.2	13.6	1.1	0	1	0.032
Flight difference over increment	$\frac{4}{500}$	0.106	0.109	0.0088	0	0.008	0.000256
Conditions at	10,996	672.9	878.4	-6.4	275	35	1.833

Thus:

$$\begin{aligned} \text{Pressure, } P &= (672.9 \text{ mb}) \left(\frac{29.53 \text{ in. Hg}}{1000 \text{ mb}} \right) \left(\frac{14.7 \text{ psi}}{29.92 \text{ in. Hg}} \right) \left(\frac{144 \text{ sq in.}}{1 \text{ sq ft}} \right) \\ &= 1408 \text{ psf} \end{aligned} \quad (87)$$

$$\begin{aligned} \text{Specific weight, } w &= (878.4 \text{ gm/cu m}) \left(\frac{1 \text{ kg}}{1000 \text{ gm}} \right) \left(\frac{2.205 \text{ lb}}{1 \text{ kg}} \right) \left(\frac{1 \text{ cu m}}{35.31 \text{ cu ft}} \right) \\ &= 0.0550 \text{ pcf} \end{aligned} \quad (88)$$

$$\begin{aligned} \text{Temperature, } T &= (-6.4\text{C}) \left(\frac{9}{5} \right) + (491.6) \\ &= 480.1 \text{ R.} \end{aligned} \quad (89)$$

$$\begin{aligned} \text{Wind speed} &= (35 \text{ k}) \left(\frac{6080 \text{ ft/hr}}{1 \text{ k}} \right) \left(\frac{1 \text{ hr}}{3600 \text{ sec}} \right) \\ &= 59.1 \text{ fps.} \end{aligned} \quad (90)$$

The acceleration of gravity, g , is calculated as follows: From page 1 of Reference 22, latitude is 33.08 deg north. The acceleration of gravity from the mechanical engineer's handbook is:

APPENDIX I

AFFDL-TR-67-25

<u>Latitude (deg)</u>	<u>Sea level g (ft/sec²)</u>
30	32.130
40	32.158
Difference	0.028
Difference $\times 3.08/10$	0.009
33.08	32.14

The reduction for altitude is:

$$\frac{0.003 \text{ ft/sec}^2}{1000 \text{ ft}} (10,910 \text{ ft}) = 0.0328 \text{ fps} \quad (91)$$

The gravity at 10,910 ft is:

$$\begin{aligned} g &= (32.14 \text{ ft/sec}^2) - (0.03 \text{ ft/sec}^2) \\ &= 32.11 \text{ ft/sec}^2 \end{aligned} \quad (92)$$

Then:

$$\begin{aligned} \text{Density, } \rho &= \frac{w}{g} = \frac{0.0550 \text{ pcf}}{32.11 \text{ ft/sec}^2} \\ &= 0.001715 \text{ lb sec}^2/\text{ft}^4 \end{aligned} \quad (93)$$

$$\begin{aligned} \text{Wind speed} &= (35 \text{ k}) \left(\frac{6080 \text{ ft/hr}}{1 \text{ k}} \right) \left(\frac{1 \text{ hr}}{3600 \text{ sec}} \right) \\ &= 59.1 \text{ fps} \end{aligned} \quad (94)$$

The acceleration of gravity is 32.11 ft/sec². Appendix A of Reference 22 gives the calculation details:

$$\begin{aligned} \text{Density, } \rho &= \frac{w}{g} = \frac{0.551 \text{ pcf}}{32.11 \text{ ft/sec}^2} \\ &= 0.001719 \text{ lb sec}^2/\text{ft}^4 \end{aligned} \quad (95)$$

$$\begin{aligned} \text{Universal gas constant, } R &= \frac{P}{T w} = \frac{1412 \text{ psf}}{(480.4 \text{ R})(0.0551 \text{ pcf})} \\ &= 53.3 \text{ ft/F} \end{aligned} \quad (96)$$

$$\text{Speed of sound, } c = \frac{\rho_c}{\rho} = \frac{1.839 \text{ lb sec/cu ft}}{0.001719 \text{ lb sec}^2/\text{ft}^4} \quad (97)$$

APPENDIX II

AMBIENT CONDITIONS AT 12.472-SEC POINT OF
LP-5 TRAJECTORY

From the data reduction report (Reference 22, page H-4), the altitude from mean sea level is 10,909 ft. The interpolation steps, from Appendix B of Reference 22, are given in Table XXIX.

TABLE XXIX - INTERPOLATION OF FLIGHT CONDITIONS (12.472 SEC)

Interpolation steps	Altitude from MSL (ft)	Pressure (millibars)	Specific weight $\frac{gm}{cu m}$	Temperature (deg C)	Wind direction (deg from true N)	Wind speed (knots)	Density \times speed of sound P_c (lb sec/cu ft)
Conditions at	10,500	686.0	891.9	-5.3	275	36	1.865
Conditions at	11,000	672.3	878.3	-6.4	275	35	1.833
Increment	500	13.2	13.6	1.1	0	1	0.032
Flight difference over increment	$\frac{91}{500}$	2.403	2.478	0.003	0	0.1821	0.00583
Conditions at	10,909	675.2	880.8	-6.2	275	35	1.839

Thus:

$$\begin{aligned} \text{Pressure, } P &= (675.2 \text{ mb}) \left(\frac{29.53 \text{ in. Hg}}{1000 \text{ mb}} \right) \left(\frac{14.7 \text{ psi}}{29.92 \text{ in. Hg}} \right) \left(\frac{144 \text{ sq in.}}{1 \text{ sq ft}} \right) \\ &= 1412 \text{ psf} \end{aligned} \quad (98)$$

$$\begin{aligned} \text{Specific weight, } w &= (880.8 \text{ gm/cu m}) \left(\frac{1 \text{ kg}}{1000 \text{ gm}} \right) \left(\frac{2.205 \text{ lb}}{1 \text{ kg}} \right) \left(\frac{1 \text{ cu m}}{35.31 \text{ cu ft}} \right) \\ &= 0.0551 \text{ pcf} \end{aligned} \quad (99)$$

$$\begin{aligned} \text{Temperature, } T &= (-6.2^\circ\text{C}) \left(\frac{9}{5} \right) + (491.6) \\ &= 480.4 \text{ R} \end{aligned} \quad (100)$$

$$\begin{aligned} \text{Universal gas constant, } R &= \frac{P}{Tw} \\ &= \frac{1408 \text{ psf}}{(480.1 \text{ R})(0.0550 \text{ pcf})} \\ &= 53.3 \text{ ft/F} \end{aligned} \quad (101)$$

$$\begin{aligned}\text{Speed of sound, } c &= \frac{\rho_c}{\rho} \\ &= \frac{1.883 \text{ lb sec/cu ft}}{0.01715 \text{ lb sec}^2/\text{ft}^4} \\ &= 1070 \text{ fps} \quad (102)\end{aligned}$$

APPENDIX III

SPECIFICATION FOR COATING ADDPEP BALLUTES WITH D-65

1. SCOPE

With respect to the textile BALLUTE decelerators, this specification establishes the general procedures for (1) preparing Nomex pattern HT-122 cloth, (2) coating with Dyna-Therm D-65, and (3) curing. Also included are the desired coating buildups and acceptable permeabilities.

2. MATERIALS

Use the following materials, supplied by Dyna-Therm Chemical Corporation, in preparing the cloth and compounding the coatings: methyl ethyl ketone, D-65 coating, and D-65-1 thinner.

3. FABRIC PREPARATION

The first step in preparing the HT-122 cloth for coating consists of the scouring and heat-setting operations, which are done by the cloth supplier before shipping. The remaining steps are:

1. Staple the cloth smoothly to a frame, wash thoroughly with MEK, and allow to air-dry.
2. For coating with D-65, do not apply primer.
3. As a cautionary step, since MEK and solvents in D-65 are highly volatile and flammable, provide adequate ventilation, keep away from heat and open flame, and avoid prolonged exposure to vapor and prolonged or repeated skin contact. After using and before eating or smoking, clean hands thoroughly with soap and water.

4. PREPARATION OF D-65

For a light coat, mix 30 min on a paint shaker equal volumes of D-65-1 thinner and D-65 coating, as received. If only part of a can of D-65 is to be cut, mix the D-65, as received, for 30 min on a paint shaker before cutting with thinner.

For a heavy coat, use D-65 as received. Mix the coating for 30 min on a paint shaker before using. Once the can is opened, the D-65 will thicken from solvent loss. Hence, occasional addition of D-65-1 thinner, followed by mixing, may be necessary to maintain the as-received consistency. It is better to err on the "light" side since an additional coat may be added to the outer side of the cloth if the specified sequence and number of coats do not result in the minimum specified buildup of coating.

Clearly mark D-65 cans "light" and "heavy" and store in tightly closed containers in a cool, covered area. Do not leave cans open except while

decanting contents for immediate use. Exercise care and cleanliness in handling, since dried D-65 in the can ridges will prevent a tight seal of the lid, with consequent solvent loss.

5. COATING WITH D-65

After the cloth has been cleaned with MEK and air-dried, apply D-65 with a soft natural bristled brush. Flow the material on and avoid excessive brushing.

Allow each coat to air-dry 10 to 15 min, or until dry to the touch, before recoating. Apply each coat evenly to ensure proper film thickness upon completion.

Air-dry D-65 at room temperature a minimum of 48 hr, or until there is a complete lack of solvent odor, before subjecting coating to high heat.

Prior to cutting the HT-122 cloth, apply one light coat to one side of the cloth. This will become the outside of the assembled BALLUTE.

Mark the fabric carefully on the coated side for gore cutting and assembly.

After all but one gore seam is sewn closed: (1) apply one light coat and one heavy coat overall to the inside; and (2) apply one additional coat to stitched areas inside of the BALLUTE.

After all gore seams are closed: (1) precoat all outside tapes and webs except -11 webs (one inch MIL-W-5625) with one light coat; and (2) coat outside of BALLUTE overall except -11 webs with two heavy coats of D-65. Add additional coats if required to attain a total coating weight (excluding first light coat) of $13 \pm 2 - 0$ lb.

Hold permeability to a maximum of $0.020 \text{ ft}^3/\text{ft}^2/\text{min}$ as measured on the Cambridge permeameter utilizing helium at 3-cm water pressure and at 73-F temperature.

If removal of D-65 from tools is necessary, soften the coating with D-65-1 thinner and remove with a suitable tool. Use D-65-1 thinner for cleaning any member of the D-65 family.

APPENDIX IV

AERODYNAMIC HEATING RATES AND TEMPERATURE RESPONSE

1. GENERAL

This appendix deals with the analytical prediction of aerodynamic heating rates and temperature response of textile BALLUTES TB-4, TB-5, and TB-6 during hypersonic test flight. The symbols are defined in the preliminary pages of this report.

The ADDPEP program includes the consideration of BALLUTE shapes in the low hypersonic flight regime. The deployment point data for these flight tests are summarized in Table XXX.

TABLE XXX - BALLUTE DEPLOYMENT POINTS FOR
HYPERSONIC FLIGHT TESTING

Mach	Altitude (ft)	Dynamic pressure (psf)	Temperature (F)
5.70	122,000	200	69.3
6.70	131,000	200	71.1
9.95	200,000	20	48.5

A preliminary thermal analysis of the BALLUTES was conducted for Mach 5.7 and 9.95, using Type 304 stainless steel for Mach 5.7 and Rem 41 for Mach 9.95. With regard to the Mach 5.7 deployment case, the stainless steel material was predicted to reach temperatures slightly less than 1000 F for an immersion in a laminar wake and about 1200 F for a turbulent wake immersion. This analysis was based on minimal prediction of wake characteristics. As a result, the temperature responses were based on pessimistic estimates of the effect of aerodynamic heating.

The Mach 9.95 deployment case was re-examined on the basis of more detailed theoretical analysis (such as Reference 64 and further review of the experimental data contained in Reference 52). The wake flow during the test flight was then predicted to be laminar. A temperature response analysis of the fabric due to aerodynamic heating for this case predicted maximum temperatures during deceleration to be about 500 F at the critical point on the BALLUTE surface.

Subsequent to these analyses, refined methods of predicting aerodynamic heating were formulated. In addition, recent decelerator flight tests resulted in modest material temperature responses to aerodynamic heating. Therefore, it was decided that the proposed hypersonic test flights of

BALLUTEs should be re-examined on the basis of updated methods of analysis, as well as the investigation of the possibility of using textile fabric decelerators. The first case examined was the Mach 5.7 deployment case. A preliminary analysis was conducted to estimate the aerodynamic heating rates as well as the material temperature response. This appendix completes the investigation by presenting the results of a thermal analysis of the three deployment cases given in Table XXX (Mach 5.7, 6.7, and 9.95) during the exit flight phase of their respective trajectories.

2. TRAJECTORY CONSIDERATIONS

A series of point mass trajectories from the BALLUTE deployment conditions given in Table XXX were computed. These trajectory paths are shown in Figures 73, 74, and 75 as a function of time from deployment. The Mach number and velocity exhibit very little variation as the altitude increases toward the 300,000-ft level. Since the amount of convective heating is proportional to the density of the air as well as to the vehicle velocity, the heating rates tend to decrease significantly with altitude due to the large decrease in air density.

3. FLOW FIELD

Figure 76 shows a sketch of the combined body configuration for the flight testing of BALLUTEs in the low hypersonic flight regime. The sketch includes the overall vehicle dimensions as well as decelerator performance

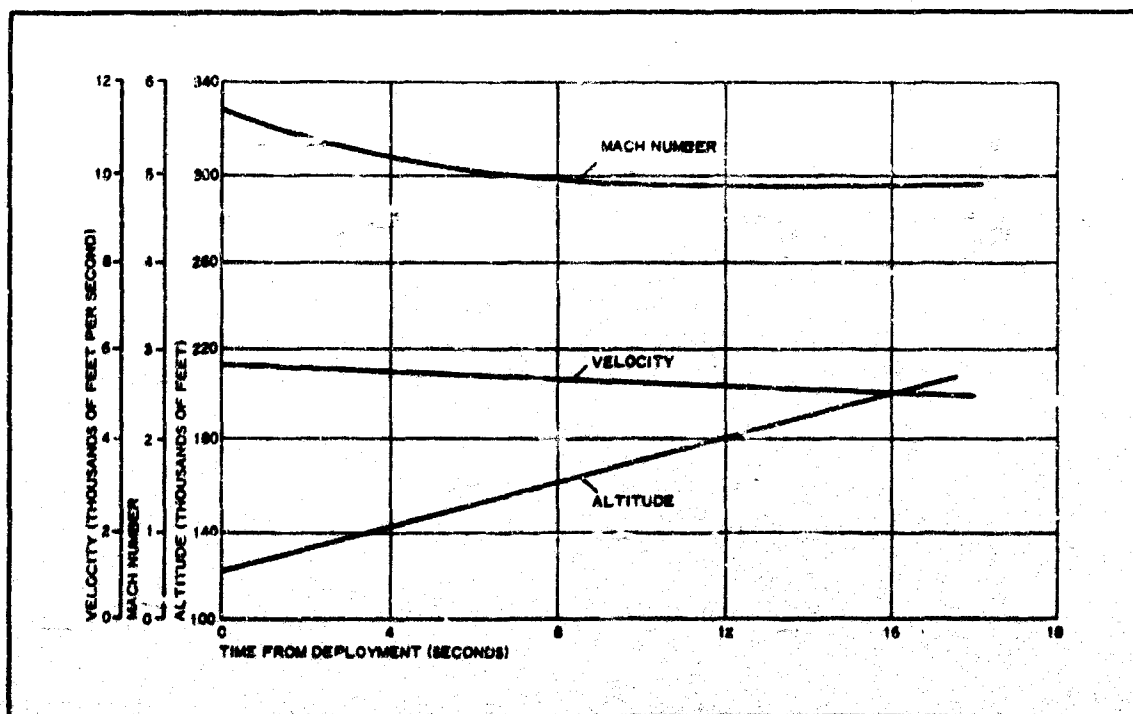


Figure 73 - Trajectory Parameters: Mach 5.7 at Deployment

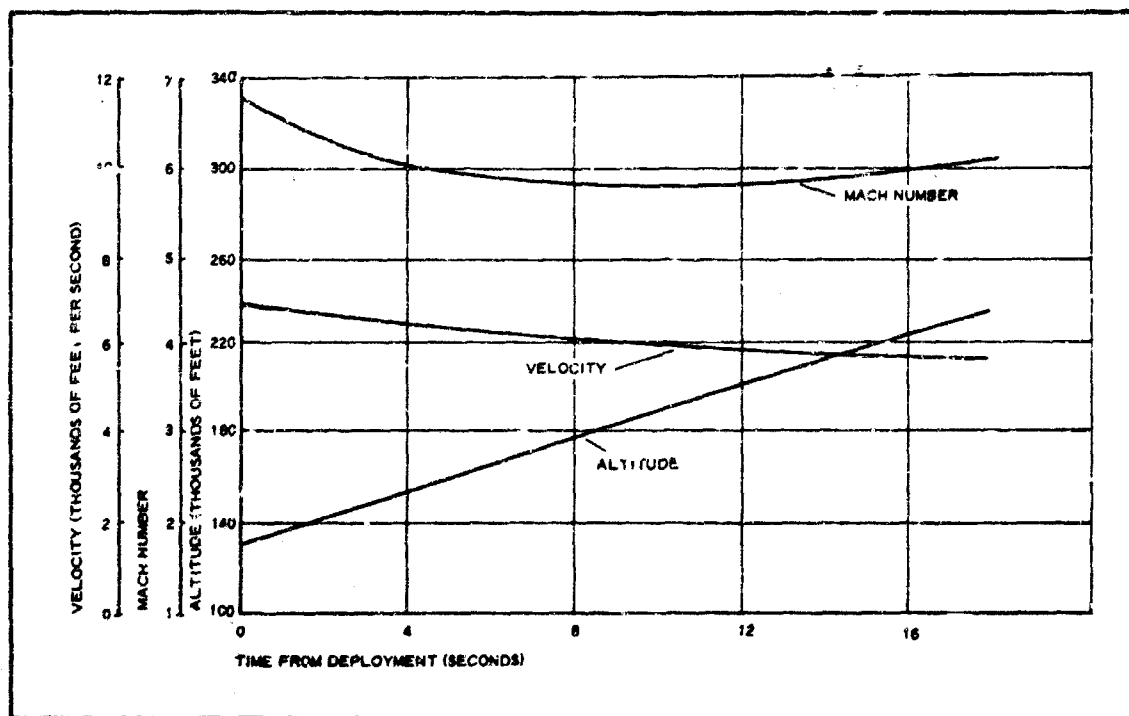


Figure 74 - Trajectory Parameters: Mach 6.7 at Deployment

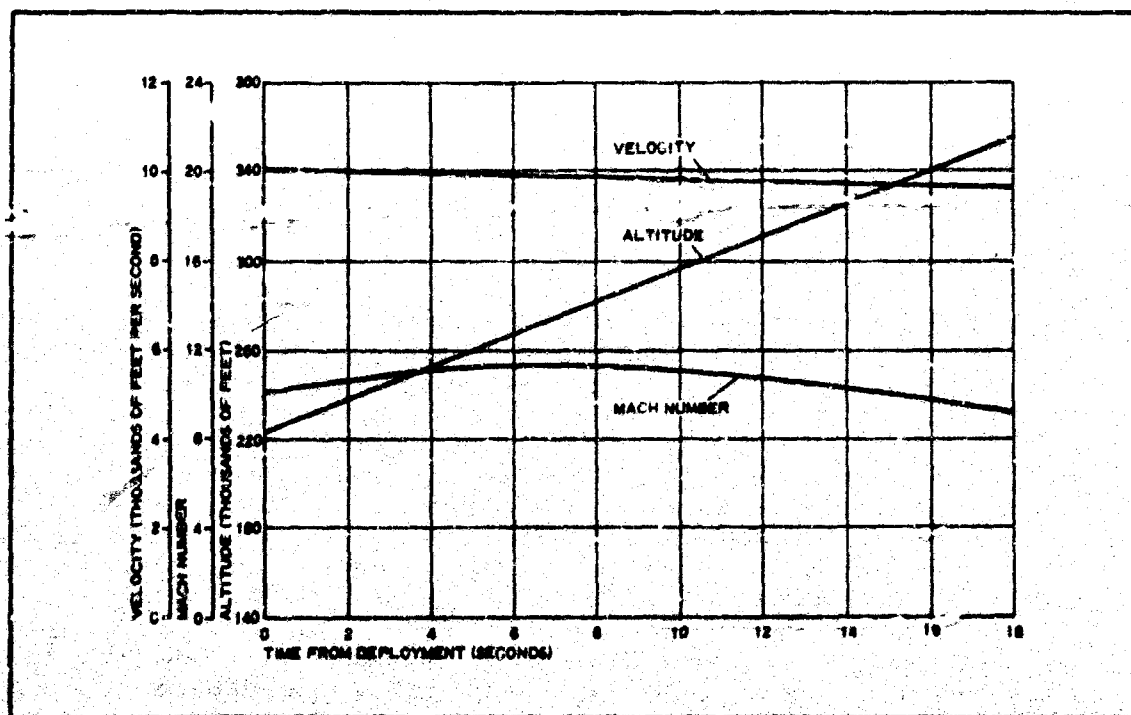


Figure 75 - Trajectory Parameters: Mach 9.95 at Deployment

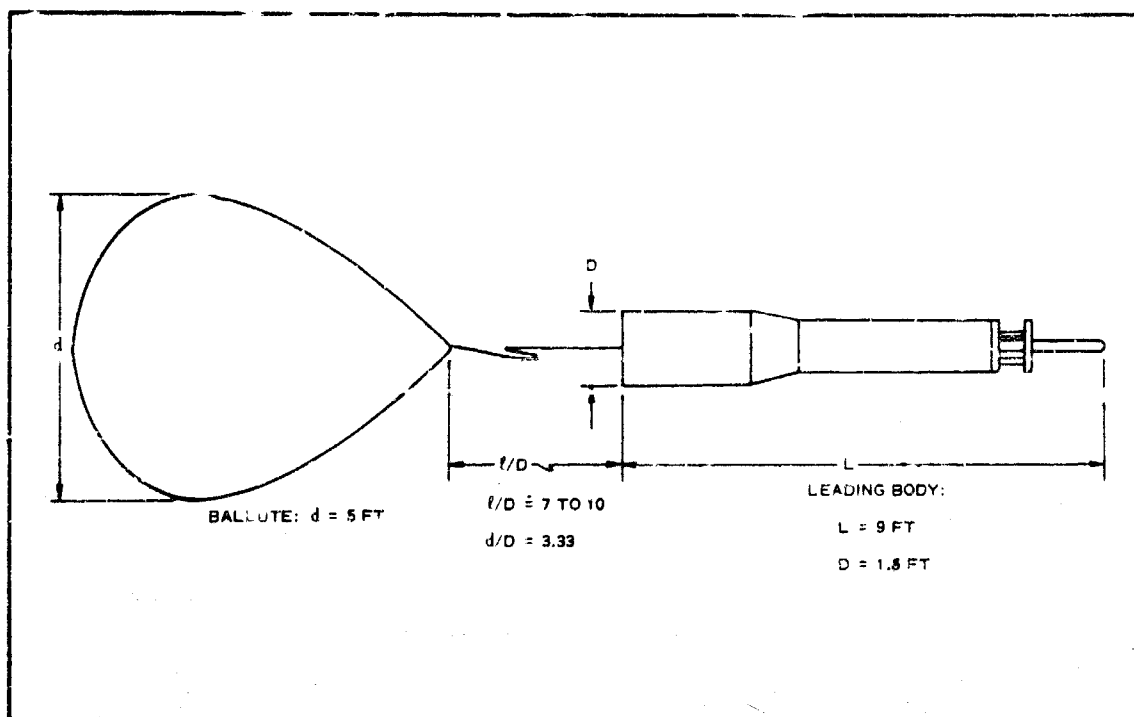


Figure 76 - Test Configuration

criteria, such as trailing length-to-leading body base diameter (l/D) and decelerator diameter-to-leading body base diameter (d/D). The apex of the BALLUTE is located about 15 ft from the leading body base and about 24 ft from the nose of the leading body. Since the heating rates at the decelerator surface will ultimately be a function of the flow field around the BALLUTE, as well as the type of boundary layer (laminar or turbulent) at the decelerator surface, it is appropriate to investigate the flow field formed by the two bodies.

It has been shown theoretically in Reference 64, and substantiated somewhat by experimental data, that due to the presence of the decelerator in the wake of the leading body, an interaction between the two bodies is produced that alters the wake flow field. In general, the wake is cylindrical and may be either laminar or turbulent. Experimental data have shown that (1) decelerators located less than about six base diameters aft of the leading body base are likely to produce transition of the wake to the turbulent type; and (2) decelerators located at distances greater than six base diameters affect the nature of the flow field. However, no data are available as to how the interaction affects the type of wake flow.

Since it is necessary to specify the type of boundary layer flow prior to conducting a heating analysis, a decision must be formulated as to whether the wake flow is laminar or turbulent. The latter type of wake may generate aerodynamic heating rates 5 to 10 times as great as those associated with a laminar type of wake. An alternate approach would be to disregard the laminar heating rates and estimate the turbulent heating rates only.

However, this approach usually leads to overdesign. In an experimental program, it is desirable to match the test vehicle as closely as possible to the test environment. In this interest, the following wake flow analysis was used.

The decelerators are to be located 7 to 10 base diameters aft of the base of the leading body. At these deployment lengths, the amount of experimental data available to formulate a decision as to the type of flow does not permit a warrantable assessment of the type of wake. However, the successful decelerator test flights completed to date at seven base diameters aft have shown a minimal amount of exposure to aerodynamic heating effects. This factor indicates either a laminar wake condition, in which the heating rates are quite low, or turbulent heating rates of decreased intensity at the distance the decelerators are located. In view of these two possibilities, two approaches are proposed to estimate the state of the wake: (1) a transition criterion for the flow over the leading body can be applied to determine the state of the boundary layer on the leading body; and (2) the state of a free wake aft of the leading body can be examined.

Consider first the leading body. As a first approximation, the flow over the leading body at the moment of deployment may be considered to have been compressed by the bow shock at the nose of the vehicle and then expanded isentropically to a lower pressure on the cylindrical portion of this body. Using momentum Reynolds number criteria, it is possible to determine whether the boundary layer is turbulent over this leading body. If a turbulent exists in the wake and over the decelerator surface, the momentum Reynolds number can be written as:

$$Re_0 = \frac{\rho V_\infty \theta}{\mu} = 0.695 \left(\frac{\rho_w k_w}{\rho \mu} \right)^{0.114} \left(\frac{\rho u x}{\mu} \right)^{0.5} \quad (103)$$

This relationship appears to have promise for ascertaining the state of flow over the leading body. For flow over a flat plate, the transition Reynolds number criterion in Equation 103 is usually taken as 400 to 600. Assuming a transition Reynolds number of 650 on the cylindrical section of the leading body and a surface temperature of 500 to 1000 F for the wall on the cylindrical section, Equation 103 can be solved for the transition length (x_{tr}).

This calculation was conducted at each of the deployment point conditions and the results showed that transition ($x_{tr} > 20$ ft) is not likely to occur over the surface of leading body. In view of these results, the wake must then be analyzed for transition characteristics if the wake is to be turbulent at the moment of deployment.

Wake transition data for a flow field between two bodies are practically nonexistent. Therefore, more common free wake data must be used to establish transition characteristics. In general, a unified wake transition correlation is the most simple and therefore is used here.

Predicting the transition of the wake using the Zeiberg correlation depends upon an evaluation of the transition parameter:

$$\left(\text{Re}_{x_{tr}} \right)_{\infty} \frac{M_{\infty}}{M_e}$$

In this parameter, the Reynolds number is to be evaluated using free stream flow properties, and the transition length is measured from the base of the leading body. The Mach number ratio is the free stream Mach number divided by the local Mach number at the edge of the viscous inner wake. Figure 77 plots this transition parameter for the flight test trajectories to be utilized.

Consider the Mach 5.7 deployment case. A unit distance aft of the base is assumed and the ratio of Mach numbers is allowed to approach unity. This yields a trace of the transition parameter as a function of Mach number that shows that the wake is definitely in the laminar region at this position for elapsed times subsequent to the deployment of the decelerator. However, by accounting for the local Mach number variation in the wake of the Mach number ratio of the transition parameter and by increasing the distance from the base (x_{tr}), the result is a transition parameter that crosses into the turbulent regime. This increase occurs at a distance approximately 3.5 ft aft of the leading body base and indicates a possibility of a turbulent wake aft of this position.

The same wake transition characteristics were evaluated for the Mach 6.7 deployment case. However, the transition distance (x_{tr}) was calculated to occur about 4 ft aft of the base. In the Mach 9.95 deployment case, no wake transition characteristic was evident. Therefore, the flow apparently is considered laminar throughout the upward deceleration path.

As a result of the flow analysis over the leading body and the wake region between the two bodies, it is concluded that the boundary layer flow at the decelerator surface is turbulent and apparently emanates from near the base of the leading body. A schematic flow field model is shown in Figure 78. The approximate transition zone shown appears to be quite close to the leading body. Therefore, there is a good possibility that the entire interacting wake is turbulent.

4. AERODYNAMIC HEATING

The flow field analysis in the previous section has shown that the flow over the decelerator at deployment is apparently turbulent for the Mach 5.7 and 6.7 cases. The turbulent heat transfer rate distribution over the decelerator surface may be calculated using the following equation:

$$\dot{q}_w = \frac{0.0296}{(\text{Re}^{0.2})(\text{Pr}^{2/3})} \rho' u' (H_1 - h_w) [G(x')]^{1/5} \quad (104)$$

The prime notation indicates the flow properties must be evaluated at the

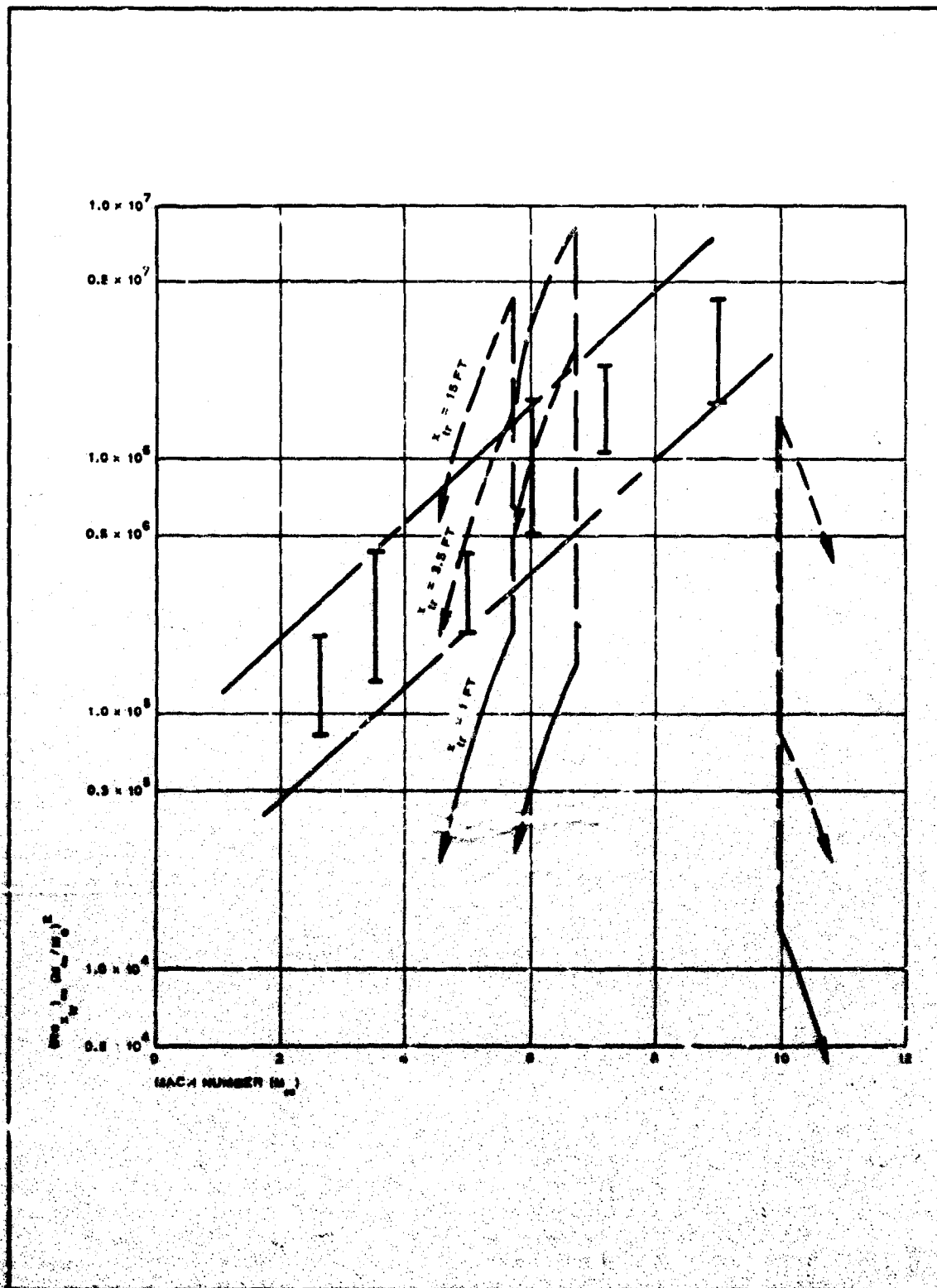


Figure 77 - Unified Wake Transition Criteria

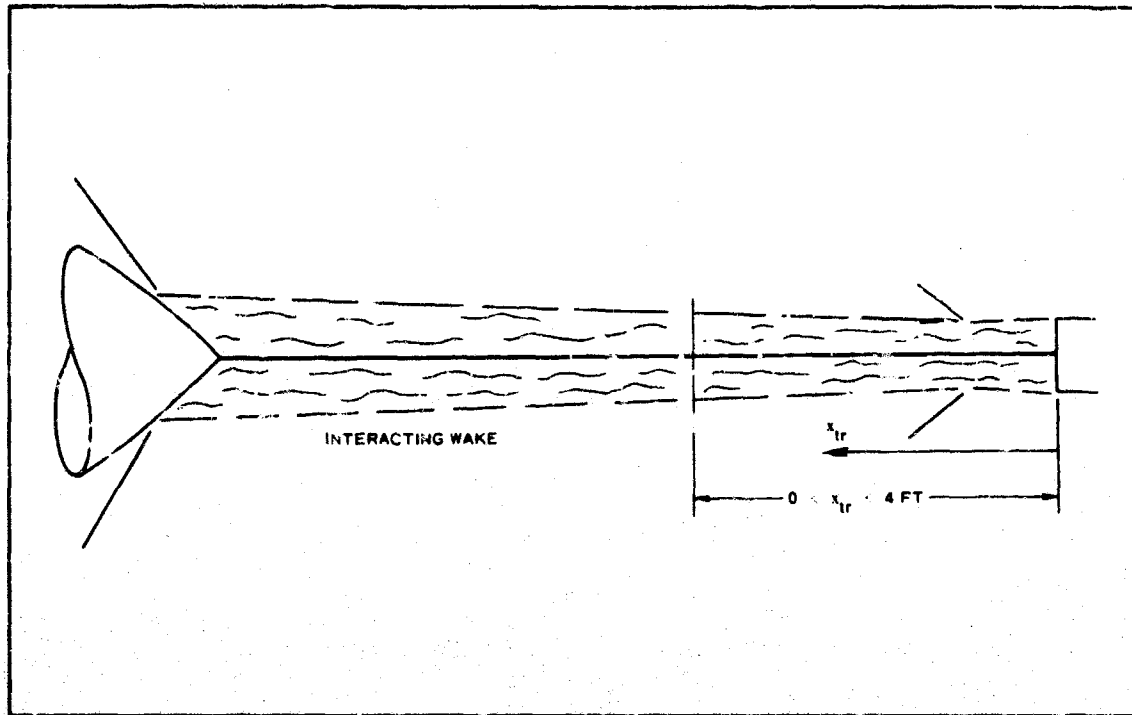


Figure 78 - Flow Field Model

edge of the boundary layer at the decelerator surface. The star superscript indicates the Reynolds number must be evaluated using the reference enthalpy method to estimate the density and viscosity.

In addition to the above flow parameters, it is necessary to specify the pressure distribution over the decelerator surface as a function of Mach number and Reynolds number for the extent of the critical deceleration time flight regime. Typical decelerator pressures were evaluated. Analysis of the pressure distribution data showed that maximum local pressure over the decelerator surface as a function of Mach number would exist at Station $Y/R = 0.5$ for the Mach 5.7 deployment, Station $Y/R = 0.4$ for the Mach 6.7 deployment, and Station $Y/R = 0.9$ for the Mach 9.95 deployment for the duration of the trajectory path during upward flight. Thus, these stations were selected for heating rate analysis.

Figures 79A and B show the cold wall heat flux rate for the Mach 5.7 and 6.7 deployment cases as a function of time from deployment. The heating rates are for two different lengths (x), which is defined as the distance from which the turbulent flow emanated. Since the flow field analysis showed that the wake is probably turbulent, only the $x = 15$ -ft data are representative of heating at the decelerator surface. However, the possibility of slightly higher heating rates exists if transition occurs further downstream. The latter situation appears to be unlikely due to wake interaction effects between the two bodies.

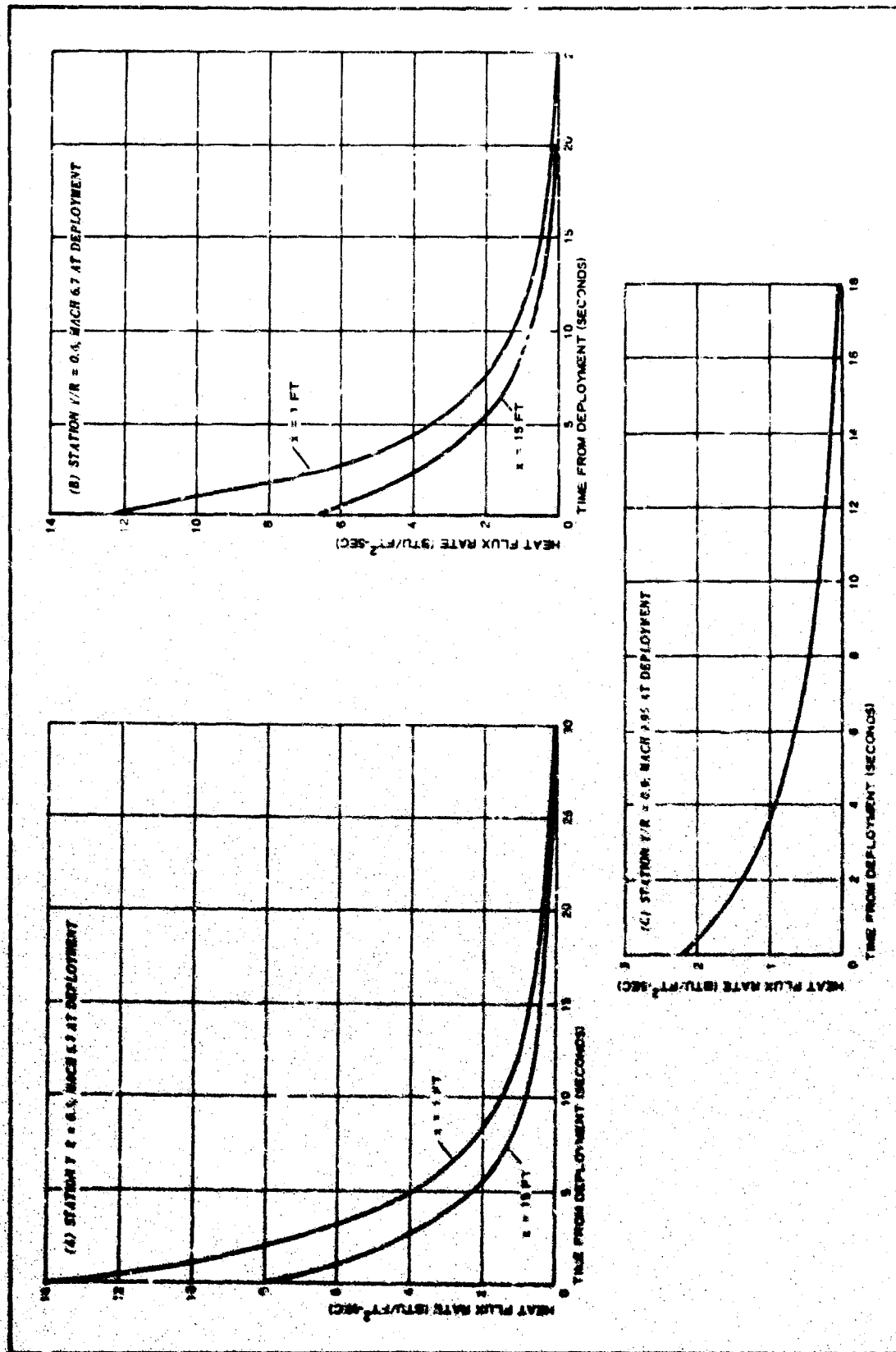


Figure 79 - Cold Wall Heat Flux Rates

The laminar heat flux rates are shown in Figure 79C. Since the methods utilized to calculate these rates are discussed thoroughly in Reference 64, they are not repeated here. It is apparent from the cold wall heat flux curves that the Mach 5.7 deployment case generates the most critical heat addition to the decelerator material. Therefore, this case is next examined for material temperature response.

5. THERMAL ANALYSIS

The temperature response of the decelerator material can be calculated as a function of the aerodynamic heating experienced during the upward leg of the trajectory path. The decelerator cloth selected was Nomex. The coating selected was Dyna-Therm D-65. Typical thermal properties of these materials are given in Table XXXI.

TABLE XXXI - THERMAL PROPERTIES OF NOMEX AND D-65

Property	Nomex	D-65
Weight/area (oz/sq yd)	11.840	. . .
Density (pcf)	42.000	68.600
Specific heat (Btu/lb-F)	0.350	0.250
Thermal conductivity (Btu/ft-hr-F)	0.032	0.053
Emissivity	. . .	0.800

The properties of the D-65 coating were obtained from the Dyna-Therm Corporation, while the Nomex properties were extrapolated from data presented in Reference 69. Since the fabric is a poor conductor and is a nonhomogeneous slab, consider its heating on the basis of one-dimensional heat conduction. The partial differential equation is as follows for heat conduction in a one-dimensional slab versus time:

$$\frac{\partial T}{\partial \tau} = \alpha \left(\frac{\partial^2 T}{\partial y^2} \right) \quad (105)$$

Specifying the inner and outer boundary conditions permits the solution of Equation 105 for the material temperature response. The outer surface boundary equation can be written as:

$$h_c(T_w - T_\infty) - \epsilon \sigma T_w^4 = -k \left\{ \frac{\partial T}{\partial y} \left[T(0, \tau) \right] \right\} \quad (106)$$

At the inner wall, the surface can be assumed to be an adiabatic wall:

$$\frac{\partial T}{\partial y} \bigg|_{y=0} = 0 \quad (107)$$

These equations are converted to finite-difference form and solved on a digital computer as a function of the heat flux rates evaluated in the previous section. The heat flux rates are coupled to the transient heat conduction solution by the following relationship:

$$h_c(T_{aw} - T_w) = \dot{q}_w = \dot{q}_{cw} \left(\frac{h_{aw} - h_w}{h_{cw} - h_{cw}} \right) \quad (108)$$

The cold wall heat flux rates are thus converted to hot wall heat flux rates by the enthalpy ratio.

6. RESULTS AND CONCLUSIONS

The material temperature response for the Mach 5.7 deployment at Station Y/R = 0.5 is shown in Figure 80. Since the heating analysis had shown that this deployment condition generates the most critical heating rates during the upward portion of the trajectory paths, it was concluded that the material temperature response for the other two Mach number cases (6.7 and 9.95) will result in a less critical temperature response. Profiles for these two cases were not calculated.

A maximum temperature of 530 F is reached on the coating surface of the slab at about 8 sec after deployment for the Mach 5.7 case. Internal temperature rise lags the surface temperature rise considerably. The temperature of the Nomex cloth reaches a maximum of 230 F about 30 sec

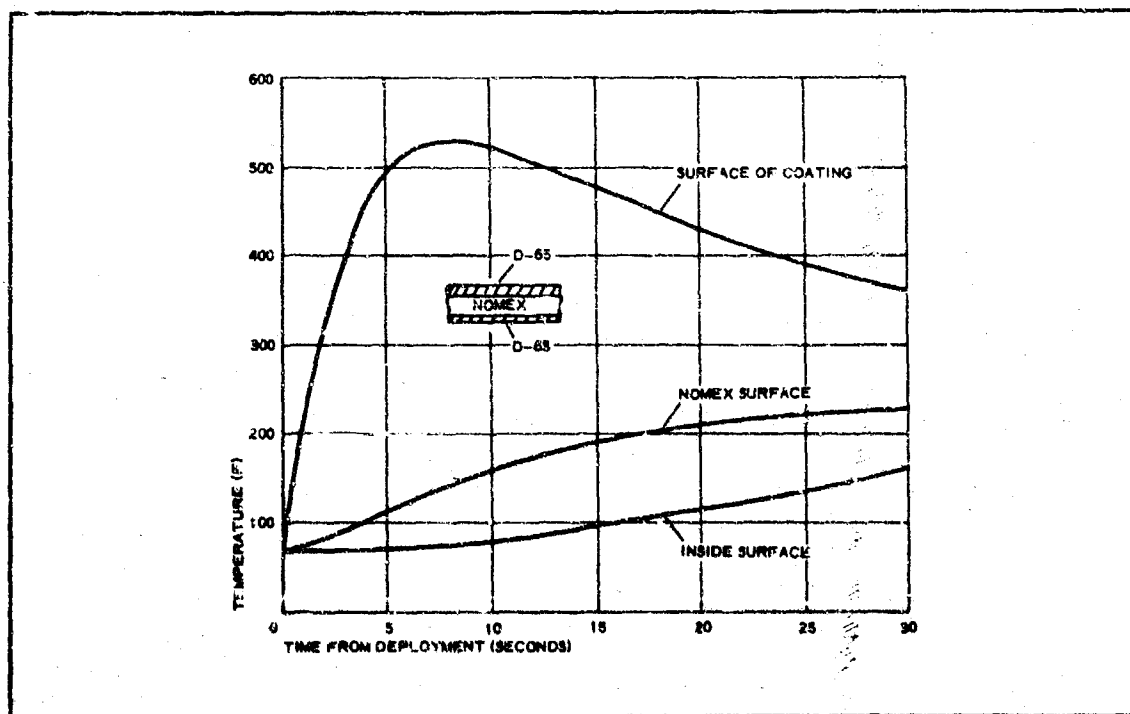


Figure 80 - Temperature Response: Y/R = 0.5, Mach 5.7 Deployment

after deployment. At this time, the combined bodies are rising above the sensible atmosphere and will continue to cool until they again re-enter the sensible atmosphere. Thus, the effects of aerodynamic heating for the flight test cases under consideration in the low hypersonic flight regime apparently are within material capabilities during upward flight. The re-entry heating conditions for these flight test cases are likely to be more critical for the Nomex.

LIST OF REFERENCES

1. Nebiker, F. R.: Aerodynamic Deployable Decelerator Performance-Evaluation Program. Phase I Technical Report. AFFDL-TR-65-27. Wright-Patterson Air Force Base, Ohio, Air Force Flight Dynamics Laboratory, Research and Technology Division, Air Force Systems Command, prepared by Goodyear Aerospace Corporation, Akron, Ohio, under Contract AF33(657)-10955, May 1965.
2. GER-11732: Static Test of "A-1" ADDPEP Vehicle. Akron, Ohio, Goodyear Aerospace Corporation, September 1964.
3. GER-11664S1: Aerodynamic Deployable Decelerator Performance-Evaluation Program. Akron, Ohio, Goodyear Aerospace Corporation, November 1964.
4. GER-11664S9: Aerodynamic Deployable Decelerator Performance-Evaluation Program. Akron, Ohio, Goodyear Aerospace Corporation, April 1965.
5. GER-11664S3: Aerodynamic Deployable Decelerator Performance-Evaluation Program. Akron, Ohio, Goodyear Aerospace Corporation, October 1964.
6. GER-11664S10: Aerodynamic Deployable Decelerator Performance-Evaluation Program. Akron, Ohio, Goodyear Aerospace Corporation, May 1965.
7. GER-11664S11: Aerodynamic Deployable Decelerator Performance-Evaluation Program. Akron, Ohio, Goodyear Aerospace Corporation, June 1965.
8. GER-11664S1: Aerodynamic Deployable Decelerator Performance-Evaluation Program. Akron, Ohio, Goodyear Aerospace Corporation, August 1964.
9. GER-11664S8: Aerodynamic Deployable Decelerator Performance-Evaluation Program. Akron, Ohio, Goodyear Aerospace Corporation, March 1965.
10. GER-11664: Aerodynamic Deployable Decelerator Performance-Evaluation Program. Akron, Ohio, Goodyear Aerospace Corporation, July 1964.
11. Deitering, J. S.: Wind Tunnel Investigation of Flexible Parachute Model Characteristics at Mach Numbers 1.5 to 5. AEDC-TDR-63-263. Arnold Air Force Station, Tenn., Arnold Engineering Development Center, Air Force Systems Command, January 1964.

LIST OF REFERENCES

AFFDL-TR-67-25

12. Lowry, J. F.: Aerodynamic Characteristics of Various Types of Full Scale Parachutes at Mach Numbers from 1.8 to 3.0. AEDC-TDR-64-120. Arnold Air Force Station, Tenn., Arnold Engineering Development Center, Air Force Systems Command, June 1964.
13. Deitering, J. S.; and Hilliard, E. E.: Wind Tunnel Investigation of Flexible Aerodynamic Decelerator Characteristics at Mach Numbers 1.5 to 6. AEDC-TR-65-110. Arnold Air Force Station, Tenn., Arnold Engineering Development Center, Air Force Systems Command, June 1965.
14. GER-11914: ADDPEP-A Vehicle Drop Test No. 1 - Parachute LP-2 Project 6065, Task 07. Akron, Ohio, Goodyear Aerospace Corporation, January 1965.
15. GER-11664S7: Aerodynamic Deployable Decelerator Performance-Evaluation Program. Akron, Ohio, Goodyear Aerospace Corporation, February 1965.
16. DR-N-7252: LP-2 Computer Run. Land Air Report. 10 February 1965.
17. Adkisson, B. N.: Supersonic Parachutes-LP-3. DR-N-7296. White Sands Missile Range, N.M., U.S. Army, 1 March 1965.
18. Adkisson, B. N.: Supersonic Parachutes-LP-3. DR-N-7294 and Addendum. White Sands Missile Range, N.M., U.S. Army, 17 March 1965.
19. Adkisson, B. N.: Supersonic Parachutes-LP-4. Vol I and II. DR-N-7350. White Sands Missile Range, N.M., U.S. Army, 15 March 1965.
20. Adkisson, B. N.: Supersonic Parachutes-LP-4. DR-N-7323. White Sands Missile Range, N.M., U.S. Army, 5 March 1965.
21. Martinelli, E.: Supersonic Parachutes-LP-5. DR-N-7423. White Sands Missile Range, N.M., U.S. Army, 2 April 1965.
22. Martinelli, E.: Supersonic Parachutes-LP-5. DR-N-7394. White Sands Missile Range, N.M., U.S. Army, 26 March 1965.
23. GER-11806: Aerodynamic Deployable Decelerator Performance-Evaluation Program Parachute Test Items LP-3 and LP-4. Akron, Ohio, Goodyear Aerospace Corporation, November 1964.
24. Stricker, W. P.: Mass Properties Data ADDPEP Test Vehicles Capabilities "A", "B", and "C". GER-11498. Contract No. AF33(657)-10955. Akron, Ohio, Goodyear Aerospace Corporation, 26 February 1964.
25. MIL-W-27657A: Webbing, Textile, Woven Nylon, for Decelerators. Washington, D. C., Department of Defense, 15 July 1963.
26. Emmons, H. W.: Gas Dynamics Tables for Air. New York, Dover Publications, Inc., 1947.

LIST OF REFERENCES

AFFDL-TR-67-25

27. Binder, R. C.: Fluid Mechanics. New York, Prentice-Hall, Inc., 1949.
28. ASD-TR-61-579: Performance of and Criteria for Deployable Aerodynamic Decelerators. Akron, Ohio, Goodyear Aerospace Corporation, December 1963.
29. Bartz, D. F.: A Simple Equation for Rapid Estimation of Rocket Nozzles Convective Heat Transfer Coefficient. Pasadena, Calif., Jet Propulsion Laboratory, January 1957, pp. 49-51.
30. Schneider, P. J.: Temperature Response Charts. New York, John Wiley and Sons, Inc., 1963.
31. GER-11482: Hypersonic Aerodynamic Heating. Akron, Ohio, Goodyear Aerospace Corporation, January 1964.
32. Specification CCC-T-191B: Textile Test Methods. Washington, D. C., Department of Defense, 15 May 1951.
33. Drawing 530A005-016 and Rev E: Canopy, Parachute, 16 Ft. and Hemisflo. Akron, Ohio, Goodyear Aerospace Corporation, 2 October 1964 and 4 August 1965.
34. MIL-W-5625E: Webbing, Textile, Nylon Tubular (Amendment 1). Washington, D. C., Department of Defense, 19 May 1964.
35. Drawing 530A005-017: Deployment Bag (16 Ft. Canopy). Akron, Ohio, Goodyear Aerospace Corporation, 16 October 1964.
36. MIL-T-5038C: Tapc and Webbing, Textile, Reinforcing, Nylon (Amendment 1). Washington, D. C., Department of Defense, 30 September 1960.
37. Drawing 530A005-303: Canopy, Parachute, 30-In. Diam. (Drogue). Akron, Ohio, Goodyear Aerospace Corporation, 12 August 1965.
38. Drawing 530A005-019: Deployment Bag (Drogue). Akron, Ohio, Goodyear Aerospace Corporation, 11 November 1964.
39. GER-11664S5: Aerodynamic Deployable Decelerator Performance-Evaluation Program. Akron, Ohio, Goodyear Aerospace Corporation, November 1964.
40. GER-11523: Aerodynamic Deployable Decelerator Performance-Evaluation Program BALLUTE Test Item B-2. Akron, Ohio, Goodyear Aerospace Corporation, April 1964.
41. GER-11523S1: Aerodynamic Deployable Decelerator Performance-Evaluation Program BALLUTE Test Item B-3. Akron, Ohio, Goodyear Aerospace Corporation, April 1964.
42. GER-12683: Aerodynamic Deployable Decelerator Performance-Evaluation Program BALLUTE Test Items TB-4, 5, and 6. Akron, Ohio, Goodyear Aerospace Corporation, May 1966.

LIST OF REFERENCES

AFFDL-TR-67-25

43. Drawing 530A005-020: BALLUTE Modification Wind-Tunnel Test Model 60-Inch Diameter. Akron, Ohio, Goodyear Aerospace Corporation, 16 November 1964.
44. GER-11664S6: Aerodynamic Deployable Decelerator Performance-Evaluation Program. Akron, Ohio, Goodyear Aerospace Corporation, January 1965.
45. MacLanahan, Jr., D. A.: An Investigation of Various Types of Decelerators at Mach Number 2.8. AEDC-TR-66-136. Arnold Air Force Station, Tenn. :, Arnold Engineering Development Center, Air Force Systems Command, July 1966.
46. GER-11665: Aerodynamic Deployable Decelerator Performance-Evaluation Program - Flight Test Report TB-1A. Akron, Ohio, Goodyear Aerospace Corporation, July 1964.
47. GER-11665S1: Aerodynamic Deployable Decelerator Performance-Evaluation Program - Flight Test Report TB-1A. Akron, Ohio, Goodyear Aerospace Corporation, February 1965.
48. GER-11665S2: Aerodynamic Deployable Decelerator Performance-Evaluation Program - Flight Test Report TB-1B. Akron, Ohio, Goodyear Aerospace Corporation, February 1965.
49. GER-11665S3: Aerodynamic Deployable Decelerator Performance-Evaluation Program - Flight Test Report TB-2. Akron, Ohio, Goodyear Aerospace Corporation, February 1965.
50. GER-11664S12: Aerodynamic Deployable Decelerator Performance-Evaluation Program - Monthly Progress Report No. 13. Akron, Ohio, Goodyear Aerospace Corporation, July 1965.
51. GER-11664S21: Aerodynamic Deployable Decelerator Performance-Evaluation Program. Akron, Ohio, Goodyear Aerospace Corporation, September 1966.
52. Alexander, W. C.: Investigation To Determine The Feasibility of Using Inflatable Balloon-Type Drag Devices For Recovery Applications In The Transonic, Supersonic, And Hypersonic Flight Regimes, Part II. ASD-TDR-62-702. Akron, Ohio, Goodyear Aerospace Corporation, October 1962.
53. Deitering, J. S.: Performance of Flexible Aerodynamic Decelerators at Mach Numbers From 1.5 to 6. AEDC-TDR-63-119, July 1963.
54. Kaupp, Jr., H.: Gemini BALLUTE Structural Test At Mach Numbers 0.55 and 1.92. AEDC-TDR-64-131. Arnold Air Force Station, Tenn. :, Arnold Engineering Development Center, Air Force Systems Command, June 1964.

LIST OF REFERENCES

AFFDL-TR-67-25

55. White, W. E.; and Brice, T. R.: Static Stability Characteristics of the ALARR Payload and the Effect of the Wake on the BALLUTE Decelerator Characteristics at Transonic Speeds. AEDC-TR-65-265, Arnold Air Force Station, Tenn., Arnold Engineering Development Center, Air Force Systems Command, December 1965.
56. Carleton, W. E.; and Anderson, C. F.: The Characteristics of a BALLUTE in the Wake of the Martin Full-Scale SV-5D Vehicle at Mach Numbers From 0.6 to 2.9 (U). AEDC-TR-65-266. Arnold Air Force Station, Tenn., Arnold Engineering Development Center, Air Force Systems Command, December 1965. CONFIDENTIAL
57. Bell, D. R.: Pressure Measurements on the Rigid Model of a Balloon Decelerator in the Wake of a Simulated Missile Payload at Mach Numbers 1.5 to 6.0. AEDC-TDR-64-65. Arnold Air Force Station, Tenn., Arnold Engineering Development Center, Air Force Systems Command, April 1964.
58. GER-11538: Gemini BALLUTE System Development - Final Report. Akron, Ohio, Goodyear Aerospace Corporation, January 1965.
59. Unpublished, Subject: Wind Tunnel Tests of TB-3 at Mach Number 3 - Tests of December 1964. Arnold Air Force Station, Tenn., Arnold Engineering Development Center, Air Force Systems Command.
60. Reichenau, David E. A.: Investigation of a BALLUTE Behind the Martin SV-5D Vehicle at Mach .6 to 2.6. AEDC-TR-66-68. Arnold Air Force Station, Tenn., Arnold Engineering Development Center, Air Force Systems Command, March 1966.
61. GER-11762: BALLUTE Evaluation Program For Project Sleigh Ride. Akron, Ohio, Goodyear Aerospace Corporation, October 1964.
62. Textile Fibers NP-33: Properties of NOMEX High Temperature Resistant Nylon Fiber. Wilmington, Del., E. I. duPont de Nemours & Company, October 1963.
63. Chauncey, C.; Gardella, J.; and Kaswell, E.: Research Leading to Optimum Fibrous Structures of HT-1 Yarn. ML-TDR-64-78. Wright-Patterson Air Force Base, Ohio, Materials Laboratory, Research and Technology Division, Air Force Systems Command, January 1964.
64. Nerem, R: Supersonic Wake Phenomena With Application to BALLUTE-Type Decelerators. GER-11820. Akron, Ohio, Goodyear Aerospace Corporation, November 1964.
65. Nerem, R: Pressure and Heat Transfer on High-Speed Aerodynamic Decelerators of the BALLUTE Type. Houston, Texas, AIAA Aerodynamic Deceleration Systems Conference, 7-9 September 1966.
66. Statson, K. F.: "Boundary Layer Transition on Blunt Bodies with Highly Cooled Boundary Layers," J. Aerospace Sciences, Vol. 27, No. 2 pp 81-90, 1960.

LIST OF REFERENCES

AFFDL-TR-67-25

67. Zeiberg, S. L.: "Transitions Correlations for Hypersonic Wakes," AIAA Journal, Vol. 2, No. 3, pp. 564-565, March 1964.
68. NACA R-1135: Equations, Tables, and Charts for Compressible Flow. Moffet Field, Calif., Ames Research Staff, 1953.
69. Engholm, G.; Lis, S. J.; and Baschierre, R. J.: Thermal Transport and Radiation Properties of Fibrous Structural Materials. ASD-TDR-62-870. Wright-Patterson Air Force Base, Ohio, Aeronautical Systems Division, Air Force Systems Command, November 1962.
70. Drawing 530A005-201: BALLUTE Assembly, 60 Inch Diameter (No Fence), TB-4, TB-5, TB-6. Akron, Ohio, Goodyear Aerospace Corporation, 14 April 1966.
71. Drawing 530A005-033: Inlet Assembly, BALLUTE. Akron, Ohio, Goodyear Aerospace Corporation, 12 April 1966.
72. Drawing 530A005-111: Fluid Bag, BALLUTE Inflation. Akron, Ohio, Goodyear Aerospace Corporation, 10 May 1966.
73. Drawing 530A005-036: Fluid Bag Installation, BALLUTE Inflation. Akron, Ohio, Goodyear Aerospace Corporation, 11 May 1966.
74. Drawing 530A005-050: Deployment Bag, BALLUTE. Akron, Ohio, Goodyear Aerospace Corporation, 19 February 1966.
75. GER-12120: Aerodynamic Deployable Decelerator Performance - Evaluation Program BALLUTE Test Item MB-1. Akron, Ohio, Goodyear Aerospace Corporation, 29 March 1965.
76. Drawing 530A005-021: BALLUTE Assembly, Wind Tunnel Test Model (MB-1WT1). Akron, Ohio, Goodyear Aerospace Corporation, 10 December 1964.
77. Drawing 530A005-023: BALLUTE Assembly, Wind Tunnel Test Model (MB-1WT2). Akron, Ohio, Goodyear Aerospace Corporation, 22 February 1965.
78. Cross, W. B.; Marco, D. M.; and Nass, F.: New and Improved Materials for Expandable Structures. ASD-TDR-62-542, Part IV. Akron, Ohio, Goodyear Aerospace Corporation, October 1963.
79. Marco, D. M.: Development of Goodyear Silicone-Ceramic High-Temperature Coating CS-105, G&R-10576. Akron, Ohio, Goodyear Aerospace Corporation, February 1962.
80. Drawing 530A005-024: Ballute Assembly, Metal (MB-1). Akron, Ohio, Goodyear Aerospace Corporation, 19 February 1966.

UNCLASSIFIED

Security Classification

DOCUMENT CONTROL DATA - R&D

(Security classification of title, body of abstract and indexing annotation must be entered when the overall report is classified)

1 ORIGINATING ACTIVITY (Corporate author)		2a REPORT SECURITY CLASSIFICATION	
Goodyear Aerospace Corporation Akron, Ohio		UNCLASSIFIED	
		2b GROUP	
3 REPORT TITLE			
Aerodynamic Deployable Decelerator Performance-Evaluation Program, Phase II			
4 DESCRIPTIVE NOTES (Type of report and inclusive dates)			
Final Report April 1964 - April 1967			
5 AUTHOR(S) (Last name, first name, initial)			
Bloetscher, Frederick			
6 REPORT DATE		7a TOTAL NO OF PAGES	7b NO OF REFS
June 1967		196	40
8a CONTRACT OR GRANT NO.		9a ORIGINATOR'S REPORT NUMBER(S)	
AF33(615)-1513		GER-12907	
b PROJECT NO 6065			
c Task No. 606505		9b OTHER REPORT NO(S) (Any other numbers that may be assigned this report)	
d.		AFFDL-TR-67-25	
10 AVAILABILITY/LIMITATION NOTICES			
This document is subject to special export controls, and each transmittal to foreign governments or foreign nationals may be made only with prior approval of the Air Force Flight Dynamics Laboratory			
11 SUPPLEMENTARY NOTES		12 SPONSORING MILITARY ACTIVITY	
		Air Force Flight Dynamics Laboratory Wright-Patterson AFB, Ohio 45433	
13 ABSTRACT			
<p>The Aerodynamic Deployable Decelerator Performance-Evaluation Program (ADDPEP) aims to advance the state of the art by developing the most effective analytical and empirical techniques for designing aerodynamic deployable decelerators and for evaluating these engineering techniques through wind-tunnel and free-flight tests. During ADDPEP Phase II, two types of decelerators were investigated: large reefed supersonic parachutes and ram-inflated balloon-type BALLUTES. The areas investigated included analytical and engineering design, material capabilities, fabrication techniques, and wind-tunnel and free-flight tests. In general, efforts were successful in developing engineering techniques for the design of decelerators capable of performing in severe environments. More specifically: (1) Free-flight tests were performed on a hemispherical parachute having a nominal 16-ft-diameter canopy, a 10-percent extended skirt, and a 14-percent porosity. This design was tested for 200,000-lb opening loads; deployment Mach numbers were 1.50, 1.63, and 1.84 at altitudes of 13,700, 15,500, and 16,500 ft, respectively. The results confirmed that this parachute has excellent aerodynamic characteristics and adequate strength. (2) Five-foot-diameter BALLUTES, both textile and metal, were fabricated. These were designed for a broad spectrum of deployment conditions ranging from Mach 2.7 at 73,000 ft to Mach 10 at 225,000 ft. The textile BALLUTES were wind-tunnel and free-flight tested; the metal BALLUTES were wind-tunnel tested only. Flight tests were limited to Mach 9.7, and wind-tunnel tests to Mach 5. The flight test data supported wind-tunnel data, which indicated that excellent stability and structurally adequate designs can be attained with five-foot-diameter BALLUTES.</p>			

DD FORM 1473
1 JAN 64

UNCLASSIFIED

Security Classification

UNCLASSIFIED
Security Classification

14. KEY WORDS	LINK A		LINK B		LINK C	
	ROLE	WT	ROLE	WT	ROLE	WT
Supersonic Decelerators						
High Dynamic Pressure Supersonic Parachutes						
Ram Air-Inflated Balloon-Type Decelerators,						
BALLUTE						
Aerodynamic						
Aerodynamic Heating						

INSTRUCTIONS

1. ORIGINATING ACTIVITY: Enter the name and address of the contractor, subcontractor, grantee, Department of Defense activity or other organization (corporate author) issuing the report.

2a. REPORT SECURITY CLASSIFICATION: Enter the overall security classification of the report. Indicate whether "Restricted Data" is included. Marking is to be in accordance with appropriate security regulations.

2b. GROUP: Automatic downgrading is specified in DoD Directive 5200.10 and Armed Forces Industrial Manual. Enter the group number. Also, when applicable, show that optional markings have been used for Group 3 and Group 4 as authorized.

3. REPORT TITLE: Enter the complete report title in all capital letters. Titles in all cases should be unclassified. If a meaningful title cannot be selected without classification, show title classification in all capitals in parenthesis immediately following the title.

4. DESCRIPTIVE NOTES: If appropriate, enter the type of report, e.g., interim, progress, summary, annual, or final. Give the inclusive dates when a specific reporting period is covered.

5. AUTHOR(S): Enter the name(s) of author(s) as shown on or in the report. Known last name, first name, middle initial. If military, show rank and branch of service. The name of the principal author is an absolute minimum requirement.

6. REPORT DATE: Enter the date of the report as day, month, year, or month, year. If more than one date appears on the report, use date of publication.

7a. TOTAL NUMBER OF PAGES: The total page count should follow normal pagination procedures, i.e., enter the number of pages containing information.

7b. NUMBER OF REFERENCES: Enter the total number of references cited in the report.

8a. CONTRACT OR GRANT NUMBER: If appropriate, enter the applicable number of the contract or grant under which the report was written.

8b, 8c, & 8d. PROJECT NUMBER: Enter the appropriate military department identification, such as project number, subject number, system number, task number, etc.

9a. ORIGINATOR'S REPORT NUMBER(S): Enter the official report number by which the document will be identified and controlled by the originating activity. This number must be unique to this report.

9b. OTHER REPORT NUMBER(S): If the report has been assigned any other report numbers (either by the originator or by the sponsor), enter this number(s).

10. AVAILABILITY/ CITATION NOTES: Enter any limitations or further dissemination of the report, other than those

imposed by security classification, using standard statements such as:

- (1) "Qualified requesters may obtain copies of this report from DDC."
- (2) "Foreign announcement and dissemination of this report by DDC is not authorized."
- (3) "U. S. Government agencies may obtain copies of this report directly from DDC. Other qualified DDC users shall request through _____."
- (4) "U. S. military agencies may obtain copies of this report directly from DDC. Other qualified users shall request through _____."
- (5) "All distribution of this report is controlled. Qualified DDC users shall request through _____."

If the report has been furnished to the Office of Technical Services, Department of Commerce, for sale to the public, indicate this fact and enter the price, if known.

11. SUPPLEMENTARY NOTES: Use for additional explanatory notes.

12. SPONSORING MILITARY ACTIVITY: Enter the name of the departmental project office or laboratory sponsoring (paying for) the research and development. Include address.

13. ABSTRACT: Enter an abstract giving a brief and factual summary of the document indicative of the report, even though it may also appear elsewhere in the body of the technical report. If additional space is required, a continuation sheet shall be attached.

It is highly desirable that the abstract of classified reports be unclassified. Each paragraph of the abstract shall end with an indication of the military security classification of the information in the paragraph, represented as (TS), (S), (C), or (U).

There is no limitation on the length of the abstract. However, the suggested length is from 150 to 225 words.

14. KEY WORDS: Key words are technically meaningful terms or short phrases that characterize a report and may be used as index entries for cataloging the report. Key words must be selected so that no security classification is required. Identifiers, such as equipment model designation, trade name, military project code name, geographic location, may be used as key words but will be followed by an indication of technical context. The assignment of links, roles, and weights is optional.

UNCLASSIFIED
Security Classification